

NANOPARTICLE DYNAMICS IN POLYMER NANOCOMPOSITES USING
TIME-OF-FLIGHT SECONDARY ION MASS SPECTROMETRY

Kaitlin Wang

A DISSERTATION

in

Materials Science and Engineering

Presented to the Faculties of the University of Pennsylvania

in

Partial Fulfillment of the Requirements for the

Degree of Doctor of Philosophy

2024

Supervisor of Dissertation

Karen I. Winey, Professor, Materials Science and Engineering and Chemical and Biomolecular Engineering

Graduate Group Chairperson

Eric A. Stach, Professor, Materials Science and Engineering

Dissertation Committee

Russell J. Composto, Professor, Materials Science and Engineering

Robert A. Riggelman, Associate Professor, Chemical and Biomolecular Engineering

Eric A. Stach, Professor, Materials Science and Engineering

NANOPARTICLE DYNAMICS IN POLYMER NANOCOMPOSITES USING TIME-OF-
FLIGHT SECONDARY ION MASS SPECTROMETRY

COPYRIGHT

2024

Kaitlin Wang

To Mom, Dad, Kam, James, and Tigerlily

ACKNOWLEDGMENT

I strongly believe the sincerest sentiments are expressed privately; however, some public thanks are in order due to the collaborative nature of this work. I'd like to acknowledge Karen's support for the past 5 years and her commitment to detailed writing and experiments. Thank you to Russell Composto for discussing particle diffusion, and for the indefinite loan of his mathematics of diffusion book. I'd like to thank Eric Stach for his support, thesis writing tips, and great conversation. My thanks to Robert Riggelman for his perspective and empathy for students.

For the staff in LRSM and Singh, special thanks to Jamie Ford for taking my calls on Sundays in the ToF-SIMS box and helping me troubleshoot over text any time of day. This thesis was contingent on continued ToF operation, and I thank him for his efforts. Thanks to Steve Szewczyk for always making the effort to solve a new unexpected lab issue during building renovations and COVID.

To the former students who chose to take the time out of their day to mentor me, I'm always grateful for your efforts and thoughts. Thank you to Eric Bailey for setting the stage for this project, for being a welcoming presence in lab, and scientific conversation and job advice years post-graduation. Thank you to James Pressly for endless continued support, but especially for those early COVID lab days and his endless patience answering the endless questions I had. Thank you to Katie Rose for her advocacy, friendship, and professional advice. Thanks to Junwei Xiang for commiserating with me during COVID, and for passing on his efforts to ensure my success. Thank you to Metin Örnek for guiding me through my first lab experience at Rutgers and ensuring that I published in time solely for my graduate applications.

The special edition global-pandemic-and-building-renovations Ph.D. was not an easy ride. Thank you to Alexander Ng for the good times whether it be playing chess, running a marathon, or building a keyboard. Thank you to Hyeongjun Koh for the deadpan humor and weekend Singh Center talk.

I am privileged to have my dearest friends and their support. Thank you to Sophie Pastore for always hyping me up and for the grey flannel I wear weekly. Thank you to Katie Sun for always being ready to weather a new challenging time or celebrate my latest achievement with me over the past eight years. Thank you to Jason Lum, Kristie Wong, Priyanka Patel, and Brandon Lebovitch for over a decade of faith in my abilities and character. Finally, thank you to Mom, Dad, Kam, and James.

ABSTRACT

NANOPARTICLE DYNAMICS IN POLYMER NANOCOMPOSITES USING TIME-OF-FLIGHT SECONDARY ION MASS SPECTROMETRY

Kaitlin Wang

Karen I. Winey

Nanocomposites are vital for their ability to enhance material properties such as mechanical strength, thermal stability, and barrier performance through the controlled integration of nanoparticles into polymer matrices. Understanding nanoparticle (NP) diffusion is crucial for tuning the dispersion, processing conditions, and in result the composite performance. This dissertation significantly advances the understanding of nanoparticle dynamics in polymer nanocomposites (PNCs) through the innovative use of time-of-flight secondary ion mass spectrometry (ToF-SIMS), focusing on the diffusion behaviors of NPs. To rigorously analyze NP diffusion, a robust methodology has been established for employing ToF-SIMS. This technique not only allows for precise measurement of NP and polymer diffusion but also expands the boundaries of possible diffusion measurements across extensive length scales and within a broader array of materials. By establishing ToF-SIMS as a reliable method for measuring nanoparticle and polymer diffusion with materials such as poly(2-vinyl pyridine), silica nanoparticles, and deuterated polystyrene, this work extends the scope of diffusion studies in PNCs.

The investigation explores NP diffusion within attractive polymer melts, adapting theoretical insights to discern two distinct diffusion modes—core-shell and vehicular—evident in

the experimental data. The presence of a bound polymer layer in attractive PNCs causes NPs to deviate significantly from classical Stokes-Einstein behavior, with the degree of deviation correlated to the monomeric desorption times (τ_{des}) of the bound polymer. We find experimentally that the τ_{des} of Al_2O_3 is significantly shorter (~ 50 s) compared to SiO_2 ($\tau_{\text{des}} > 6000$ s) at 180°C , and that this desorption time is independent of NP diameter.

Moreover, the dissertation addresses the practical application of NPs in crowded environments, which introduces complex behaviors. Applying ToF-SIMS, this study successfully differentiates smaller Al_2O_3 NPs from a PNC with larger SiO_2 NPs and quantifies the Al_2O_3 NP diffusion in crowded PNCs. NP loading and interparticle distance are shown to critically influence NP diffusion and subsequently modulate the local polymer dynamics, affecting both the monomeric desorption times and overall NP diffusion mode.

This foundational work significantly enhances the understanding of polymer-bound layers and complex NP diffusion mechanisms, setting the stage for future advancements in PNCs. These insights are poised to improve the processability of PNCs and expand their applications in dynamic environments, from self-healing materials to targeted drug delivery systems.

CONTENTS

ACKNOWLEDGMENT	IV
ABSTRACT	VI
LIST OF TABLES	XI
LIST OF FIGURES	XII
CHAPTER 1 : POLYMER AND NANOPARTICLE DYNAMICS IN NANOCOMPOSITES AND TIME-OF-FLIGHT SECONDARY ION MASS SPECTROSCOPY	1
1.1 Introduction.....	1
1.2 Nanoparticle Diffusion in Polymer Melts	4
1.2.1 Athermal PNCs	4
1.2.2 Attractive PNCs	8
1.2.3 Confined NP Diffusion	10
1.3 Prior Methods to Determine Polymer and Nanoparticle Dynamics in PNCs	12
1.4 Polymer Applications of Time-of-Flight Secondary Ion Mass Spectrometry	15
1.4.1 Comparison of ToF-SIMS to other Surface-Sensitive Methods	19
1.5 Outline of Thesis	22
1.6 References	26
CHAPTER 2 : TOF-SIMS DEPTH PROFILING TO MEASURE NANOPARTICLE AND POLYMER DIFFUSION IN POLYMER MELTS	46
2.1 Introduction.....	46
2.2 Experimental Section.....	50
2.3 Results	54
2.4 Discussion.....	67
2.5 Conclusion	69
2.6 References	71
CHAPTER 3 : VEHICULAR AND CORE-SHELL NANOPARTICLE DIFFUSION IN ENTANGLED ATTRACTIVE POLYMER MELTS	76
3.1 Introduction.....	76
3.2 Experimental Details	80
3.3 Results and Discussion.....	83
3.4 Conclusions.....	93
3.5 References	94
CHAPTER 4 : BOUND LAYER DESORPTION AND NANOPARTICLE DIFFUSION IN CROWDED POLYMER MELTS.....	99
4.1 Introduction.....	99
4.2 Results	101

4.3 Methods.....	111
4.4 References.....	113
CHAPTER 5 : SUMMARY AND FUTURE WORK.....	118
5.1 Summary.....	118
5.2 Future Work.....	120
APPENDIX A : SUPPORTING INFORMATION FOR CHAPTER 2.....	148
A.1 NP and Polymer Characterization	148
A.2 Pixel Resolution and Depth Measurements	149
A.3 Fit Quality (R^2).....	152
A.4 Theoretical D_{NP} Calculations.....	153
A.5 Deuterated Polymer ToF-SIMS Images and Measurements	154
A.6 D_{poly} Comparison to Literature Values	156
A.7 References	157
APPENDIX B : SUPPORTING INFORMATION FOR CHAPTER 3.....	158
B.1 Processing Conditions and Data Fits.....	158
B.2 Tabulated Diffusion Coefficients	167
B.3 Vehicular and Core-shell Diffusion Calculations	169
B.4 References	174
APPENDIX C : SUPPORTING INFORMATION FOR CHAPTER 4.....	188
C.1 ToF-SIMS Characterization of the $SiO_2-Al_2O_3$ -PNC trilayer Films	191
C.2 Diffusion Coefficients for Al_2O_3	194
C.3 Derivation of Bimodal Interparticle Distance Model and Calculation	195
C.4 Higher Loading ($\phi_{Al_2O_3} = 0.05$) Arrested Diffusion at $ID_{bi} < 1$	199
APPENDIX D : TOF-SIMS OPERATION AND DATA ANALYSIS.....	200
D.1 Introduction to Tescan S8252X FIB-SEM.....	200
D.1.1 Fundamentals of ToF-SIMS.....	200
D.1.2 Primary vs. Cluster Ion Beams in ToF Systems.....	203
D.2 ToFWERK Software.....	204
D.3 Tilt-Correction Program – MATLAB Code.....	206
D.3.1 The Computer Vision Toolbox.....	206
D.3.2 Workflow Overview	208
D.4 References	217
APPENDIX E : PREPARATION OF ALUMINA NANOPARTICLES.....	233
E.1 Preparation of Alumina-P2VP Solution.....	234
E.2 Qualitative Notes	236
APPENDIX F : SOLVENT EXCHANGE OF LUDOX NANOPARTICLES	238

F.1 Materials and Motivation	238
---	------------

LIST OF TABLES

Table A.1: Table summarizing quality of fits (R^2) for Figure 2.4 and Figure 2.5 . Best fit is bolded.....	152
Table A.2: Expected D_{NP} range for $R_{NP} = 26.1$ nm using Eqn. S1-3 with ϕ_{eff} and η_{PNC} values.	154
Table A.3: D_{dPS} from individual fits and their respective R^2 values, for various annealing times.	155
Table B.1: Molecular weight characterization of poly(2-vinylpyridine) and calculated R_g . All samples were measured with tetrahydrofuran as the carrier solvent and normalized using a polystyrene standard. The radius of gyration was calculated using Rubinstein and Colby. ³⁴	158
Table B.2 : Spincoating conditions to create poly(2-vinylpyridine) films. Parameters include weight-averaged molecular weights, solution concentrations, spincoating speeds, and spin times to create the ~ 4 μ m thick P2VP matrix films.	159
Table B.3: Spincoating conditions to create polymer nanocomposite films. Parameters include weight-averaged molecular weights, solution concentrations, spincoating speeds, and spin times to create thin PNC center layers (200 ± 60 nm).	159
Table B.4: Measured diffusion coefficients for large SiO_2 ($R_{NP} = 26.2$ nm) in P2VP (14.0 – 474 kDa). Annealing times range from 30 min to 10 days.	167
Table B.5: Measured diffusion coefficients for small Al_2O_3 ($R_{NP} = 6.5$ nm) in P2VP (14.0 – 1220 kDa). Annealing times range from 10 min to 5 days.	168
Table B.6 : Measured diffusion coefficients for small SiO_2 ($R_{NP} = 8.3$ nm) in P2VP (474 and 1220 kDa). Annealing times range from 3 to 5 days.	168
Table B.7: Nanoparticle diffusion coefficients from the core-shell model ($D_{core-shell}$) at $T = 180$ °C as a function of molecular weight. Due to the lower ($\phi_{NP} = 0.05$) initial Al_2O_3 concentration, $\phi_{NP} = 0.01$ is used as the dilute limit. Details of the calculations are below.....	169
Table B.8: Evidence for Regime II vehicular diffusion. The difference between the average D_{NP} and $D_{core-shell}$ for Al_2O_3 NPs ($R_{NP} = 6.5$ nm) as a function of molecular weight. When $R_g/R_{NP} \geq 2.4$ (blue highlight), the difference becomes independent of molecular weight.	173
Table C.1: D_{NP} values for Al_2O_3 nanoparticles from composites with $\phi_{\text{Al}_2\text{O}_3} = 0.01$ and annealed for 1 - 6 hours at 180 °C. Fits are shown above in Figure C.2.....	194
Table C.2: Tabulated intensities taken from individual samples at the FWHM, the calculated $\phi_{\text{Al}_2\text{O}_3-local}$, the number of small and larger NPs used for bimodal interparticle distance calculation, and IsD_{bi}	198
Table C.3: D_{NP} values for Al_2O_3 nanoparticles from composites with $\phi_{\text{Al}_2\text{O}_3} = 0.05$ and annealed for 1 - 7 days at 180 °C. These diffusion coefficients decrease systematically with annealing time indicating that system has evolved upon annealing. Crossed out cells indicate no sample was measured.	199

LIST OF FIGURES

Figure 1.1: Illustration of a particle transitioning from one polymer network cage to an adjacent cage. This hop involves the slippage of a single polymer loop (highlighted in red) around the particle, demonstrating the energy landscape and the free energy barrier (ΔU_{hop}) associated with the hopping mechanism. Adapted from Reference 39.	7
Figure 1.2: Sticky (COOH capped) and nonsticky (CH ₃ capped) nanoparticles in polar polymer melts display different effective radii and diffusion behavior relative to Stokes-Einstein due to the presence of the polymer bound layer. Adapted from Reference 35.	8
Figure 1.3: The diagram on the left illustrates an athermal system with a nanoparticle surrounded by non-adsorbed polymer chains (red). The right diagram depicts an attractive system where polymer adsorbs onto the NP surface, forming a bound polymer layer (blue), significantly increasing its effective NP size.	9
Figure 1.4: Compositional images in two dimensions showing the distributions of Li ⁺ ions ($m/q = 7$) (a–c) and LiO ⁺ ($m/q = 23$) ions (d–f). These images detail the distribution at various depths of the outermost surface, the central region, and the interface with ITO in a PNC, displaying the capability for ToF-SIMS to map heterogeneity. Adapted from Reference 89.	17
Figure 2.1: Sample preparation schematic for P2VP-PNC-P2VP trilayers. After drying and annealing, the samples were cleaved and mounted for cross-sectional imaging and ToF-SIMS. SEM (30 keV) shows an unannealed 10 vol% NP film between P2VP layers; the free surface of this trilayer sample is visible at upper-right of the image.	52
Figure 2.2 : a) m/Q spectra at 100 pA, 30 keV accelerating voltage for 300 frames for a cross-sectional PNC trilayer sample with 10 vol% NP. Characteristic peak for Si ⁺ ion at $m/Q = 28$. b) Integrated Si ⁺ intensity in the X-Y plane as a function of frame. Inset: Projected Si ⁺ concentration on the XZ plane displays higher intensity at low frames. c) Tilt-corrected 1D Si ⁺ profile perpendicular to the film fit by convoluting the film profile and the experimental resolution given by a Gaussian FWHM = 0.25 μm . Data is 3-point averaged (binned). Inset: SEM image after 300 frames displays a flat etched surface.	56
Figure 2.3: a) 3D data of Si ⁺ density (frames 101-300) of an unannealed trilayer film and the plane fit of maximum Si ⁺ density (cyan). b) X'Y' projection of the Si ⁺ density after tilt-correction and conversion from pixels to lengths such that Y' = 0 intersects with the tilt-corrected plane. c) 1D profile of Si ⁺ intensity across the unannealed trilayer sample integrated before and after tilt-correction. Line fit is a convolution of the PNC film thickness (0.5 μm) and the experimental resolution, FWHM = 0.25 μm .	58
Figure 2.4: The Si ⁺ concentration profiles are fit with Eqn. 2.1 as described in the text to find the NP tracer diffusion coefficient D_{NP} . Fits for $D_{NP} \pm \delta$ are shown in grey. a) The Si ⁺ profiles for all annealed samples. D_{NP} from samples annealed at 180 °C for b) 1 day, c) 3 days, and d) 5 days show excellent agreement.	62
Figure 2.5: a) Diffusion profiles of 5 (squares, 101-600 frames), 10 (circles, 101-300 frames), and 15 (triangles, 101-300 frames) vol % NPs annealed for 3 days at 180 °C. b) D_{NP} as a function of NP loading and at 10 vol% as a function of annealing time. Shaded area (blue) shows an estimate based on previous work using RBS to measure NP tracer diffusion.	64
Figure 2.6: a) The C ₂ D ₂ ⁺ concentration profiles are fit with Eqn. 1 to find the dPS tracer diffusion coefficient D_{poly} . Trilayers were annealed at 174°C for a) 69-65k dPS/PS for 1 and 3 hours, and b) 423-450k dPS/PS for 1 and 3 days. Data is binned for noise reduction.	66

Figure 2.7: Diffusion coefficient ($D = x^2/4t$) as a function of diffusion distance (x) for a range of annealing times (10 min to 7 days). ToF-SIMS can measure concentration profiles with resolutions from 0.3 - ~ 200 μm indicating the ability to measure diffusion coefficients from 10^{-15} to 10^{-6} cm^2/s (blue). 68

Figure 3.1 : **a)** Initial sample state at $t = 0$, where thick P2VP layers border a thin center PNC layer. **b)** Schematic of sample after annealing for a specified time t . **c)** Concentration profiles and fits to Eqn. 6 of Si^+ signal indicating diffusion of SiO_2 NPs in 41 kDa P2VP ($R_g/R_{NP} = 0.21$) at three annealing times. **d)** Concentration profiles and fits of integrated Al^+ data indicating Al_2O_3 NP diffusion in 41 kDa P2VP ($R_g/R_{NP} = 0.85$) at three annealing times. 86

Figure 3.2 Nanoparticle diffusion coefficients normalized by **a)** $D_{\text{Stokes-Einstein}}$ and **b)** $D_{\text{core-shell}}$ as a function of the polymer R_g normalized by R_{NP} . Silica nanoparticles are displayed in blue squares ($R_{NP} = 26.2$ nm) and light blue triangles ($R_{NP} = 8.3$ nm). Alumina nanoparticles are displayed in red circles ($R_{NP} = 6.5$ nm). All annealing times are plotted. 88

Figure 3.3 a) D_{NP} (blue points) for SiO_2 (26.2 nm) NPs in P2VP as a function of molecular weight. Solid line corresponds to D_{theory} in Eqn. 7 where $D_{\text{vehicle}} \rightarrow 0$ as $\tau_{des} \gg \tau_{\text{Rouse}}$. **b)** D_{NP} (red points) for Al_2O_3 (6.5 nm) NPs in P2VP as a function of molecular weight. Red line is the best fit to Eqn 3.7 and corresponds to $\tau_{des} = 50$ s. Black dashed and dot-dash lines correspond to $\tau_{des} = \tau_e$ and $\tau_{des} = \tau_{\text{Rouse}}$, respectively. 91

Figure 4.1: Schematic and concentration profiles of small Al_2O_3 NPs diffusing into SiO_2 -P2VP layers. **(a)** Cross-sectional view of the trilayer sample with a central Al_2O_3 NP layer ($\phi_{\text{Al}_2\text{O}_3} = 0.01$, orange) diffusing into the surrounding SiO_2 -loaded P2VP matrix (blue). **b)** Representational concentration profiles before ($t = 0$) and after annealing ($t > 0$) showing Al_2O_3 NP diffusion into the SiO_2 -P2VP nanocomposite. 101

Figure 4.2: Concentration profiles of Al^+ ions indicating the spatial distribution of Al_2O_3 NPs within trilayer samples with SiO_2 -P2VP nanocomposite with $\phi_{\text{SiO}_2} = 0.025$. The samples, with an initial $\phi_{\text{Al}_2\text{O}_3} = 0.01$ concentration in the mid-layer, were annealed at 180°C ($T_g + \sim 50^\circ\text{C}$) for 1, 3, and 6 hours. The normalized intensity profiles have been smoothed by adjacent averaging over four data points to minimize noise. The local Al_2O_3 concentrations, $\phi_{\text{Al}_2\text{O}_3, \text{local}}$, are the concentration at the FWHM of the normalized concentration profiles, as illustrated in orange. Red lines are best fits of Eqn. 4.1 to the data to find the Al_2O_3 nanoparticle diffusion coefficients, see Table C.1 102

Figure 4.3: **a)** D_{NP} (red) as a function of matrix SiO_2 NP loading. Samples were annealed for 1-6 hours. Benchmark diffusion measurements of Al_2O_3 NPs into an unmodified P2VP matrix ($\phi_{\text{SiO}_2} = 0$) were annealed 12 – 72 hours. Line indicate $D_{\text{core-shell}}$ (solid), $D_{\text{core-shell}} + D_{\text{vehicle}}$ (dashed, upper ($\tau_{des} \sim 1$ s) and lower ($\tau_{des} \sim 70$ s)), and $D_{\text{core-shell}} + D_{\text{vehicle-II}}$ (dotted, $\tau_{des} \sim 50$). 105

Figure 4.4: Schematic of ID_{bi} for a bimodal mixture of nanoparticles for bare nanoparticles **(a)** and for nanoparticles with bound polymer **(b)**. **c)** ID_{bi} as a function of $\phi_{\text{Al}_2\text{O}_3, \text{local}}$. Curves correspond to fixed values of ϕ_{SiO_2} (0.001 to 0.050). Red dashed and blue solid lines correspond to bare NPs (r_L and r_S) and NPs with bound polymer layers ($r_{L, \text{eff}}$ and $r_{S, \text{eff}}$). 109

Figure 4.5: $D_{NP} - D_{\text{core-shell}}$ as a function of $ID_{bi}/2R_{\text{eff-Al}_2\text{O}_3}$ with linear regression (red) displaying an inverse power law. Dotted line is $D_{\text{vehicle-II}}$ ($\tau_{des} = 50$ s) for neat for comparison. 109

Figure A.1: SANS data of 100 kg/mol P2VP in methanol solvent fit to a Gaussian polymer chain model results in an R_g of 7.2 nm and PDI of 1.34. 148

Figure A.2: SAXS data displaying the form factor of the Nissan-STL NP system fit to the hard sphere model (red). Results in $R_{NP} = 26.1$ nm with a size dispersity of 1.19. 148

Figure A.3 : a) 15 vol% NP sample (3 day anneal) taken with 256×256 pixel resolution with a rate of 4 mins/300 frames (pixel size = 156 nm post 2×2 binning). b) Same sample taken at 1024×1024 pixel resolution at a rate of 52 mins/300 frames (pixel size = 39 nm post 2×2 binning).	149
Figure A.4: a) AFM image of a PNC film of 500 nm thickness after 300 frames of ToF-SIMS collection (100 pA, 30 keV accelerating voltage, 20 μ m FoV, 512 x 512 pixels post 2×2 binning). b) Depth of traces shown in (a) with an average depth of 280 ± 5.3 nm.	150
Figure A.5: a) The Si^+ concentration profile of an unannealed trilayer sample measured with a 10 pA beam current displays a FWHM of 0.49 μ m. b) The same sample measured with a 300 pA beam current has a FWHM of 0.83 μ m. Si^+ concentration profiles were integrated after the tilt correction described in the manuscript.....	151
Figure A.6: a) 2D C^+ ($m/q = 12$) concentration map and b) $\text{C}_2\text{D}_2^+/\text{Si}^+$ ($m/q = 28$) composition maps from a single data set (423 k – 450 k dPS/PS, annealed for 1 day at 174°C). High $m/q = 28$ signal that is commensurate with high $m/q = 12$ signal indicates the location of dPS and the presence of C_2D_2^+ ions. Conversely, high $m/q = 28$ signal and to low intensity in C^+ indicate Si^+ ions from the Si wafer.	154
Figure A.7 : Data (black) reproduction from Green et al. for the tracer diffusion coefficient of dPS into PS ($M_w = 2 \times 10^7$) as a function of dPS molecular weight. Their linear fit corresponds to $D_{\text{dPS}} = 0.008\text{M}^{-2}$. The results from this study using ToF-SIMS are shown in red.....	156
Figure B.1: Mass spectra from ToF-SIMS displaying distinct $m/q = 27$ (Al^+) and $m/q = 28$ (Si^+) peaks. This mass spectra demonstrates the ability to use ToF-SIMS to distinguish silica and alumina nanoparticles. Sample is 158 kDa P2VP sample with 5 vol% Al_2O_3 NPs and 5 vol% SiO_2 NPs. ToF-SIMS was collected at 100 pA and 30 kV conditions for 400 frames. In ToF-SIMS relative peak intensities do not quantitatively indicate sample composition.	160
Figure B.2: Normalized concentration profiles from ToF-SIMS for SiO_2 nanoparticles ($R_{\text{NP}} = 26.2$ nm) diffusing into P2VP. (a) 14.0 kDa, (b) 41.0 kDa, (c) 158 kDa, (d) 310 kDa, and (e) 474 kDa. Lines correspond to Fick's 2 nd law and the D_{NP} and R^2 values are tabulated in Table B.4	162
Figure B.3 : Normalized concentration profiles from ToF SIM for Al_2O_3 nanoparticles ($R_{\text{NP}} = 6.5$ nm) diffusing into P2VP ($M_w = 14.0 - 1220$ kDa). (a) 14.0 kDa, (b) 41.0 kDa, (c) 158 kDa, (d) 219 kDa e) 310 kDa, (f) 474 kDa, (g) 1220 kDa. Lines correspond to Fick's 2 nd law and the D_{NP} and R^2 values are tabulated in Table B.5	164
Figure B.4: Normalized concentration profiles from ToF SIM for SiO_2 nanoparticles ($R_{\text{NP}} = 8.3$ nm) diffusing into P2VP ($M_w = 474$ and 1220 kDa). (a) 474 kDa and (b) 1220 kDa. Lines correspond to Fick's 2 nd law and the D_{NP} and R^2 values are tabulated in Table B.6.	166
Figure B.5 : Experimental measurements of η_{poly} with linear fit used in red, including the unentangled molecular weight, and in blue to demonstrate the minimal difference in scaling when excluding the unentangled sample.....	171
Figure B.6 : $D_{\text{NP}}/D_{\text{core-shell}}$ versus R_g/R_{NP} showing data from all annealing times. Silica nanoparticles are displayed in blue triangles ($R_{\text{NP}} = 26.2$ nm) and light blue squares ($R_{\text{NP}} = 8.3$ nm). Alumina nanoparticles are displayed in red circles ($R_{\text{NP}} = 6.5$ nm). Specific annealing times are provided in Table B.4 . Additional data from single particle tracking experiments of methyl-capped (black stars) or carboxyl-capped (gray circles) quantum dot nanoparticles ($R_{\text{NP}} = 6.6$ nm) in poly(propylene glycol) ($M_w = 0.425 - 8$ kDa; $R_g = 0.6 - 2.8$ nm). ³⁵	172

Figure B.7: Shortest Rouse time (τ_0) for P2VP measured at 140 °C and scaled to 180 °C. The τ_0 values were measured at 140 °C (black) using dielectric relaxation spectroscopy.²⁶ Data scaled to 180 °C (red) by assuming $\tau_0 \sim 1/T$ (Kelvin)..... 173

Figure C.1: ToF-SIMS mass spectra and compositional maps for Al^+ ($m/q = 27$) and Si^+ ($m/q = 28$) ions. ToF-SIMS mass spectra and compositional maps for Al^+ ($m/q = 27$) and Si^+ ($m/q = 28$) ions where white indicates signal. Trilayer sample of 5 vol% SiO_2 NP / 5 vol% Al_2O_3 NP / 5 vol% SiO_2 NP in P2VP and annealed for 3 h at 180 °C. **a)** Total mass spectra from $m/q = 20 - 30$ with Al^+ ($m/q = 27$) and Si^+ ($m/q = 28$) peaks labeled. ToF-SIMS mass spectra images collapsed along the z-axis for **b)** Al^+ ($m/q = 27$) and **c)** Si^+ ($m/q = 28$). Images demonstrate that ToF SIMS distinguishes the Al_2O_3 NPs in the midlayer (~ 500 nm) and the SiO_2 NPs in the thicker top and bottom layers. 191

Figure C.2 : Normalized concentration profiles from ToF-SIMS for Al_2O_3 nanoparticles ($R_{\text{NP}} = 6.5$ nm) diffusing into polymer nanocomposites with $\phi_{\text{SiO}_2} = 0.001 - 0.050$. a) $\phi_{\text{SiO}_2} = 0.001$, b) $\phi_{\text{SiO}_2} = 0.005$, c) $\phi_{\text{SiO}_2} = 0.01$, d) $\phi_{\text{SiO}_2} = 0.025$, and e) $\phi_{\text{SiO}_2} = 0.05$. Areas were normalized to 0.2 such that the initial film of thickness 0.2 μm is a square function of intensity = 1 from -0.1 to 0.1 μm 193

Figure C.3 : Concentration profiles for $\phi_{\text{Al}_2\text{O}_3} = 0.05$ annealed from 1 - 7 days. The profiles overlap and exhibit no significant broadening of the FWHM, indicating restricted diffusion behavior over these extended annealing periods at these nanoparticle concentrations. 199

Figure F.1: The DLS size distribution by number shows a single, well-defined peak, indicating the absence of significant aggregation or large aggregate peaks. $2 \cdot R_{\text{hydro}} = 27 \pm 10$ nm. 242

CHAPTER 1 : POLYMER AND NANOPARTICLE DYNAMICS IN NANOCOMPOSITES AND TIME-OF-FLIGHT SECONDARY ION MASS SPECTROSCOPY

1.1 Introduction

Polymer nanocomposites (PNCs) play a transformative role in materials science by improving macroscopic properties and expanding applications.¹ The controlled integration of nanoparticles (NPs) into polymer matrices enables precise control over material behaviors, impacting mechanical, thermal, and transport properties.^{2,3} This control, achieved through manipulating chemistry, NP dispersion, loading, processing, and polymer chemistry and molecular weight extends to designing materials for aerospace,⁴ automotive components,⁵ and everyday products.⁶ Traditionally, PNCs find applications in everyday products like tires, where their enhanced mechanical properties contribute to improved durability and performance. The engineering of PNCs, considering chemistry and nanoparticle size, enables advancements in cutting-edge technologies and established industries, showcasing the broad spectrum of their impact.

Within the realm of PNCs, the influence of polymer-NP interaction and polymer to NP size and shape stands as a critical determinant of material properties.⁷⁻⁹ The surface chemistry and size of the NPs or polymer selected enables precise control over interactions with the polymer matrix. The tailored chemical makeup and nanoparticle size contribute to the unique interplay between NPs and polymers, presenting an avenue for achieving desired material characteristics.

The dispersion and alignment of NPs within the polymer matrix influences properties like thermal conductivity or mechanical toughness.^{4,10,11} Beyond mechanical and thermal enhancements, the tunable nature of PNCs extends to diverse applications, including targeted drug delivery^{12,13} and membrane science.^{14,15} Nanocomposites demonstrate versatile applications in both packaging and optics. In packaging, the integration of antimicrobial nanoparticles with antioxidant properties like zinc oxide enhances barrier properties against oxygen and moisture, contributing to prolonged shelf life and reduced contamination risks.^{16,17} Meanwhile, in optical applications, nanocomposites offer unique optical properties due to the interaction of light with nanoparticles, presenting opportunities for developing advanced optical devices and coatings.¹⁸ For example, the addition of low volumes of well-dispersed silica or zirconia particles maintain transparency, while improving abrasion resistance.¹⁹ The adaptability of nanocomposites underscores their potential to revolutionize various industries. To achieve the potential of PNCs, a comprehensive understanding of nanocomposite dynamics is crucial. While significant strides have been made, there remains a need for continued exploration. Key areas of interest include a deeper investigation into the effect of interactions between NPs and polymers and a more nuanced understanding of dynamic processes across length scales. By addressing these knowledge gaps, researchers can unlock new possibilities and propel the field of nanocomposite dynamics towards innovative applications and enhanced material performance.

The introduction to this thesis focuses on crucial aspects essential for understanding polymer nanocomposites (PNCs). In Section 1.2, we emphasize the critical role of nanoparticle diffusion within PNCs in the melt state, due to its significant influence on the overall properties of the materials. For example, the dispersion of nanoparticles plays a crucial role in determining

mechanical properties. Well-dispersed nanoparticles significantly enhance both short-term mechanical stiffness and long-term creep resistance.²⁰ In creep reduction studies, the formation of networked nanoparticle morphologies facilitates uniform stress distribution and delays mechanical failure under sustained loads.²⁰ Consequently, optimizing nanoparticle dispersion within the polymer matrix is essential for improving the durability and functional performance of nanocomposites in demanding applications. Section 1.3 provides an overview of the current methods used to measure NP diffusion, emphasizing the need for a diverse set of analytical techniques to address the range of materials and length scales of interest.

Moving forward, Section 1.4 explores the precedence of application of Time-of-Flight Secondary Ion Mass Spectrometry (ToF-SIMS) in polymer systems. Traditionally used for surface analysis in the semiconductor industry, ToF-SIMS proves valuable in measuring chemical contaminants and providing real-space 3D chemical composition data and depth-profiling capability. Its adaptability enhances our ability to study complex polymer systems and accurately determine diffusion coefficients. Lastly, Section 1.5 outlines the thesis structure, mapping out the exploration from method development in Chapter 2 to the study of nanoparticle diffusion in attractive polymer melts in Chapter 3, and concluding with an investigation of crowded nanoparticle diffusion in Chapter 4. Our ongoing collaborations are investigating several key areas: surface saturation in direct air carbon capture using polyethyleneimine, molecular diffusion of triclosan in star polymer systems, and NP diffusion of bottlebrush-grafted nanoparticles using the ToF-SIMS methods developed in this work. The thesis aims to significantly broaden the scope of our research into polymer dynamics, enabling us to explore complex interactions and dynamics within nanocomposite or polymer systems.

1.2 Nanoparticle Diffusion in Polymer Melts

Nanoparticle diffusion within polymer melts is a complex yet crucial aspect, profoundly influencing the mechanical strength,¹¹ thermal stability,^{9,21} electrical conductivity,^{22,23} and barrier¹⁶ properties of polymer nanocomposites (PNCs). Understanding how nanoparticles move within the molten polymer matrix is essential for tailoring polymer processing for ultimate performance of these composite materials. The diffusion process is intricately linked to factors such as particle size, polymer chain dynamics, and interfacial interactions.^{24,25} As the size of nanoparticles approaches the characteristic length scales of polymer chains, their movement is significantly affected by the surrounding polymer matrix.²⁶

The dynamic interplay between nanoparticles and polymer chains in melts is governed by polymer chain entanglement, relative nanoparticle to polymer size, and polymer-nanoparticle interactions. Larger nanoparticles, specifically those with radius exceeding the radius of gyration (R_g) of the polymer size, may exhibit restricted mobility due to entanglements with polymer chains or interactions with the surrounding polymer matrix, resulting in altered diffusion behaviors.^{27,28} Conversely, smaller nanoparticles may exhibit more fluid-like behavior, allowing them to navigate through the polymer matrix more freely.^{26,29} The presence of attractive forces at the polymer-nanoparticle interface further dictates the diffusion characteristics, influencing the dispersion and aggregation of nanoparticles within polymer melts.

1.2.1 Athermal PNCs

Theoretical frameworks have been instrumental in unraveling the mechanisms underlying nanoparticle diffusion in polymer matrices. Among the most notable is the Stokes-Einstein

equation, which accounts for factors such as the hydrodynamic radius of the nanoparticles and the viscosity of the polymer matrix. The Stokes-Einstein equation, crucial for describing the diffusion of spherical particles in simple fluids, is based on several key assumptions. It presumes particles are spherical and move through a homogeneous, isotropic fluid treated as a continuum.³⁰ The equation applies under conditions of low Reynolds number, ensuring laminar flow where viscous forces dominate over inertial effects.³⁰ The fluid and particle are assumed to adhere to a no-slip boundary condition, indicating that the fluid at the particle's surface moves at the same velocity as the particle itself. Additionally, the system is considered to be at thermal equilibrium with no temperature gradients influencing particle movement, and interactions among particles are deemed negligible.³⁰ This equation describes the diffusion rate as inversely proportional to the nanoparticle radius and directly influenced by the polymer's viscoelastic properties.³¹

$$D_{SE} = \frac{k_B T}{6\pi\eta R} \quad (1.1)$$

where k_B is the Boltzmann constant, T is the temperature in Kelvin, η is the macroscopic medium viscosity, R is the radius of the object. For polymer nanocomposites, these theoretical models often require refinement to incorporate the effects of polymer-nanoparticle interactions, which can significantly alter the predicted diffusion behaviors.^{24,32,33}

Experimental studies have provided valuable insights that both support and challenge Stokes-Einstein (SE) behavior. Nanoparticle dynamics in athermal or chemically neutral systems, characterized by their lack of significant attractive or repulsive interactions between the nanoparticles and the polymer matrix, were first explored to understand the fundamental aspects of nanoparticle diffusion. To quantify the polymer length scale, we first define the radius of

gyration (R_g) which represents the average distance of the chain's segments from the center of mass. This parameter is crucial for understanding the polymer's spatial dimensions and how it behaves in solution or within a matrix.

$$R_g^2 = C_\infty n l^2 \quad (1.2)$$

where l is the bond length, n is the number of backbone bonds, and C_∞ is the characteristic ratio.³⁴ Typically, in the case of large ($R_{NP} > R_g$) nanoparticles in an athermal melt, Stokes-Einstein behavior holds true.³⁵ In contrast, the seminal work by Brochard and de Gennes laid the groundwork for this understanding, proposing a decoupling of nanoparticle dynamic timescale from the bulk viscosity of the polymer matrix.³⁶ At NP length scales smaller than the polymer coil (defined by the tube diameter d_t), their observations highlighted notable deviations from the classical Stokes-Einstein behavior, introducing the concept of scale-dependent viscosity, $\eta(q)$ (where q is the length scale of the particle), to account for these anomalies.³⁶

Building on this foundation, the behavior of nanoparticles in athermal PNCs has been further developed through the extension of de Gennes's model for entangled polymer melts, supplemented by geometric considerations. This framework suggests that the diffusion of small nanoparticles, those smaller relative to the mesh size of the polymer matrix ($R_{NP} < \text{the mesh size, } a_t$), is governed by a "hopping" mechanism.³⁶ In this model, nanoparticles are envisioned to overcome energy barriers at long timescales, facilitating their movement through the entangled polymer network (**Figure 1.1**). This perspective provides a mechanistic understanding of how nanoparticles navigate the complex landscape of the polymer matrix, highlighting the influence of the matrix's topological constraints on nanoparticle mobility. Recent work using grafted

nanoparticles³⁷ or molecular dynamics³⁸ resulting in weakly attractive or repulsive interactions show strong evidence of the hopping mechanism.

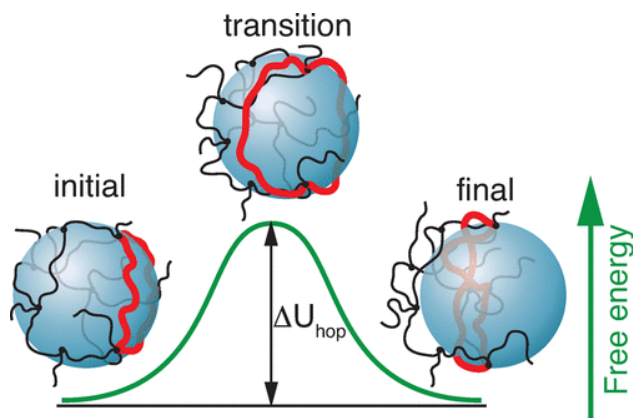


Figure 1.1: Illustration of a particle transitioning from one polymer network cage to an adjacent cage. This hop involves the slippage of a single polymer loop (highlighted in red) around the particle, demonstrating the energy landscape and the free energy barrier (ΔU_{hop}) associated with the hopping mechanism. Adapted from Reference 39.³⁹

Further investigations into nanoparticle diffusion within athermal systems have refined our understanding of size-dependent dynamics. As summarized by Cai et al.,⁴⁰ spherical nanoparticles of varying sizes exhibit distinct diffusion behaviors in response to the polymer matrix's characteristics. Small nanoparticles, due to their size being comparable to or smaller than the polymer's mesh size, exhibit diffusion rates largely unaffected by the surrounding polymer.⁴⁰ Rotational diffusion behavior similarly is faster than SE predictions in athermal systems dependent on chain contour length.⁴¹ Intermediate-sized and large nanoparticles, however, are primarily influenced by the effective viscosity of the polymer matrix, aligning with SE predictions.

Experimental results of methyl-capped SiO₂ NP diffusion in poly(propylene glycol) (PPG) with neutral surface functionalization support these results (**Figure 1.2**).⁴²

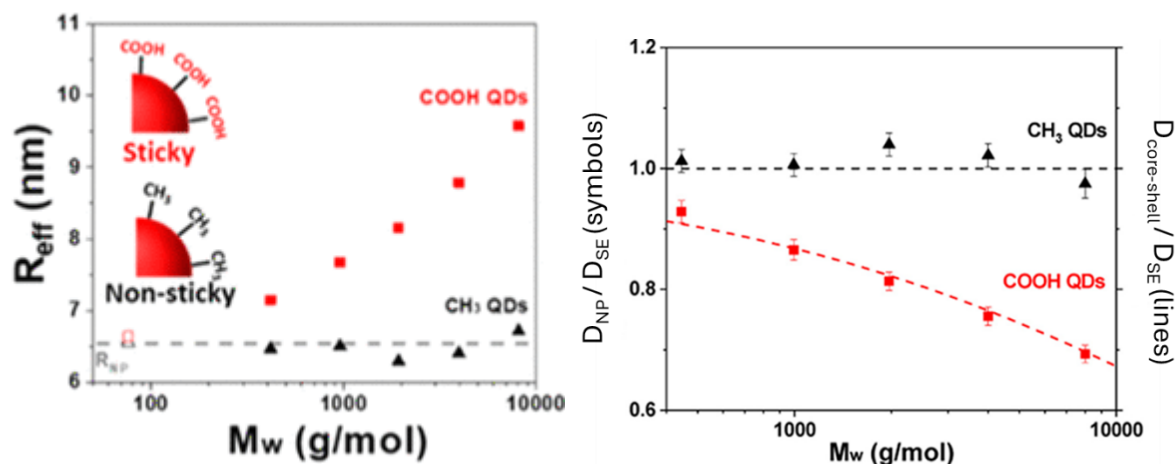


Figure 1.2: Sticky (COOH capped) and nonsticky (CH₃ capped) nanoparticles in polar polymer melts display different effective radii and diffusion behavior relative to Stokes-Einstein due to the presence of the polymer bound layer. Adapted from Reference 35.³⁵

These findings collectively demonstrate the nature of nanoparticle diffusion in athermal PNCs, revealing an interdependence between nanoparticle size, interfacial interactions, and diffusion mechanisms. As this thesis delves deeper into the dynamics and diffusion of nanoparticles within PNCs, the insights gleaned from athermal systems will serve as a reference point, informing the exploration of nanoparticle behavior in more complex attractive systems.

1.2.2 Attractive PNCs

The interactions between the nanoparticles and the polymer matrix play a pivotal role in defining the composite's properties. In cases of strong attractive interactions, such as hydrogen bonding between functionalized nanoparticles and polymer chains, a distinct interfacial layer

known as the bound layer of polymer forms around the nanoparticles, leading to a significant slowing down of the local segmental dynamics. This bound layer's thickness and properties are influenced by factors such as the molecular weight of the polymer and the surface grafting density of the nanoparticles.^{35,43–45}

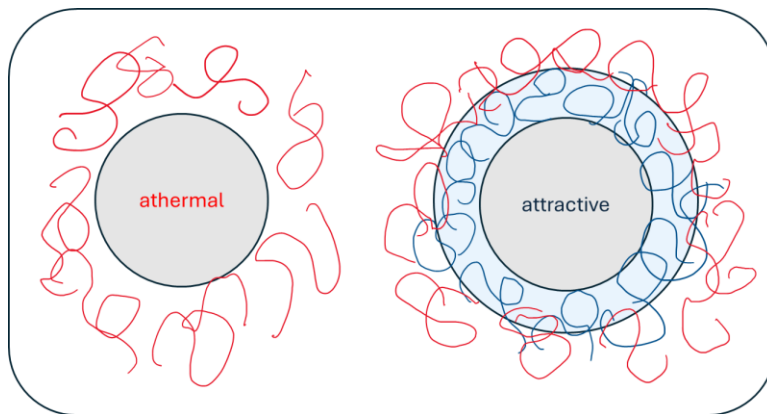


Figure 1.3: The diagram on the left illustrates an athermal system with a nanoparticle surrounded by non-adsorbed polymer chains (red). The right diagram depicts an attractive system where polymer adsorbs onto the NP surface, forming a bound polymer layer (blue), significantly increasing its effective NP size.

The bound layer is crucial for understanding the viscoelastic behavior of PNCs, demonstrating that NP mobility is influenced by more than just particle size and matrix viscosity. For instance, in attractive poly(2-vinyl pyridine) (P2VP)-SiO₂ systems, the bound layer modifies NP diffusion by increasing the effective viscosity due to its thickness and the attractive interactions within the matrix.^{45,46} The addition of the bound polymer affects the hydrodynamic radius of the nanoparticles, thereby impacting their movement through the polymer matrix and altering the composite's overall rheological properties.^{47,48} Additionally, the lifetime of the bound layer plays a pivotal role in maintaining good NP dispersion, preventing agglomeration and ensuring NP

uniform distribution within the matrix,^{20,44,49} which is essential for optimizing the mechanical and thermal characteristics of the composite. Consequently, the presence of a stable bound layer is a significant factor in designing PNCs with desired mechanical and thermal characteristics.^{48,50} In attractive poly (2-vinyl pyridine) (P2VP)-SiO₂ systems,⁴⁵ it has been found that NP diffusion is modified by the size of the bound layer and increased viscosity due to attractive interactions in the matrix.

$$D_{core-shell} = \frac{k_B T}{6\pi\eta_{PNC}R_{eff}} \quad (1.3)$$

where η_{PNC} is the effective viscosity after accounting for the attractive interactions of the added NPs, and R_{eff} is the size of the particle with the bound layer.⁴⁵ Attractive PNCs with small NPs ($R_{NP} < R_g$) exhibit NP diffusion faster than SE behavior experimentally.⁵¹ However, in accounting for the attractive melt interactions, current theory defines this faster than SE behavior “vehicular” motion,⁵² in which the primary mechanism of adsorption and desorption of surrounding polymer chains affects NP diffusion relative to the desorption length scale. From the theoretical models predicting diffusion behaviors to the experimental insights, it becomes evident that nanoparticle diffusion behavior is multifaceted. Nanoparticles in complicated PNC environments require a comprehensive understanding that considers nanoparticle size, shape, and surface chemistry combined with the polymer matrix's molecular weight and viscoelastic properties. These insights will guide the design of the experimental work in this thesis.

1.2.3 Confined NP Diffusion

The study of crowded polymer nanocomposites is not merely of academic interest but is crucial for the design and development of new materials with tailored properties for specific

applications. Understanding the confined dynamics of nanoparticles within a polymer matrix sheds light on the fundamental processes that govern the macroscopic behavior of these composites. While polymer diffusion has been studied in confined environments of a variety of geometries, NP diffusion has been more difficult to study.

Understanding and measuring crowded nanoparticle diffusion are of importance in various scientific and technological domains. In biological and medical contexts, such as drug delivery systems navigating cellular environments, the ability of nanoparticles to efficiently diffuse through crowded spaces directly influences their therapeutic efficacy.^{53,54} In electrodes, densely packed metallic-oxide nanoparticles in a polymer matrix can enhance electrical and thermal conductivity, making these composites suitable for use in electronic and optoelectronic devices.⁵⁵ For example, crowded metal-oxide (ex. SnO_2) PNCs can be used in flexible electronics, sensors, and displays, where the polymers provide mechanical flexibility and the nanoparticles contribute to electronic functionality.⁵⁶ Knowledge of crowded diffusion dynamics is essential for optimizing the performance of nanocomposite materials. Accurate measurements in these crowded conditions provide insights into the behavior of nanoparticles in realistic scenarios, guiding the design and development of advanced materials and applications.

The addition of nanoparticles influences the dynamics of the polymer chains in multiple ways. For instance, the presence of NPs can alter the center-of-mass diffusion of the polymer chains, impacting the polymer's viscosity and processability.^{25,57,58} Moreover, the segmental dynamics of the polymer chains, particularly near the NP surface, undergo significant changes, affecting the material's glass transition temperature^{8,59,60} and its mechanical properties.⁶¹ The nature of these changes is multifaceted, governed by the size, shape, and surface properties of the

nanoparticles, as well as the chemistry and molecular weight of the polymer matrix.^{9,11,59,60} The degree of these changes is directly affected by the particle loading, but at non dilute loadings, this effect becomes more prominent as polymer confinement occurs.

One of the critical aspects of PNC dynamics is the confinement effect imposed by the nanoparticles. When the size of the NP is comparable to the size of the polymer coil, the physical confinement and the altered local environment can lead to changes in the polymer chains' conformations, reduce the entanglement density, and modify the segmental motions at the polymer-NP interface.^{62–65} This nanoparticle-induced confinement can result in a complex, non-monotonic behavior in polymer mobility, characterized by a pronounced minimum in diffusion rates at certain nanoparticle loadings.⁶⁶

Observing crowded nanoparticle diffusion poses unique challenges due to the intricacies arising from densely packed environments. The high concentration of nanoparticles within these systems can result in restricted mobility, hindering conventional tracking methods. Traditional techniques, such as single-particle tracking (SPT) or dynamic light scattering (DLS), face limitations in accurately capturing the diffusion of individual nanoparticles amidst crowded conditions. The proximity of particles can lead to overlapping signals, making it challenging to discern individual trajectories and accurately quantify diffusion coefficients.

1.3 Prior Methods to Determine Polymer and Nanoparticle Dynamics in PNCs

The investigation of nanoparticle diffusion within polymer melts uses a range of techniques such as dynamic light scattering (DLS), X-ray photon correlation spectroscopy (XPCS), single particle tracking (SPT), and Rutherford backscattering spectroscopy (RBS). Each method offers

unique insights into the dynamic behavior of nanoparticles within the matrix of polymer melts and solutions.

Using a laser to illuminate the sample, DLS measures the fluctuations in scattered light intensity from nanoparticles as they undergo Brownian motion. This method derives the diffusion coefficients and particle size distribution based on the hydrodynamic radius, providing good temporal resolution but limited spatial resolution via the autocorrelation function. DLS has proven instrumental in analyzing nanoparticle diffusion within various mediums, including polymer solutions⁵³ and poly(propylene glycol) (PPG) melts ($T_g < T_{\text{room}}$).⁵¹ The ease of sample preparation, relative low expense, and effectiveness for NPs of a range of sizes make DLS a reliable tool for NP diffusion measurements, especially in polymer solutions. However, its effectiveness diminishes with high particle loadings due to multiple scattering events, complicating data interpretation. DLS is most suitable for liquid mediums, making it less versatile for studying nanoparticle diffusion in highly viscous or solid-state polymer melts at room temperature. This limits the candidate materials for conducting PNC diffusion measurements, especially in the melt state.

In contrast, XPCS utilizes coherent X-ray scattering to monitor temporal fluctuations in scattered X-ray intensities, providing both high spatial and temporal resolutions.⁶⁷ This allows XPCS to probe dynamics on nanometer scales and over time scales from microseconds to seconds, making it suitable for studying complex systems including opaque or concentrated samples. XPCS has been successfully used to probe NP diffusion in polymer solution⁶⁸ and polymer melt systems at room temperature.²⁴ XPCS requires synchrotron radiation sources that limits its accessibility and can increase the cost of research. While DLS is more accessible and easier to use for routine

analyses, XPCS offers deeper insights into structural dynamics, though at a higher logistical complexity and cost.

Single particle tracking (SPT) provides high spatial and temporal resolution by tracking the real-time movement of individual nanoparticles. On a nanometer scale, this technique involves labeling individual particles and monitoring their trajectories over time to obtain mean-squared displacement of particles. SPT offers detailed insights into the diffusion behavior, revealing information about local interactions, spatial confinement, and potential anomalous diffusion. SPT has been used to measure NP diffusion in polymer gels,¹³ and quantum dots in PPG.⁴² Challenges arise with high particle loading ($> 0.1\%$ volume), as crowded trajectories may hinder accurate analysis. Furthermore, SPT requires liquid medium samples at room temperature, and the technique may be limited by Brownian motion in dense or highly viscous environments, impacting the duration of single-particle observations.⁶⁹ The best experimental parameters include particles that scatter or fluorescent particles which ease viewing.⁷⁰

Other techniques like fluorescence correlation spectroscopy (FCS) measure nanoparticle diffusion by analyzing fluctuations in fluorescence intensity within a small volume using gold nanoparticles, typically in solution,⁷¹ but can be modified for polymer melts.^{32,72} These fluctuations occur as nanoparticles move in and out of the focal volume, allowing for the determination of diffusion coefficients and concentration of the fluorescent species. This methodology requires fluorescent NP species.

Forward recoil spectrometry (FRES) is an ion beam method used to analyze the composition and diffusion mechanisms in polymer systems,^{73,74} providing depth profiles and elemental distribution. Similarly, elastic recoil detection (ERD) is employed to study nanoparticle

systems, offering crucial insights into nanoparticle diffusion via depth profiling.⁷⁵ ERD, taking advantage of lighter elemental detection compared to RBS, has been used to successfully measure polymer diffusion in melts in foundational polymer work involving polystyrene mutual diffusion as well as copolymer systems.^{73,76} In RBS, high-energy ions are directed at the sample, and the backscattering of these ions provides information about the depth and concentration of nanoparticles.⁷⁵ This enables a real-space measurement of NP concentration profiles as a depth-profile.^{26,45,77} RBS serves as a depth profiling tool useful for probing the composition of nanoparticles within polymer matrices. The technique is primarily applicable to thin films with < 1 μm depth, limiting its scope for three-dimensional investigations of nanoparticle diffusion.

In this thesis, we aim to address the unexplored aspects of nanoparticle (NP) diffusion by developing methodologies that overcome existing limitations in measurement techniques. We have identified key constraints such as a limited selection of candidate materials, restricted length scales, the narrow scope of applicable models for NP diffusion, and the requirement for dilute NP systems. Our goal is to broaden the understanding and capability of NP diffusion analysis using time-of-flight secondary ion mass spectrometry (ToF-SIMS).

1.4 Polymer Applications of Time-of-Flight Secondary Ion Mass Spectrometry

ToF-SIMS has emerged as a novel tool in the characterization of polymeric materials, offering unparalleled insights into the chemical composition and spatial distribution of elements and molecules on polymer surfaces and interfaces.^{78–80} The essence of ToF-SIMS is a focused ion beam used to sputter atoms and molecular fragments from the surface of a sample. These sputtered entities, now ionized, are directed towards a charged plate known as the time-of-flight (ToF)

detector.⁷⁸ The detector, by measuring the time these ions take to traverse a known distance, accurately determines their mass-to-charge ratios (m/q), enabling the identification of a vast array of chemical species with high resolution.⁷⁸

The capabilities of ToF-SIMS extend to submicron lateral resolution (source dependent), making it ideal for micro and nanoscale mapping of chemical composition across sample surfaces.^{78,81} The focused primary ion beam enables detailed investigations into the chemical structure of various materials, including polymers, ceramics, and semiconductors. Additionally, ToF-SIMS offers depth profiling capabilities, allowing researchers to study compositional variations within a material.⁸² The high sensitivity of ToF-SIMS makes it invaluable for detecting trace elements and compounds. Traditionally, ToF-SIMS has found applications across a spectrum of scientific disciplines.^{83–85} In the field of material science, ToF-SIMS is used for surface and interface analysis, providing insights into the composition of materials such as thin films and coatings.⁸²

A pivotal aspect of ToF-SIMS is its versatility in operation modes—spectral analysis, imaging, and depth profiling—each catering to specific analytical needs. Spectral analysis, for instance, is adept at acquiring high-resolution mass spectra to identify surface contaminants or to determine the relative abundances of various elements and molecules on the polymer surface.^{79,86,87} This mode is particularly beneficial for evaluating the uniformity of a system like polymer coatings and for detecting functional groups, thereby informing the modification and optimization of polymer surfaces for desired applications.

Imaging mode, on the other hand, leverages the focused primary ion beam to raster across the sample surface, creating detailed mass spectral images. This mode is instrumental in

characterizing chemically distinct regions on polymer surfaces, such as in the analysis of micropatterned surfaces or in examining phase separation in polymer blends.^{81,88} The ability to visually map chemical heterogeneities at the micro- or nanoscale provides critical insights into the material's properties and performance, especially in applications where surface chemistry plays a pivotal role.⁸⁹

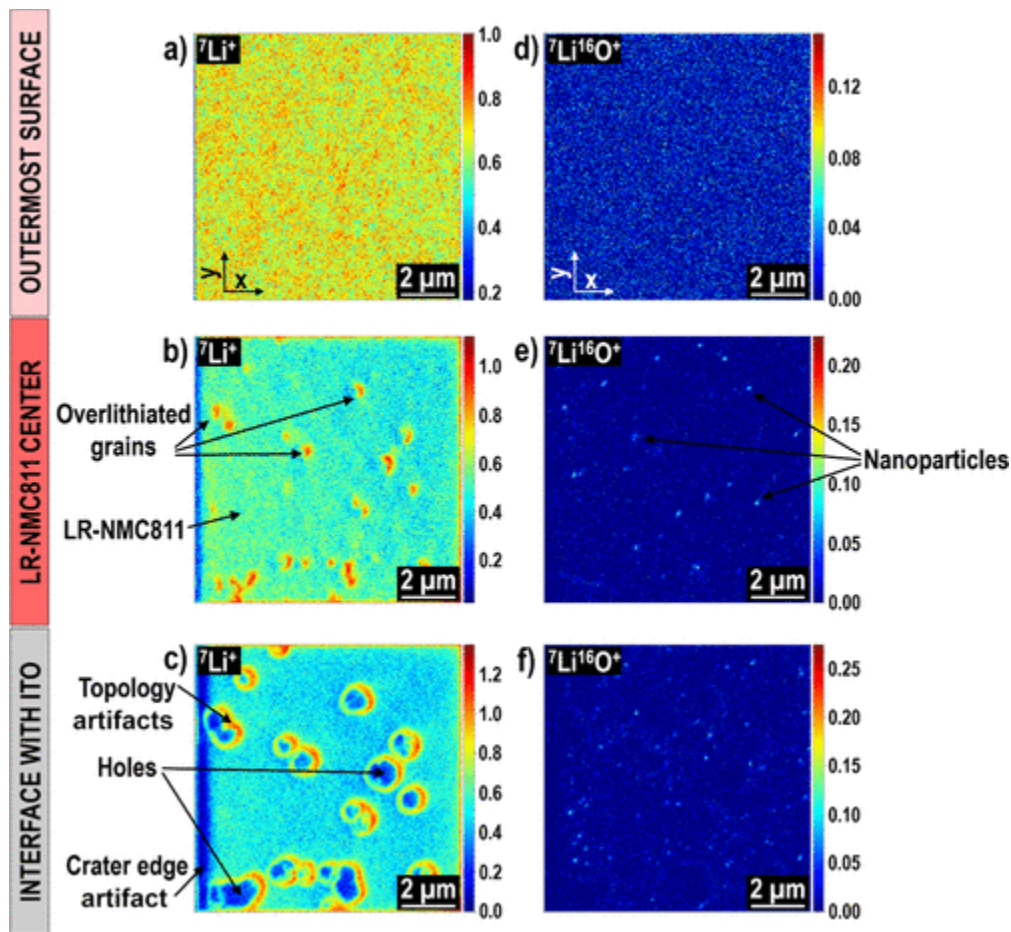


Figure 1.4: Compositional images in two dimensions showing the distributions of Li^+ ions ($m/q = 7$) (a–c) and LiO^+ ($m/q = 23$) ions (d–f). These images detail the distribution at various depths of the outermost surface, the central region, and the interface with ITO in a

PNC, displaying the capability for ToF-SIMS to map heterogeneity. Adapted from

Reference 89.⁸⁹

Depth profiling extends the capabilities of ToF-SIMS into the third dimension, offering a dynamic view of the chemical composition as a function of depth. This mode is achieved through the incorporation of a secondary ion beam for sputtering, allowing for the sequential removal of material layers and the acquisition of mass spectra at varying depths. Such depth-resolved analysis is invaluable in studying phenomena like surface segregation in polymer blends, the distribution of additives, or the integrity of multilayer structures.⁹⁰⁻⁹² Polymer morphology and composition has been studied in block copolymer systems, where depth-profiling has allowed 3D reconstruction of the systems.⁹³ Depth profiling, combined with lateral imaging, furnishes a comprehensive three-dimensional chemical mapping of the sample, revealing details about the spatial distribution of components within complex polymer systems.

The applications of ToF-SIMS in polymer science are vast and varied, encompassing the analysis of polymer films and coatings, polymer blends, composites, and electronic materials. In polymer films and coatings, ToF-SIMS aids in understanding the surface chemistry and its homogeneity, which are crucial for applications including biomedical devices and protective coatings.^{79,86} For polymer blends, ToF-SIMS provides essential information on the surface composition^{87,94,95} and phase behavior,^{93,96} directly impacting the material's macroscopic properties. In the realm of polymer composites, ToF-SIMS helps in understanding the filler-matrix organization.^{92,97} Lastly, in electronic materials, such as organic light-emitting diodes (OLEDs) and photovoltaics, ToF-SIMS offers vital insights into the distribution of materials and the integrity of interfaces, directly influencing device efficiency and longevity.⁹⁸

Despite its capabilities, ToF-SIMS is not without challenges, particularly in quantitative analysis due to the matrix effect, where the secondary ion yield can vary significantly with the local chemical environment.⁷⁸ Overcoming this hurdle requires sophisticated data analysis techniques and calibration strategies to extract quantitative information from the ToF-SIMS spectra. Advances in instrumentation, such as in combination with X-Ray photoelectron spectroscopy (XPS)⁹⁹ and the integration of ToF-SIMS with other analytical techniques like atomic force microscopy (AFM), will enable more detailed and accurate characterization of polymeric materials.¹⁰⁰

1.4.1 Comparison of ToF-SIMS to other Surface-Sensitive Methods

Characterizing surface properties is essential for applications ranging from biomaterials to protective coatings, as these properties significantly influence the polymers' functionality and applications. In the pursuit of understanding these intricate surfaces, three analytical tools—ToF-SIMS, energy dispersive X-ray spectroscopy (EDX), and XPS— have emerged as critical tools. Each technique brings a unique set of capabilities to the table, offering distinct perspectives on the chemical and elemental composition of polymer surfaces. We provide a brief comparison of ToF-SIMS, EDS, and XPS, exploring their synergies and distinctions in polymer surface analysis.

EDX operates by focusing an electron beam onto a sample, causing the sample to emit characteristic X-rays, allowing for the elemental composition of the sample to be determined.¹⁰¹ EDX is commonly used in conjunction with scanning electron microscopy (SEM), providing a complementary analysis of the elemental distribution within the scanned area.¹⁰¹ This technique is valued for its straightforward interpretation, rapid analysis, and minimal sample preparation. EDX

provides a spatial resolution of about 1 micron (although this is improved in thinner ~100 nm samples)¹⁰² and is effective for elements heavier than boron ($z = 5$), but struggles with light elements like C, H, and O, making it less costly and suitable for bulk analysis.¹⁰¹ In contrast, ToF-SIMS offers superior spatial resolution around 100 nm,¹⁰³ exceptional surface sensitivity up to 2 nm deep, and can detect all elements including light isotopes, ideal for detailed surface and molecular studies but at a higher cost. The choice between EDX and ToF-SIMS depends on the specific analysis needs, particularly regarding the resolution, sensitivity, and elemental range required.

X-ray photoelectron spectroscopy (XPS) involves irradiating a material with X-rays to eject photoelectrons from the surface atoms.¹⁰⁴ By measuring the kinetic energy and number of electrons escaping from the top 1-10 nm of the material's surface,¹⁰⁵ XPS can deduce the elemental composition, chemical state, and electronic state of the elements within the material. This surface-sensitive quantitative spectroscopic technique is particularly useful for studying the chemical composition of surfaces, thin films, and interfaces, providing insights into the chemical bonding and electronic structure of materials.¹⁰⁶

ToF-SIMS stands out for its exceptional molecular sensitivity, a critical advantage when analyzing complex polymer surfaces.^{78,79} Unlike EDX, which primarily provides elemental composition, ToF-SIMS can infer the molecular intricacies of the polymer surface depending on the secondary ions produced, offering detailed insights into organic components, additives, and contaminants.^{86,100} This capability is particularly beneficial for polymers where surface modifications or the presence of specific molecular fragments are key to their functionality.

XPS offers a complementary perspective to ToF-SIMS, excelling in identifying elemental compositions and revealing the chemical states of atoms at the polymer surface.¹⁰⁷ Its capacity to reveal the bonding environment provides crucial insights into the surface chemistry that governs polymer interactions and functionality. The quantitative nature of XPS, coupled with its non-destructive analysis, makes it an invaluable tool for a broad spectrum of polymer applications.

ToF-SIMS stands out for its sensitivity to surface compositions, offering a molecular-level understanding for polymers where surface properties can significantly diverge from the bulk. The technique's ability to generate ~ 100 nm lateral imaging¹⁰³ is useful for analyzing intricate structures like multilayer composites or thin films. Furthermore, ToF-SIMS's depth profiling capability extends its utility to exploring compositional variations across different polymer blend layers, providing a three-dimensional chemical landscape across submicron to ~ 100 s micron length scales.^{78,79} When the depth profile is combined with AFM measurements, ToF-SIMS spatial imaging can create 3D compositional reconstructions of the sample.^{93,108}

Despite its impressive molecular specificity, quantitative compositional analysis of ToF-SIMS data is difficult due to the complex interplay of matrix effects and the nature of the spectra it generates. In addition to the sample composition, the ionization rates, mass, and chemical bonding strongly influence the quantity of secondary ions. Additionally, the technique's reliance on an ion beam for surface sputtering introduces the potential for sample damage, posing challenges for the analysis of sensitive or soft polymer matrices. This can be alleviated with cryo capabilities, but contrasts with the quantitative and non-destructive nature of XPS and the elemental analysis capabilities of EDX.

The main drawback of XPS lies in its limited ability to provide detailed molecular information, which is useful in more complicated polymer systems. Similarly, in both EDX and XPS, the depth and lateral resolution of the probe are not tunable, nor is the volume-probed precise. In contrast, with ToF-SIMS the beam conditions, field of view (FoV), sample geometry, and more advanced 3D data processing techniques allow for greater flexibility in sample preparation and length scale of interest.⁹³ While capable of some degree of depth profiling, XPS cannot match the depth resolution and specificity afforded by ToF-SIMS, particularly in the analysis of complex, layered polymer systems.

Quantitative polymer compositional analysis is unlocked when ToF-SIMS and XPS are employed in tandem. ToF-SIMS's detailed molecular insights complemented by the elemental and chemical state information from XPS provide a holistic view of the polymer. This synergistic approach allows researchers to navigate the complexities of polymer systems, addressing the quantification challenges posed by ToF-SIMS.^{79,91,94,109}

1.5 Outline of Thesis

This thesis begins by building a methodology for measuring nanoparticle and polymer diffusion in polymeric systems utilizing ToF-SIMS. In Chapter 2, we perform proof-of-concept work that establishes ToF-SIMS as a novel and powerful tool for measuring diffusion coefficients in polymer systems. Our approach involves constructing trilayer samples consisting of polymer/diffusing medium/polymer and scanning the cross-section to determine the distribution of NPs or deuterated polymers using ToF-SIMS. We process the raw data by correcting for sample tilt, deconvolving the beam resolution, and integrating the data to develop one-dimensional

concentration profiles from which we derive the diffusion coefficients. The results obtained from cross-sectional ToF-SIMS align closely with those from prior studies that utilized established ion beam techniques. This validation not only underscores the reliability of ToF-SIMS as a tool for measuring NP and polymer diffusion coefficients but also broadens the scope for exploring diffusion dynamics in more intricate polymer systems and over extended spatial and temporal scales.

We apply the methodology established in Chapter 2 to explore diffusion coefficients across multiple orders of magnitude in Chapter 3. We explore NP diffusion in polymer melts, identifying two distinct modes: core-shell and vehicular. We diffused small alumina NPs ($R_{NP} = 6.5$ nm) and silica NPs ($R_{NP} = 8.3, 26.2$ nm) into poly(2-vinylpyridine) of varying molecular weights (14 - 1220 kDa) to assess the impact of NP radius, polymer size, and surface chemistry on diffusion. Silica NPs consistently exhibit core-shell behavior, while alumina NPs exhibit vehicular diffusion with increasing polymer molecular weight. Fitting the Al_2O_3 NP diffusion coefficients as a function of molecular weight provides an experimental estimate monomeric desorption time of 50 s at 180° C. By comparison, SiO_2 NPs regardless of NP size exhibit a desorption time of > 6000 s under the same annealing conditions.

In Chapter 4, the examination extends to crowded nanocomposites, exploring the effects of interparticle spacing and loading on nanoparticle and bound layer dynamics. This builds upon the insights from Chapter 3, revealing a relationship between polymer desorption and attractive particle loading, inferred via the change in diffusion behavior in a crowded PNC. Through building a model to describe bimodal NP systems, we also infer the role of the bound layer on diffusion in crowded NP systems.

Chapter 5 provides a summary of the work and details future work, identifying bound layer dynamics as a continued area for ongoing exploration. Future research could focus on deepening our understanding of nanoparticle diffusion in polymer nanocomposites. Key areas include examining the effects of nanoparticle-polymer interaction strength, particularly using random copolymer systems to adjust these interactions, and studying the influence of nanoparticle geometry, especially for non-spherical shapes like nanorods, on diffusion behavior. Additionally, the impact of polymer chain architecture on diffusion mechanisms can be explored, offering insights into the bound layer's behavior and its evolution with physical aging. This research aims to refine the design of nanocomposites optimized for enhanced functional properties.

Appendix A supports Chapter 2 with details on ToF-SIMS beam parameters and particle analysis. Appendix B enhances Chapter 3 with additional insights into desorption times. Appendix C augments Chapter 4 with extra data and analysis on interparticle spacing in a bimodal PNC. Appendix D provides extensive information on the Tescan S8252X at Penn, ToF-SIMS applications, and data analysis techniques. Appendix E outlines the preparation of alumina nanoparticle solutions, and Appendix F describes the solvent exchange process for Ludox SiO₂ nanoparticles.

This dissertation significantly advances the understanding of nanoparticle dynamics in polymer nanocomposites through the innovative use of ToF-SIMS. By developing a robust methodology for ToF-SIMS, this work provides insight into nanoparticle diffusion at unprecedented length scales, effectively allowing diffusion coefficients to be measured across a much wider variety of polymer matrices. This not only validates the method's utility but also enables the testing of theoretical models that were previously difficult to probe. Overall, the

application of ToF-SIMS sets a new standard for investigating nanoparticle dynamics in complex systems, and our work provides a new way to investigate the bound layer. The findings establish the presence of both the core-shell and vehicular mechanisms in PNCs as solid groundwork for future research, paving the way to investigate how nanoparticle shape, surface chemistry, and polymer chain architecture influence the polymer bound layer. This exploration will provide deeper insights into PNC solution stability, nanoparticle diffusion, and dispersion—critical elements for optimizing polymer nanocomposite applications.

1.6 References

- (1) Kumar, S. K.; Benicewicz, B. C.; Vaia, R. A.; Winey, K. I. 50th Anniversary Perspective: Are Polymer Nanocomposites Practical for Applications? *Macromolecules* **2017**, *50*, 714–731.
- (2) Iqbal, A.; Saeed, A.; Ul-Hamid, A. A Review Featuring the Fundamentals and Advancements of Polymer/CNT Nanocomposite Application in Aerospace Industry. *Polym. Bull.* **2021**, *78*, 539–557.
- (3) Thakur, V. K.; Kessler, M. R. Self-Healing Polymer Nanocomposite Materials: A Review. *Polymer (Guildf)*. **2015**, *69*, 369–383.
- (4) Rafique, M. M. A.; Kandare, E.; Sprenger, S. Fiber-Reinforced Magneto-Polymer Matrix Composites (FR-MPMCs) - A Review. *J. Mater. Res.* **2017**, *32*, 1020–1046.
- (5) Shah, V.; Bhaliya, J.; Patel, G. M.; Deshmukh, K. Advances in Polymeric Nanocomposites for Automotive Applications: A Review. *Polym. Adv. Technol.* **2022**, *33*, 3023–3048.
- (6) Kedzior, S. A.; Zoppe, J. O.; Berry, R. M.; Cranston, E. D. Recent Advances and an Industrial Perspective of Cellulose Nanocrystal Functionalization through Polymer Grafting. **2018**.
- (7) Mu, M.; Composto, R. J.; Clarke, N.; Winey, K. I. Minimum in Diffusion Coefficient with Increasing {MWCNT} Concentration Requires Tracer Molecules to Be Larger than Nanotubes. *Macromolecules* **2009**, *42*, 8365–8369.
- (8) Cheng, S.; Carroll, B.; Bocharova, V.; Carrillo, J. M.; Sumpter, B. G.; Sokolov, A. P. Focus: Structure and Dynamics of the Interfacial Layer in Polymer Nanocomposites with Attractive Interactions. *J. Chem. Phys.* **2017**, *146*, 203201.

- (9) Lin, C.-C.; Gam, S.; Meth, J. S.; Clarke, N.; Winey, K. I.; Composto, R. J. Do Attractive Polymer–Nanoparticle Interactions Retard Polymer Diffusion in Nanocomposites? **2013**, *46*, 42.
- (10) Lin, Y.; Li, P.; Liu, W.; Chen, J.; Liu, X.; Jiang, P.; Huang, X. Application-Driven High-Thermal-Conductivity Polymer Nanocomposites. *ACS Nano* **2024**, *18*, 3851–3870.
- (11) Bocharova, V.; Genix, A.-C.; Carrillo, J.-M. Y.; Kumar, R.; Carroll, B.; Erwin, A.; Voylov, D.; Kisliuk, A.; Wang, Y.; Sumpter, B. G.; Sokolov, A. P. Addition of Short Polymer Chains Mechanically Reinforces Glassy Poly(2-Vinylpyridine)–Silica Nanoparticle Nanocomposites. *Cite This ACS Appl. Nano Mater* **2021**, *2020*, 21.
- (12) Raemdonck, K.; Braeckmans, K.; Demeester, J.; De Smedt, S. C. Merging the Best of Both Worlds: Hybrid Lipid-Enveloped Matrix Nanocomposites in Drug Delivery. *Chem. Soc. Rev* **2014**, *43*, 444.
- (13) Parrish, E.; Caporizzo, M. A.; Composto, R. J. Network Confinement and Heterogeneity Slows Nanoparticle Diffusion in Polymer Gels. *J. Chem. Phys.* **2017**, *146*, 203318.
- (14) Merkel, T. C.; Freeman, B. D.; Spontak, R. J.; He, Z.; Pinnau, I.; Meakin, P.; Hill, A. J. Ultrapерmeable, Reverse-Selective Nanocomposite Membranes. *Science (80-.)*. **2002**, *296*, 519–522.
- (15) Yin, J.; Deng, B. Polymer-Matrix Nanocomposite Membranes for Water Treatment. *J. Memb. Sci.* **2015**, *479*, 256–275.
- (16) Duncan, T. V. Applications of Nanotechnology in Food Packaging and Food Safety: Barrier Materials, Antimicrobials and Sensors. *J. Colloid Interface Sci.* **2011**, *363*, 1–24.
- (17) Huang, J.-Y.; Li, X.; Zhou, W. Safety Assessment of Nanocomposite for Food Packaging

Application. **2015**.

- (18) Beecroft, L. L.; Ober, C. K. Nanocomposite Materials for Optical Applications. *Chem. Mater.* **1997**, *9*, 1302–1317.
- (19) Barna, E.; Bommer, B.; Kürsteiner, J.; Vital, A.; Trzebiatowski, O. V; Koch, W.; Schmid, B.; Graule, T. Innovative, Scratch Proof Nanocomposites for Clear Coatings.
- (20) Buitrago, C. F.; Pressly, J. F.; Yang, A. S.; Gordon, P. A.; Riggelman, R. A.; Natarajan, B.; Winey, K. I. Creep Attenuation in Glassy Polymer Nanocomposites with Variable Polymer–Nanoparticle Interactions. *Soft Matter* **2020**, *16*, 8912–8924.
- (21) Vilay, V.; Mariatti, M.; Ahmad, Z.; Pasomsouk, K.; Todo, M. Characterization of the Mechanical and Thermal Properties and Morphological Behavior of Biodegradable Poly(L-Lactide)/Poly(ϵ -Caprolactone) and Poly(L-Lactide)/Poly(Butylene Succinate-L-Lactate) Polymeric Blends. *J. Appl. Polym. Sci.* **2009**, *114*, 1784–1792.
- (22) Mutiso, R. M.; Winey, K. I. Electrical Properties of Polymer Nanocomposites Containing Rod-like Nanofillers. *Prog. Polym. Sci.* **2015**, *40*, 63–84.
- (23) Lebedev, O. V.; Goncharuk, G. P.; Ozerin, A. N. Changes in Electrical Conductance of Polymer Composites Melts Due to Carbon Nanofiller Particles Migration. *Polym.* *2021*, *Vol. 13*, Page 1030 **2021**, *13*, 1030.
- (24) Tuteja, A.; Mackay, M. E.; Narayanan, S.; Asokan, S.; Wong, M. S. Breakdown of the Continuum Stokes-Einstein Relation for Nanoparticle Diffusion. *Nano Lett.* **2007**, *7*, 1276–1281.
- (25) Bailey, E. J.; Winey, K. I. Dynamics of Polymer Segments, Polymer Chains, and Nanoparticles in Polymer Nanocomposite Melts: A Review. *Prog. Polym. Sci.* **2020**, *105*,

101242.

- (26) Bailey, E. J.; Griffin, P. J.; Composto, R. J.; Winey, K. I. Multiscale Dynamics of Small, Attractive Nanoparticles and Entangled Polymers in Polymer Nanocomposites. *Macromolecules* **2019**, *52*, 2181–2188.
- (27) Grabowski, C. A.; Mukhopadhyay, A. Size Effect of Nanoparticle Diffusion in a Polymer Melt. *Macromolecules* **2014**, *47*, 7238–7242.
- (28) Shrestha, U. M.; Han, L.; Saito, T.; Schweizer, K. S.; Dadmun, M. D. Mechanism of Soft Nanoparticle Diffusion in Entangled Polymer Melts. **2022**, *14*, 45.
- (29) Cheng, S.; Xie, S.-J.; Carrillo, J.-M. Y.; Carroll, B.; Martin, H.; Cao, P.-F.; Dadmun, M. D.; Sumpter, B. G.; Novikov, V. N.; Schweizer, K. S.; Sokolov, A. P. Big Effect of Small Nanoparticles: A Shift in Paradigm for Polymer Nanocomposites. *ACS Nano* **2017**, *11*, 752–759.
- (30) Cruickshank, C. The Stokes-Einstein Law for Diffusion in Solution. *Proc. R. Soc. London. Ser. A, Contain. Pap. a Math. Phys. Character* **1924**, *106*, 724–749.
- (31) Kalathi, J. T.; Yamamoto, U.; Schweizer, K. S.; Grest, G. S.; Kumar, S. K. Nanoparticle Diffusion in Polymer Nanocomposites. *Phys. Rev. Lett.* **2014**, *112*, 108301.
- (32) Grabowski, C. A.; Mukhopadhyay, A. Size Effect of Nanoparticle Diffusion in a Polymer Melt. *Macromolecules* **2014**, *47*, 7238–7242.
- (33) Karatrantos, A.; Composto, R. J.; Winey, K. I.; Clarke, N. Polymer and Spherical Nanoparticle Diffusion in Nanocomposites. *J. Chem. Phys.* **2017**, *146*, 203331.
- (34) Rubinstein, M.; Colby, R. H. *Polymer Physics*; Oxford University Press, 2003.
- (35) Park, J.; Bailey, E. J.; Composto, R. J.; Winey, K. I. Single-Particle Tracking of Nonsticky

- and Sticky Nanoparticles in Polymer Melts. *Macromolecules* **2020**, *53*, 3933–3939.
- (36) Brochard Wyart, F.; de Gennes, P. G. Viscosity at Small Scales in Polymer Melts. *Eur. Phys. J. E Soft Matter* **2000**, *1*, 93–97.
- (37) Wang, L.; Ma, J.; Hong, W.; Zhang, H.; Lin, J. Nanoscale Diffusion of Polymer-Grafted Nanoparticles in Entangled Polymer Melts. *Macromolecules* **2020**, *53*, 8393–8399.
- (38) Sorichetti, V.; Hugouvieux, V.; Kob, W. Dynamics of Nanoparticles in Polydisperse Polymer Networks: From Free Diffusion to Hopping. *Macromolecules* **2021**, *54*, 8575–8589.
- (39) Cai, L. H.; Panyukov, S.; Rubinstein, M. Hopping Diffusion of Nanoparticles in Polymer Matrices. *Macromolecules* **2015**, *48*, 847–862.
- (40) Cai, L.-H.; Panyukov, S.; Rubinstein, M. Mobility of Nonsticky Nanoparticles in Polymer Liquids. *Macromolecules* **2011**, *44*, 7853–7863.
- (41) Maldonado-Camargo, L.; Rinaldi, C. Breakdown of the Stokes-Einstein Relation for the Rotational Diffusivity of Polymer Grafted Nanoparticles in Polymer Melts. *Nano Lett.* **2016**, *16*, 6767–6773.
- (42) Park, J.; Bailey, E. J.; Composto, R. J.; Winey, K. I. Single-Particle Tracking of Nonsticky and Sticky Nanoparticles in Polymer Melts. *Macromolecules* **2020**, *53*, 3933–3939.
- (43) Jimenez, A. M.; Zhao, D.; Misquitta, K.; Jestin, J.; Kumar, S. K. Exchange Lifetimes of the Bound Polymer Layer on Silica Nanoparticles. *ACS Macro Lett.* **2019**, *8*, 166–171.
- (44) Harton, S. E.; Kumar, S. K.; Yang, H.; Koga, T.; Hicks, K.; Lee, H.; Mijovic, J.; Liu, M.; Vallery, R. S.; Gidley, D. W. Immobilized Polymer Layers on Spherical Nanoparticles. *Macromolecules* **2010**, *43*, 3415–3421.

- (45) Griffin, P. J.; Bocharova, V.; Middleton, L. R.; Composto, R. J.; Clarke, N.; Schweizer, K. S.; Winey, K. I. Influence of the Bound Polymer Layer on Nanoparticle Diffusion in Polymer Melts. *ACS Macro Lett.* **2016**, *5*, 1141–1145.
- (46) Holt, A. P.; Griffin, P. J.; Bocharova, V.; Agapov, A. L.; Imel, A. E.; Dadmun, M. D.; Sangoro, J. R.; Sokolov, A. P. Dynamics at the Polymer/Nanoparticle Interface in Poly(2-Vinylpyridine)/ Silica Nanocomposites. *Macromolecules* **2014**, *47*, 1837–1843.
- (47) Holt, A. P.; Sangoro, J. R.; Wang, Y.; Agapov, A. L.; Sokolov, A. P. Chain and Segmental Dynamics of Poly(2-Vinylpyridine) Nanocomposites. **2013**.
- (48) Gong, C.; Weiblen, D.; Rende, D.; Akcora, P.; Ozisik, R. Stability of Particle Dispersion and Heterogeneous Interfacial Layers in Polymer Nanocomposites. *Polymer (Guildf)*. **2021**, *226*, 123813.
- (49) Giovino, M.; Pribyl, J.; Benicewicz, B.; Kumar, S.; Schadler, L. Linear Rheology of Polymer Nanocomposites with Polymer-Grafted Nanoparticles. *Polymer (Guildf)*. **2017**, *131*, 104–110.
- (50) Yang, S.; Akcora, P. Deformation of Chemically Heterogeneous Interfacial Layers of Polymer Nanocomposites. **2019**, *8*, 1635–1641.
- (51) Carroll, B.; Bocharova, V.; Carrillo, J.-M. Y.; Kisliuk, A.; Cheng, S.; Yamamoto, U.; Schweizer, K. S.; Sumpter, B. G.; Sokolov, A. P. Diffusion of Sticky Nanoparticles in a Polymer Melt: Crossover from Suppressed to Enhanced Transport. *Macromolecules* **2018**, *51*, 2268–2275.
- (52) Yamamoto, U.; Carrillo, J.-M. Y.; Bocharova, V.; Sokolov, A. P.; Sumpter, B. G.; Schweizer, K. S. Theory and Simulation of Attractive Nanoparticle Transport in Polymer

- Melts. *Macromolecules* **2018**, *51*, 2258–2267.
- (53) Mun, E. A.; Hannell, C.; Rogers, S. E.; Hole, P.; Williams, A. C.; Khutoryanskiy, V. V. On the Role of Specific Interactions in the Diffusion of Nanoparticles in Aqueous Polymer Solutions. *Langmuir* **2014**, *30*, 308–317.
- (54) Al-Obaidi, H.; Florence, A. T. Nanoparticle Delivery and Particle Diffusion in Confined and Complex Environments. *J. Drug Deliv. Sci. Technol.* **2015**, *30*, 266–277.
- (55) Wang, D.; Kou, R.; Choi, D.; Yang, Z.; Nie, Z.; Li, J.; Saraf, L. V.; Hu, D.; Zhang, J.; Graff, G. L.; Liu, J.; Pope, M. A.; Aksay, I. A. Ternary Self-Assembly of Ordered Metal Oxide-Graphene Nanocomposites for Electrochemical Energy Storage. *ACS Nano* **2010**, *4*, 1587–1595.
- (56) Gong, M.; Zhang, L.; Wan, P. Polymer Nanocomposite Meshes for Flexible Electronic Devices. *Prog. Polym. Sci.* **2020**, *107*, 101279.
- (57) Ge, T. Scaling Perspective on Dynamics of Nanoparticles in Polymers: Length- and Time-Scale Dependent Nanoparticle-Polymer Coupling. *Macromolecules* **2023**, *56*, 3809–3837.
- (58) Bailey, E. J.; Griffin, P. J.; Composto, R. J.; Winey, K. I. Multiscale Dynamics of Small, Attractive Nanoparticles and Entangled Polymers in Polymer Nanocomposites. *Macromolecules* **2019**, *52*, 2181–2188.
- (59) Genix, A.-C.; Bocharova, V.; Kisliuk, A.; Carroll, B.; Zhao, S.; Oberdisse, J.; Sokolov, A. P. Enhancing the Mechanical Properties of Glassy Nanocomposites by Tuning Polymer Molecular Weight. **2018**.
- (60) Holt, A. P.; Bocharova, V.; Cheng, S.; Kisliuk, A. M.; White, B. T.; Saito, T.; Uhrig, D.; Mahalik, J. P.; Kumar, R.; Imel, A. E.; Etampawala, T.; Martin, H.; Sikes, N.; Sumpter, B.

- G.; Dadmun, M. D.; Sokolov, A. P. Controlling Interfacial Dynamics: Covalent Bonding versus Physical Adsorption in Polymer Nanocomposites. *ACS Nano* **2016**, *10*, 6843–6852.
- (61) Cheng, S.; Holt, A. P.; Wang, H.; Fan, F.; Bocharova, V.; Martin, H.; Etampawala, T.; White, B. T.; Saito, T.; Kang, N.-G.; Dadmun, M. D.; Mays, J. W.; Sokolov, A. P. Unexpected Molecular Weight Effect in Polymer Nanocomposites. *Phys. Rev. Lett.* **2016**, *116*, 038302-1–4.
- (62) Holt, A. P.; Bocharova, V.; Cheng, S.; Kisliuk, A. M.; White, B. T.; Saito, T.; Uhrig, D.; Mahalik, J. P.; Kumar, R.; Imel, A. E.; Etampawala, T.; Martin, H.; Sikes, N.; Sumpter, B. G.; Dadmun, M. D.; Sokolov, A. P. Controlling Interfacial Dynamics: Covalent Bonding versus Physical Adsorption in Polymer Nanocomposites. **2016**.
- (63) Holt, A. P.; Griffin, P. J.; Bocharova, V.; Agapov, A. L.; Imel, A. E.; Dadmun, M. D.; Sangoro, J. R.; Sokolov, A. P. Dynamics at the Polymer/Nanoparticle Interface in Poly(2-Vinylpyridine)/ Silica Nanocomposites. *Macromolecules* **2014**, *47*, 1837–1843.
- (64) Bailey, E. J.; Griffin, P. J.; Tyagi, M.; Winey, K. I. Segmental Diffusion in Attractive Polymer Nanocomposites: A Quasi-Elastic Neutron Scattering Study. *Macromolecules* **2019**, *52*, 669–678.
- (65) Popov, I.; Carroll, B.; Bocharova, V.; Genix, A.-C.; Cheng, S.; Khamzin, A.; Kisliuk, A.; Sokolov, A. P. Strong Reduction in Amplitude of the Interfacial Segmental Dynamics in Polymer Nanocomposites. **2020**.
- (66) Lin, C. C.; Parrish, E.; Composto, R. J. Macromolecule and Particle Dynamics in Confined Media. *Macromolecules* **2016**, *49*, 5755–5772.
- (67) Roseker, W.; Hruszkewycz, S. O.; Lehmkuhler, F.; Walther, M.; Schulte-Schrepping, H.;

- Lee, S.; Osaka, T.; Strüder, L.; Hartmann, R.; Sikorski, M.; Song, S.; Robert, A.; Fuoss, P. H.; Sutton, M.; Stephenson, G. B.; Grübel, G. Towards Ultrafast Dynamics with Split-Pulse X-Ray Photon Correlation Spectroscopy at Free Electron Laser Sources. *Nat. Commun.* **2018**, *9*, 1–6.
- (68) Guo, H.; Bourret, G.; Lennox, R. B.; Sutton, M.; Harden, J. L.; Leheny, R. L. Entanglement-Controlled Subdiffusion of Nanoparticles within Concentrated Polymer Solutions. *Phys. Rev. Lett.* **2012**, *109*, 055901.
- (69) Manzo, C.; Garcia-Parajo, M. F. A Review of Progress in Single Particle Tracking: From Methods to Biophysical Insights. *Reports Prog. Phys.* **2015**, *78*, 124601.
- (70) Rose, K. A.; Molaei, M.; Boyle, M. J.; Lee, D.; Crocker, J. C.; Composto, R. J. Particle Tracking of Nanoparticles in Soft Matter. *J. Appl. Phys.* **2020**, *127*, 191101.
- (71) Kohli, I.; Mukhopadhyay, A. Diffusion of Nanoparticles in Semidilute Polymer Solutions: Effect of Different Length Scales. *Macromolecules* **2012**, *45*, 6143–6149.
- (72) Grabowski, C. A.; Adhikary, B.; Mukhopadhyay, A. Dynamics of Gold Nanoparticles in a Polymer Melt. *Appl. Phys. Lett.* **2009**, *94*, 021903.
- (73) Composto, R. J.; Kramer, E. J. Mutual Diffusion Studies of Polystyrene and Poly(Xylenyl Ether) Using Rutherford Backscattering Spectrometry. *J. Mater. Sci.* **1991**, *26*, 2815–2822.
- (74) Composto, R. J.; Walters, R. M.; Genzer, J. Application of Ion Scattering Techniques to Characterize Polymer Surfaces and Interfaces. *Mater. Sci. Eng. R Reports* **2002**, *38*, 107–180.
- (75) Cole, D. H.; Shull, K. R.; Rehn, L. E.; Baldo, P. M. RBS Analysis of the Diffusion of Nano-Size Spheres in a Polymer Matrix. *Nucl. Instruments Methods Phys. Res. Sect. B Beam*

- Interact. with Mater. Atoms* **1998**, 136–138, 283–289.
- (76) Green, P. F.; Palmstrom, C. J.; Mayer, J. W.; Kramer, E. J. Marker Displacement Measurements of Polymer-Polymer Interdiffusion. *Macromolecules* **1985**, 18, 501–507.
 - (77) Choi, J.; Cargnello, M.; Murray, C. B.; Clarke, N.; Winey, K. I.; Composto, R. J. Fast Nanorod Diffusion through Entangled Polymer Melts. *ACS Macro Lett.* **2015**, 4, 952–956.
 - (78) Spool, A. M. *The Practice of TOF-SIMS: Time of Flight Secondary Ion Mass Spectrometry* - Alan M. Spool - Google Books; Momentum Press, 2016.
 - (79) Mei, H.; Laws, T. S.; Terlier, T.; Verduzco, R.; Stein, G. E. Characterization of Polymeric Surfaces and Interfaces Using Time-of-Flight Secondary Ion Mass Spectrometry. *Journal of Polymer Science*. John Wiley and Sons Inc April 1, 2021, pp 1174–1198.
 - (80) Zhang, A. C.; Maguire, S. M.; Ford, J. T.; Composto, R. J. Using Focused Ion Beam Time-of-Flight Secondary Ion Mass Spectrometry to Depth Profile Nanoparticles in Polymer Nanocomposites. *Microsc. Microanal.* **2023**, 29, 1557–1565.
 - (81) Karar, N.; Gupta, T. K. Study of Polymers and Their Blends Using TOF-SIMS Ion Imaging. *Vacuum* **2015**, 111, 119–123.
 - (82) Smentkowski, V.; Goswami, S.; Kollmer, F.; Zakel, J.; Arlinghaus, H.; Rading, D. Analysis of Thin Film Specimens Using {ToF-SIMS} Wedge Protocol, A Comparison with Depth Profiling. *Microsc. Microanal.* **2021**, 27, 1564–1565.
 - (83) Sui, T.; Song, B.; Dluhos, J.; Lu, L.; Korsunsky, A. M. Nanoscale Chemical Mapping of Li-Ion Battery Cathode Material by {FIB-SEM} and {TOF-SIMS} Multi-Modal Microscopy. *Nano Energy* **2015**, 17, 254–260.
 - (84) Karar, N.; Singh, B. P.; Elizabeth, I. Analysis of Multi-Wall Carbon Nanotube Based Porous

- Li Battery Electrodes' Using {TOF-SIMS} Ion Imaging. *Appl. Surf. Sci.* **2015**, *349*, 644–649.
- (85) Richardin, P.; Mazel, V.; Walter, P.; Lapr v te, O.; Brunelle, A. Identification of Different Copper Green Pigments in Renaissance Paintings by Cluster-TOF-SIMS Imaging Analysis. *J. Am. Soc. Mass Spectrom.* **2011**, *22*, 1729–1736.
- (86) Prasad, A.; Salim, N. V.; Mozeti , M.; Kailas, L.; Thomas, S. Time-of-flight Secondary Ion Mass Spectrometric Analysis of Polymer Surfaces: A Review. *J. Appl. Polym. Sci.* **2022**, 52286.
- (87) Kobayashi, K.; Watanabe, H.; Maekawa, K.; Kashihara, K.; Yamaguchi, T.; Asai, K.; Hirose, Y. Oxygen Distribution in Nickel Silicide Films Analyzed by Time-of-Flight Secondary Ion Mass Spectrometry. *Micron* **2010**, *41*, 412–415.
- (88) Lianos, L.; Quet, C.; Duc, T. M. Surface Structural Studies of Polyethylene, Polypropylene and Their Copolymers with ToF SIMS. *Surf. Interface Anal.* **1994**, *21*, 14–22.
- (89) Priebe, A.; Aribia, A.; Sastre, J.; Romanyuk, Y. E.; Michler, J. 3D High-Resolution Chemical Characterization of Sputtered Li-Rich NMC811 Thin Films Using TOF-SIMS. *Anal. Chem.* **2023**, *95*, 1074–1084.
- (90) Poleunis, C.; M dard, N.; Bertrand, P. Additive Quantification on Polymer Thin Films by ToF-SIMS: Aging Sample Effects. *Appl. Surf. Sci.* **2004**, *231–232*, 269–273.
- (91) Xie, W.; Weng, L. T.; Yeung, K. L.; Chan, C. M. Segregation of Dioctyl Phthalate to the Surface of Polystyrene Films Characterized by ToF-SIMS and XPS. *Surf. Interface Anal.* **2018**, *50*, 1302–1309.
- (92) Lu, X.; Sj vall, P.; Soenen, H. Structural and Chemical Analysis of Bitumen Using Time-

- of-Flight Secondary Ion Mass Spectrometry (TOF-SIMS). *Fuel* **2017**, *199*, 206–218.
- (93) Bailey, J.; Havelund, R.; Shard, A. G.; Gilmore, I. S.; Alexander, M. R.; Sharp, J. S.; Scurr, D. J. 3D ToF-SIMS Imaging of Polymer Multilayer Films Using Argon Cluster Sputter Depth Profiling. *ACS Appl. Mater. Interfaces* **2015**, *7*, 2654–2659.
- (94) Prasad, A.; Salim, N. V.; Mozetič, M.; Kailas, L.; Thomas, S. Time-of-Flight Secondary Ion Mass Spectrometric Analysis of Polymer Surfaces: A Review. *J. Appl. Polym. Sci.* **2022**, *139*.
- (95) Chan, C. M.; Weng, L. T. Surface Characterization of Polymer Blends by XPS and ToF-SIMS. *Materials (Basel)*. **2016**, *9*.
- (96) Ravati, S.; Poulin, S.; Piyakis, K.; Favis, B. D. Phase Identification and Interfacial Transitions in Ternary Polymer Blends by ToF-SIMS. *Polymer (Guildf)*. **2014**, *55*, 6110–6123.
- (97) Brennan, B.; Spencer, S. J.; Belsey, N. A.; Faris, T.; Cronin, H.; Silva, S. R.; Sainsbury, T.; Gilmore, I. S.; Stoeva, Z.; Pollard, A. J. Structural, Chemical and Electrical Characterisation of Conductive Graphene-Polymer Composite Films. *Appl. Surf. Sci.* **2017**, *403*, 403–412.
- (98) Chen, W. Y.; Ling, Y. C.; Chen, B. J.; Shih, H. H.; Cheng, C. H. Diffusion Study of Multi-Organic Layers in OLEDs by ToF-SIMS. *Appl. Surf. Sci.* **2006**, *252*, 6594–6596.
- (99) Chan, C. M.; Weng, L. T. Surface Characterization of Polymer Blends by XPS and ToF-SIMS. *Mater. 2016, Vol. 9, Page 655* **2016**, *9*, 655.
- (100) Fardim, P.; Gustafsson, J.; Von Schoultz, S.; Peltonen, J.; Holmbom, B. Extractives on Fiber Surfaces Investigated by XPS, ToF-SIMS and AFM. *Colloids Surfaces A Physicochem. Eng. Asp.* **2005**, *255*, 91–103.

- (101) Abd Mutalib, M.; Rahman, M. A.; Othman, M. H. D.; Ismail, A. F.; Jaafar, J. Scanning Electron Microscopy (SEM) and Energy-Dispersive X-Ray (EDX) Spectroscopy. *Membr. Charact.* **2017**, 161–179.
- (102) Sakurada, T.; Hashimoto, S.; Tsuchiya, Y.; Tachibana, S.; Suzuki, M.; Shimizu, K. Lateral Resolution of EDX Analysis with Ultra Low Acceleration Voltage SEM. *sasj.jp* T Sakurada, S Hashimoto, Y Tsuchiya, S Tachibana, M Suzuki, K Shimizu *Journal Surf. Anal.* **2005**•*sasj.jp* **2005**, 12.
- (103) Kubicek, M.; Holzlechner, G.; Opitz, A. K.; Larisegger, S.; Hutter, H.; Fleig, J. A Novel ToF-SIMS Operation Mode for Sub 100 Nm Lateral Resolution: Application and Performance. *Appl. Surf. Sci.* **2014**, 289, 407.
- (104) Moffitt, C. Fundamental Aspects of XPS and the Development of XPS Imaging. *Micros. Today* **2011**, 19, 16–21.
- (105) Powell, C. J.; Jablonski, A. Surface Sensitivity of X-Ray Photoelectron Spectroscopy. *Nucl. Instruments Methods Phys. Res. Sect. A Accel. Spectrometers, Detect. Assoc. Equip.* **2009**, 601, 54–65.
- (106) Watts, J. F.; Wolstenholme, J. An Introduction to Surface Analysis by XPS and AES. *An Introd. to Surf. Anal. by XPS AES* **2003**.
- (107) Chung, Y.; Pak, C.; Park, G.-S.; Jeon, W. S.; Kim, J.-R.; Lee, Y.; Chang, H.; Seung, D. Understanding a Degradation Mechanism of Direct Methanol Fuel Cell Using {TOF-SIMS} and {XPS}. *J. Phys. Chem. C Nanomater. Interfaces* **2008**, 112, 313–318.
- (108) Wang, K.; Composto, R. J.; Winey, K. I. ToF-SIMS Depth Profiling to Measure Nanoparticle and Polymer Diffusion in Polymer Melts. *Macromolecules* **2023**.

- (109) Harrison, E. T.; Peczoneczyk, S. L.; Sharafi, A.; Wujcik, K. H.; Drews, A.; Simko, S. Surface Characterization of Battery Electrode/Electrolyte Materials Using {XPS} and {ToF-SIMS}. *Meet. abstr.* **2019**, *MA2019-01*, 521.
- (110) Balazs, A. C.; Emrick, T.; Russell, T. P. Nanoparticle Polymer Composites: Where Two Small Worlds Meet. *Science* (80-.). **2006**, *314*, 1107–1110.
- (111) Mills, P. J.; Green, P. F.; Palmstrøm, C. J.; Mayer, J. W.; Kramer, E. J. Polydispersity Effects on Diffusion in Polymers: Concentration Profiles of d-Polystyrene Measured by Forward Recoil Spectrometry. *J. Polym. Sci. Part B Polym. Phys.* **1986**, *24*, 1–9.
- (112) Green, P. F.; Kramer, E. J. Matrix Effects on the Diffusion of Long Polymer Chains. *Macromolecules* **1986**, *19*, 1108–1114.
- (113) Mackay, M. E.; Dao, T. T.; Tuteja, A.; Ho, D. L.; van Horn, B.; Kim, H.-C.; Hawker, C. J. Nanoscale Effects Leading to Non-Einstein-like Decrease in Viscosity. *Nat. Mater.* **2003**, *2*, 762–766.
- (114) Composto, R. J.; Mayer, J. W.; Kramer, E. J.; White, D. M. Fast Mutual Diffusion in Polymer Blends. *Phys. Rev. Lett.* **1986**, *57*, 1312–1315.
- (115) Composto, R. J.; Kramer, E. J.; White, D. M. Mutual Diffusion in the Miscible Polymer Blend Polystyrene/Poly(Xylenyl Ether). *Macromolecules* **1988**, *21*, 2580–2588.
- (116) Barrat, J.-L.; Fredrickson, G. H. Diffusion of a Symmetric Block Copolymer in a Periodic Potential. *Macromolecules* **1991**, *24*, 6378–6383.
- (117) Gam, S.; Meth, J. S.; Zane, S. G.; Chi, C.; Wood, B. A.; Seitz, M. E.; Winey, K. I.; Clarke, N.; Composto, R. J. Macromolecular Diffusion in a Crowded Polymer Nanocomposite. *Macromolecules* **2011**, *44*, 3494–3501.

- (118) Shrestha, U. M.; Han, L.; Saito, T.; Schweizer, K. S.; Dadmun, M. D. Mechanism of Soft Nanoparticle Diffusion in Entangled Polymer Melts. *Macromolecules* **2020**, *53*, 7580–7589.
- (119) Imel, A. E.; Rostom, S.; Holley, W.; Baskaran, D.; Mays, J. W.; Dadmun, M. D. The Tracer Diffusion Coefficient of Soft Nanoparticles in a Linear Polymer Matrix. *RSC Adv.* **2017**, *7*, 15574–15581.
- (120) Jo, K. Il; Oh, Y.; Kim, T. H.; Bang, J.; Yuan, G.; Satija, S. K.; Sung, B. J.; Koo, J. Position-Dependent Diffusion Dynamics of Entangled Polymer Melts Nanoconfined by Parallel Immiscible Polymer Films. *ACS Macro Lett.* **2020**, *9*, 1483–1488.
- (121) Lin, C.-C.; Griffin, P. J.; Chao, H.; Hore, M. J. A.; Ohno, K.; Clarke, N.; Riggleman, R. A.; Winey, K. I.; Composto, R. J. Grafted Polymer Chains Suppress Nanoparticle Diffusion in Athermal Polymer Melts. *J. Chem. Phys.* **2017**, *146*, 203332.
- (122) Mills, P. J.; Green, P. F.; Palmstrom, C. J.; Mayer, J. W.; Kramer, E. J. Analysis of Diffusion in Polymers by Forward Recoil Spectrometry. *Appl. Phys. Lett.* **1998**, *45*, 957.
- (123) Martín, J.; Hernández-Vélez, M.; de Abril, O.; Luna, C.; Muñoz-Martín, A.; Vázquez, M.; Mijangos, C. Fabrication and Characterization of Polymer-Based Magnetic Composite Nanotubes and Nanorods. *Eur. Polym. J.* **2012**, *48*, 712–719.
- (124) Bailey, E. J.; Griffin, P. J.; Composto, R. J.; Winey, K. I. Characterizing the Areal Density and Desorption Kinetics of Physically Adsorbed Polymer in Polymer Nanocomposite Melts. *Macromolecules* **2020**, *53*, 2744–2753.
- (125) Fit plane to 3-D point cloud - MATLAB pcfitplane
<https://www.mathworks.com/help/vision/ref/pcfitplane.html> (accessed Jun 22, 2022).

- (126) Fischler, M. A.; Bolles, R. C. Random Sample Consensus. *Commun. ACM* **1981**, *24*, 381–395.
- (127) Belu, A. M.; Davies, M. C.; Newton, J. M.; Patel, N. TOF-SIMS Characterization and Imaging of Controlled-Release Drug Delivery Systems. *Anal. Chem.* **2000**, *72*, 5625–5638.
- (128) Méar, F.; Coillot, D.; Podor, R.; Montagne, L. Self-Healing Nanocomposites: Role and Activation of Inorganic Moieties and Hybrid Nanophases. In *{Self-Healing} at the Nanoscale*; CRC Press, 2011; pp 188–223.
- (129) Mallakpour, S.; Naghdi, M. {Polymer/SiO₂} Nanocomposites: Production and Applications. *Prog. Mater. Sci.* **2018**, *97*, 409–447.
- (130) Young, W. W.; Katsumata, R. Intermediate Polymer Relaxation Explains the Anomalous Rheology of Nanocomposites with Ultrasmall Attractive POSS Nanoparticles. *ACS Polym. Au* **2023**, *3*, 466–474.
- (131) Lin, C.-C.; Parrish, E.; Composto, R. J. Macromolecule and Particle Dynamics in Confined Media. *Macromolecules* **2016**, *49*, 5755–5772.
- (132) Papakonstantopoulos, G. J.; Yoshimoto, K.; Doxastakis, M.; Nealey, P. F.; De Pablo, J. J. Local Mechanical Properties of Polymeric Nanocomposites. *Phys. Rev. E - Stat. Nonlinear, Soft Matter Phys.* **2005**, *72*, 031801-031801–031806.
- (133) Cheng, S.; Carroll, B.; Bocharova, V.; Carrillo, J.-M.; Sumpter, B. G.; Sokolov, A. P.; Carrillo, J.-M. Y. Perspective: Outstanding Theoretical Questions in Polymer-Nanoparticle Hybrids. *J. Chem. Phys.* **2017**, *146*, 203201.
- (134) Liu, J.; Cao, D.; Zhang, L. Molecular Dynamics Study on Nanoparticle Diffusion in Polymer Melts: A Test of the Stokes-Einstein Law. *J. Phys. Chem. C* **2008**, *112*, 6653–

6661.

- (135) Mendez, N. F.; Dhara, D.; Zhang, Q.; Narayanan, S.; Schadler, L. S.; Müller, A. J.; Kumar, S. K. Nanoparticle Diffusion in Miscible Polymer Nanocomposite Melts. *Macromolecules* **2023**, *56*, 4658–4668.
- (136) Kwon, N. K.; Park, C. S.; Lee, C. H.; Kim, Y. S.; Zukoski, C. F.; Kim, S. Y. Tunable Nanoparticle Stability in Concentrated Polymer Solutions On the Basis of the Temperature Dependent Solvent Quality. *Macromolecules* **2016**, *20*, 25.
- (137) Jin, J.; Wang, X.; Wick, C. D.; Dang, L. X.; Miller, J. D. Silica Surface States and Their Wetting Characteristics. <https://doi.org/10.1680/jsuin.19.00053> **2020**, *8*, 145–157.
- (138) Watcharenwong, A.; Saijaioup, N.; Bailuang, Y.; Kajitvichyanukul, P. Morphology and Wettability of Nanoporous Aluminium Oxide Film Prepared by Anodization. *Key Eng. Mater.* **2017**, *737*, 174–178.
- (139) Bronstein, N. D.; Li, L.; Xu, L.; Yao, Y.; Ferry, V. E.; Alivisatos, A. P.; Nuzzo, R. G. Luminescent Solar Concentration with Semiconductor Nanorods and Transfer-Printed Micro-Silicon Solar Cells. *ACS Nano* **2014**, *8*, 44–53.
- (140) Mun, E. A.; Hannell, C.; Rogers, S. E.; Hole, P.; Williams, A. C.; Khutoryanskiy, V. V. On the Role of Specific Interactions in the Diffusion of Nanoparticles in Aqueous Polymer Solutions. *Langmuir* **2014**, *30*, 308–317.
- (141) Senses, E.; Ansar, S. M.; Kitchens, C. L.; Mao, Y.; Narayanan, S.; Natarajan, B.; Faraone, A. Small Particle Driven Chain Disentanglements in Polymer Nanocomposites. *Phys. Rev. Lett.* **2017**, *118*.
- (142) Gong, S.; Chen, Q.; Moll, J. F.; Kumar, S. K.; Colby, R. H. Segmental Dynamics of Polymer

- Melts with Spherical Nanoparticles. *ACS Macro Lett.* **2014**, *3*, 773–777.
- (143) Tuteja, A.; Mackay, M. E.; Hawker, C. J.; Van Horn, B. Effect of Ideal, Organic Nanoparticles on the Flow Properties of Linear Polymers: Non-Einstein-like Behavior. *Macromolecules* **2005**, *38*, 8000–8011.
- (144) Meth, J. S.; Gam, S.; Choi, J.; Lin, C. C.; Composto, R. J.; Winey, K. I. Excluded Volume Model for the Reduction of Polymer Diffusion into Nanocomposites. *J. Phys. Chem. B* **2013**, *117*, 15675–15683.
- (145) Gam, S.; Meth, J. S.; Zane, S. G.; Chi, C.; Wood, B. A.; Winey, K. I.; Clarke, N.; Composto, R. J. Polymer Diffusion in a Polymer Nanocomposite: Effect of Nanoparticle Size and Polydispersity. *Soft Matter* **2012**, *8*, 6512.
- (146) Xue, C.; Zheng, X.; Chen, K.; Tian, Y.; Hu, G. Probing Non-Gaussianity in Confined Diffusion of Nanoparticles. *J. Phys. Chem. Lett.* **2016**, *7*, 514–519.
- (147) Babayekhorasani, F.; Dunstan, D. E.; Krishnamoorti, R.; Conrad, J. C. Nanoparticle Diffusion in Crowded and Confined Media. *Soft Matter* **2016**, *12*, 8407–8416.
- (148) Schneider, G. J.; Nusser, K.; Willner, L.; Falus, P.; Richter, D. Dynamics of Entangled Chains in Polymer Nanocomposites. *Macromolecules* **2011**, *44*, 5857–5860.
- (149) Bailey, E. J.; Riggleman, R. A.; Winey, K. I. Polymer Conformations and Diffusion through a Monolayer of Confining Nanoparticles. *Macromolecules* **2020**, *53*, 8171–8180.
- (150) Wang, K.; Winey, K. I. Vehicular and Core-Shell Nanoparticle Diffusion in Entangled Polymer Melts. Submitted.
- (151) Tonelli, A. E. Conformational Characteristics of Poly(2-Vinylpyridine). *Macromolecules* **1985**, *18*, 2579–2583.

- (152) Sko, T.; Vaghefikia, F.; Fitter, rg; Kondrat, S. Macromolecular Crowding: How Shape and Interactions Affect Diffusion. *J. Phys. Chem* **2023**, 2020, 19.
- (153) Hao, T.; Riman, R. E. Calculation of Interparticle Spacing in Colloidal Systems. *J. Colloid Interface Sci.* **2006**, 297, 374–377.
- (154) Brouwers, H. J. H. Particle-Size Distribution and Packing Fraction of Geometric Random Packings. *Phys. Rev. E - Stat. Nonlinear, Soft Matter Phys.* **2006**, 74, 031309.
- (155) Karatrantos, A.; Composto, R. J.; Winey, K. I.; Clarke, N. Nanorod Diffusion in Polymer Nanocomposites by Molecular Dynamics Simulations. *Macromolecules* **2019**, 52, 2513–2520.
- (156) Asgari, N.; Baaske, M. D.; Orrit, M. Burst-by-Burst Measurement of Rotational Diffusion at Nanosecond Resolution Reveals Hot-Brownian Motion and Single-Chain Binding. *ACS Nano* **2023**, 17, 12684–12692.
- (157) Jouault, N.; Zhao, D.; Kumar, S. K. Role of Casting Solvent on Nanoparticle Dispersion in Polymer Nanocomposites. **2014**.
- (158) Murphy, T. M.; Langhe, D. S.; Ponting, M.; Baer, E.; Freeman, B. D.; Paul, D. R. Physical Aging of Layered Glassy Polymer Films via Gas Permeability Tracking. *Polymer (Guildf)*. **2011**, 52, 6117–6125.
- (159) Karen, A.; Ito, K.; Kubo, Y. {TOF-SIMS} Analysis of Lithium Air Battery Discharge Products Utilizing Gas Cluster Ion Beam Sputtering for Surface Stabilization. *Surf. Interface Anal.* **2014**, 46, 344–347.
- (160) Foley, J. D.; Fischler, M. A.; Bolles, R. C. Graphics and Image Processing Random Sample Consensus: A Paradigm for Model Fitting with Apphcatlons to Image Analysis and

Automated Cartography. **1981**.

- (161) Point Cloud Processing - MATLAB & Simulink
<https://www.mathworks.com/help/vision/point-cloud-processing.html> (accessed May 6, 2024).
- (162) Wang, X.; Tilley, R. D.; Watkins, J. J. Simple Ligand Exchange Reactions Enabling Excellent Dispersibility and Stability of Magnetic Nanoparticles in Polar Organic, Aromatic, and Protic Solvents. *Langmuir* **2014**, *30*, 1514–1521.
- (163) Cook, E.; Labiento, G.; Chauhan, B. P. S. Fundamental Methods for the Phase Transfer of Nanoparticles. *Molecules* **2021**, *26*.

CHAPTER 2 : TOF-SIMS DEPTH PROFILING TO MEASURE NANOPARTICLE AND POLYMER DIFFUSION IN POLYMER MELTS

Content in this chapter was published in 2023 in *Macromolecules*, volume 56, issue 6, pages 2277-2285, in a modified version. The authors of this chapter are Kaitlin Wang, Russell Composto, and Karen I. Winey.

Kaitlin Wang and Karen I. Winey conceived the presented idea. Kaitlin Wang conducted the literature search, designed and performed the experiments, developed the methodology, and carried out the data analysis. She also wrote the first draft of the manuscript and incorporated feedback from Karen I. Winey and Russell Composto. Karen I. Winey supervised the experiments and provided revisions to the manuscript drafts. Russell Composto suggested additional details for the experimental methodology and data analysis.

2.1 Introduction

Polymer nanocomposites (PNCs) are valued for their tunable and enhanced properties that lead to applications in industrial rubbers, gas separation membranes, and dielectric materials.¹ Their properties depend on the composition (components) and PNC morphology, as well as the mobility of the polymer and nanoparticles in the PNC. Nanoparticle (NP) diffusion plays an important role during PNC processing and the resulting PNC structure and properties.²⁵ For example, NP diffusion is essential for PNC applications in self-healing materials^{3,110} and drug delivery.¹² Similarly, polymer diffusion is foundational to understanding polymer melts including homopolymers, copolymers, binary polymer blends, and PNCs.^{111–116}

Current methods for measuring NP and polymer diffusion are limited on their time and length scales, the accessible geometries, and the availability of the experimental tools.^{66,117} Previous NP diffusion studies in polymer melts have used dynamic light scattering (DLS), X-ray photon correlation spectroscopy (XPCS),^{24,51} single particle tracking (SPT)³⁵, and Rutherford backscattering spectroscopy (RBS).^{45,75} DLS is an affordable and accessible method that probes diffusion in liquid environments through fitting the intensity correlation function to determine reflecting translational Fickian diffusion,⁵¹ and provides an ensemble measurement of the diffusion coefficient. Using the same fundamental principles, XPCS requires a synchrotron to probe NP diffusion. SPT instruments are fairly accessible and directly measure mean squared displacement of particles to probe diffusion and has been used to capture heterogenous diffusion.¹³ Because DLS/XPCS and SPT require both low T_g ($T_g < T_{room}$) matrices or liquid environments and very dilute systems, these methods are unable to explore many industrially relevant conditions of PNCs with crowded, polydisperse, strongly attractive, or non-spherical nanoparticles.⁶⁶ On the smallest length scales (nm), neutron reflectivity (NR) has been used to probe diffusion of soft nanoparticles and polymer tracer diffusion in polymer melts.^{118–120} Polymer diffusion studies have also used elastic recoil detection (ERD), formerly known as forward recoil spectroscopy (FRES), to determine self-diffusion coefficients^{76,114} but similar to RBS, ERD is becoming less accessible and probes a limited length scale.

RBS and ERD, which use MeV incident ions, are the closest analogs to our time-of-flight secondary ion mass spectroscopy (ToF-SIMS) method and are well-established for measuring polymer and NP diffusion.^{43,45,73,121} Similar to ToF-SIMS, RBS determines the NP diffusion coefficient independent by measuring the depth profile of the NP and then fitting the profile with

a diffusion model. In Griffin's work, the NP concentration of a bilayer sample comprising a PNC film (~100-200 nm) on a thick polymer layer (~10 μm) was measured using RBS after *ex situ* annealing for 0-30 minutes at 180°C.⁴⁵ RBS is limited to measuring NP diffusion in polymer melts with $T_g > T_{room}$ to depths of ~1 μm and has limited chemical sensitivity.⁴⁵ For polymer diffusion, ERD was similarly applied to depth-profile deuterated polymer/non-deuterated polymer bilayers due to its ability to measure a deuterium concentration profiles.^{74,76,111,122–124} These 1-D concentration profiles are fit with Fickian diffusion equations to find the NP and polymer diffusion coefficients. Due to limitations on NP and polymer diffusion measurements including detection limits or specialized materials (deuteration or fluorescence), and increasingly limited access to RBS and ERD, we developed a method applying ToF-SIMS, an increasingly available experimental tool. Our cross-sectional ToF-SIMS method significantly expands accessible compositions and diffusion length scales (0.5-200 μm) and increases the feasibility of diffusion studies in polymer systems across an exceptionally broad range of diffusion coefficients ($\sim 10^{-16}$ to $10^{-6} \text{ cm}^2/\text{s}$).

ToF-SIMS operates by accelerating a focused beam of keV ions of a specified energy towards a sample to eject secondary ions to a time-of-flight detector, which measures the mass and charge of the ejected species.⁷⁸ Mass-to-charge ratios (m/q) are characteristic of the species (atomic or clusters) to provide compositional information of the sample, including distinguishing isotopes, e.g. hydrogen and deuterium.⁷⁹ ToF-SIMS is traditionally used to measure composition as a function of depth from the sample surface. In contrast to this traditional sample orientation, compositional variations deeper within a sample can be expedited by scanning a cross-section of the sample, as demonstrated in our method. As the primary beam sputters the sample, ToF-SIMS

collects three-dimensional compositional data, providing 3D maps for each secondary ion detected with $< 1\ \mu\text{m}$ lateral resolution. ToF-SIMS is a well-established method for depth profiling inorganic systems, with more recent applications in polymer systems.^{78,94} Cluster ion beams, with improved high mass sensitivity compared to primary ion sources, have been used successfully to depth profile polystyrene (PS) and polyvinylpyrrolidone (PVP) layers to depths of $15\ \mu\text{m}$, with depth resolution comparable to ellipsometry ($< 10\ \text{nm}$).⁹³ Depth profiling in ToF-SIMS has also been applied to polymer-based cathode materials, for which dopant and ion concentration distributions determine conductive properties.⁸³ Primary ion beam ToF-SIMS is also capable of measuring filler distribution in polymer composites as Karar and Gupta accomplished in a carbon nanotube (CNT)-polyurethane composite on $100\ \mu\text{m}$ length scales.⁸¹

Applying ToF-SIMS to polymer systems has known challenges, especially when using a primary ion source. With primary ion sources like our own, signal intensity in the high mass range is drastically lowered due to the high rate of fragmentation.^{78,94} The destructive nature of SIMS and the yield-decreasing effects of charging on polymer samples make quantification difficult. ToF-SIMS data analysis is also complicated by the matrix effect, wherein ion yield is dependent on the atom's local environment. For example, surface oxidation causes high yield of secondary ions, skewing counts in the initial frames of collection.^{78,94} Depth profiling analysis is likewise complicated by ion beam mixing, reducing depth resolution.

Here, we demonstrate the capability of ToF-SIMS to measure NP and polymer diffusion in polymer melts by using trilayer samples, optimizing instrumental parameters, and developing a data analysis method to extract 1D NP or deuterated polymer concentration profiles. We determine the tracer NP diffusion coefficient in a silica/poly(2-vinylpyridine) ($\text{SiO}_2/\text{P2VP}$) PNC system.

After varying annealing from 1-5 days, we can extract a concentration profile of the silica by scanning across an exposed cross-section and determine a time independent diffusion coefficient (D_{NP}) from 10 vol% PNC films. We also measured the NP diffusion coefficient in P2VP as a function of NP concentration. We compare our NP diffusion coefficient with well-established RBS results and find excellent agreement, noting that our ToF-SIMS method accesses length scales an order of magnitude larger by performing laterally resolved depth-profiling on a cross-sectioned trilayer sample. In a second study, we determine the concentration profile of a deuterated polystyrene (dPS) tracer film diffusing into PS and comparing the resulting diffusion coefficients with ERD studies find excellent agreement using the ToF-SIMS on cross-sectioned trilayers. Taken together, these two studies validate our ToF-SIMS method as a reliable method to measure NP and polymer diffusion, establishing it as a valuable tool to rejuvenate diffusion studies by expanding the range of accessible diffusion length scales to test current models, and investigate systems that were previously limited by compositional contrast or particle loading.

2.2 Experimental Section

Materials: Poly(2-vinylpyridine) (P2VP) (100 kg/mol, PDI 1.3, $R_g = 7$ nm) was purchased from Polymer Source and used as-received. R_g was determined at the National Institute of Standards and Technology (NIST) using small-angle neutron scattering (SANS) (**Figure A.1**). Nissan-STL silica (SiO_2) nanoparticles ($R_{NP} = 26.1$ nm, PDI 1.19) were solvent-exchanged from methyl-ethyl ketone (MEK) to methanol (MeOH) via crashing the particles out of MEK. Specifically, the MEK-NP solution was diluted with 50 vol% hexane, then centrifuged at 3000 rpm for 3 minutes to form a pellet. The supernatant was then removed via pipette, and the

remaining pellet was immediately re-dispersed into MeOH via alternating vortexing and sonication for > 10 min. Nanoparticle size and dispersity were determined using small-angle x-ray scattering (SAXS) of a capillary filled with a dilute NP in MeOH suspension and was fit using the hard sphere model (**Figure A.2**). Silicon wafers (<100>) with a thick thermal oxide layer (referred as SiO₂ wafer hereafter) were purchased from Nova Electronic Materials. Silicon wafers (<100>) (Si wafer) were purchased from Wafer World Inc. Higher M_w deuterated polystyrene (dPS, 423 kg/mol, PDI = 1.09) and polystyrene (PS, M_w = 450 kg/mol, PDI = 1.12) were purchased from Polymer Source Inc. Relatively lower M_w dPS (69 kg/mol, PDI = 1.09) was purchased from Polymer Laboratories, and 65 kg/mol (PDI = 1.06) PS was purchased from Pressure Chemical Co. Polymer molecular weights were confirmed via gel permeation chromatography.

Trilayer Fabrication for Nanoparticle Diffusion: We produced trilayer samples with a thin PNC layer between two thick P2VP matrix layers to ensure tracer NP diffusion in our system. This process is summarized in Error! Reference source not found.. P2VP matrix films (~6 μm) were prepared via spin coating; the P2VP base-layer was created by spin coating 300 g/L P2VP-methanol (MeOH) solutions at 2000 rpm for 1 minute onto a silicon (Si) wafer. To prepare the PNC mid-layer, 5, 10, or 15 vol% NP in 50 g/L concentration P2VP MeOH solutions were spin coated onto thermal oxide Si wafers at 2000 rpm for 1 min for a thickness of 500 ± 60 nm. PNC layers were measured via scanning electron microscopy (SEM) and thickness was averaged over two samples. The P2VP top layers were spin coated from 200 g/L P2VP solution onto a thermal oxide treated Si wafer (5 μm). All solutions were filtered through a 1 μm mesh filter prior to spin coating.

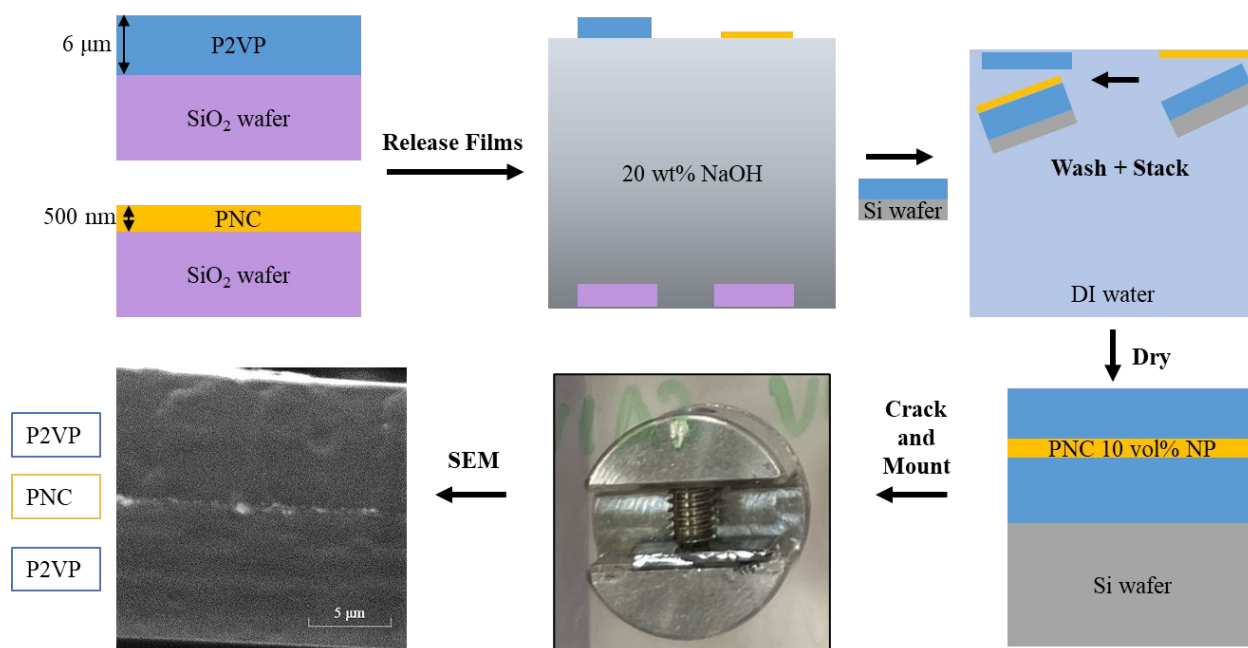


Figure 2.1: Sample preparation schematic for P2VP-PNC-P2VP trilayers. After drying and annealing, the samples were cleaved and mounted for cross-sectional imaging and ToF-SIMS. SEM (30 keV) shows an unannealed 10 vol% NP film between P2VP layers; the free surface of this trilayer sample is visible at upper-right of the image.

To assemble the trilayer samples, the PNC and top P2VP layers on SiO₂ wafers were gently floated on 20 wt% sodium hydroxide (NaOH)-deionized (DI) water solution until the thin films detached (1.5 hours). Using a glass slide, the films were transferred to DI water to remove excess NaOH. A Si wafer with a P2VP bottom layer was slid under the floating film to deposit a PNC layer and then a P2VP top layer. Between deposition samples were briefly dried on a hotplate at 80°C for 5-10 minutes to enhance layer adhesion and avoid trapping water between layers. The trilayer samples were then placed in a custom-built oven at 180°C for 1, 3, or 5 days under vacuum (< 50 Pa).

Trilayer Fabrication for Polymer Diffusion: Polymer diffusion trilayers containing a thin dPS mid-layer and thick hPS (65 kg/mol, 450kg/mol) matrices were fabricated to measure polymer diffusion. The 69k and 423k dPS-toluene solutions (100 g/L and 65 g/L, respectively) were spun coat at 2000 rpm for 1 min on clean glass slides to produce 400-nm thick mid-layers. 65k and 450k PS-toluene solutions (330 g/L and 250 g/L respectively) were spun coat at 1000 rpm for 1 min onto an Si wafer for the base layer, and onto a clean glass slide for the top layer. The mid and top layers of the sample were floated off the glass slides using DI water and stacked onto the base PS layer to create the trilayer sample similar to the process shown in **Figure 2.1**.

Preparing Trilayer Samples for ToF-SIMS: To obtain the cross-sectional view, a diamond scribe was used to fracture samples along a crystallographic plane of the Si wafer to preserve the polymer/wafer interface and ensure the cross section was as flat as possible. Samples were cleaned with a nitrogen gas gun to remove SiO₂ dust on the surface. To reduce surface charging and improve ion yield, all samples were coated with carbon paint suspended in MEK across the entire back of the wafer and along the front of the polymer film, leaving only ~1 mm of bare polymer and cross-sectional interface.

ToF-SIMS method: ToF-SIMS measurements were performed using the Tescan S8252X dual-beam plasma FIB-SEM with Xe⁺. Unless otherwise noted, measurements were taken with Xe⁺ FIB parameters at 30 keV and 100 pA with 1024 × 1024 pixel resolution on positive ion mode for 300 frames. A FIB dwell time of 10 μs and a pulse width of 1000 ns were chosen to measure SiO₂ NP diffusion, because only a low ($m/q < 50$) mass range is required, and the pulse width displayed sufficient m/q range. To improve the signal of deuterated PS fragments (C₂D₂⁺) using the Xe⁺ ion beam, polymer diffusion measurements were taken with a pulse width of 3000 ns and

for 700 frames. For PNC trilayers, a $20 \times 20 \mu\text{m}^2$ field of view (FoV) was used and the ToF-SIMS images were produced using a 2×2 bin width (the minimum required for noise reduction), resulting in an image of 512×512 pixels after processing such that each pixel corresponds to $39 \times 39 \text{ nm}$. This pixel size is smaller than the nanoparticle diameter ($2R_{NP}$), ideally permitting single nanoparticle detection. Polymer diffusion measurements were taken with a $15 \times 15 \mu\text{m}$ FoV to further improve resolution due to the lower intensity signal from the dPS/PS system. While higher pixel resolution is accessible by increasing the pixel count/FoV, it is unnecessary for this experiment and would exponentially increase collection time (**Figure A.3**).

2.3 Results

Measuring NP Concentration Profiles using ToF-SIMS

In this section we demonstrate our data collection and analysis methods that use ToF-SIMS on a cross-sectional trilayer samples to measure the nanoparticle concentration profiles perpendicular to a PNC film. We begin by establishing that ToF-SIMS detects the PNC layer using a relatively small $20 \times 20 \mu\text{m}$ FoV on the trilayer cross-section and the silicon secondary ion (Si^+) (**Figure 2.2a**). The mass spectra clearly shows that a FIB dwell time of $10 \mu\text{s}$ and pulse width of 1000 ns are sufficient to resolve $m/q = 28$ on our instrument. Note that the first 100 frames are omitted due to surface oxidation that distorts the trilayer composition due to the matrix effect previously mentioned (**Figure 2.2b**). Removing the first 100 frames also eliminates resolution changes due to surface topography, as the sample is smoothed by the FIB. We determined etching rate via atomic force microscopy using a spin coated PNC film milled under the same conditions as the cross-sectional trilayer sample. We found the etching rate to be $\sim 1 \text{ nm/frame}$ (**Figure A.4**).

These collection parameters result in a total collection time of 52 mins per sample, with pixel size and frame count most significantly affecting collection time.

We next determine an experimental resolution function to account for instrumental broadening observed in the concentration profiles. We find the FWHM of the beam resolution function by modeling the unannealed film as a step function of width $0.5\ \mu\text{m}$ (as measured by SEM) convoluted with a Gaussian probability density function. By minimizing the residuals between the tilt-corrected 1D concentration profile and the convolution by varying only the FWHM of the Gaussian, we determine the $\text{FWHM} = 0.25\ \mu\text{m}$, which is less than the thickness of the film (**Figure 2.2c**). In addition, **Figure 2.2c** demonstrates the success of our sample preparation method to create flat trilayer samples for cross-sectional analysis. We confirm that etching rates across the FoV are nonpreferential across the trilayer sample (that is, a flat etching profile is achieved) via SEM, and noting there is no significant change in experimental resolution between frames 101-200 and frames 201-300 of data collection. Given that the film is clearly resolved and that its thickness is roughly consistent with SEM measurement ($0.5 \pm 0.06\ \mu\text{m}$), we demonstrated that ToF-SIMS has sufficient lateral resolution to measure NP diffusion on micron length scales, as well as sufficient Si^+ signal from 10 vol% NPs.

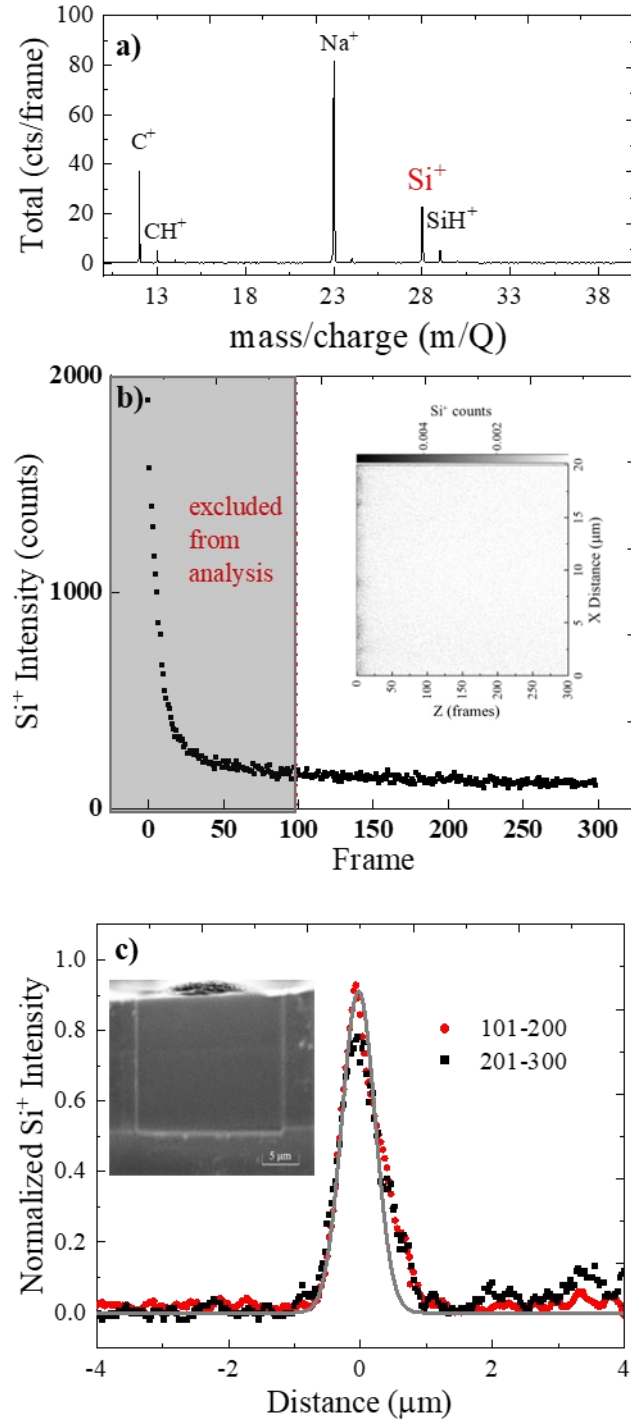


Figure 2.2 : a) m/Q spectra at 100 pA, 30 keV accelerating voltage for 300 frames for a cross-sectional PNC trilayer sample with 10 vol% NP. Characteristic peak for Si^+ ion at $m/Q = 28$. b)

Integrated Si^+ intensity in the X-Y plane as a function of frame. Inset: Projected Si^+ concentration on the XZ plane displays higher intensity at low frames. c) Tilt-corrected 1D Si^+ profile perpendicular to the film fit by convoluting the film profile and the experimental resolution given by a Gaussian FWHM = 0.25 μm . Data is 3-point averaged (binned). Inset: SEM image after 300 frames displays a flat etched surface.

We process the 3D compositional maps (**Figure 2.3a**) using MATLAB to obtain a 1D concentration profiles for fitting the diffusion coefficients. We detect the SiO_2 NPs in the PNC trilayer samples using frames 101-300 of the Si^+ ion signal from a 30 keV 100 pA beam current with a spot size of 400 nm. Before extracting 1D concentration profiles perpendicular to the trilayer samples, we rotate the data set and integrate the Si^+ signal in parallel to the film, which lies approximately in the XZ plane. Rotating the ToF-SIMS data before integrating the intensities in the nominal Z-direction is necessary to avoid broadening the Si^+ concentration profile. We fit a plane of highest Si^+ intensity within a region of interest (ROI) determined visually (pixels 150-450 in Y in this data set) and then define the normal vector to that Si-rich plane. Specifically, we fit the plane using the M-estimator SAmple Consensus (MSAC) algorithm, a variant of the RANdom SAmple Consensus (RANSAC) algorithm, within the MATLAB Computer Vision toolbox to automatically discard background noise from the fitting.^{125,126} We select an inlier distance threshold of 25 pixels between the plane and points of consideration to produce a plane fitting and visually inspect for accuracy. After defining the Si-rich plane, we apply the appropriate rotational matrix to orient the film parallel to the Z' -axis and center the film at $Y' = 0$. Given the 3D nature of ToF-SIMS data, this methodology is required to maximize concentration profile resolution by

accounting for sample orientation during sample mounting and data collection. Next, we project the rotated data along the Z' -axis (**Figure 2.3b**) and integrate along X' to extract a 1D concentration profile. Comparing the raw and rotated profiles in **Figure 2.3c** demonstrates that the Si^+ concentration profile of the unannealed trilayer sample narrows from $\text{FWHM} = 2.1 \mu\text{m}$ to $0.59 \mu\text{m}$, respectively.

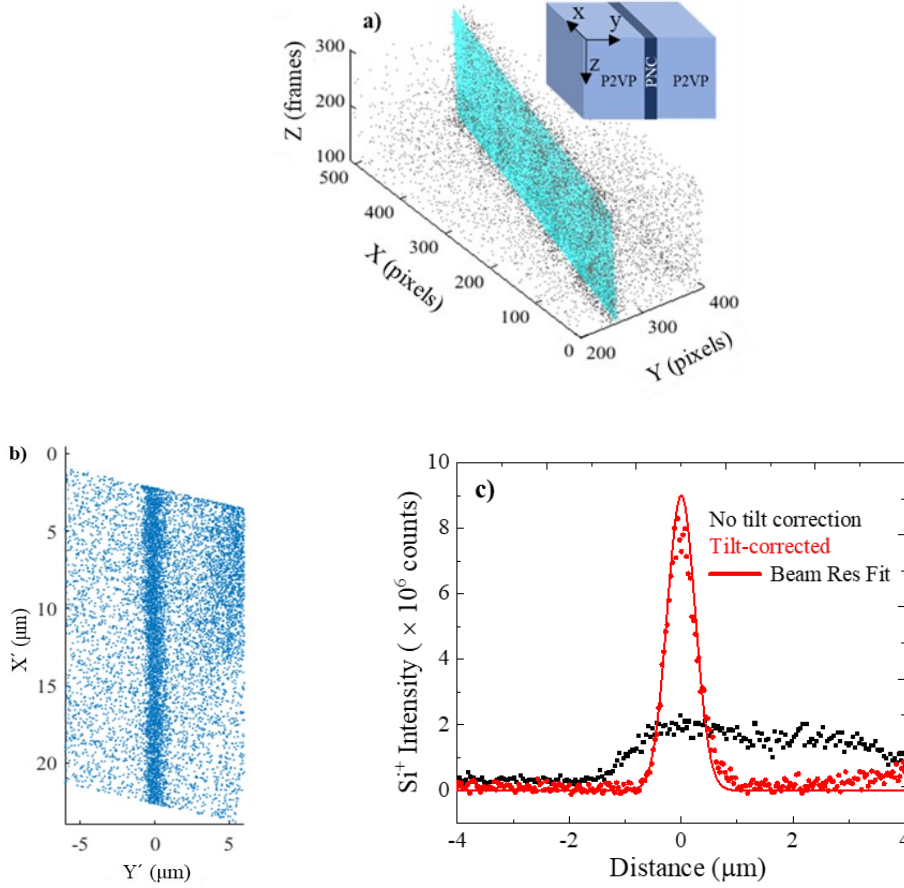


Figure 2.3: **a)** 3D data of Si^+ density (frames 101-300) of an unannealed trilayer film and the plane fit of maximum Si^+ density (cyan). **b)** $X'Y'$ projection of the Si^+ density after tilt-correction and conversion from pixels to lengths such that $Y' = 0$ intersects with the tilt-corrected plane. **c)** 1D profile of Si^+ intensity across the unannealed trilayer sample integrated before and after tilt-

correction. Line fit is a convolution of the PNC film thickness ($0.5\ \mu\text{m}$) and the experimental resolution, $\text{FWHM} = 0.25\ \mu\text{m}$.

Having developed a robust data analysis technique to obtain 1D concentration profiles from ToF-SIMS measurements of trilayer samples, we next optimize the beam conditions for measuring NP diffusion. We choose 30 keV (the maximum) for the accelerating voltage to minimize the spot size and maximize lateral resolution, because lateral resolution is the most important parameter when optimizing measurements of the concentration profile in these cross-sectional trilayer samples. We next determine how beam current impacts the signal-to-background noise ratio on a trilayer sample. By comparing the FWHM of the (tilt-corrected) Si^+ profiles for 10, 100, and 300 pA Xe^+ ions, we found a beam current of 100 pA performs with equal resolution to 10 pA, both being superior to 300 pA in these trilayer samples (**Figure A.5**). While a 10 pA beam current has a smaller spot size and higher depth resolution (more frames/nm) compared to the 100 pA current, the Si^+ signal-to-noise ratio suffers significantly due to low ion extraction counts for equal ToF-SIMS collection duration and does not improve lateral resolution at this length scale. Therefore, 100 pA balances spot size and signal intensity, and is the ideal beam current to measure NP diffusion over micron length scales.

For comparison, we also investigated a cross-section of a PNC trilayer with EDX, finding the line scans to have lower resolution of the Si^+ signal concentration profile with $\text{FWHM} = 2.2\ \mu\text{m}$. The higher resolution of ToF-SIMS ($0.25\ \mu\text{m}$) is in part the result of tilt correcting the 3D data. ToF-SIMS provides the unique advantage of direct 3D compositional information from the sample, improving statistics through integrating a 3D dataset compared to a 1D EDX line scan.

This 3D data also detects local sample inhomogeneity. Relative to EDX, this improves concentration profile quality from ToF-SIMS by allowing the user to mitigate the effect of sample irregularities like sample tilt, surface contamination, or texture during data processing. The close match between FWHM of the EDX film and uncorrected ToF-SIMS data set (2.2 vs. 2.1 μm , respectively) demonstrates that tilt correction is a major contributor to the improved experimental resolution with ToF-SIMS. In addition, the 400-nm spot size of ToF-SIMS is likely smaller than the spot size of EDX, although this was not precisely determined. ToF-SIMS can attain smaller spot sizes, when necessary. In summary, the 3D data and smaller spot size are the most significant advantages of ToF-SIMS over EDX for measuring NP concentration profiles. Also, unlike EDX ToF-SIMS detects various polymer fragments to measure polymer concentration profiles and thus polymer diffusion, as demonstrated below.

Tracer Diffusion Coefficients of NPs in Polymer

The tilt-corrected 1D Si^+ concentration profiles were used to determine the tracer diffusion coefficient of silica NPs sandwiched between two polymer matrix films. We analyzed trilayer samples annealed at 180°C for 1, 3, and 5-days with 10 vol% NPs using aforementioned beam conditions (**Figure 2.4**). First, we deconvoluted the instrumental beam resolution function from the tilt-corrected 1D Si^+ profile to obtain the NP concentration profile. Then, we iteratively fit the solution of Fick's second law for a finite source diffusing into a semi-infinite medium to the concentration profiles.

$$\varphi(y) = \frac{1}{2} \left[\text{erf} \left(\frac{h-y}{\sqrt{4D_{NP}t}} \right) + \text{erf} \left(\frac{h+y}{\sqrt{4D_{NP}t}} \right) \right] \quad (2.1)$$

where $\varphi(y)$ is the concentration as a function of position y , h indicates the film's initial thickness ($h = 0.50 \text{ } \mu\text{m}$), D_{NP} is the NP diffusion coefficient, and t is time in seconds. The fits resulted in D_{NP} of 2.2, 1.9, and $2.5 \times 10^{-14} \text{ cm}^2/\text{s}$ respectively for the 1, 3, and 5 day anneals. Averaging over all three samples yields $D_{NP} = 2.3 \times 10^{-14} \text{ cm}^2/\text{s}$, with NPs traveling $\sim 1.4 \text{ } \mu\text{m}$ at 5 days ($x \sim 2(Dt)^{0.5}$). A standard deviation of $0.4 \times 10^{-14} \text{ cm}^2/\text{s}$ across three samples shows good consistency as a function of annealing time, indicating a single-mode NP diffusion. Deviating the best D_{NP} by a factor $\delta = 0.3 \times 10^{-14} \text{ cm}^2/\text{s}$ results in a significant decrease in R^2 (**Fit Quality** (R2) **Table A.1**) and visually worse goodness-of-fit (**Figure 2.4**), confirming the reliability of our fitting procedure.

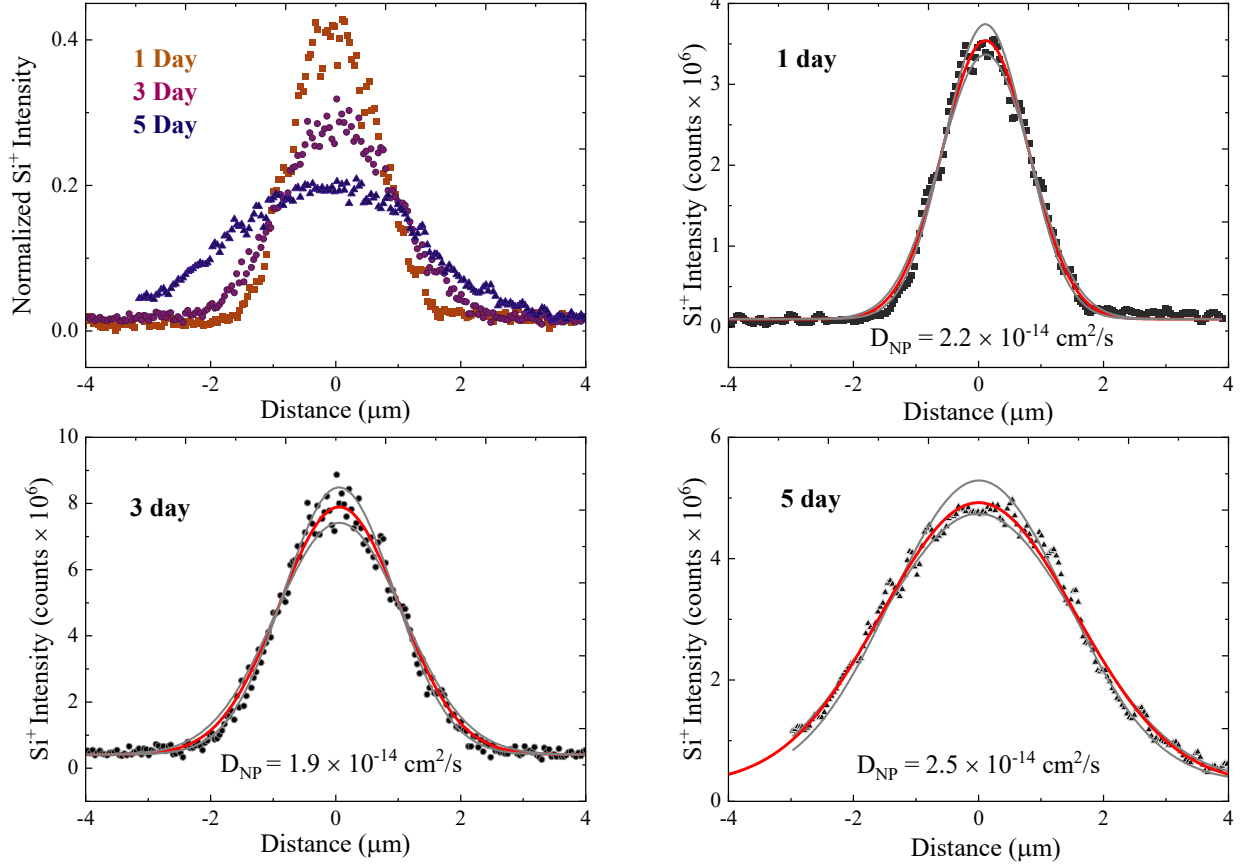


Figure 2.4: The Si^+ concentration profiles are fit with Eqn. 2.1 as described in the text to find the NP tracer diffusion coefficient D_{NP} . Fits for $D_{\text{NP}} \pm \delta$ are shown in grey. a) The Si^+ profiles for all annealed samples. D_{NP} from samples annealed at 180 °C for b) 1 day, c) 3 days, and d) 5 days show excellent agreement.

Our NP diffusion coefficient is in excellent agreement with an earlier study that used RBS.⁴⁵ There, Griffin et al. determined D_{NP} for silica NPs with $R_{\text{NP}} = 13$ nm in a 100 kg/mol P2VP system at $T = 180^\circ\text{C}$. We linearly extrapolate their result using the Stokes-Einstein model to estimate D_{NP} for our experiment ($R_{\text{NP}} = 26.1$ nm, 100 kg/mol P2VP, 180°C): $D_{\text{NP-est}} = 1.9 - 3.3 \times$

10^{-14} cm²/s. The range is due to estimations of the true volume fraction of NP during annealing;⁴⁵ see : **SUPPORTING INFORMATION FOR CHAPTER 2** for additional details. Our ToF-SIMS results are in excellent agreement with the D_{NP-est} . Notably, the RBS measurements were performed in a bilayer sample on the length scale of < 500 nm, leading to diffusion time scales limited to ~ 30 min. These ToF-SIMS measurements capture diffusion distances of several μ m and allow for a wider range of diffusion times and speeds, in particular for faster diffusing species that require this extended accessible length scale.

Finally, we note that tracer diffusion experiments require low NP concentrations, so that D_{NP} is independent of NP concentration. While using the experimental and analysis protocols established above, we measure D_{NP} after a 3-day anneal at 180 °C using PNC layers with 5 and 15 vol% (**Figure 2.5**). As expected, the 5 vol% sample displays a decrease in the Si⁺ intensity compared to background; therefore 600 frames were collected to improve signal while maintaining the same beam resolution. Collecting additional frames would produce better signal-to-noise statistics at all loadings but is only necessary for lower particle loadings. The D_{NP} values determined for 5 and 10 vol% are **2.0** and **1.9×10^{-14} cm²/s**, respectively, and in excellent agreement with one another and with ERD values. Comparatively, raising the particle loading to 15% results in a substantially lower the diffusion coefficient, $D_{NP} = 0.36 \times 10^{-14}$ cm²/s. By this study of NP loading, we determine that 15 vol% is above the tracer diffusion regime. Goodness of fit (R^2) results for each sample are provided in **Fit Quality (R2)**

Table A.1.

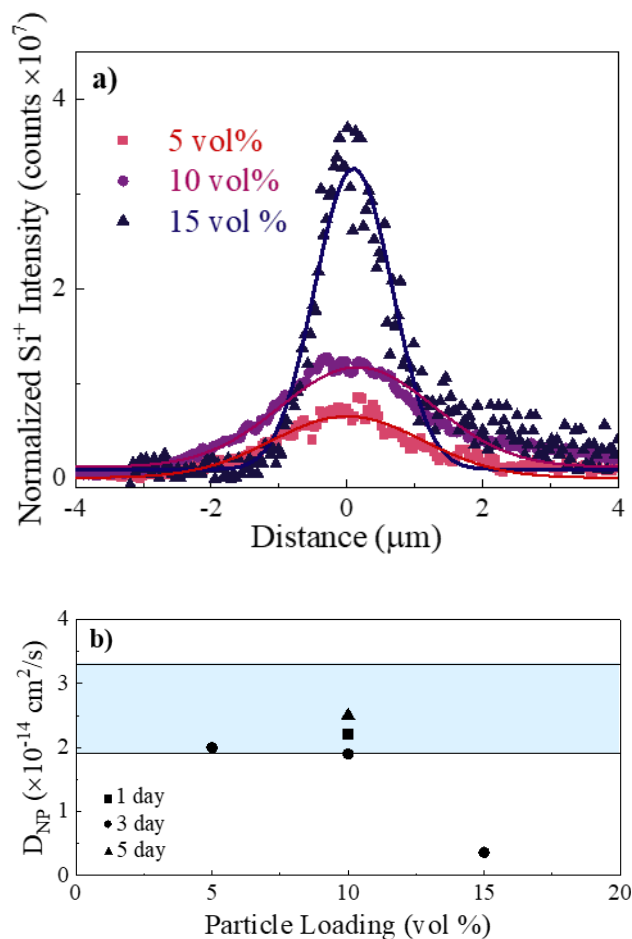


Figure 2.5: a) Diffusion profiles of 5 (squares, 101-600 frames), 10 (circles, 101-300 frames), and 15 (triangles, 101-300 frames) vol % NPs annealed for 3 days at 180 °C. b) D_{NP} as a function of NP loading and at 10 vol% as a function of annealing time. Shaded area (blue) shows an estimate based on previous work using RBS to measure NP tracer diffusion.

Polymer Tracer Diffusion Coefficients

We modified our ToF-SIMS methodology for measuring NP concentration profiles to measure polymer concentration profiles by adjusting a few instrument parameters to improve

signal. Applying ToF-SIMS to trilayers of polystyrene/deuterated polystyrene/polystyrene, we measure the $C_2D_2^+$ ($m/q = 28$) concentration profiles and compute the dPS tracer diffusion coefficients. Both $C_2D_2^+$ and Si^+ ions have $m/q = 28$, so we used the C^+ ($m/q = 12$) signal to confirm the location of the deuterated polymer layer within the trilayer sample (**Figure A.6**). After tilt correction of the ToF-SIMS data, the 1D $C_2D_2^+$ profiles were deconvoluted from the experimental resolution function and fit to Eqn. 2.1, **Figure 2.6**. For the 65k-69k hPS/dPS system, annealed for 1h and 3h at 174°C, the D_{dPS} values are **1.0** and **$1.3 \times 10^{-12} \text{ cm}^2/\text{s}$** . The D_{dPS} values are **2.8** and **$3.0 \times 10^{-14} \text{ cm}^2/\text{s}$** for the 450k-423k hPS/dPS system annealed at 174°C for 1 and 3 days, respectively. Excellent agreement was found for both molecular weights as a function of annealing time. Goodness of fit (R^2) for each sample are provided in

Table A.3.

Polystyrene tracer diffusion was previously measured using ERD by Green et al., where a 10-20 nm deuterated PS layer diffused into a $\sim 4 \mu\text{m}$ PS ($M_w = 2 \times 10^7$) bottom layer upon annealing at 174 °C.¹²² In the limit of high PS molecular weight, the tracer diffusion coefficient was found to depend on the dPS molecular weight at $D_{PS} = 0.008M^{-2}$ (**Figure A.7**).^{76,122} Applying this result to our molecular weights gives $D_{Green(69k)} = 1.7 \times 10^{-12} \text{ cm}^2/\text{s}$ and $D_{Green(423k)} = 4.0 \times 10^{-14} \text{ cm}^2/\text{s}$. Our results with ToF-SIMS are in excellent agreement with these earlier results using ERD, further demonstrating the value of ToF-SIMS for measuring diffusion coefficients in polymer systems.

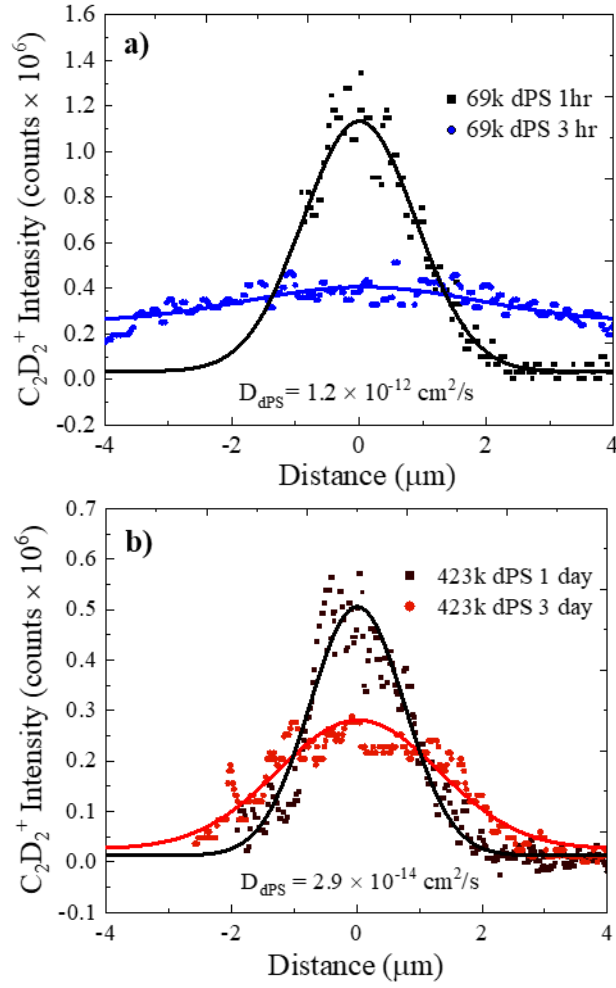


Figure 2.6: **a)** The $C_2D_2^+$ concentration profiles are fit with Eqn. 1 to find the dPS tracer diffusion coefficient D_{poly} . Trilayers were annealed at 174°C for **a)** 69-65k dPS/PS for 1 and 3 hours, and **b)** 423-450k dPS/PS for 1 and 3 days. Data is binned for noise reduction.

2.4 Discussion

Future Potential of ToF-SIMS for Measuring Diffusion Coefficients

While we demonstrated the ability of ToF-SIMS to measure NP and polymer tracer diffusion coefficients on a large length scale ($\sim 2 \mu\text{m}$), a key advantage of ToF-SIMS is its ability to vary resolution to access a variety of length scales. Specifically, diffusion lengths across an exceptionally large range ($0.3 - 100\text{'s } \mu\text{m}$) can be accommodated by selecting appropriate FoV and pixel count settings.^{85,127} Beam current, accelerating voltage, and frame count can likewise be adjusted to improve intensity or lateral resolution as needed. Therefore, in any PNC or polymer melt trilayer sample with a diffusing layer that can be identified by a contrasting m/q value, a diffusion coefficient can be determined. To estimate of the accessible diffusion coefficients, we use $x = 2\sqrt{Dt}$, where D is the diffusion coefficient, t is the diffusing time in seconds, and x is the distance diffused. Assuming a minimum practical spot size of 200 nm for our Xe^+ ToF-SIMS instrument and convenient annealing times from 10 min to 7 days, ToF-SIMS can measure diffusion coefficients from 10^{-15} to $10^{-6} \text{ cm}^2/\text{s}$, **Figure 2.7**. In this paper, we've demonstrated a range of diffusion coefficients from 10^{-15} to $10^{-12} \text{ cm}^2/\text{s}$ as noted by the symbols in **Figure 2.7**.

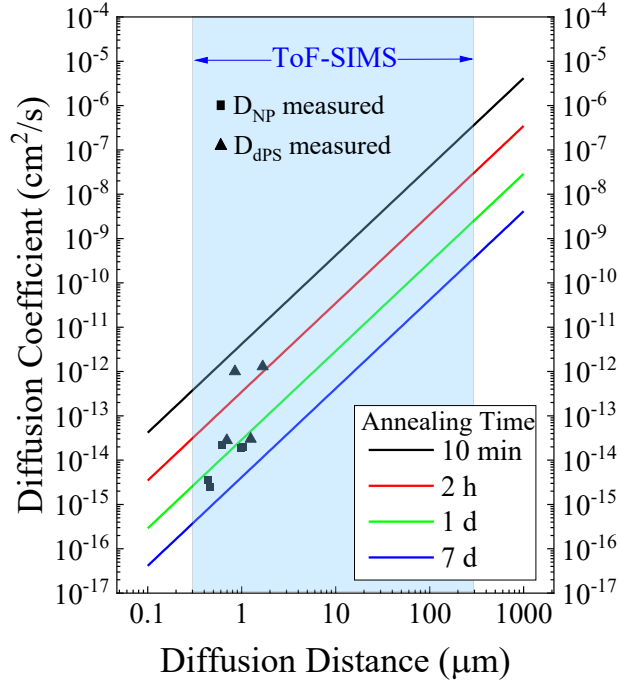


Figure 2.7: Diffusion coefficient ($D = x^2/4t$) as a function of diffusion distance (x) for a range of annealing times (10 min to 7 days). ToF-SIMS can measure concentration profiles with resolutions from 0.3 - $\sim 200 \mu\text{m}$ indicating the ability to measure diffusion coefficients from 10^{-15} to $10^{-6} \text{ cm}^2/\text{s}$ (blue).

Ideal systems for Xe^+ ToF-SIMS contain polar components such as oxide-based particles that take advantage of the matrix effect, or low mass fragments ($m < 50$).⁷⁸ These factors are important when choosing a PNC system to maximize signal in a primary ion beam system. Cluster ion beams are preferred for polymer systems for their ability to identify larger organic fragments as the diffusing species. Crowded NP systems, which are commercially more important and can be analogs to biological systems, can be investigated with no upper limit on particle loading. Conversely, very dilute NP systems, as necessary to avoid NP aggregation, can likewise be

investigated with ToF-SIMS by compensating with higher frame counts. With a cryo-stage attachment, ToF-SIMS can also be used to probe materials that are a melt at room temperature ($T_g < T_{room}$). While our ToF-SIMS method using cross-sectional trilayers has been demonstrated for two specific cases of NP and polystyrene diffusion, the future opportunities abound.

2.5 Conclusion

We demonstrate a versatile ToF-SIMS method to measure diffusion coefficients using a trilayer sample geometry and a cross-sectional measurement by optimizing sample preparation, ToF-SIMS parameters, and data processing. An accelerating voltage of 30 keV is most appropriate to maximize lateral resolution in our Xe^+ ToF-SIMS. The beam current impacts lateral resolution and depth resolution, and 100 pA performs best for our materials with a lateral spot size of $< 0.5 \mu\text{m}$ and etching rate of $\sim 1 \text{ nm/frame}$. We use an image size of 1024×1024 pixel resolution (pre-binning) which balances collection times (typically $\sim 1 \text{ h}$) and lateral resolution to give a pixel size smaller than the NP diameter. This pixel size is also sufficiently smaller than the spot size of the ion beam (spot size $\gg 2 \times$ pixel size) to ensure the entire pixel area is milled per frame, and a 2×2 bin is applied to the image to reduce noise. A dwell time of $10 \mu\text{s}$ is sufficient to resolve the Si^+ ion in our PNC system, the significant species for identifying NP location, and to resolve C_2D_2^+ in our dPS/PS system. We also established a protocol for rotating and centering the 3D composition data prior to integrating to a 1D concentration profile perpendicular to the trilayer sample.

We demonstrate the accuracy of measuring diffusion coefficients of nanoparticles and polymers using ToF-SIMS by comparing to previous studies. Excellent agreement was found for D_{NP} of silica NPs in P2VP and for D_{dPS} in polystyrene at two molecular weights. In addition, we

establish that in a 10 vol% NP trilayer, D_{NP} is independent of annealing time (1-5 days), and that with a 3 day anneal, D_{NP} is independent of NP vol% when < 10 vol%.

This ToF-SIMS methodology has great potential for investigating unexplored PNCs across a wide range of chemistries, lateral resolutions, length scales, and concentrations, thus, expanding the understanding of NP diffusion in polymer melts. ToF-SIMS can likewise expand polymer-polymer diffusion in miscible polymer system with or without the use of deuterated polymers, if there are unique polymer fragments for the two polymers. ToF-SIMS can reinvigorate diffusion studies vital to open polymer physics questions and interesting PNC systems.

2.6 References

References

- (1) Kumar, S. K.; Benicewicz, B. C.; Vaia, R. A.; Winey, K. I. 50th Anniversary Perspective: Are Polymer Nanocomposites Practical for Applications? *Macromolecules* **2017**, *50*, 714–731.
- (2) Bailey, E. J.; Winey, K. I. Dynamics of Polymer Segments, Polymer Chains, and Nanoparticles in Polymer Nanocomposite Melts: A Review. *Prog. Polym. Sci.* **2020**, *105*, 101242.
- (3) Thakur, V. K.; Kessler, M. R. Self-Healing Polymer Nanocomposite Materials: A Review. *Polymer (Guildf)*. **2015**, *69*, 369–383.
- (4) Balazs, A. C.; Emrick, T.; Russell, T. P. Nanoparticle Polymer Composites: Where Two Small Worlds Meet. *Science (80-.)*. **2006**, *314*, 1107–1110.
- (5) Raemdonck, K.; Braeckmans, K.; Demeester, J.; De Smedt, S. C. Merging the Best of Both Worlds: Hybrid Lipid-Enveloped Matrix Nanocomposites in Drug Delivery. *Chem. Soc. Rev* **2014**, *43*, 444.
- (6) Mills, P. J.; Green, P. F.; Palmstrøm, C. J.; Mayer, J. W.; Kramer, E. J. Polydispersity Effects on Diffusion in Polymers: Concentration Profiles of d-Polystyrene Measured by Forward Recoil Spectrometry. *J. Polym. Sci. Part B Polym. Phys.* **1986**, *24*, 1–9.
- (7) Green, P. F.; Kramer, E. J. Matrix Effects on the Diffusion of Long Polymer Chains. *Macromolecules* **1986**, *19*, 1108–1114.
- (8) Mackay, M. E.; Dao, T. T.; Tuteja, A.; Ho, D. L.; van Horn, B.; Kim, H.-C.; Hawker, C. J. Nanoscale Effects Leading to Non-Einstein-like Decrease in Viscosity. *Nat. Mater.* **2003**,

- 2, 762–766.
- (9) Composto, R. J.; Mayer, J. W.; Kramer, E. J.; White, D. M. Fast Mutual Diffusion in Polymer Blends. *Phys. Rev. Lett.* **1986**, *57*, 1312–1315.
 - (10) Composto, R. J.; Kramer, E. J.; White, D. M. Mutual Diffusion in the Miscible Polymer Blend Polystyrene/Poly(Xylenyl Ether). *Macromolecules* **1988**, *21*, 2580–2588.
 - (11) Barrat, J.-L.; Fredrickson, G. H. Diffusion of a Symmetric Block Copolymer in a Periodic Potential. *Macromolecules* **1991**, *24*, 6378–6383.
 - (12) Gam, S.; Meth, J. S.; Zane, S. G.; Chi, C.; Wood, B. A.; Seitz, M. E.; Winey, K. I.; Clarke, N.; Composto, R. J. Macromolecular Diffusion in a Crowded Polymer Nanocomposite. *Macromolecules* **2011**, *44*, 3494–3501.
 - (13) Lin, C. C.; Parrish, E.; Composto, R. J. Macromolecule and Particle Dynamics in Confined Media. *Macromolecules* **2016**, *49*, 5755–5772.
 - (14) Tuteja, A.; Mackay, M. E.; Narayanan, S.; Asokan, S.; Wong, M. S. Breakdown of the Continuum Stokes-Einstein Relation for Nanoparticle Diffusion. *Nano Lett.* **2007**, *7*, 1276–1281.
 - (15) Carroll, B.; Bocharova, V.; Carrillo, J.-M. Y.; Kisliuk, A.; Cheng, S.; Yamamoto, U.; Schweizer, K. S.; Sumpter, B. G.; Sokolov, A. P. Diffusion of Sticky Nanoparticles in a Polymer Melt: Crossover from Suppressed to Enhanced Transport. *Macromolecules* **2018**, *51*, 2268–2275.
 - (16) Park, J.; Bailey, E. J.; Composto, R. J.; Winey, K. I. Single-Particle Tracking of Nonsticky and Sticky Nanoparticles in Polymer Melts. *Macromolecules* **2020**, *53*, 3933–3939.
 - (17) Griffin, P. J.; Bocharova, V.; Middleton, L. R.; Composto, R. J.; Clarke, N.; Schweizer, K.

- S.; Winey, K. I. Influence of the Bound Polymer Layer on Nanoparticle Diffusion in Polymer Melts. *ACS Macro Lett.* **2016**, *5*, 1141–1145.
- (18) Cole, D. H.; Shull, K. R.; Rehn, L. E.; Baldo, P. M. RBS Analysis of the Diffusion of Nano-Size Spheres in a Polymer Matrix. *Nucl. Instruments Methods Phys. Res. Sect. B Beam Interact. with Mater. Atoms* **1998**, *136–138*, 283–289.
- (19) Parrish, E.; Caporizzo, M. A.; Composto, R. J. Network Confinement and Heterogeneity Slows Nanoparticle Diffusion in Polymer Gels. *J. Chem. Phys.* **2017**, *146*, 203318.
- (20) Shrestha, U. M.; Han, L.; Saito, T.; Schweizer, K. S.; Dadmun, M. D. Mechanism of Soft Nanoparticle Diffusion in Entangled Polymer Melts. *Macromolecules* **2020**, *53*, 7580–7589.
- (21) Imel, A. E.; Rostom, S.; Holley, W.; Baskaran, D.; Mays, J. W.; Dadmun, M. D. The Tracer Diffusion Coefficient of Soft Nanoparticles in a Linear Polymer Matrix. *RSC Adv.* **2017**, *7*, 15574–15581.
- (22) Jo, K. Il; Oh, Y.; Kim, T. H.; Bang, J.; Yuan, G.; Satija, S. K.; Sung, B. J.; Koo, J. Position-Dependent Diffusion Dynamics of Entangled Polymer Melts Nanoconfined by Parallel Immiscible Polymer Films. *ACS Macro Lett.* **2020**, *9*, 1483–1488.
- (23) Green, P. F.; Palmstrom, C. J.; Mayer, J. W.; Kramer, E. J. Marker Displacement Measurements of Polymer-Polymer Interdiffusion. *Macromolecules* **1985**, *18*, 501–507.
- (24) Jimenez, A. M.; Zhao, D.; Misquitta, K.; Jestin, J.; Kumar, S. K. Exchange Lifetimes of the Bound Polymer Layer on Silica Nanoparticles. *ACS Macro Lett.* **2019**, *8*, 166–171.
- (25) Lin, C.-C.; Griffin, P. J.; Chao, H.; Hore, M. J. A.; Ohno, K.; Clarke, N.; Riggleman, R. A.; Winey, K. I.; Composto, R. J. Grafted Polymer Chains Suppress Nanoparticle Diffusion in

- Athermal Polymer Melts. *J. Chem. Phys.* **2017**, *146*, 203332.
- (26) Composto, R. J.; Kramer, E. J. Mutual Diffusion Studies of Polystyrene and Poly(Xylenyl Ether) Using Rutherford Backscattering Spectrometry. *J. Mater. Sci.* **1991**, *26*, 2815–2822.
 - (27) Mills, P. J.; Green, P. F.; Palmstrom, C. J.; Mayer, J. W.; Kramer, E. J. Analysis of Diffusion in Polymers by Forward Recoil Spectrometry. *Appl. Phys. Lett.* **1998**, *45*, 957.
 - (28) Martín, J.; Hernández-Vélez, M.; de Abril, O.; Luna, C.; Muñoz-Martin, A.; Vázquez, M.; Mijangos, C. Fabrication and Characterization of Polymer-Based Magnetic Composite Nanotubes and Nanorods. *Eur. Polym. J.* **2012**, *48*, 712–719.
 - (29) Bailey, E. J.; Griffin, P. J.; Composto, R. J.; Winey, K. I. Characterizing the Areal Density and Desorption Kinetics of Physically Adsorbed Polymer in Polymer Nanocomposite Melts. *Macromolecules* **2020**, *53*, 2744–2753.
 - (30) Composto, R. J.; Walters, R. M.; Genzer, J. Application of Ion Scattering Techniques to Characterize Polymer Surfaces and Interfaces. *Mater. Sci. Eng. R Reports* **2002**, *38*, 107–180.
 - (31) Spool, A. M. *The Practice of TOF-SIMS: Time of Flight Secondary Ion Mass Spectrometry* - Alan M. Spool - Google Books; Momentum Press, 2016.
 - (32) Mei, H.; Laws, T. S.; Terlier, T.; Verduzco, R.; Stein, G. E. Characterization of Polymeric Surfaces and Interfaces Using Time-of-Flight Secondary Ion Mass Spectrometry. *Journal of Polymer Science*. John Wiley and Sons Inc April 1, 2021, pp 1174–1198.
 - (33) Prasad, A.; Salim, N. V.; Mozetič, M.; Kailas, L.; Thomas, S. Time-of-Flight Secondary Ion Mass Spectrometric Analysis of Polymer Surfaces: A Review. *J. Appl. Polym. Sci.* **2022**, *139*.

- (34) Bailey, J.; Havelund, R.; Shard, A. G.; Gilmore, I. S.; Alexander, M. R.; Sharp, J. S.; Scurr, D. J. 3D ToF-SIMS Imaging of Polymer Multilayer Films Using Argon Cluster Sputter Depth Profiling. *ACS Appl. Mater. Interfaces* **2015**, *7*, 2654–2659.
- (35) Sui, T.; Song, B.; Dluhos, J.; Lu, L.; Korsunsky, A. M. Nanoscale Chemical Mapping of Li-Ion Battery Cathode Material by {FIB-SEM} and {TOF-SIMS} Multi-Modal Microscopy. *Nano Energy* **2015**, *17*, 254–260.
- (36) Karar, N.; Gupta, T. K. Study of Polymers and Their Blends Using TOF-SIMS Ion Imaging. *Vacuum* **2015**, *111*, 119–123.
- (37) Fit plane to 3-D point cloud - MATLAB pcfitplane
<https://www.mathworks.com/help/vision/ref/pcfitplane.html> (accessed Jun 22, 2022).
- (38) Fischler, M. A.; Bolles, R. C. Random Sample Consensus. *Commun. ACM* **1981**, *24*, 381–395.
- (39) Richardin, P.; Mazel, V.; Walter, P.; Laprévotte, O.; Brunelle, A. Identification of Different Copper Green Pigments in Renaissance Paintings by Cluster-TOF-SIMS Imaging Analysis. *J. Am. Soc. Mass Spectrom.* **2011**, *22*, 1729–1736.
- (40) Belu, A. M.; Davies, M. C.; Newton, J. M.; Patel, N. TOF-SIMS Characterization and Imaging of Controlled-Release Drug Delivery Systems. **2000**.

CHAPTER 3 : VEHICULAR AND CORE-SHELL NANOPARTICLE DIFFUSION IN ENTANGLED ATTRACTIVE POLYMER MELTS

Content in this chapter was published in July 2024 in *Macromolecules*, in a modified version. The authors of this chapter are Kaitlin Wang and Karen I. Winey.

Kaitlin Wang and Karen I. Winey conceived the presented idea. Kaitlin Wang conducted the literature search, designed and performed the experiments, developed the methodology, and carried out the data analysis. She also wrote the first draft of the manuscript and incorporated feedback from Karen I. Winey. Karen I. Winey supervised the experiments and provided revisions to the manuscript drafts.

3.1 Introduction

Polymer nanocomposites (PNCs) have garnered considerable interest as advanced materials, due to their tunable properties. Introducing nanoparticles (NPs) into a polymer matrix permits nuanced adjustments to optimize mechanical, thermal, electrical, and optical attributes to meet specific performance criteria. This adaptability positions PNCs as a promising material class across diverse sectors including electronics, aerospace, automotive, and biomedical industries.¹⁻⁴

Previous work has clearly established that the spatial distribution of NPs significantly impacts processability and properties, including mechanical properties, rheology, and gas permeability within PNCs.⁵⁻⁸ To achieve and maintain the desired properties, understanding and predicting nanoparticle diffusion is critically important. Factors such as NP size, NP shape, NP concentration, and the interaction between polymer and NPs must be managed to achieve desired NP distributions and properties for effective PNC applications.⁹⁻¹¹ PNCs with strong attractions between the NPs and polymer matrix are distinguished by improved NP dispersion and maintain industrially relevant processability advantages compared to their neutral counterparts. Thus, NP

diffusion behavior in these attractive nanocomposites is of particular interest and a crucial cornerstone for PNC applications.¹²

When particles are microscopic, particle diffusion in a viscous medium is well described by Stokes-Einstein (SE) behavior, $D_{SE} = \frac{k_B T}{6\pi\eta R}$. However, significant deviations have been reported for nanoparticle diffusion, particularly in the presence of attractive polymer-nanoparticle interactions.^{13–19} Nanoparticle diffusion studies in neutral melts have also highlighted substantial deviations from SE, depending on the NP radius and polymer tube diameter, d_T .^{18,20,21} In athermal systems, spherical nanoparticles with diameters larger than d_T exhibit a hopping diffusion mechanism in which the NPs overcome topological energy barriers to move faster than Stokes-Einstein predictions.²² Small nanoparticles, due to their size being comparable to or smaller than the polymer's mesh size, exhibit diffusion rates largely unaffected by the surrounding polymer.²³ Within attractive melts, Schweizer's group introduced two simultaneous NP diffusion modes—the core-shell and vehicle modes—where the relative time scales of polymer and NP dynamics dictate the dominant mode.^{16,17} The total diffusion coefficient of a nanoparticle is described by the sum of the core-shell and vehicle modes.

$$D_{NP,theory} = D_{core-shell} + D_{vehicle} \quad (3.1)$$

The core-shell contribution follows the SE behavior and accounts for 1) the viscosity of the PNC rather than the neat polymer and 2) the effective nanoparticle size rather than the bare NP size due to a bound polymer layer,

$$D_{core-shell} = \frac{k_B T}{6\pi\eta_{PNC} R_{eff}} \quad (3.2)$$

where k_B is the Boltzmann constant, T is the annealing temperature in Kelvin, η_{PNC} is the PNC viscosity in Pa·s, and the effective nanoparticle radius is $R_{eff} = R_{NP} + R_g$. These modifications to SE behavior result in slower NP diffusion. A variety of experimental methods have been used to measure diffusion coefficients of nanoparticles in polymer melts include Rutherford backscattering (RBS) ($R_{NP} = 13$ nm),^{14,24} dynamic light scattering (DLS) ($R_{NP} = 0.88, 5$ nm),¹⁷ and single particle tracking (SPT) ($R_{NP} = 6.5-6.6$ nm).²⁵ The core-shell mechanism (Eqn. 3.2) alone has been sufficient to understand NP diffusion in various experimental systems with strong polymer-nanoparticle interactions: unentangled poly(propylene glycol) (PPG) melts with octaamino-phenylsilsesquioxane (OAPS) nanoparticles,¹⁷ PPG with small silica (SiO₂) NPs,¹⁷ and poly(2-vinyl pyridine) (P2VP) with SiO₂ NPs.¹⁴ In addition, there are examples of $D_{NP} < D_{SE}$ in poly(ethylene oxide) with SiO₂ NPs,²⁶ and PPG with strongly interacting quantum dot samples through COOH surface functionalization.²⁷ These systems represent a wide range of R_g/R_{NP} (~0.1 to 1.2), and the core-shell model well explains the decrease in D_{NP} compared to Stokes-Einstein behavior.

The vehicular mode for NP diffusion involves polymer desorption and results in diffusion coefficients faster than SE behavior when the desorption of the polymer is faster than the polymer chain dynamics. This mechanism is described by using four polymer time scales: τ_{des} – monomer desorption time, τ_e – entanglement onset time, τ_{Rouse} – longest chain Rouse relaxation time, and τ_{rep} – reptation time.¹⁶ In Regime I, the monomer desorption time is relatively quick, meaning shorter than the entanglement onset time ($\tau_{des} < \tau_e$). In this regime the vehicular contribution to $D_{NP,theory}$ scales as $\sim \tau_{des}^{-1}$ as

$$D_{vehicle-I} = Ab \times \frac{D_0}{\tau_{des}} \quad (3.3)$$

where A is a numerical prefactor, b is the Kuhn monomer length, and D_0 is the segmental diffusion constant. In this study, Regime I will be neglected because the nanoparticles have surface hydroxyl groups that interact favorably with the polymer, such that τ_{des} is expected to be longer than τ_e . In Regime II, the desorption time is longer than the entanglement onset time and shorter than the Rouse time ($\tau_e < \tau_{des} < \tau_{Rouse}$), indicating an intermediately strong NP-polymer attraction, such that the vehicular contribution to NP diffusion scales $\sim 1/\tau_{des}^{3/4}$ as

$$D_{vehicle-II} = Ad_T(b^2 D_0)^{\frac{1}{4}} \times \left(\frac{1}{\tau_{des}}\right)^{\frac{3}{4}} \quad (3.4)$$

where d_T is the tube diameter. At slower desorption times, although still faster than polymer reptation ($\tau_R < \tau_{des} < \tau_{rep}$), the vehicular contribution to NP diffusion in Regime III has a molecular weight dependence,

$$D_{vehicle-III} = Ad_T \left(\frac{D_0}{N\tau_{des}}\right)^{\frac{1}{2}} \quad (3.5)$$

where N is the degree of polymerization. Regime III is the only case in which $D_{vehicle}$ depends on both the desorption time and the polymer molecular weight with a scaling dependence of $(N\tau_{des})^{-1/2}$. To date, the experimental systems that suggest a vehicular mechanism for NP diffusion have used very small nanoparticles ($R_{NP} < 1$ nm). Specifically, nanocomposites of PPG with OAPS and P2VP with OAPS exhibit fast NP diffusion relative to the core-shell model.^{17,13}

In this manuscript, we experimentally identify PNCs with NP diffusion controlled by both the core-shell and the vehicular modes. Leveraging the capabilities of our previously demonstrated time-of-flight secondary ion mass spectrometry (ToF-SIMS) method,²⁸ we accurately measure NP

diffusion coefficients on micron length scales and across a considerable range, $D_{NP} = 10^{-18} - 10^{-11}$ cm²/s. By employing a wide range of P2VP molecular weights (14 – 1220 kg/mol) and three NPs that vary in size and surface chemistry, we reveal systems dominated by core-shell and by vehicle NP diffusion. Finally, we discuss the implications of these distinct diffusion modes and estimate desorption times (τ_{des}) of the bound layer.

3.2 Experimental Details

Materials: Poly(2-vinylpyridine) (P2VP) of weight averaged molecular weights 14.0, 41.0, 158, 219, 310, 474, and 1220 kDa (narrow distribution, PDI <1.10) were purchased from Scientific Polymer Products Inc. and used as-received. Gel permeation chromatography (GPC) was used to measure the polymers' molecular weights and respective PDIs (**Table B.1**). Nissan-STL silica (SiO₂) nanoparticles were solvent-exchanged from methyl-ethyl ketone (MEK) to methanol (MeOH) via crashing the particles out of MEK.²⁸ Aluminum oxide (Al₂O₃) NPs were purchased from Sigma Aldrich, then suspended in a 50 g/L MeOH solution, vortexed for 1 min, sonicated for > 30 min, and filtered through 1 µm and 0.2 µm filters subsequently. A small amount of the respective molecular weight P2VP (5 g/L) was added to the MeOH-Al₂O₃ solution to form a bound layer on the bare NPs to prevent subsequent aggregation. The solution was stirred constantly, and excess MeOH was evaporated to achieve the desired NP vol % after filtration. Ludox silica nanoparticles are solvent exchanged from water to ethanol through creating a miscible water/ethanol solution, then adding concentrated P2VP/ethanol solution. The solution is then diluted with ethanol to the desired concentration. Nanoparticle sizes and size dispersities were determined using small-angle X-ray scattering (SAXS) on a capillary filled with a dilute NP

suspension and fit using the hard sphere model. The Nissan SiO₂ NPs fit to hard sphere resulted in $R_{NP} = 26.1$ nm, PDI 1.19, and the Ludox SiO₂ NPs measured $R_{NP} = 8.3$ nm, PDI 1.15. Aluminum oxide (Al₂O₃) NPs measured $R_{NP} = 6.5 \pm 2.5$ nm, PDI = 1.14, with dynamic light scattering (DLS) measuring hydrodynamic diameter consistent with $\sim R_{NP} + R_g$. Silicon wafers (<100>) with a thick thermal oxide layer (referred to as SiO₂ wafers hereafter) were purchased from Nova Electronic Materials. Silicon wafers (<100>) (Si wafer) were purchased from Wafer World Inc.

Trilayer Fabrication and Nanoparticle Diffusion: Building upon our earlier study,²⁸ we crafted trilayer-samples comprised of a thin PNC layer placed between two thick P2VP matrix layers. Upon annealing NPs diffuse into the homopolymer layers and we measure the NP tracer diffusion coefficient, D_{NP} .²⁸ The P2VP matrix films were prepared via spin coating; the P2VP base-layer was created by spin coating a viscous P2VP-methanol (MeOH) solutions at 1000-2000 rpm for 1 minute onto Si wafers to achieve a ~ 4 μ m matrix film. To prepare the PNC mid-layers, 10 vol% SiO₂ NP or 5 vol% Al₂O₃ NP were suspended in P2VP MeOH solutions of varying concentrations and spin-coated onto SiO₂ wafers at 1000-2000 rpm for 1 min to achieve a thickness of 200 ± 60 nm. PNC layer thicknesses were measured via scanning electron microscopy (SEM), and thickness averaged over two samples. The P2VP top layers were spin-coated from varying concentration P2VP solutions onto SiO₂ wafers (~ 4 μ m). Specific solution concentrations and spin coating conditions for each layer are noted in **Table B.2** and **Table B.3**. Similar to our previous report,²⁸ each PNC layer was transferred to a P2VP base-layer by etching the spuncoat PNC layer off the SiO₂ wafer using a 20 wt% NaOH solution, resulting in a floating PNC film that can be rinsed with DI water and stacked on top of the P2VP base-layer. The top P2VP layer was transferred to the bilayer similarly. Each trilayer specimen was annealed in a specialized custom-

built oven, precisely set at 180 °C under vacuum conditions (< 50 Pa) for durations spanning from 10 minutes to 10 days. Annealing times were selected to achieve diffusion distances of $\sim 0.5 - 3$ μm .

Preparing Trilayer Samples for ToF-SIMS: To obtain the cross-sectional view, a diamond scribe was used to fracture samples along a crystallographic plane of the silicon wafer to preserve the polymer/wafer interface. Samples were cleaned with a nitrogen gas gun to remove SiO_2 dust on the surface. Carbon paint suspended in MEK was applied across the back of the wafer to reduce surface charging and improve ion yield.

ToF-SIMS: Time-of-flight secondary ion mass spectrometry is a powerful surface analysis technique that provides 3D compositional information. In ToF-SIMS, a focused beam of high-energy ions sputters molecular fragments from the material and a mass spectrometer analyzes the resulting secondary ions to determine their mass-to-charge ratio, resulting in a 2D compositional map as each layer is removed.²⁹ ToF-SIMS has a wide range of applications in polymer science, particularly for the analysis of surface and interface properties of polymers and polymer composites.³⁰⁻³³ Our previous work produced accurate SiO_2 NP and polystyrene diffusion coefficients, and established ToF-SIMS as a powerful technique to measure both polymer and NP diffusion given the diffusing species produce ions that are distinct from the background matrix.²⁸

ToF-SIMS measurements were performed using the Tescan S8252X dual-beam plasma FIB-SEM with Xe^+ . Unless otherwise noted, measurements were taken with Xe^+ FIB parameters at 30 keV and 100 pA with 1024×1024 pixel resolution on positive ion mode for 300 (SiO_2 NPs) or 400 frames (Al_2O_3 NPs). Additional frames were collected for the Al_2O_3 NPs to improve the signal due to the lower NP loading (5 vol%) present. A $20 \times 20 \mu\text{m}^2$ field of view (FoV) was used

during collection, and the ToF-SIMS images were produced using a 2×2 bin width, resulting in a 512×512 -pixel image.

NP diffusion coefficients are determined by allowing NPs to travel for a set time ($t = 10$ min – 10 days) at a chosen temperature ($T = 180^\circ\text{C}$) and measuring the corresponding NP concentration profiles using ToF-SIMS. Cross-sectioned trilayer samples were measured by scanning across the P2VP/PNC/P2VP interfaces using the Xe^+ beam, which produces the 3D ion intensity map for each mass/charge (m/q) value. To detect the SiO_2 and Al_2O_3 NP concentrations, we use $m/q = 28$ and 27, respectively (**Figure B.1**). 1D concentration profiles were extracted from the 3D dataset by integrating along the x and z directions after tilting the data set to align the plane of the highest NP concentration within the sample to $y = 0$.²⁸ We then deconvolute the beam resolution function (Gaussian with FWHM = $0.2 \mu\text{m}$) from the raw concentration profile to obtain the ion concentration profile. This 1D concentration profile was iteratively fit to Fick's second law for a finite source diffusing into a semi-infinite medium using

$$\varphi(y) = \frac{1}{2} \left[\text{erf} \left(\frac{h-y}{\sqrt{4D_{NP}t}} \right) + \text{erf} \left(\frac{h+y}{\sqrt{4D_{NP}t}} \right) \right] \quad (3.6)$$

where $\varphi(y)$ is the NP concentration as a function of position y , h is the initial thickness of the PNC layer, t is time in seconds, and D_{NP} is the NP diffusion coefficient. By this process we determine D_{NP} and demonstrated in our prior work.²⁸

3.3 Results and Discussion

NP Diffusion Coefficients as a Function of Molecular Weight

We measured NP diffusion into P2VP matrices of molecular weights from 14 – 1220 kDa using our ToF-SIMS method to measure NP diffusion coefficients, D_{NP} , in entangled polymer

melts. We obtain diffusion coefficients after annealing for two or three annealing times to demonstrate that the NP tracer diffusion is independent of annealing time. We employ the radius of gyration (R_g) as a metric for polymer size. **Figure 3.1** shows representative SiO₂ ($R_{NP} = 26.2$ nm) and Al₂O₃ ($R_{NP} = 6.5$ nm) NP concentration profiles after various annealing times at 180 °C in 41 kDa P2VP ($R_g = 5.5$ nm) along with fits to Eqn. 6 to obtain the diffusion coefficients. In this $R_g < R_{NP}$ regime ($d_T = 23.5$ nm), the smaller Al₂O₃ NPs diffuse faster than the larger SiO₂ NPs and the results are consistent with $D_{core-shell}$ (Eqn 2). Specifically, $\langle D_{NP}(\text{SiO}_2, 26.2 \text{ nm}) \rangle = 2.8 \pm 2.0 \times 10^{-13} \text{ cm}^2/\text{s}$ and $D_{core-shell}$ for this system is $3.1 \times 10^{-13} \text{ cm}^2/\text{s}$ and $\langle D_{NP}(\text{Al}_2\text{O}_3, 6.5 \text{ nm}) \rangle = 7.4 \pm 2.5 \times 10^{-13} \text{ cm}^2/\text{s}$ and $D_{core-shell}$ for this system is $9.0 \times 10^{-13} \text{ cm}^2/\text{s}$. Fitting the NP concentrations profiles is repeated in six other molecular weights and allows us to obtain diffusion coefficients across orders of magnitude by adjusting the annealing time. The experimental concentration profiles for all NP/P2VP systems and their respective fits are given in **Figure B.2-B.4**, with tabulated data in **Table B.4-B.6**. While most of the systems studied found $D_{NP} \approx D_{core-shell}$, we also found systems having $D_{NP} > D_{core-shell}$ indicating the presence of a vehicular mechanism of NP diffusion in entangled polymer melts.

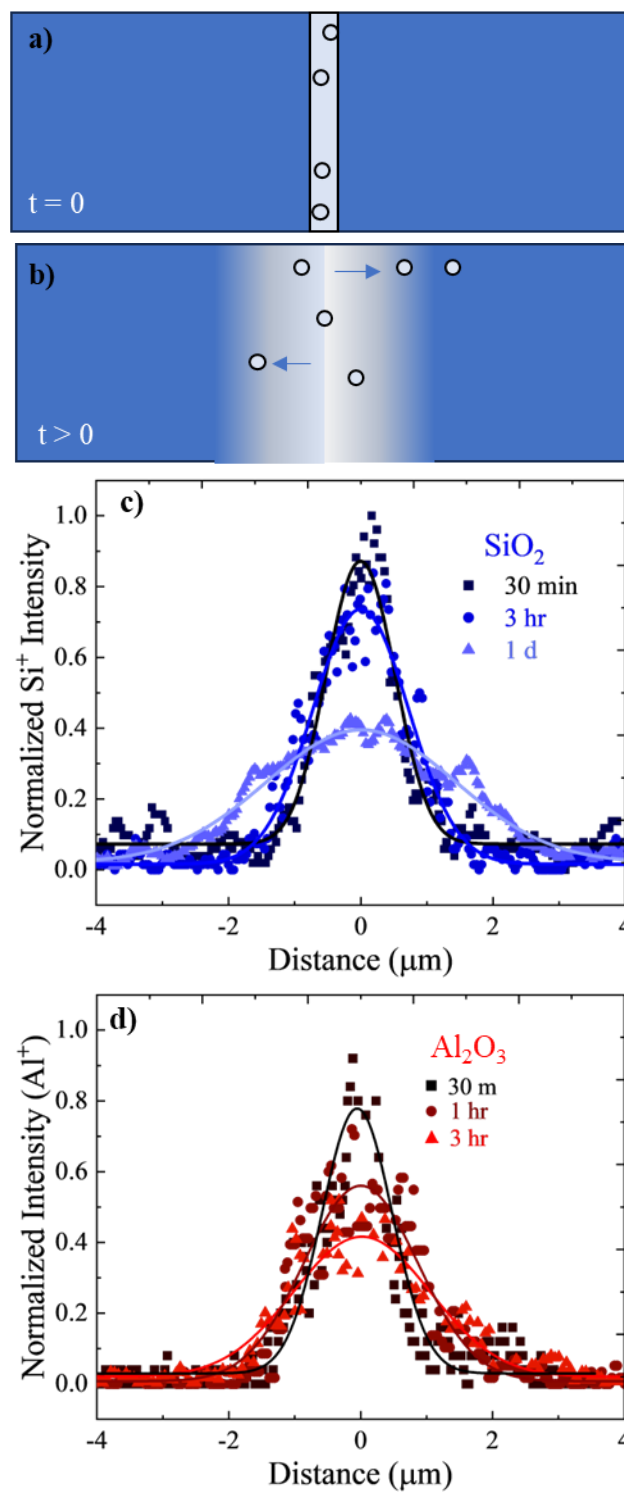


Figure 3.1 : **a)** Initial sample state at $t = 0$, where thick P2VP layers border a thin center PNC layer. **b)** Schematic of sample after annealing for a specified time t . **c)** Concentration profiles and fits to Eqn. 6 of Si^+ signal indicating diffusion of SiO_2 NPs in 41 kDa P2VP ($R_g/R_{NP} = 0.21$) at three annealing times. **d)** Concentration profiles and fits of integrated Al^+ data indicating Al_2O_3 NP diffusion in 41 kDa P2VP ($R_g/R_{NP} = 0.85$) at three annealing times.

Core-Shell and Vehicle Diffusion Behavior

In contrast to our earlier experimental investigations, this study involves P2VP matrices spanning a wider molecular weight range of 14 – 1220 kDa, which includes unentangled to well-entangled ($M_e \approx 18$ kDa) polymer melts. To accommodate the high viscosity matrices, diffusion times were carefully controlled from 10 min – 10 days to achieve diffusion lengths commensurate with ToF-SIMS measurements. Thus, we measure D_{NP} values ranging from 7×10^{-18} to 1.3×10^{-11} cm^2/s , which is sufficient to capture both the core-shell and vehicular NP diffusion mechanism.

The larger SiO_2 NPs ($R_{NP} = 26$ nm) clearly exhibit core-shell model behavior across the entire molecular weight range. In **Figure 3.2**, the D_{NP} values from the different annealing times are normalized by $D_{core-shell}$ (Eqn. 3.2) and the values are on the order of 1. Similarly, the diffusion coefficients for smaller SiO_2 NPs ($R_{NP} = 8.3$ nm) also follow core-shell behavior even at $R_g/R_{NP} > 1$. **Figure B.5** plots these D_{NP} values on a log scale wherein the data from the different annealing times are easier to distinguish. Figure 2 also includes earlier data from our group studying quantum dots in PPG where $R_g/R_{NP} < 1$ and the surface chemistry of the quantum dots was either attractive ($R_{eff} = R_{NP} + R_g$) or neutral ($R_{eff} = R_{NP}$) toward the PPG. In both cases, D_{NP} is well-described by $D_{core-shell}$.²⁵

In contrast, the diffusion coefficient of the Al₂O₃ NPs ($R_{NP} = 6.5$ nm) deviates significantly from the core-shell mechanism of NP diffusion, Figure 2. While $D_{NP}/D_{core-shell} \approx 1$ when $R_g/R_{NP} < 1.4$, $D_{NP}/D_{core-shell}$ increases dramatically at higher R_g/R_{NP} . For example, when the P2VP matrix is $M_w = 310$ kg/mol and $R_g/R_{NP} = 2.4$, $\langle D_{NP} \rangle / D_{core-shell}$ is 17 and when the P2VP matrix is $M_w = 474$ kg/mol and $R_g/R_{NP} = 2.9$, $\langle D_{NP} \rangle / D_{core-shell}$ is 60. Consequently, we conclude that the Al₂O₃ NPs diffuse by a combination of core-shell and vehicular mechanisms. Interestingly, the Al₂O₃ NPs exhibit vehicular diffusion while similarly sized SiO₂ NPs exhibit only core-shell diffusion (see blue squares at $R_g/R_{NP} > 2$), which implies a difference in surface chemistry leads to a faster desorption time for Al₂O₃ NPs. In Figure 2b, Al₂O₃ NP behavior diverges strongly from $D_{core-shell}$ predictions and at $R_g/R_{NP} \geq 2.4$ the discrepancy between D_{NP} and $D_{core-shell}$ is $\sim 10^{-14}$ cm²/s, **Table B.8**. Importantly, this difference ($D_{NP} - D_{core-shell}$) is nominally independent of molecular weight. Thus, we attribute the faster NP diffusion to the vehicular mechanism given by $D_{vehicle-II}$ (Eqn 3.4), which is independent of M_w and has a strong dependence on monomer desorption time, $\tau_{des}^{-3/4}$.

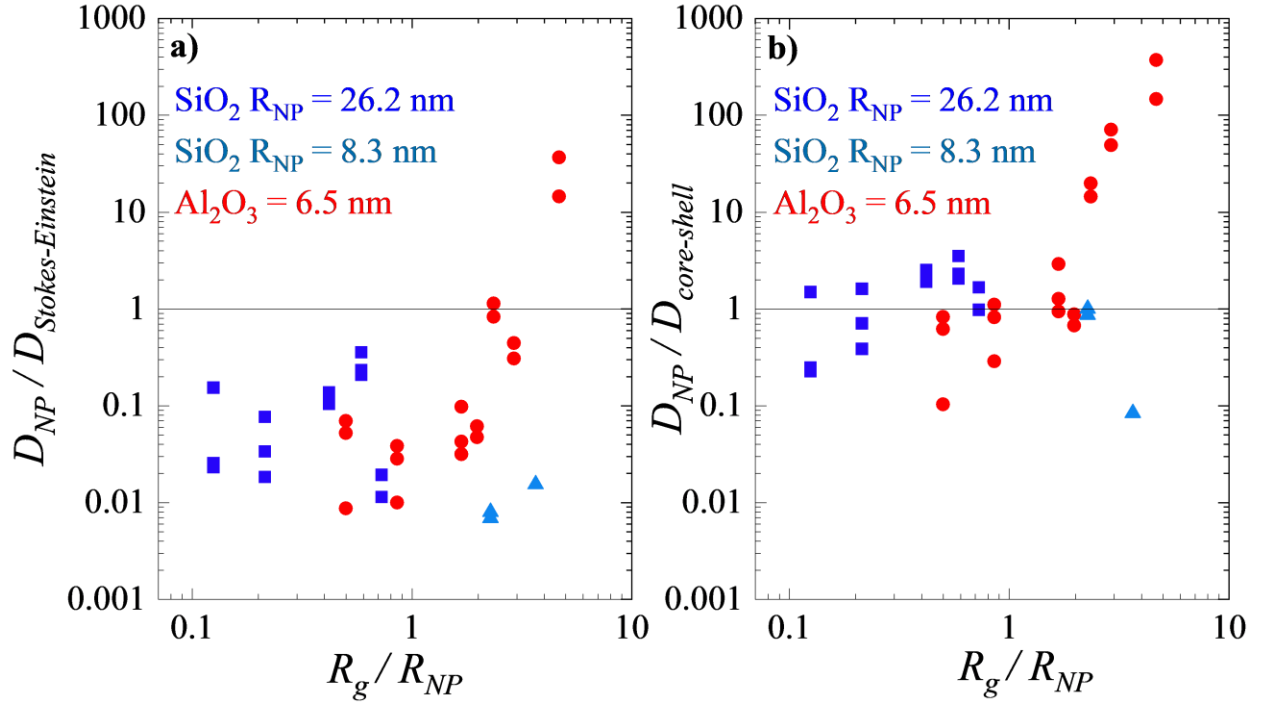


Figure 3.2 Nanoparticle diffusion coefficients normalized by **a)** $D_{Stokes-Einstein}$ and **b)** $D_{core-shell}$ as a function of the polymer R_g normalized by R_{NP} . Silica nanoparticles are displayed in blue squares ($R_{NP} = 26.2$ nm) and light blue triangles ($R_{NP} = 8.3$ nm). Alumina nanoparticles are displayed in red circles ($R_{NP} = 6.5$ nm). All annealing times are plotted.

Monomer Desorption Time of the Bound Layer

The vehicular and core-shell diffusion mechanisms both contribute to the nanoparticle diffusion coefficient (D_{NP}) and are predicated on the existence and lifetime of a bound polymer layer formed through physical adsorption. Core-shell diffusion dominates in systems where the bound layer is long-lived. In contrast, vehicular diffusion occurs in intermediately attractive systems where the rate of stochastic polymer-NP desorption is faster than that observed in core-shell behavior. An essential facet of vehicular diffusion involves understanding the monomer desorption time (τ_{des}), a topic not fully explored in nanocomposites with attractive polymer-NP

interactions.^{17,34} Previous studies of silica NPs in P2VP have hinted at a temperature dependence on the bound layer, revealing an effective shell radius and an exchange rate of approximately ~100 hours.³⁵ However, factors influencing desorption time, including polymer-NP interaction strength, molecular weight, entanglement, and NP curvature, remain largely uncharted. This knowledge gap about τ_{des} complicates our grasp of vehicular diffusion, making it challenging to pinpoint the predominant factors influencing fast diffusion. Here, we extract timescales from our prior work to interpret our NP diffusion results, refine our understanding of the vehicular mechanism, and estimate τ_{des} in these PNCs.

To isolate the effect of τ_{des} , we refine Eqn. 3.1 to account for both nanoparticle size and polymer molecular weight and to specify Regime II of the vehicular mechanism,

$$D_{NP,theory}(R_{NP}, M_w) = D_{core-shell}(R_{NP}, M_w) + Ad_T(b^2 D_0)^{\frac{1}{4}} \times \left(\frac{1}{\tau_{des}}\right)^{\frac{3}{4}} \quad (3.7)$$

Note that Regime I of the vehicular mechanism was dismissed because the NPs in this study have surface hydroxyl groups that have favorable interactions with the nitrogen in P2VP, resulting in slower desorption times. Given $\tau_e \sim 1$ s and $D_0 = 1.0 \times 10^{-9}$ cm²/s, we estimate $D_{vehicle-I} \sim 10^{-9}$ cm²/s, which is faster than any of our results even in the lowest M_w . This is consistent with prior results demonstrating that silica nanoparticles with hydroxyl surface groups strongly interact with P2VP to have long desorption times.^{35–37} Regime III is dismissed because $D_{vehicle}$ fails to demonstrate a $\sim 1/N^{-1/2}$ scaling across M_w 310 – 474 kDa (Eqn. 3.5). The molecular weight dependence of $D_{core-shell}$ (Eqn. 2) is caused by the molecular weight dependence of R_{eff} and η_{PNC} . The effective nanoparticle radius, R_{eff} , includes a strongly polymer bound layer, $R_{eff} = R_{NP} + R_g$ and the molecular weight dependence of R_g in the melt is well known.³⁸ The viscosity of the PNC (η_{PNC}) is a function

of the average volume fraction of the nanoparticles after dilution ϕ_{NP} , and polymer molecular weight

$$\eta_{PNC} = \eta_{poly}(1 + 2.5\phi_{eff} + 6.2\phi_{eff}^2) \quad (3.8)$$

$$\phi_{eff} = \phi_{NP} \left(\frac{R_{eff}}{R_{NP}} \right)^3 \quad (3.9)$$

We measured the melt viscosity of the P2VP polymers in this study and fit the data to obtain $\eta_{poly}(M_w)$ for Eqn 3.8. To capture the Regime II vehicular contribution to $D_{NP,theory}$, we start with the molecular weight dependence of the shortest Rouse time (τ_0) for P2VP as previously measured by broadband dielectric spectroscopy (BDS) at $T = 413$ °K.¹³ By assuming a $1/T$ dependence we adjust the measured values to temperature of interest $T = 453$ °K (180 °C), and $\tau_0 \approx 10^{-5}$ s, **Figure B.6**. Then we compute all the relevant timescales by

$$\tau_e = \tau_0 * N_e^2 \quad (3.10)$$

$$\tau_{Rouse} = \tau_0 * N^2 \quad (3.11)$$

$$\tau_{rep} = \tau_{Rouse} * \frac{N}{N_e} \quad (3.12)$$

As previously mentioned, the Al_2O_3 nanoparticles appear to be in Regime II because the difference between the measured D_{NP} and $D_{core-shell}$ is independent of molecular weight. Regime II corresponds to $\tau_e < \tau_{des} < \tau_{Rouse}$, which for P2VP at 180°C indicates that τ_{des} is expected to be longer than $\tau_e \sim 1$ s and shorter than 30 – 6,000 sec corresponding to ~ 100 to 1220 kDa.

Figure 3.3 shows the fit of Eqn. 3.7 to D_{NP} for the large SiO₂ NPs as a function of molecular weight. Consistent with Figure 3.2, the core-shell mechanism is sufficient to describe NP diffusion of the SiO₂ NPs across all molecular weights. This implies $D_{vehicle} \sim 0$, and therefore τ_{des} (> 6000 s) is exceedingly large and consistent with a highly attractive P2VP- SiO₂ interaction. **Figure 3b** shows the experimental data for the Al₂O₃ NPs along with the fit to Eqn. 7 using $A = 1$, $d_T = 23.5$ nm, $b = 1.8$ nm, and $D_0 = 1.0 \times 10^{-9}$ cm²/s.¹³ The best fit corresponds to $\tau_{des} = 50$ s, which falls within the bounds established above. To illustrate the bounds corresponding to Regime II of vehicular NP diffusion, we plot Eqn 7 using the $\tau_{des} = \tau_e$, which is independent of M_w , and $\tau_{des} = \tau_{Rouse}$, which increases with M_w . These upper and lower limits of D_{NP} for the Al₂O₃ NPs in P2VP further to confirm that this system is in Regime II at 180 °C.

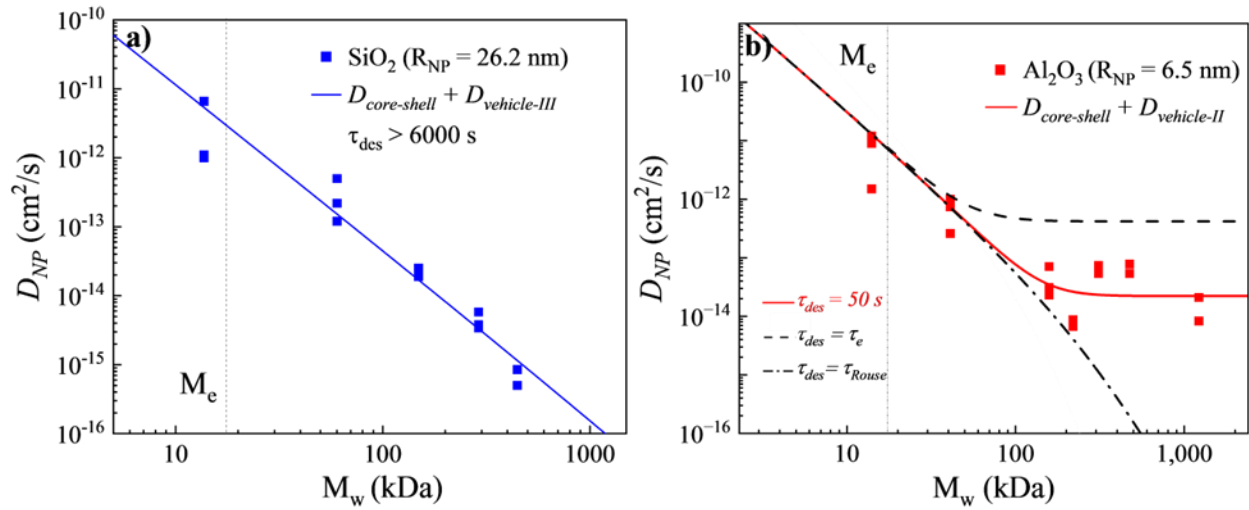


Figure 3.3 a) D_{NP} (blue points) for SiO₂ (26.2 nm) NPs in P2VP as a function of molecular weight. Solid line corresponds to D_{theory} in Eqn. 7 where $D_{vehicle} \rightarrow 0$ as $\tau_{des} \gg \tau_{Rouse}$. **b)** D_{NP} (red points) for Al₂O₃ (6.5 nm) NPs in P2VP as a function of molecular weight. Red line is the best fit to Eqn

3.7 and corresponds to $\tau_{des} = 50$ s. Black dashed and dot-dash lines correspond to $\tau_{des} = \tau_e$ and $\tau_{des} = \tau_{Rouse}$, respectively.

These results indicate that NP diffusion coefficients can provide valuable insight into the monomer desorption times and polymer-NP interactions. Given that the core-shell behavior of small SiO₂ NPs (Figure 3.2) and the vehicular mechanism found in Al₂O₃ NPs of similar size, our results show that Al₂O₃ NPs exhibit weaker polymer-NP interactions. This finding is consistent with water contact angle measurements for silica ($\sim 80^\circ$) and alumina ($\sim 90^\circ$) that suggest a lower areal density of hydroxyl groups on alumina leading to weaker interactions consistent with a short τ_{des} .^{39,40} Additionally, poly(vinylpyrrolidone) (PVP) preferentially adsorbs to unmodified silica particles over alumina-coated counterparts in aqueous solution, and the preadsorbed PVP transfers from the alumina-coated particles to silica particles as the system equilibrates. Adsorption isotherms further demonstrate that PVP adhesion to silica particles is stronger than to alumina-coated silica particles, which demonstrates that the silica particle surface is more polar.⁴¹ This result is consistent with our finding that the monomeric desorption time of P2VP is longer for silica NPs than for alumina NPs. Overall, this study establishes that both the relative size of the polymer to the nanoparticle (R_g/R_{NP}) and the polymer-NP interfacial interactions dictate the transition for NP diffusion from a solely core-shell behavior mechanism to the addition of vehicular mechanisms. Further investigations could explore various methods for controlling polymer-NP interactions, including using random copolymers, as well as the effect of nanoparticle shape on diffusion.

3.4 Conclusions

We experimentally demonstrate both the core-shell and the vehicle mechanisms for nanoparticle diffusion. While large and small silica NPs demonstrate the core-shell mechanism (Eqn. 2) due to highly attractive polymer-NP interactions and long monomer desorption times, τ_{des} , small alumina nanoparticles display a crossover from core-shell to vehicular NP diffusion. For the Al_2O_3 NPs, D_{NP} exhibits a plateau as M_w increases and $R_g > R_{NP}$, and this molecular weight independent behavior is consistent with Regime II of the vehicular mechanism. At high M_w , the Al_2O_3 NP diffusion coefficients are one or two orders of magnitude faster than predicted by the core-shell model alone. Fitting the data reveals a τ_{des} of ~ 50 s that is independent of M_w and indicates a weaker polymer-NP interaction in P2VP/ Al_2O_3 than in P2VP/ SiO_2 nanocomposites. We have demonstrated that by measuring nanoparticle diffusion coefficients in polymer melts, one can determine the polymer-NP interaction strengths, which has previously been difficult to ascertain. This study provides a pathway to measure monomer desorption times (τ_{des}) for a variety of PNC systems to explore the role of temperature, NP size, NP surface functionality, and polymer composition to understand the lifetime of the polymer bound layer on nanoparticles. We found that the core-shell and vehicle diffusion modes apply broadly to entangled melts with attractive polymer-NP interactions.

3.5 References

- (1) Kumar, S. K.; Benicewicz, B. C.; Vaia, R. A.; Winey, K. I. 50th Anniversary Perspective: Are Polymer Nanocomposites Practical for Applications? *Macromolecules* **2017**, *50*, 714–731.
- (2) Méar, F.; Coillot, D.; Podor, R.; Montagne, L. Self-Healing Nanocomposites: Role and Activation of Inorganic Moieties and Hybrid Nanophases. In *{Self-Healing} at the Nanoscale*; CRC Press, 2011; pp 188–223.
- (3) Mallakpour, S.; Naghdi, M. {Polymer/SiO₂} Nanocomposites: Production and Applications. *Prog. Mater. Sci.* **2018**, *97*, 409–447.
- (4) Thakur, V. K.; Kessler, M. R. Self-Healing Polymer Nanocomposite Materials: A Review. *Polymer (Guildf)*. **2015**, *69*, 369–383.
- (5) Young, W. W.; Katsumata, R. Intermediate Polymer Relaxation Explains the Anomalous Rheology of Nanocomposites with Ultrasmall Attractive POSS Nanoparticles. *ACS Polym. Au* **2023**, *3*, 466–474.
- (6) Merkel, T. C.; Freeman, B. D.; Spontak, R. J.; He, Z.; Pinnau, I.; Meakin, P.; Hill, A. J. Ultrapervious, Reverse-Selective Nanocomposite Membranes. *Science (80-.)*. **2002**, *296*, 519–522.
- (7) Yin, J.; Deng, B. Polymer-Matrix Nanocomposite Membranes for Water Treatment. *J. Memb. Sci.* **2015**, *479*, 256–275.
- (8) Cheng, S.; Xie, S.-J.; Carrillo, J.-M. Y.; Carroll, B.; Martin, H.; Cao, P.-F.; Dadmun, M. D.; Sumpter, B. G.; Novikov, V. N.; Schweizer, K. S.; Sokolov, A. P. Big Effect of Small Nanoparticles: A Shift in Paradigm for Polymer Nanocomposites. *ACS Nano* **2017**, *11*, 752–759.
- (9) Balazs, A. C.; Emrick, T.; Russell, T. P. Nanoparticle Polymer Composites: Where Two Small Worlds Meet. *Science (80-.)*. **2006**, *314*, 1107–1110.
- (10) Lin, C.-C.; Parrish, E.; Composto, R. J. Macromolecule and Particle Dynamics in Confined Media.

Macromolecules **2016**, *49*, 5755–5772.

- (11) Cheng, S.; Holt, A. P.; Wang, H.; Fan, F.; Bocharova, V.; Martin, H.; Etampawala, T.; White, B. T.; Saito, T.; Kang, N.-G.; Dadmun, M. D.; Mays, J. W.; Sokolov, A. P. Unexpected Molecular Weight Effect in Polymer Nanocomposites. *Phys. Rev. Lett.* **2016**, *116*, 038302-1–4.
- (12) Papakonstantopoulos, G. J.; Yoshimoto, K.; Doxastakis, M.; Nealey, P. F.; De Pablo, J. J. Local Mechanical Properties of Polymeric Nanocomposites. *Phys. Rev. E - Stat. Nonlinear, Soft Matter Phys.* **2005**, *72*, 031801-031801–031806.
- (13) Bailey, E. J.; Griffin, P. J.; Composto, R. J.; Winey, K. I. Multiscale Dynamics of Small, Attractive Nanoparticles and Entangled Polymers in Polymer Nanocomposites. *Macromolecules* **2019**, *52*, 2181–2188.
- (14) Griffin, P. J.; Bocharova, V.; Middleton, L. R.; Composto, R. J.; Clarke, N.; Schweizer, K. S.; Winey, K. I. Influence of the Bound Polymer Layer on Nanoparticle Diffusion in Polymer Melts. *ACS Macro Lett.* **2016**, *5*, 1141–1145.
- (15) Cheng, S.; Carroll, B.; Bocharova, V.; Carrillo, J.-M.; Sumpter, B. G.; Sokolov, A. P.; Carrillo, J.-M. Y. Perspective: Outstanding Theoretical Questions in Polymer-Nanoparticle Hybrids. *J. Chem. Phys.* **2017**, *146*, 203201.
- (16) Yamamoto, U.; Carrillo, J.-M. Y.; Bocharova, V.; Sokolov, A. P.; Sumpter, B. G.; Schweizer, K. S. Theory and Simulation of Attractive Nanoparticle Transport in Polymer Melts. *Macromolecules* **2018**, *51*, 2258–2267.
- (17) Carroll, B.; Bocharova, V.; Carrillo, J.-M. Y.; Kisliuk, A.; Cheng, S.; Yamamoto, U.; Schweizer, K. S.; Sumpter, B. G.; Sokolov, A. P. Diffusion of Sticky Nanoparticles in a Polymer Melt: Crossover from Suppressed to Enhanced Transport. *Macromolecules* **2018**, *51*, 2268–2275.
- (18) Tuteja, A.; Mackay, M. E.; Narayanan, S.; Asokan, S.; Wong, M. S. Breakdown of the Continuum Stokes-Einstein Relation for Nanoparticle Diffusion. *Nano Lett.* **2007**, *7*, 1276–1281.

- (19) Lin, C.-C.; Gam, S.; Meth, J. S.; Clarke, N.; Winey, K. I.; Composto, R. J. Do Attractive Polymer–Nanoparticle Interactions Retard Polymer Diffusion in Nanocomposites? **2013**, *46*, 42.
- (20) Liu, J.; Cao, D.; Zhang, L. Molecular Dynamics Study on Nanoparticle Diffusion in Polymer Melts: A Test of the Stokes-Einstein Law. *J. Phys. Chem. C* **2008**, *112*, 6653–6661.
- (21) Grabowski, C. A.; Mukhopadhyay, A. Size Effect of Nanoparticle Diffusion in a Polymer Melt. *Macromolecules* **2014**, *47*, 7238–7242.
- (22) Cai, L. H.; Panyukov, S.; Rubinstein, M. Hopping Diffusion of Nanoparticles in Polymer Matrices. *Macromolecules* **2015**, *48*, 847–862.
- (23) Cai, L.-H.; Panyukov, S.; Rubinstein, M. Mobility of Nonsticky Nanoparticles in Polymer Liquids. *Macromolecules* **2011**, *44*, 7853–7863.
- (24) Cole, D. H.; Shull, K. R.; Rehn, L. E.; Baldo, P. M. RBS Analysis of the Diffusion of Nano-Size Spheres in a Polymer Matrix. *Nucl. Instruments Methods Phys. Res. Sect. B Beam Interact. with Mater. Atoms* **1998**, *136–138*, 283–289.
- (25) Park, J.; Bailey, E. J.; Composto, R. J.; Winey, K. I. Single-Particle Tracking of Nonsticky and Sticky Nanoparticles in Polymer Melts. *Macromolecules* **2020**, *53*, 3933–3939.
- (26) Mendez, N. F.; Dhara, D.; Zhang, Q.; Narayanan, S.; Schadler, L. S.; Müller, A. J.; Kumar, S. K. Nanoparticle Diffusion in Miscible Polymer Nanocomposite Melts. *Macromolecules* **2023**, *56*, 4658–4668.
- (27) Kwon, N. K.; Park, C. S.; Lee, C. H.; Kim, Y. S.; Zukoski, C. F.; Kim, S. Y. Tunable Nanoparticle Stability in Concentrated Polymer Solutions On the Basis of the Temperature Dependent Solvent Quality. *Macromolecules* **2016**, *20*, 25.
- (28) Wang, K.; Composto, R. J.; Winey, K. I. ToF-SIMS Depth Profiling to Measure Nanoparticle and Polymer Diffusion in Polymer Melts. *Macromolecules* **2023**.
- (29) Spool, A. M. *The Practice of TOF-SIMS: Time of Flight Secondary Ion Mass Spectrometry* - Alan

M. Spool - Google Books; Momentum Press, 2016.

- (30) Mei, H.; Laws, T. S.; Terlier, T.; Verduzco, R.; Stein, G. E. Characterization of Polymeric Surfaces and Interfaces Using Time-of-Flight Secondary Ion Mass Spectrometry. *Journal of Polymer Science*. John Wiley and Sons Inc April 1, 2021, pp 1174–1198.
- (31) Prasad, A.; Salim, N. V.; Mozetič, M.; Kailas, L.; Thomas, S. Time-of-flight Secondary Ion Mass Spectrometric Analysis of Polymer Surfaces: A Review. *J. Appl. Polym. Sci.* **2022**, 52286.
- (32) Karar, N.; Gupta, T. K. Study of Polymers and Their Blends Using TOF-SIMS Ion Imaging. *Vacuum* **2015**, *111*, 119–123.
- (33) Chan, C. M.; Weng, L. T. Surface Characterization of Polymer Blends by XPS and ToF-SIMS. *Materials (Basel)*. **2016**, *9*.
- (34) Ge, T. Scaling Perspective on Dynamics of Nanoparticles in Polymers: Length- and Time-Scale Dependent Nanoparticle-Polymer Coupling. *Macromolecules* **2023**, *56*, 3809–3837.
- (35) Jimenez, A. M.; Zhao, D.; Misquitta, K.; Jestin, J.; Kumar, S. K. Exchange Lifetimes of the Bound Polymer Layer on Silica Nanoparticles. *ACS Macro Lett.* **2019**, *8*, 166–171.
- (36) Bailey, E. J.; Griffin, P. J.; Composto, R. J.; Winey, K. I. Characterizing the Areal Density and Desorption Kinetics of Physically Adsorbed Polymer in Polymer Nanocomposite Melts. *Macromolecules* **2020**, *53*, 2744–2753.
- (37) Harton, S. E.; Kumar, S. K.; Yang, H.; Koga, T.; Hicks, K.; Lee, H.; Mijovic, J.; Liu, M.; Vallery, R. S.; Gidley, D. W. Immobilized Polymer Layers on Spherical Nanoparticles. *Macromolecules* **2010**, *43*, 3415–3421.
- (38) Rubinstein, M.; Colby, R. H. *Polymer Physics*; Oxford University Press, 2003.
- (39) Jin, J.; Wang, X.; Wick, C. D.; Dang, L. X.; Miller, J. D. Silica Surface States and Their Wetting Characteristics. <https://doi.org/10.1680/jsuin.19.00053> **2020**, *8*, 145–157.
- (40) Watcharenwong, A.; Saijaioup, N.; Bailuang, Y.; Kajitvichyanukul, P. Morphology and Wettability

- of Nanoporous Aluminium Oxide Film Prepared by Anodization. *Key Eng. Mater.* **2017**, 737, 174–178.
- (41) Cooper, C. L.; Cosgrove, T.; Van Duijneveldt, J. S.; Murray, M.; Prescott, S. W. Colloidal Particles in Competition for Stabilizer: A Solvent Relaxation NMR Study of Polymer Adsorption and Desorption. *Langmuir* **2012**, 28, 16588–16595.

CHAPTER 4 : NANOPARTICLE DIFFUSION IN CROWDED POLYMER NANOCOMPOSITE MELTS

Content in this chapter has been submitted to *ACS Macroletters* in June 2024.

The authors of this chapter are Kaitlin Wang and Karen I. Winey.

Kaitlin Wang and Karen I. Winey conceived the presented idea. Kaitlin Wang conducted the literature search, designed and performed the experiments, developed the methodology, and carried out the data analysis. She also wrote the first draft of the manuscript and incorporated feedback from Karen I. Winey. Karen I. Winey supervised the experiments and provided revisions to the manuscript drafts.

4.1 Introduction

Incorporating nanoparticles into polymer nanocomposites (PNCs) enhances material characteristics and allows tunability.¹⁻⁵ Understanding diffusion in crowded nanocomposites is crucial for predicting material behavior, impacting fields like drug delivery and advanced materials.⁶⁻⁸ Crowded PNCs simulate densely packed environments, allowing control over matrix and nanoparticle (NP) parameters.^{7,9} Polymers and NPs in confined environments experience unique interactions due to spatial restrictions¹⁰ and increased surface area,¹¹⁻¹³ altering their behaviors compared to dilute environments.

Previous work highlights the impact of nanoparticle attributes on polymer dynamics. Interaction strength, NP size, and NP distribution can alter the glass transition temperature^{12,14} and mechanical properties. Particle loading's effect on polymer diffusion has been studied in both athermal and attractive PNC systems.¹⁵⁻¹⁷ With attractive interactions, like in our system, the

polymer diffusion coefficient drops by fivefold with increasing NP concentration and remains depressed even at interparticle distances (ID) $\gg 2R_g$.¹⁸

Nanoparticle diffusion in crowded environments differs from classical Brownian motion as crowding effects dominate.^{17,19,20} Xue et al. reported hopping diffusion and polymer network interactions influencing NP diffusion when NP size is comparable to or smaller than the polymer matrix mesh size.²¹ Many studies on NP diffusion in crowded media focus on polymer solutions²² or gels²³ that are compatible with low particle concentrations.

Here, we measure NP diffusion coefficients of small Al_2O_3 nanoparticles into polymer nanocomposites of large SiO_2 nanoparticles with loading from dilute to crowded ($\phi_{\text{SiO}_2} = 0.001 - 0.05$). Using time-of-flight secondary ion mass spectrometry (ToF-SIMS) and previously demonstrated,²⁴ we distinguish between diffusing Al_2O_3 and background SiO_2 nanoparticles in the PNC with two NP sizes. **Figure 4.1** illustrates idealized Al^+ concentration profiles before and after annealing.

4.2 Results

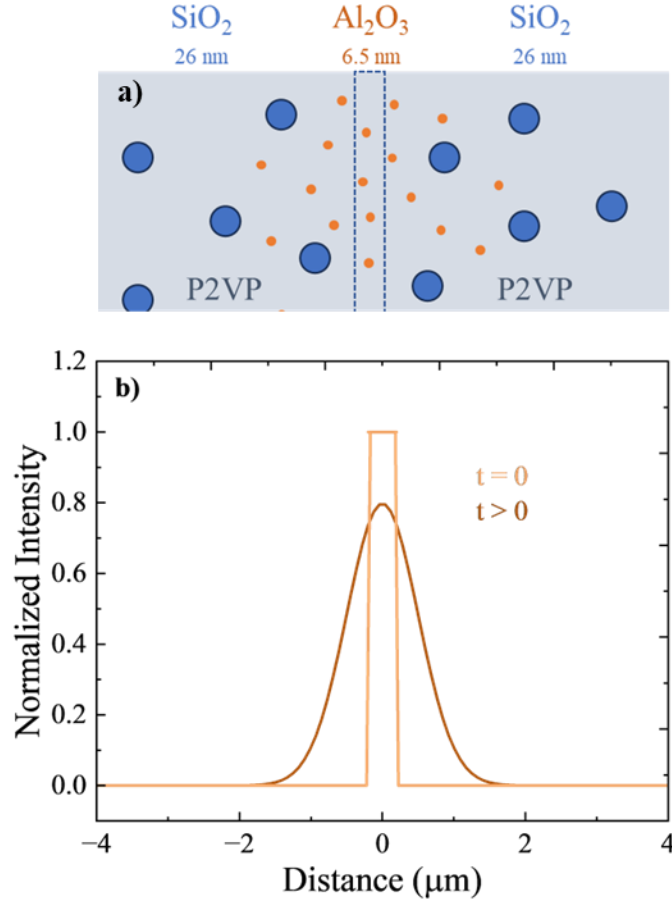


Figure 4.1: Schematic and concentration profiles of small Al_2O_3 NPs diffusing into SiO_2 -P2VP layers. **(a)** Cross-sectional view of the trilayer sample with a central Al_2O_3 NP layer ($\phi_{\text{Al}_2\text{O}_3} = 0.01$, orange) diffusing into the surrounding SiO_2 -loaded P2VP matrix (blue). **(b)** Representational concentration profiles before ($t = 0$) and after annealing ($t > 0$) showing Al_2O_3 NP diffusion into the SiO_2 -P2VP nanocomposite.

The initial concentration of Al_2O_3 nanoparticles in the mid-layer is $\phi_{\text{Al}_2\text{O}_3} = 0.01$. Each trilayer sample was annealed for 1, 3, and 6 hours and the normalized Al^+ concentration profiles were fit to Fick's second law solution for a finite source diffusing into a semi-infinite medium,

$$\varphi(y) = \frac{1}{2} \left[\text{erf} \left(\frac{h-y}{\sqrt{4D_{NP}t}} \right) + \text{erf} \left(\frac{h+y}{\sqrt{4D_{NP}t}} \right) \right] \quad (4.1)$$

where $\varphi(y)$ is the concentration as a function of position y , h is the film's initial thickness ($\sim 0.2 \mu\text{m}$), D_{NP} is the NP diffusion coefficient, and t is the annealing time in seconds. **Figure 4.2** and **Figure C.2** present time series showing the progression of Al_2O_3 NPs moving into a SiO_2 -P2VP nanocomposite ($\varphi_{\text{SiO}_2} = 0.025$) when annealed at 180°C ($\sim T_g + 50^\circ\text{C}$) along with best fits to Eqn. 4.1 to give experimental D_{NP} values, **Table C.1**.

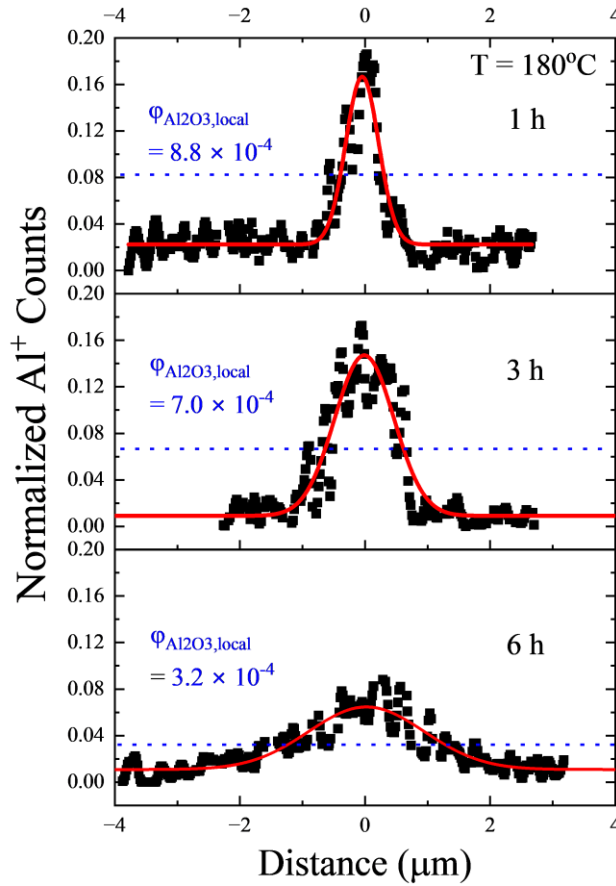


Figure 4.2: Concentration profiles of Al^+ ions indicating the spatial distribution of Al_2O_3 NPs within trilayer samples with SiO_2 -P2VP nanocomposite with $\varphi_{\text{SiO}_2} = 0.025$. The samples, with an initial $\varphi_{\text{Al}_2\text{O}_3} = 0.01$ concentration in the mid-layer, were annealed at 180°C ($T_g + \sim 50^\circ\text{C}$) for 1,

3, and 6 hours. The normalized intensity profiles have been smoothed by adjacent averaging over four data points to minimize noise. The local Al_2O_3 concentrations, $\varphi_{\text{Al}_2\text{O}_3, \text{local}}$, are the concentration at the FWHM of the normalized concentration profiles, as illustrated in orange. Red lines are best fits of Eqn. 4.1 to the data to find the Al_2O_3 nanoparticle diffusion coefficients, see

Table C.1

The Schweizer group proposed two simultaneous mechanisms of NP diffusion in nanocomposites with dilute monodisperse spherical NPs: core-shell and vehicular modes of NP diffusion.^{25,26}

$$D_{NP, \text{theory}} = D_{\text{core-shell}} + D_{\text{vehicle}} \quad (4.2)$$

The core-shell mode is a modified Stokes-Einstein model accounting for the increased NP radius due to the bound layer (R_{eff}) and the increased viscosity in nanocomposites (η_{PNC}),

$$D_{\text{core-shell}} = \frac{k_B T}{6\pi\eta_{PNC}R_{\text{eff}}} \quad (4.3)$$

$$\eta_{PNC} = \eta_{\text{poly}}(1 + 2.5\varphi_{\text{eff}} + 6.2\varphi_{\text{eff}}^2) \quad (4.4)$$

where η_{poly} is the viscosity of the neat polymer and φ_{eff} accounts for R_{eff} . Core-shell diffusion has been demonstrated with quantum dots in poly(propylene glycol) (PPG), and SiO_2 NPs in PPG and P2VP.^{25,27–29}

Vehicular diffusion is influenced by monomeric desorption times (τ_{des}) from NP surfaces and is partitioned into three regimes based on the desorption time relative to polymer dynamic time scales (entanglement onset time, τ_e , Rouse time, τ_{Rouse} , and reptation time, τ_{Rep}). For the 158 kDa P2VP at 180 °C, $\tau_e = 0.90$ s and $\tau_{\text{Rouse}} = 70$ s.^{29,30} Regime I corresponds to the fastest desorption times ($\tau_{\text{des}} < \tau_e$) not relevant to our system due to hydrogen bonding of the Al_2O_3 NPs

and P2VP. Regime III describes desorption times $\tau_{Rouse} < \tau_{des} < \tau_{rep}$ not relevant in this system. Moreover, in our recent work,²⁹ we established that 6.5-nm Al₂O₃ NPs diffusing into neat P2VP transition from predominantly core-shell diffusion to vehicular Regime II diffusion as polymer molecular weight increases from 14 - 1220 kDa. We found $\tau_{des} \sim 50$ s at 180 °C. Regime II is defined by intermediate desorption times ($\tau_e < \tau_{des} < \tau_{Rouse}$), and $D_{vehicle-II}$ is inversely proportional to $\tau_{des}^{3/4}$,

$$D_{vehicle-II} = A d_T (b^2 D_0)^{\frac{1}{4}} \times \left(\frac{1}{\tau_{des}} \right)^{\frac{3}{4}} \quad (4.5)$$

where A is a numerical prefactor, d_T is the tube diameter, b is the Kuhn monomer length, and D_0 is the segmental diffusion constant. For the following calculations, $A = 1$, $d_T = 23.5$ nm, $b = 1.8$ nm, and $D_0 = 1.0 \times 10^{-9}$ cm²/s.^{29,30} The Al₂O₃ NP diffusion into neat 158 kDa P2VP is well described by $D_{NP,theory}$ (Eqn. 2), that accounts for the increased viscosity of the NP loading and bound polymer layer thickness (Eqn. 3) and vehicular motion from polymer desorption (Eqn. 4.5).

Figure 4.3 presents D_{NP} for the small NPs as a function of the concentration of the large NPs, ϕ_{SiO_2} . In neat 158 kDa P2VP ($\phi_{SiO_2} = 0$), we previously²⁹ demonstrated that these Al₂O₃ NPs have a diffusion coefficient of $4.3 \pm 2.4 \times 10^{-14}$ cm²/s (Figure 3). In the Al₂O₃ NPs diffusing into nanocomposites studied here, we begin by comparing the measured D_{NP} with $D_{NP,theory}$ (Eqn. 2). At dilute PNC loadings, the D_{NP} agrees with $D_{core-shell} + D_{vehicleII}$ at $\tau_{des} \sim 50$ s (dotted line), consistent with our neat P2VP results. At higher PNC loading, D_{NP} deviates by an order of magnitude from this prediction, which might indicate a shorter τ_{des} in crowded systems.

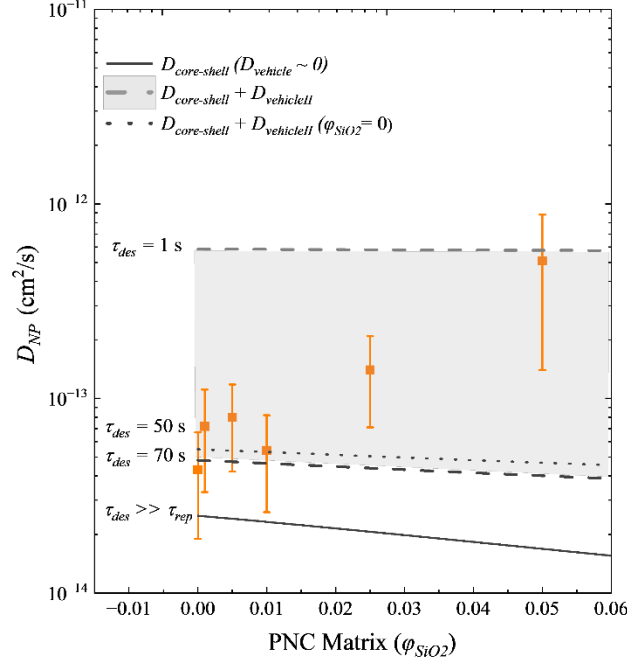


Figure 4.3: a) D_{NP} (red) as a function of matrix SiO_2 NP loading. Samples were annealed for 1-6 hours. Benchmark diffusion measurements of Al_2O_3 NPs into an unmodified P2VP matrix ($\phi_{\text{SiO}_2} = 0$) were annealed 12 – 72 hours. Line indicate $D_{\text{core-shell}}$ (solid), $D_{\text{core-shell}} + D_{\text{vehicle}}$ (dashed, upper ($\tau_{\text{des}} \sim 1$ s) and lower ($\tau_{\text{des}} \sim 70$ s)), and $D_{\text{core-shell}} + D_{\text{vehicleII}}$ (dotted, $\tau_{\text{des}} \sim 50$).

Here, Al_2O_3 NPs diffuse into SiO_2 -P2VP nanocomposites, creating Al_2O_3 - SiO_2 -P2VP nanocomposites. To account for the increasing Al_2O_3 NP concentration in the surrounding SiO_2 -P2VP nanocomposite, we define the local time-dependent concentration for Al_2O_3 NPs, $\phi_{\text{Al}_2\text{O}_3, \text{local}}$, as the normalized intensity at the FWHM of the Al^+ concentration profiles, **Figure 4.2**. This intensity is then scaled by the initial concentration of the nanoparticles in the film, **Table C.2**.

The NP surface-to-surface interparticle distance, ID , quantifies crowding as a function of particle size and loading, and is crucial for understanding polymer diffusion in nanocomposites.^{8,17,31} We explored bimodal NP ID (ID_{bi}) $< 2R_{\text{eff}}$ with $\phi_{\text{Al}_2\text{O}_3} = 0.05$ ($\phi_{\text{Al}_2\text{O}_3} = 0.01$

used in this work) and found loss of tracer diffusion and overlapping concentration profiles, indicating non-Fickian motion for samples annealed 1-7 days (see **Table C.3** and **Figure C.3**). This demonstrates the necessity of accounting for bound layer size and bimodal ID , as it hinders diffusion if the effective particle size exceeds ID_{bi} .

In a monodisperse system of spherical nanoparticles, ID is ³²

$$ID = 2r_{NP} \left[\left(\frac{\varphi_{max}}{\varphi_{NP}} \right)^{\frac{1}{3}} - 1 \right] \quad (4.6)$$

where φ_{max} is the nanoparticle volume fraction at maximum packing, φ_{NP} is the volume fraction of NPs, and r_{NP} is the radius of the nanoparticle. For this study, we extend Eqn. 6 to consider two nanoparticle sizes. Using geometric arguments involving cells that include the volume of an average particle and the excess volume per particle, we express the number-averaged ID in a bimodal-sized NP system as

$$ID_{bi} = 2(r_{cell} - \bar{r}_{NP}) = 2 \left([r_L^3 * \frac{n_L}{n_T} + r_S^3 \frac{n_S}{n_{Total}} + \frac{3}{4\pi} \psi]^{\frac{1}{3}} - \bar{r}_{NP} \right) \quad (4.7)$$

$$\psi = \frac{(\varphi_{max-bi} - \varphi_L - \varphi_S)}{\frac{\frac{4}{3}\pi r_L^3}{\varphi_L} + \frac{\frac{4}{3}\pi r_S^3}{\varphi_S}} \quad (4.8)$$

where r_{cell} is derived from the volume of a cell $\sim V_{cell}^{1/3}$; \bar{r}_{NP} is the number average radius of the two particles; r_L , n_L and φ_L are the radius, number and volume fraction of the large particles; r_S , n_S and φ_S are the radius, number and volume fraction of the small particles; n_{Total} is the total number of particles; ψ is the excess volume per particle; and φ_{max-bi} is the maximum nanoparticle volume fraction in a bimodal system. The full derivation is in **APPENDIX C**. In our experiments, the large nanoparticles are SiO₂ with $r_L = 26$ nm, the small nanoparticles are Al₂O₃ with $r_S = 6.5$ nm.

Our expression for ID_{bi} uses fixed Al_2O_3 and SiO_2 concentrations. While the concentration of SiO_2 NPs is uniform and independent of annealing time, the concentration of Al_2O_3 NPs evolves with annealing time (see Figure 2). We use the local time-dependent loading of Al_2O_3 NPs, $\varphi_{\text{Al}_2\text{O}_3, \text{local}}$, as the concentration of small nanoparticles, $\varphi_S = \varphi_{\text{Al}_2\text{O}_3, \text{local}}$. Thus, at fixed SiO_2 NP concentrations, as diffusion continues and $\varphi_{\text{Al}_2\text{O}_3, \text{local}}$ decreases, the average ID_{bi} increases, **Figure 4.4** (dashed curves).

Next, we account for the polymer bound layer associated with strong polymer-NP interactions. The effective NP radii, $r_{L, \text{eff}}$ and $r_{S, \text{eff}}$, are the nanoparticle radii plus the radius of gyration of the 158 kDa P2VP ($R_g = 10.9$ nm). The presence of bound layer also increases the NP concentrations to effective NP concentration, $\varphi_{L, \text{eff}}$, and $\varphi_{S, \text{eff}}$, and given by²⁷

$$\varphi_{L, \text{eff}} = \varphi_{\text{SiO}_2} \left(\frac{r_{L, \text{eff}}}{r_L} \right)^3 \quad (4.9)$$

$$\varphi_{S, \text{eff}} = \varphi_{\text{Al}_2\text{O}_3, \text{local}} \left(\frac{r_{S, \text{eff}}}{r_S} \right)^3 \quad (4.10)$$

Relative to nanocomposites with bare nanoparticles, ID_{bi} is smaller when the bound layer is included, **Figure 4.4** (solid lines).

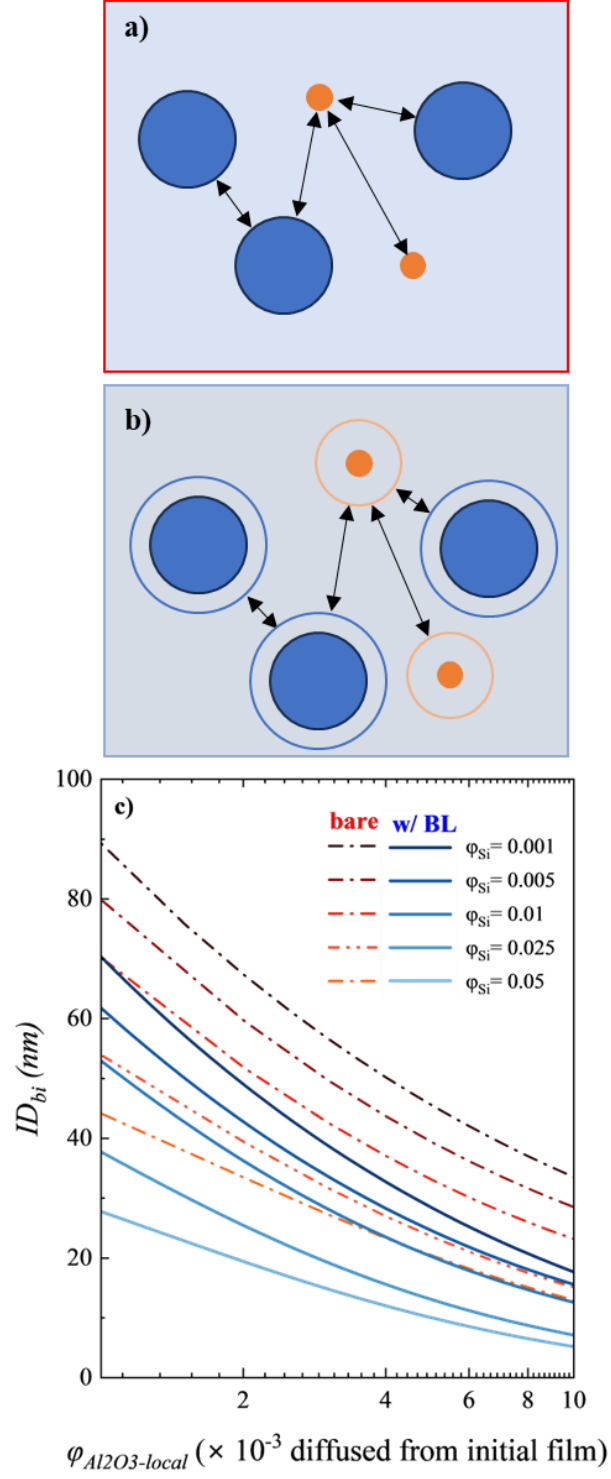


Figure 4.4: Schematic of ID_{bi} for a bimodal mixture of nanoparticles for bare nanoparticles **(a)** and for nanoparticles with bound polymer **(b)**. **(c)** ID_{bi} as a function of $\phi_{Al_2O_3,local}$. Curves correspond to fixed values of ϕ_{SiO_2} (0.001 to 0.050). Red dashed and blue solid lines correspond to bare NPs (r_L and r_S) and NPs with bound polymer layers ($r_{L,eff}$ and $r_{S,eff}$).

The Schweizer model^{25,26} best describes the diffusion of isolated particles in polymer melts, and is proven to be an accurate model for isolated Al_2O_3 NP diffusion.²⁹ **Figure 4.5** rearranges Eqn 4. 2 to isolate $D_{vehicleII}$ ($D_{NP} - D_{core-shell}$), which should be constant at a single M_w . We fit our data to an inverse power law scaling: $(D_{NP} - D_{core-shell}) \sim (ID_{bi}/2R_{eff-Al_2O_3})^{-1}$ (statistically significant, $p = 0.027 < 0.05$). This deviation from a slope of 0 indicates D_{theory} alone is not an appropriate model for crowded PNCs, and the deviation becomes more significant as the length scale of confinement approaches the NP effective size.

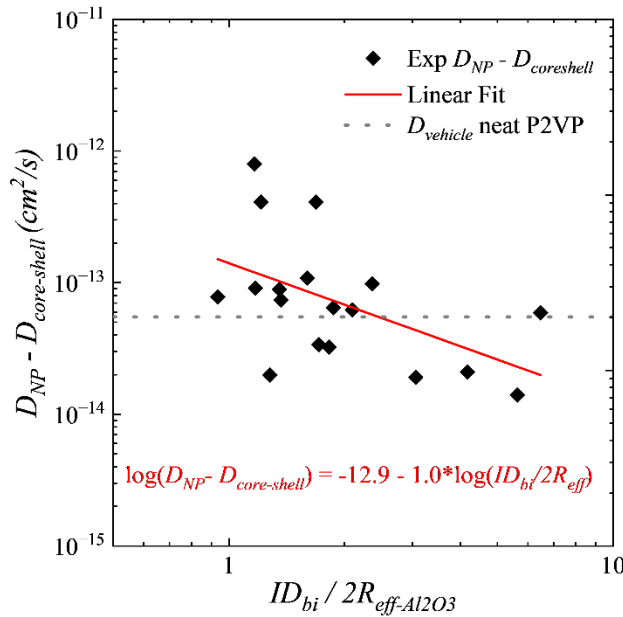


Figure 4.5: $D_{NP} - D_{core-shell}$ as a function of $ID_{bi}/2R_{eff-Al_2O_3}$ with linear regression (red) displaying an inverse power law. Dotted line is $D_{vehicle-II}$ ($\tau_{des} = 50$ s) for neat for comparison.

As the PNC becomes more crowded, the small NPs diffuse faster than in the neat polymer. This is somewhat counter intuitive, so we consider two contributions to NP diffusion to interpret this finding. One, polymer dynamics are known to slowdown in crowded PNC systems, but their effect on the bound layer τ_{des} is difficult to determine. Polymer diffusion coefficients (D_{poly}) are significantly depressed in PNCs at $ID < 2R_g$, and remain somewhat depressed even at $ID \sim 20R_g$.^{9,18,33} On a segmental scale, SiO₂ P2VP PNCs displayed interfacial α -relaxation times ~ 100 times slower in loaded systems ($\phi = 0.15$),³⁴ and a greater slowdown in systems with higher interfacial area of equivalent loading.¹² The effect of chain dynamics on desorption is implied by temperature effects on bound layer exchange timescales.³⁵ These changes in polymer dynamics may impact τ_{des} or change the vehicular regime (τ_{des} scaling) by changing $\tau_{Rouse/Rep}$, leading to faster NP diffusion. In our experiments, strongly bound P2VP on SiO₂ may decrease the free polymer available for exchange and thus alter the vehicular diffusion mechanisms that hasten NP diffusion.

Two, particle-induced chain disentanglement has been demonstrated experimentally, with $\sim 25\%$ dilation in d_t in highly-loaded small-NP systems ($\phi = 0.20$), with a commensurate decrease in the bulk viscosity.^{10,16} Notably, Tuteja et al. found that particle interactions at low loadings increase matrix viscosity, until reaching strong confinement conditions.¹⁵ In attractive octaaminophenyl polyhedral oligomeric silsesquioxan (OAPS)/P2VP ($R_{OAPS} = 1.8$ nm) systems, disentanglement was observed at high loading ($\phi \sim 27\%$), but was not observed in similarly loaded SiO₂ NP ($R_{NP} \sim 12$ nm) systems, confirming small NP size is an essential factor in chain disentanglement.¹⁴ In our system, ID_{bi} normalized by the polymer $2R_g$ is $\sim 1.7 - 10$, which is not considered strong confinement ($ID/2R_g < 1$). Furthermore, our SiO₂/P2VP PNCs ($R_{NP} = 26.2$ nm

$\gg R_g$, $\phi_{SiO_2} = 0.001-0.05$) are unlikely to reduce the viscosity due to tube dilation and thus unlikely to be the sole cause of fast Al_2O_3 NP diffusion. Regardless, given $D_{vehicleII}$ and $D_{vehicleIII}$ scale $\sim d_T$ (Eqn. 4.5, 4.6), tube dilation could play a role in faster NP diffusion in crowded NP systems.

In summary, we observed faster than expected D_{NP} for small NPs diffusing with increased crowding PNCs. To contextualize our results, we developed a geometric model for the bimodal interparticle distance, ID_{bi} , to quantify spatial confinement. Increased crowding resulted in positive deviations of D_{NP} relative to our previously measured D_{NP} into neat polymer. We attributed this increase to greater vehicular diffusion due to (1) changes in local chain dynamics or (2) chain disentanglement induced by the NPs. Overall, these ToF SIMS experiments demonstrate a method to measure NP diffusion in complex PNCs by distinguishing NPs of different sizes in a crowded system. Future work could explore the effects of polymer molecular weight, interaction strength, and particle shape on D_{NP} in crowded and complex PNC systems.

4.3 Methods

Poly(2-vinyl pyridine) (P2VP) (158 kDa, PDI = 1.06, R_g = 10.9 nm) was obtained from Scientific Polymer Products Inc. and used as received. Silica (SiO_2) nanoparticles (R_{NP-SiO_2} = 26.2 nm, PDI = 1.19) from Nissan-STL were transferred from methyl-ethyl ketone to methanol. Aluminum oxide (Al_2O_3) nanoparticles ($R_{NP-Al_2O_3}$ = 6.5 nm, PDI = 1.14) from Sigma Aldrich were prepared in a 50 g/L MeOH solution with P2VP to prevent aggregation. Trilayer samples comprised an Al_2O_3 -P2VP layer ($\phi_{Al_2O_3} = 0.01$, 200 ± 60 nm) sandwiched between two $\sim 4 \mu m$ SiO_2 -P2VP layers ($\phi_{SiO_2} = 0.001, 0.005, 0.010, 0.025, 0.050$). The assembled trilayer samples were annealed at 180 °C under vacuum (< 50 Pa) for 1-6 hours. ToF-SIMS experiments were conducted using a Tescan

S8252X FIB-SEM equipped with a Xe^+ beam. We collected and analyzed 400 frames at 30 keV and 100 pA with 1024×1024 pixel resolution on positive ion mode to extract the Al_2O_3 nanoparticle diffusion coefficient. Details are provided in previous work.²⁴

4.4 References

- (1) Bronstein, N. D.; Li, L.; Xu, L.; Yao, Y.; Ferry, V. E.; Alivisatos, A. P.; Nuzzo, R. G. Luminescent Solar Concentration with Semiconductor Nanorods and Transfer-Printed Micro-Silicon Solar Cells. *ACS Nano* **2014**, *8*, 44–53.
- (2) Kwon, N. K.; Park, C. S.; Lee, C. H.; Kim, Y. S.; Zukoski, C. F.; Kim, S. Y. Tunable Nanoparticle Stability in Concentrated Polymer Solutions On the Basis of the Temperature Dependent Solvent Quality. *Macromolecules* **2016**, *20*, 25.
- (3) Kumar, S. K.; Benicewicz, B. C.; Vaia, R. A.; Winey, K. I. 50th Anniversary Perspective: Are Polymer Nanocomposites Practical for Applications? *Macromolecules* **2017**, *50*, 714–731.
- (4) Ge, T. Scaling Perspective on Dynamics of Nanoparticles in Polymers: Length- and Time-Scale Dependent Nanoparticle-Polymer Coupling. *Macromolecules* **2023**, *56*, 3809–3837.
- (5) Bailey, E. J.; Winey, K. I. Dynamics of Polymer Segments, Polymer Chains, and Nanoparticles in Polymer Nanocomposite Melts: A Review. *Prog. Polym. Sci.* **2020**, *105*, 101242.
- (6) Mun, E. A.; Hannell, C.; Rogers, S. E.; Hole, P.; Williams, A. C.; Khutoryanskiy, V. V. On the Role of Specific Interactions in the Diffusion of Nanoparticles in Aqueous Polymer Solutions. *Langmuir* **2014**, *30*, 308–317.
- (7) Al-Obaidi, H.; Florence, A. T. Nanoparticle Delivery and Particle Diffusion in Confined and Complex Environments. *J. Drug Deliv. Sci. Technol.* **2015**, *30*, 266–277.
- (8) Lin, C.-C.; Parrish, E.; Composto, R. J. Macromolecule and Particle Dynamics in

- Confined Media. *Macromolecules* **2016**, *49*, 5755–5772.
- (9) Lin, C. C.; Parrish, E.; Composto, R. J. Macromolecule and Particle Dynamics in Confined Media. *Macromolecules* **2016**, *49*, 5755–5772.
- (10) Senses, E.; Ansar, S. M.; Kitchens, C. L.; Mao, Y.; Narayanan, S.; Natarajan, B.; Faraone, A. Small Particle Driven Chain Disentanglements in Polymer Nanocomposites. *Phys. Rev. Lett.* **2017**, *118*.
- (11) Jo, K. Il; Oh, Y.; Kim, T. H.; Bang, J.; Yuan, G.; Satija, S. K.; Sung, B. J.; Koo, J. Position-Dependent Diffusion Dynamics of Entangled Polymer Melts Nanoconfined by Parallel Immiscible Polymer Films. *ACS Macro Lett.* **2020**, *9*, 1483–1488.
- (12) Gong, S.; Chen, Q.; Moll, J. F.; Kumar, S. K.; Colby, R. H. Segmental Dynamics of Polymer Melts with Spherical Nanoparticles. *ACS Macro Lett.* **2014**, *3*, 773–777.
- (13) Thakur, V. K.; Kessler, M. R. Self-Healing Polymer Nanocomposite Materials: A Review. *Polymer (Guildf)*. **2015**, *69*, 369–383.
- (14) Cheng, S.; Xie, S.-J.; Carrillo, J.-M. Y.; Carroll, B.; Martin, H.; Cao, P.-F.; Dadmun, M. D.; Sumpter, B. G.; Novikov, V. N.; Schweizer, K. S.; Sokolov, A. P. Big Effect of Small Nanoparticles: A Shift in Paradigm for Polymer Nanocomposites. *ACS Nano* **2017**, *11*, 752–759.
- (15) Tuteja, A.; Mackay, M. E.; Hawker, C. J.; Van Horn, B. Effect of Ideal, Organic Nanoparticles on the Flow Properties of Linear Polymers: Non-Einstein-like Behavior. *Macromolecules* **2005**, *38*, 8000–8011.
- (16) Schneider, G. J.; Nusser, K.; Willner, L.; Falus, P.; Richter, D. Dynamics of Entangled Chains in Polymer Nanocomposites. *Macromolecules* **2011**, *44*, 5857–5860.

- (17) Gam, S.; Meth, J. S.; Zane, S. G.; Chi, C.; Wood, B. A.; Seitz, M. E.; Winey, K. I.; Clarke, N.; Composto, R. J. Macromolecular Diffusion in a Crowded Polymer Nanocomposite. *Macromolecules* **2011**, *44*, 3494–3501.
- (18) Lin, C.-C.; Gam, S.; Meth, J. S.; Clarke, N.; Winey, K. I.; Composto, R. J. Do Attractive Polymer–Nanoparticle Interactions Retard Polymer Diffusion in Nanocomposites? **2013**, *46*, 42.
- (19) Meth, J. S.; Gam, S.; Choi, J.; Lin, C. C.; Composto, R. J.; Winey, K. I. Excluded Volume Model for the Reduction of Polymer Diffusion into Nanocomposites. *J. Phys. Chem. B* **2013**, *117*, 15675–15683.
- (20) Gam, S.; Meth, J. S.; Zane, S. G.; Chi, C.; Wood, B. A.; Winey, K. I.; Clarke, N.; Composto, R. J. Polymer Diffusion in a Polymer Nanocomposite: Effect of Nanoparticle Size and Polydispersity. *Soft Matter* **2012**, *8*, 6512.
- (21) Xue, C.; Zheng, X.; Chen, K.; Tian, Y.; Hu, G. Probing Non-Gaussianity in Confined Diffusion of Nanoparticles. *J. Phys. Chem. Lett.* **2016**, *7*, 514–519.
- (22) Babayekhorasani, F.; Dunstan, D. E.; Krishnamoorti, R.; Conrad, J. C. Nanoparticle Diffusion in Crowded and Confined Media. *Soft Matter* **2016**, *12*, 8407–8416.
- (23) Parrish, E.; Caporizzo, M. A.; Composto, R. J. Network Confinement and Heterogeneity Slows Nanoparticle Diffusion in Polymer Gels. *J. Chem. Phys.* **2017**, *146*, 203318.
- (24) Wang, K.; Composto, R. J.; Winey, K. I. ToF-SIMS Depth Profiling to Measure Nanoparticle and Polymer Diffusion in Polymer Melts. *Macromolecules* **2023**, *56*, 2277–2285.
- (25) Carroll, B.; Bocharova, V.; Carrillo, J.-M. Y.; Kisliuk, A.; Cheng, S.; Yamamoto, U.;

- Schweizer, K. S.; Sumpter, B. G.; Sokolov, A. P. Diffusion of Sticky Nanoparticles in a Polymer Melt: Crossover from Suppressed to Enhanced Transport. *Macromolecules* **2018**, *51*, 2268–2275.
- (26) Yamamoto, U.; Carrillo, J.-M. Y.; Bocharova, V.; Sokolov, A. P.; Sumpter, B. G.; Schweizer, K. S. Theory and Simulation of Attractive Nanoparticle Transport in Polymer Melts. *Macromolecules* **2018**, *51*, 2258–2267.
- (27) Griffin, P. J.; Bocharova, V.; Middleton, L. R.; Composto, R. J.; Clarke, N.; Schweizer, K. S.; Winey, K. I. Influence of the Bound Polymer Layer on Nanoparticle Diffusion in Polymer Melts. *ACS Macro Lett.* **2016**, *5*, 1141–1145.
- (28) Park, J.; Bailey, E. J.; Composto, R. J.; Winey, K. I. Single-Particle Tracking of Nonsticky and Sticky Nanoparticles in Polymer Melts. *Macromolecules* **2020**, *53*, 3933–3939.
- (29) Wang, K.; Winey, K. I. Vehicular and Core-Shell Nanoparticle Diffusion in Entangled Polymer Melts. *Accepted*.
- (30) Bailey, E. J.; Griffin, P. J.; Composto, R. J.; Winey, K. I. Multiscale Dynamics of Small, Attractive Nanoparticles and Entangled Polymers in Polymer Nanocomposites. *Macromolecules* **2019**, *52*, 2181–2188.
- (31) Skóra, T.; Vaghefikia, F.; Fitter, J.; Kondrat, S. Macromolecular Crowding: How Shape and Interactions Affect Diffusion. *J. Phys. Chem* **2020**, *124*, 7537–7543.
- (32) Hao, T.; Riman, R. E. Calculation of Interparticle Spacing in Colloidal Systems. *J. Colloid Interface Sci.* **2006**, *297*, 374–377.
- (33) Bailey, E. J.; Riggleman, R. A.; Winey, K. I. Polymer Conformations and Diffusion through a Monolayer of Confining Nanoparticles. *Macromolecules* **2020**, *53*, 8171–8180.

- (34) Holt, A. P.; Griffin, P. J.; Bocharova, V.; Agapov, A. L.; Imel, A. E.; Dadmun, M. D.; Sangoro, J. R.; Sokolov, A. P. Dynamics at the Polymer/Nanoparticle Interface in Poly(2-Vinylpyridine)/ Silica Nanocomposites. *Macromolecules* **2014**, *47*, 1837–1843.
- (35) Jimenez, A. M.; Zhao, D.; Misquitta, K.; Jestin, J.; Kumar, S. K. Exchange Lifetimes of the Bound Polymer Layer on Silica Nanoparticles. *ACS Macro Lett.* **2019**, *8*, 166–171.

CHAPTER 5 : SUMMARY AND FUTURE WORK

5.1 Summary

Studies of NP diffusion in polymer nanocomposites (PNCs) is crucial for understanding how materials properties evolve under various processing and use conditions due to the influence of NP dispersion on mechanical, thermal, and electrical properties. Early diffusion studies predominantly employed techniques such as DLS/XPCS and RBS and laid the foundational understanding despite facing limitations in resolution, chemical sensitivity, and material diversity, especially in systems with high nanoparticle loading or complex matrix interactions. By employing ToF-SIMS, this thesis overcomes previous challenges in chemical and spatial resolution, providing diffusion coefficients across six orders of magnitude, in systems of varying NP size, particle loading, and chemistry. This experimental advancement enriches our ability to explore theoretical models of diffusion in a wider range of polymer nanocomposites and, thus, facilitates more refined designs of PNCs.

The second chapter of this dissertation establishes a reliable methodology for using ToF-SIMS to measure the diffusion of NPs or polymers within PNCs. We showcase the effectiveness of ToF-SIMS in measuring the diffusion coefficients of nanoparticles and polymers within polymer melts by employing a novel trilayer sample geometry and conducting cross-sectional analysis. Our results confirm that our ToF-SIMS results align remarkably well with established ion beam methods such as RBS and ERD, showcasing its reliability for diffusion studies in complex systems. The validated method opens new avenues for exploring diffusion phenomena

across larger length scales and more varied systems, thereby broadening the scope of future polymer or NP diffusion work.

Chapter 3 explores the diffusion mechanisms of NPs in entangled, attractive polymer melts. By investigating the diffusion behaviors of Al_2O_3 and SiO_2 nanoparticles within P2VPs of varying molecular weights (14 - 1200 kDa), we demonstrate how NP size, polymer molecular weight, and NP-polymer interactions influence diffusion dynamics. We identify two distinct diffusion modes, core-shell and vehicular, that are consistent with recent theoretical work.⁵² The SiO_2 NPs ($R_{\text{NP}} = 8.3, 26.2$ nm) consistently exhibit core-shell diffusion across all molecular weights regardless of relative polymer size, while Al_2O_3 NPs ($R_{\text{NP}} = 6.5$ nm) exhibit a transition from core-shell to vehicular diffusion as the polymer molecular weight increases. This demonstrates that the vehicular mode is present in PNCs with weaker NP-polymer attractions that facilitate faster monomer desorption times compared to core-shell diffusion in which NPs with strongly adsorbed polymers closely mimic a modified Stokes-Einstein model. We estimate the monomeric desorption time, τ_{des} for the first time experimentally as faster in Al_2O_3 NPs ($\tau_{des} = 50$ s) and slow in SiO_2 NPs ($\tau_{des} > 6000$ s). These findings allow us to quantify our understanding of the interplay of NP size, molecular weight, and bound layer desorption time on NP diffusion.

With higher particle loading, NP diffusion in PNCs exhibits unique behavior, as explored in Chapter 4. Using our methodology developed in Chapter 2, we leverage our ToF-SIMS capabilities to measure the diffusion coefficients of Al_2O_3 nanoparticles by distinguishing them from a homogenous background of larger SiO_2 NPs. A key innovation of the study is the development of a geometric model for calculating interparticle distance in a bimodal mixture of spherical nanoparticles, and accounting for particle confinement relative to the effective NP size,

which includes the bound polymer layer. Crowded environments lead to altered Al_2O_3 NP dynamics, with NPs displaying the core-shell and vehicular diffusion behavior described in Chapter 3. Markedly, through examining the change in the vehicular mode contribution, we determine that bound layer desorption times are ~ 5 x slower in confined systems compared to neat P2VP. This suggests that spatial constraints significantly alter the timescale of NP-polymer interactions and consequently NP diffusion. This study provides a framework for further investigation into the effects of nanoparticle size, shape, and spatial distribution within crowded nanocomposite systems, offering a pathway to tailor PNCs requiring precise control over NP distribution and behavior.

These findings inform the future work suggested below, where the influence of NP shape, surface chemistry, and polymer chain architecture on diffusion behavior could be explored. This future research aims to refine PNC design further by controlling these variables to optimize material properties for enhanced performance in practical applications. Such investigations will extend the foundational work of this dissertation, potentially revolutionizing PNC development through deeper insights into the intricate dynamics of NP diffusion and their practical implications.

5.2 Future Work

In this section, we outline several targeted research directions to further enhance the understanding of NP diffusion within PNCs. The proposed studies will explore the influence of nanoparticle shape, specifically examining how non-spherical nanoparticles like nanorods behave differently from their spherical counterparts in terms of diffusion dynamics. Additionally, the role of surface chemistry will be investigated to determine how variations in surface treatments affect

NP and polymer interactions and ultimately influence diffusion processes. Furthermore, the impact of polymer chemistry, molecular weight, and the processing conditions will be examined to see how they modify the interfacial dynamics between NPs and the polymer matrix. These studies will significantly contribute to the field of polymer physics by providing new insights into the fundamental processes governing nanoparticle behavior in complex material systems.

5.2.1 Nanorod Diffusion and the Vehicular Mechanism

The effect of NP curvature and shape is of great interest. Previous studies, such as those by Choi et al.⁷⁷, used elastic recoil detection (ERD) to examine nanorod behavior finding that diffusivity along the parallel direction of nanorods is faster when compared to the perpendicular direction. The application of ToF-SIMS allows for the investigation of NP curvature and shape over greater length scales and longer annealing times. This expanded scope provides a more detailed view of anisotropic diffusion of anisotropic particles. This phenomenon can provide experimental validation of MD results, which indicate that diffusion does not scale with the length increase of the nanorod.¹⁵⁵ By studying nanorods with varying aspect ratios within a single polymer system, further insights into anisotropic diffusion can be gained.

Controlling the aspect ratio of nanorods could provide new insights into the vehicular diffusion mechanism, which is currently only developed for spherical nanoparticles. Little work has been done to establish the presence of bound polymer on nanorods, with preliminary work of rotational diffusion coefficients of gold nanorods exhibiting behavior consistent with the addition of bound polyvinyl alcohol layer in water.^{77,156} Comparison to spherical NPs may give insight into the effect of curvature as well as surface area on the bound layer through varying aspect ratio. For

example, by increasing the aspect ratio to a fixed diameter, the surface to volume ratio increases and this might extend the desorption time in the vehicular mechanism. The onset of the vehicular mode in nanorod diffusion, as indicated by faster-than-SE diffusion, is particularly interesting given the two diffusion coefficients: parallel diffusion ($D_{||}$) along the nanorod length and slower perpendicular diffusion (D_{\perp}). While faster polymer desorption and the vehicular mechanism is expected to result in faster $D_{||}$ and D_{\perp} than the core-shell mechanism, the increase might be more pronounced for one or the other. Gold nanorods are available for purchase commercially. This interaction strength can be further tuned with P2VP-PS copolymer content, or through surface nanorod functionalization.

5.2.2 Tuning Interfacial Strength and Desorption Time with Random Copolymers

In neat P2VP, we detected polymer-NP desorption for a single NP-polymer interaction strength, and determined an effective desorption time, τ_{des} . However, many factors are expected to affect bound layer desorption behavior including NP radius, interaction strength, and polymer molecular weight. Our work in Chapter 3 with Al_2O_3 ($R_{NP} = 6.5$ nm) diffusing into P2VP assumes a molecular weight independent τ_{des} in accordance with a current theory of vehicle II.⁵² However, studies comparing OAPS to larger SiO_2 NPs have found a size dependency on desorption.²⁹ Investigating NP diffusion across varying degrees of NP-polymer attraction could clarify the relationship between interaction strength and monomeric desorption times τ_{des} , and effectively isolate interaction strength from other variables that influence NP diffusion

Following the experimental approach applied in Chapter 3, vehicular diffusion and τ_{des} could be explored using poly(styrene-*co*-2 vinyl pyridine) random copolymers as the matrix. Given

the non-polar nature of PS, the copolymer composition will tune the average interaction strength between the nanoparticles and polymer. Specifically, increasing the PS content will decrease the NP-polymer interaction strength. A caveat in these experiments is the risk of NP aggregation during sample preparation and annealing. Lower interaction strengths, and the expected shorter bound layer lifetimes, will result in a higher tendency for aggregation which will disrupt accurate diffusion measurements. Measuring samples at very dilute loadings ($\phi = 0.01$) will mitigate these risks, as well as shorter annealing times. Previous experiments using phenyl capped NPs or SiO₂/PS systems have witnessed aggregation and structure factor development at particle loadings > 5 vol%.²⁰ Small-angle X-ray scattering and possibly TEM on freestanding PNC films should be used to detect aggregation. Poly (styrene-*co*-2 vinyl pyridine) random copolymers are available for purchase from Polymer Source and have been purchased.

5.2.3 Tuning Interfacial Strength and Desorption Time in Various Ways

There are a wide range of experimental parameters that control the interfacial strength and desorption times in polymer nanocomposites. In addition to copolymer composition discussed above, the temperature of the diffusion experiments will alter the NP-polymer interfacial strength. Importantly, the effect of polymer molecular weight and polymer architecture (linear, branched, etc.) will impact the number of NP-polymer contacts and thus the desorption time. Also, the interfacial energy can be tuned by controlling the surface chemistry of the nanoparticles, whether by the chemical moieties, polymer brush chemistry, or polymer brush characteristics (molecular weight, grafting density, etc.) In the absence of the vehicular mechanism (strong NP-polymer interactions), the effective core-shell radius as a function of NP surface chemistry can be

understood in terms of the bound layer thickness, as previously demonstrated by Griffin et al.⁴⁵ These methods for tuning the interfacial strength have not yet been explored in the presence of the vehicular mechanism of NP diffusion.

5.2.4 Effect of Processing and Aging on Desorption Times

Previous work has established a significant effect of the casting solvent quality on NP dispersion in PNCs.¹⁵⁷ In this work, the P2VP / SiO₂ NP nanocomposites were only prepared by casting from a good solvent for P2VP, methanol. Casting from a worse solvent (or solvent mixture) would change the polymer bound layer in the solution and this collapse might persist. For example, the addition of chloroform to methanol reduces solvent quality and this could collapse the bound layer polymer conformation with the result of a smaller effective radius in the core-shell mechanism and perhaps a longer desorption time when the vehicular mechanism is applicable. Inferences can be made about the bound layer as a function of solvent quality. This line of inquiry is equally viable for both homopolymers and copolymers. Solution behavior of the polymers or copolymers, as well as the solution behavior of the nanoparticles with adsorbed polymer, can be explored with static or dynamic light scattering, and will provide valuable insights for interpreting NP diffusion results as a function of casting solvents. The effect of casting solvent will be most pronounced in systems with strong interactions, such that the nature of the bound layer is unaffected by annealing.

Long-term aging effects on nanoparticle dynamics within polymer nanocomposites are an underexplored area that merits attention. Physical aging has been observed on polymers in thin film 2D confinement, changing their permeability.¹⁵⁸ The number of polymer-NP contacts could

be probed as a function of aging by measuring the diffusion coefficients to infer either the core-shell diameter or the desorption times. For example, during the aging of PNC with strong polymer/NP interactions, the bound layer might exchange polymers with a few contacts for a smaller number of polymers with more contacts. The result might be a thinner bound layer and faster NP diffusion in the core-shell regime. When the vehicular mechanism is active, the bound layer might become more tightly bound with a corresponding increase in the desorption time. This study could be conducted by annealing the center PNC layer of our trilayer at $\sim T_g + 80^\circ \text{ K}$ for extended periods of time to allow the polymer to rearrange. Then, using our ToF SIM methodology, the annealed PNC layer can be placed in a trilayer and annealed to allow NP diffusion. A significant change in D_{NP} would indicate a change in either a) the effective NP radius or b) the desorption time through altering the core-shell or vehicular mechanisms respectively, providing insight into the aging of the bound layer.

5.3 References

- (1) Kumar, S. K.; Benicewicz, B. C.; Vaia, R. A.; Winey, K. I. 50th Anniversary Perspective: Are Polymer Nanocomposites Practical for Applications? *Macromolecules* **2017**, *50*, 714–731.
- (2) Iqbal, A.; Saeed, A.; Ul-Hamid, A. A Review Featuring the Fundamentals and Advancements of Polymer/CNT Nanocomposite Application in Aerospace Industry. *Polym. Bull.* **2021**, *78*, 539–557.
- (3) Thakur, V. K.; Kessler, M. R. Self-Healing Polymer Nanocomposite Materials: A Review. *Polymer (Guildf)*. **2015**, *69*, 369–383.
- (4) Rafique, M. M. A.; Kandare, E.; Sprenger, S. Fiber-Reinforced Magneto-Polymer Matrix Composites (FR-MPMCs) - A Review. *J. Mater. Res.* **2017**, *32*, 1020–1046.
- (5) Shah, V.; Bhaliya, J.; Patel, G. M.; Deshmukh, K. Advances in Polymeric Nanocomposites for Automotive Applications: A Review. *Polym. Adv. Technol.* **2022**, *33*, 3023–3048.
- (6) Kedzior, S. A.; Zoppe, J. O.; Berry, R. M.; Cranston, E. D. Recent Advances and an Industrial Perspective of Cellulose Nanocrystal Functionalization through Polymer Grafting. **2018**.
- (7) Mu, M.; Composto, R. J.; Clarke, N.; Winey, K. I. Minimum in Diffusion Coefficient with Increasing {MWCNT} Concentration Requires Tracer Molecules to Be Larger than Nanotubes. *Macromolecules* **2009**, *42*, 8365–8369.

- (8) Cheng, S.; Carroll, B.; Bocharova, V.; Carrillo, J. M.; Sumpter, B. G.; Sokolov, A. P. Focus: Structure and Dynamics of the Interfacial Layer in Polymer Nanocomposites with Attractive Interactions. *J. Chem. Phys.* **2017**, *146*, 203201.
- (9) Lin, C.-C.; Gam, S.; Meth, J. S.; Clarke, N.; Winey, K. I.; Composto, R. J. Do Attractive Polymer–Nanoparticle Interactions Retard Polymer Diffusion in Nanocomposites? **2013**, *46*, 42.
- (10) Lin, Y.; Li, P.; Liu, W.; Chen, J.; Liu, X.; Jiang, P.; Huang, X. Application-Driven High-Thermal-Conductivity Polymer Nanocomposites. *ACS Nano* **2024**, *18*, 3851–3870.
- (11) Bocharova, V.; Genix, A.-C.; Carrillo, J.-M. Y.; Kumar, R.; Carroll, B.; Erwin, A.; Voylov, D.; Kisliuk, A.; Wang, Y.; Sumpter, B. G.; Sokolov, A. P. Addition of Short Polymer Chains Mechanically Reinforces Glassy Poly(2-Vinylpyridine)–Silica Nanoparticle Nanocomposites. *Cite This ACS Appl. Nano Mater* **2021**, *2020*, 21.
- (12) Raemdonck, K.; Braeckmans, K.; Demeester, J.; De Smedt, S. C. Merging the Best of Both Worlds: Hybrid Lipid-Enveloped Matrix Nanocomposites in Drug Delivery. *Chem. Soc. Rev* **2014**, *43*, 444.
- (13) Parrish, E.; Caporizzo, M. A.; Composto, R. J. Network Confinement and Heterogeneity Slows Nanoparticle Diffusion in Polymer Gels. *J. Chem. Phys.* **2017**, *146*, 203318.
- (14) Merkel, T. C.; Freeman, B. D.; Spontak, R. J.; He, Z.; Pinnau, I.; Meakin, P.; Hill, A. J. Ultrapерmeable, Reverse-Selective Nanocomposite Membranes. *Science (80-.)*. **2002**, *296*, 519–522.

- (15) Yin, J.; Deng, B. Polymer-Matrix Nanocomposite Membranes for Water Treatment. *J. Memb. Sci.* **2015**, *479*, 256–275.
- (16) Duncan, T. V. Applications of Nanotechnology in Food Packaging and Food Safety: Barrier Materials, Antimicrobials and Sensors. *J. Colloid Interface Sci.* **2011**, *363*, 1–24.
- (17) Huang, J.-Y.; Li, X.; Zhou, W. Safety Assessment of Nanocomposite for Food Packaging Application. **2015**.
- (18) Beecroft, L. L.; Ober, C. K. Nanocomposite Materials for Optical Applications. *Chem. Mater.* **1997**, *9*, 1302–1317.
- (19) Barna, E.; Bommer, B.; Kürsteiner, J.; Vital, A.; Trzebiatowski, O. V; Koch, W.; Schmid, B.; Graule, T. Innovative, Scratch Proof Nanocomposites for Clear Coatings.
- (20) Buitrago, C. F.; Pressly, J. F.; Yang, A. S.; Gordon, P. A.; Riggleman, R. A.; Natarajan, B.; Winey, K. I. Creep Attenuation in Glassy Polymer Nanocomposites with Variable Polymer–Nanoparticle Interactions. *Soft Matter* **2020**, *16*, 8912–8924.
- (21) Vilay, V.; Mariatti, M.; Ahmad, Z.; Pasomsouk, K.; Todo, M. Characterization of the Mechanical and Thermal Properties and Morphological Behavior of Biodegradable Poly(L-Lactide)/Poly(ϵ -Caprolactone) and Poly(L-Lactide)/Poly(Butylene Succinate-L-Lactate) Polymeric Blends. *J. Appl. Polym. Sci.* **2009**, *114*, 1784–1792.
- (22) Mutiso, R. M.; Winey, K. I. Electrical Properties of Polymer Nanocomposites Containing Rod-like Nanofillers. *Prog. Polym. Sci.* **2015**, *40*, 63–84.

- (23) Lebedev, O. V.; Goncharuk, G. P.; Ozerin, A. N. Changes in Electrical Conductance of Polymer Composites Melts Due to Carbon Nanofiller Particles Migration. *Polym.* **2021**, *13*, 1030.
- (24) Tuteja, A.; Mackay, M. E.; Narayanan, S.; Asokan, S.; Wong, M. S. Breakdown of the Continuum Stokes-Einstein Relation for Nanoparticle Diffusion. *Nano Lett.* **2007**, *7*, 1276–1281.
- (25) Bailey, E. J.; Winey, K. I. Dynamics of Polymer Segments, Polymer Chains, and Nanoparticles in Polymer Nanocomposite Melts: A Review. *Prog. Polym. Sci.* **2020**, *105*, 101242.
- (26) Bailey, E. J.; Griffin, P. J.; Composto, R. J.; Winey, K. I. Multiscale Dynamics of Small, Attractive Nanoparticles and Entangled Polymers in Polymer Nanocomposites. *Macromolecules* **2019**, *52*, 2181–2188.
- (27) Grabowski, C. A.; Mukhopadhyay, A. Size Effect of Nanoparticle Diffusion in a Polymer Melt. *Macromolecules* **2014**, *47*, 7238–7242.
- (28) Shrestha, U. M.; Han, L.; Saito, T.; Schweizer, K. S.; Dadmun, M. D. Mechanism of Soft Nanoparticle Diffusion in Entangled Polymer Melts. **2022**, *14*, 45.
- (29) Cheng, S.; Xie, S.-J.; Carrillo, J.-M. Y.; Carroll, B.; Martin, H.; Cao, P.-F.; Dadmun, M. D.; Sumpter, B. G.; Novikov, V. N.; Schweizer, K. S.; Sokolov, A. P. Big Effect of Small Nanoparticles: A Shift in Paradigm for Polymer Nanocomposites. *ACS Nano* **2017**, *11*, 752–759.

- (30) Cruickshank, C. The Stokes-Einstein Law for Diffusion in Solution. *Proc. R. Soc. London. Ser. A, Contain. Pap. a Math. Phys. Character* **1924**, *106*, 724–749.
- (31) Kalathi, J. T.; Yamamoto, U.; Schweizer, K. S.; Grest, G. S.; Kumar, S. K. Nanoparticle Diffusion in Polymer Nanocomposites. *Phys. Rev. Lett.* **2014**, *112*, 108301.
- (32) Grabowski, C. A.; Mukhopadhyay, A. Size Effect of Nanoparticle Diffusion in a Polymer Melt. *Macromolecules* **2014**, *47*, 7238–7242.
- (33) Karatrantos, A.; Composto, R. J.; Winey, K. I.; Clarke, N. Polymer and Spherical Nanoparticle Diffusion in Nanocomposites. *J. Chem. Phys.* **2017**, *146*, 203331.
- (34) Rubinstein, M.; Colby, R. H. *Polymer Physics*; Oxford University Press, 2003.
- (35) Park, J.; Bailey, E. J.; Composto, R. J.; Winey, K. I. Single-Particle Tracking of Nonsticky and Sticky Nanoparticles in Polymer Melts. *Macromolecules* **2020**, *53*, 3933–3939.
- (36) Brochard Wyart, F.; de Gennes, P. G. Viscosity at Small Scales in Polymer Melts. *Eur. Phys. J. E Soft Matter* **2000**, *1*, 93–97.
- (37) Wang, L.; Ma, J.; Hong, W.; Zhang, H.; Lin, J. Nanoscale Diffusion of Polymer-Grafted Nanoparticles in Entangled Polymer Melts. *Macromolecules* **2020**, *53*, 8393–8399.
- (38) Sorichetti, V.; Hugouvieux, V.; Kob, W. Dynamics of Nanoparticles in Polydisperse Polymer Networks: From Free Diffusion to Hopping. *Macromolecules* **2021**, *54*, 8575–8589.
- (39) Cai, L. H.; Panyukov, S.; Rubinstein, M. Hopping Diffusion of Nanoparticles in Polymer

- Matrices. *Macromolecules* **2015**, *48*, 847–862.
- (40) Cai, L.-H.; Panyukov, S.; Rubinstein, M. Mobility of Nonsticky Nanoparticles in Polymer Liquids. *Macromolecules* **2011**, *44*, 7853–7863.
- (41) Maldonado-Camargo, L.; Rinaldi, C. Breakdown of the Stokes-Einstein Relation for the Rotational Diffusivity of Polymer Grafted Nanoparticles in Polymer Melts. *Nano Lett.* **2016**, *16*, 6767–6773.
- (42) Park, J.; Bailey, E. J.; Composto, R. J.; Winey, K. I. Single-Particle Tracking of Nonsticky and Sticky Nanoparticles in Polymer Melts. *Macromolecules* **2020**, *53*, 3933–3939.
- (43) Jimenez, A. M.; Zhao, D.; Misquitta, K.; Jestin, J.; Kumar, S. K. Exchange Lifetimes of the Bound Polymer Layer on Silica Nanoparticles. *ACS Macro Lett.* **2019**, *8*, 166–171.
- (44) Harton, S. E.; Kumar, S. K.; Yang, H.; Koga, T.; Hicks, K.; Lee, H.; Mijovic, J.; Liu, M.; Vallery, R. S.; Gidley, D. W. Immobilized Polymer Layers on Spherical Nanoparticles. *Macromolecules* **2010**, *43*, 3415–3421.
- (45) Griffin, P. J.; Bocharova, V.; Middleton, L. R.; Composto, R. J.; Clarke, N.; Schweizer, K. S.; Winey, K. I. Influence of the Bound Polymer Layer on Nanoparticle Diffusion in Polymer Melts. *ACS Macro Lett.* **2016**, *5*, 1141–1145.
- (46) Holt, A. P.; Griffin, P. J.; Bocharova, V.; Agapov, A. L.; Imel, A. E.; Dadmun, M. D.; Sangoro, J. R.; Sokolov, A. P. Dynamics at the Polymer/Nanoparticle Interface in Poly(2-Vinylpyridine)/ Silica Nanocomposites. *Macromolecules* **2014**, *47*, 1837–1843.

- (47) Holt, A. P.; Sangoro, J. R.; Wang, Y.; Agapov, A. L.; Sokolov, A. P. Chain and Segmental Dynamics of Poly(2-Vinylpyridine) Nanocomposites. **2013**.
- (48) Gong, C.; Weiblen, D.; Rende, D.; Akcora, P.; Ozisik, R. Stability of Particle Dispersion and Heterogeneous Interfacial Layers in Polymer Nanocomposites. *Polymer (Guildf)*. **2021**, 226, 123813.
- (49) Giovino, M.; Pribyl, J.; Benicewicz, B.; Kumar, S.; Schadler, L. Linear Rheology of Polymer Nanocomposites with Polymer-Grafted Nanoparticles. *Polymer (Guildf)*. **2017**, 131, 104–110.
- (50) Yang, S.; Akcora, P. Deformation of Chemically Heterogeneous Interfacial Layers of Polymer Nanocomposites. **2019**, 8, 1635–1641.
- (51) Carroll, B.; Bocharova, V.; Carrillo, J.-M. Y.; Kisliuk, A.; Cheng, S.; Yamamoto, U.; Schweizer, K. S.; Sumpter, B. G.; Sokolov, A. P. Diffusion of Sticky Nanoparticles in a Polymer Melt: Crossover from Suppressed to Enhanced Transport. *Macromolecules* **2018**, 51, 2268–2275.
- (52) Yamamoto, U.; Carrillo, J.-M. Y.; Bocharova, V.; Sokolov, A. P.; Sumpter, B. G.; Schweizer, K. S. Theory and Simulation of Attractive Nanoparticle Transport in Polymer Melts. *Macromolecules* **2018**, 51, 2258–2267.
- (53) Mun, E. A.; Hannell, C.; Rogers, S. E.; Hole, P.; Williams, A. C.; Khutoryanskiy, V. V. On the Role of Specific Interactions in the Diffusion of Nanoparticles in Aqueous Polymer Solutions. *Langmuir* **2014**, 30, 308–317.

- (54) Al-Obaidi, H.; Florence, A. T. Nanoparticle Delivery and Particle Diffusion in Confined and Complex Environments. *J. Drug Deliv. Sci. Technol.* **2015**, *30*, 266–277.
- (55) Wang, D.; Kou, R.; Choi, D.; Yang, Z.; Nie, Z.; Li, J.; Saraf, L. V.; Hu, D.; Zhang, J.; Graff, G. L.; Liu, J.; Pope, M. A.; Aksay, I. A. Ternary Self-Assembly of Ordered Metal Oxide-Graphene Nanocomposites for Electrochemical Energy Storage. *ACS Nano* **2010**, *4*, 1587–1595.
- (56) Gong, M.; Zhang, L.; Wan, P. Polymer Nanocomposite Meshes for Flexible Electronic Devices. *Prog. Polym. Sci.* **2020**, *107*, 101279.
- (57) Ge, T. Scaling Perspective on Dynamics of Nanoparticles in Polymers: Length- and Time-Scale Dependent Nanoparticle-Polymer Coupling. *Macromolecules* **2023**, *56*, 3809–3837.
- (58) Bailey, E. J.; Griffin, P. J.; Composto, R. J.; Winey, K. I. Multiscale Dynamics of Small, Attractive Nanoparticles and Entangled Polymers in Polymer Nanocomposites. *Macromolecules* **2019**, *52*, 2181–2188.
- (59) Genix, A.-C.; Bocharova, V.; Kisliuk, A.; Carroll, B.; Zhao, S.; Oberdisse, J.; Sokolov, A. P. Enhancing the Mechanical Properties of Glassy Nanocomposites by Tuning Polymer Molecular Weight. **2018**.
- (60) Holt, A. P.; Bocharova, V.; Cheng, S.; Kisliuk, A. M.; White, B. T.; Saito, T.; Uhrig, D.; Mahalik, J. P.; Kumar, R.; Imel, A. E.; Etampawala, T.; Martin, H.; Sikes, N.; Sumpter, B. G.; Dadmun, M. D.; Sokolov, A. P. Controlling Interfacial Dynamics: Covalent Bonding versus Physical Adsorption in Polymer Nanocomposites. *ACS Nano* **2016**, *10*, 6843–6852.

- (61) Cheng, S.; Holt, A. P.; Wang, H.; Fan, F.; Bocharova, V.; Martin, H.; Etampawala, T.; White, B. T.; Saito, T.; Kang, N.-G.; Dadmun, M. D.; Mays, J. W.; Sokolov, A. P. Unexpected Molecular Weight Effect in Polymer Nanocomposites. *Phys. Rev. Lett.* **2016**, *116*, 038302-1–4.
- (62) Holt, A. P.; Bocharova, V.; Cheng, S.; Kisliuk, A. M.; White, B. T.; Saito, T.; Uhrig, D.; Mahalik, J. P.; Kumar, R.; Imel, A. E.; Etampawala, T.; Martin, H.; Sikes, N.; Sumpter, B. G.; Dadmun, M. D.; Sokolov, A. P. Controlling Interfacial Dynamics: Covalent Bonding versus Physical Adsorption in Polymer Nanocomposites. **2016**.
- (63) Holt, A. P.; Griffin, P. J.; Bocharova, V.; Agapov, A. L.; Imel, A. E.; Dadmun, M. D.; Sangoro, J. R.; Sokolov, A. P. Dynamics at the Polymer/Nanoparticle Interface in Poly(2-Vinylpyridine)/ Silica Nanocomposites. *Macromolecules* **2014**, *47*, 1837–1843.
- (64) Bailey, E. J.; Griffin, P. J.; Tyagi, M.; Winey, K. I. Segmental Diffusion in Attractive Polymer Nanocomposites: A Quasi-Elastic Neutron Scattering Study. *Macromolecules* **2019**, *52*, 669–678.
- (65) Popov, I.; Carroll, B.; Bocharova, V.; Genix, A.-C.; Cheng, S.; Khamzin, A.; Kisliuk, A.; Sokolov, A. P. Strong Reduction in Amplitude of the Interfacial Segmental Dynamics in Polymer Nanocomposites. **2020**.
- (66) Lin, C. C.; Parrish, E.; Composto, R. J. Macromolecule and Particle Dynamics in Confined Media. *Macromolecules* **2016**, *49*, 5755–5772.
- (67) Roseker, W.; Hruszkewycz, S. O.; Lehmkuhler, F.; Walther, M.; Schulte-Schrepping, H.;

- Lee, S.; Osaka, T.; Strüder, L.; Hartmann, R.; Sikorski, M.; Song, S.; Robert, A.; Fuoss, P. H.; Sutton, M.; Stephenson, G. B.; Grübel, G. Towards Ultrafast Dynamics with Split-Pulse X-Ray Photon Correlation Spectroscopy at Free Electron Laser Sources. *Nat. Commun.* **2018**, *9*, 1–6.
- (68) Guo, H.; Bourret, G.; Lennox, R. B.; Sutton, M.; Harden, J. L.; Leheny, R. L. Entanglement-Controlled Subdiffusion of Nanoparticles within Concentrated Polymer Solutions. *Phys. Rev. Lett.* **2012**, *109*, 055901.
- (69) Manzo, C.; Garcia-Parajo, M. F. A Review of Progress in Single Particle Tracking: From Methods to Biophysical Insights. *Reports Prog. Phys.* **2015**, *78*, 124601.
- (70) Rose, K. A.; Molaei, M.; Boyle, M. J.; Lee, D.; Crocker, J. C.; Composto, R. J. Particle Tracking of Nanoparticles in Soft Matter. *J. Appl. Phys.* **2020**, *127*, 191101.
- (71) Kohli, I.; Mukhopadhyay, A. Diffusion of Nanoparticles in Semidilute Polymer Solutions: Effect of Different Length Scales. *Macromolecules* **2012**, *45*, 6143–6149.
- (72) Grabowski, C. A.; Adhikary, B.; Mukhopadhyay, A. Dynamics of Gold Nanoparticles in a Polymer Melt. *Appl. Phys. Lett.* **2009**, *94*, 021903.
- (73) Composto, R. J.; Kramer, E. J. Mutual Diffusion Studies of Polystyrene and Poly(Xylenyl Ether) Using Rutherford Backscattering Spectrometry. *J. Mater. Sci.* **1991**, *26*, 2815–2822.
- (74) Composto, R. J.; Walters, R. M.; Genzer, J. Application of Ion Scattering Techniques to Characterize Polymer Surfaces and Interfaces. *Mater. Sci. Eng. R Reports* **2002**, *38*, 107–180.

- (75) Cole, D. H.; Shull, K. R.; Rehn, L. E.; Baldo, P. M. RBS Analysis of the Diffusion of Nano-Size Spheres in a Polymer Matrix. *Nucl. Instruments Methods Phys. Res. Sect. B Beam Interact. with Mater. Atoms* **1998**, 136–138, 283–289.
- (76) Green, P. F.; Palmstrom, C. J.; Mayer, J. W.; Kramer, E. J. Marker Displacement Measurements of Polymer-Polymer Interdiffusion. *Macromolecules* **1985**, 18, 501–507.
- (77) Choi, J.; Cargnello, M.; Murray, C. B.; Clarke, N.; Winey, K. I.; Composto, R. J. Fast Nanorod Diffusion through Entangled Polymer Melts. *ACS Macro Lett.* **2015**, 4, 952–956.
- (78) Spool, A. M. *The Practice of TOF-SIMS: Time of Flight Secondary Ion Mass Spectrometry* - Alan M. Spool - Google Books; Momentum Press, 2016.
- (79) Mei, H.; Laws, T. S.; Terlier, T.; Verduzco, R.; Stein, G. E. Characterization of Polymeric Surfaces and Interfaces Using Time-of-Flight Secondary Ion Mass Spectrometry. *Journal of Polymer Science*. John Wiley and Sons Inc April 1, 2021, pp 1174–1198.
- (80) Zhang, A. C.; Maguire, S. M.; Ford, J. T.; Composto, R. J. Using Focused Ion Beam Time-of-Flight Secondary Ion Mass Spectrometry to Depth Profile Nanoparticles in Polymer Nanocomposites. *Microsc. Microanal.* **2023**, 29, 1557–1565.
- (81) Karar, N.; Gupta, T. K. Study of Polymers and Their Blends Using TOF-SIMS Ion Imaging. *Vacuum* **2015**, 111, 119–123.
- (82) Smentkowski, V.; Goswami, S.; Kollmer, F.; Zakel, J.; Arlinghaus, H.; Rading, D. Analysis of Thin Film Specimens Using {ToF-SIMS} Wedge Protocol, A Comparison with Depth Profiling. *Microsc. Microanal.* **2021**, 27, 1564–1565.

- (83) Sui, T.; Song, B.; Dluhos, J.; Lu, L.; Korsunsky, A. M. Nanoscale Chemical Mapping of Li-Ion Battery Cathode Material by {FIB-SEM} and {TOF-SIMS} Multi-Modal Microscopy. *Nano Energy* **2015**, *17*, 254–260.
- (84) Karar, N.; Singh, B. P.; Elizabeth, I. Analysis of Multi-Wall Carbon Nanotube Based Porous Li Battery Electrodes' Using {TOF-SIMS} Ion Imaging. *Appl. Surf. Sci.* **2015**, *349*, 644–649.
- (85) Richardin, P.; Mazel, V.; Walter, P.; Laprévotte, O.; Brunelle, A. Identification of Different Copper Green Pigments in Renaissance Paintings by Cluster-TOF-SIMS Imaging Analysis. *J. Am. Soc. Mass Spectrom.* **2011**, *22*, 1729–1736.
- (86) Prasad, A.; Salim, N. V.; Mozetič, M.; Kailas, L.; Thomas, S. Time-of-flight Secondary Ion Mass Spectrometric Analysis of Polymer Surfaces: A Review. *J. Appl. Polym. Sci.* **2022**, 52286.
- (87) Kobayashi, K.; Watanabe, H.; Maekawa, K.; Kashiwara, K.; Yamaguchi, T.; Asai, K.; Hirose, Y. Oxygen Distribution in Nickel Silicide Films Analyzed by Time-of-Flight Secondary Ion Mass Spectrometry. *Micron* **2010**, *41*, 412–415.
- (88) Lianos, L.; Quet, C.; Duc, T. M. Surface Structural Studies of Polyethylene, Polypropylene and Their Copolymers with ToF SIMS. *Surf. Interface Anal.* **1994**, *21*, 14–22.
- (89) Priebe, A.; Aribia, A.; Sastre, J.; Romanyuk, Y. E.; Michler, J. 3D High-Resolution Chemical Characterization of Sputtered Li-Rich NMC811 Thin Films Using TOF-SIMS. *Anal. Chem.* **2023**, *95*, 1074–1084.

- (90) Poleunis, C.; Médard, N.; Bertrand, P. Additive Quantification on Polymer Thin Films by ToF-SIMS: Aging Sample Effects. *Appl. Surf. Sci.* **2004**, *231–232*, 269–273.
- (91) Xie, W.; Weng, L. T.; Yeung, K. L.; Chan, C. M. Segregation of Dioctyl Phthalate to the Surface of Polystyrene Films Characterized by ToF-SIMS and XPS. *Surf. Interface Anal.* **2018**, *50*, 1302–1309.
- (92) Lu, X.; Sjövall, P.; Soenen, H. Structural and Chemical Analysis of Bitumen Using Time-of-Flight Secondary Ion Mass Spectrometry (TOF-SIMS). *Fuel* **2017**, *199*, 206–218.
- (93) Bailey, J.; Havelund, R.; Shard, A. G.; Gilmore, I. S.; Alexander, M. R.; Sharp, J. S.; Scurr, D. J. 3D ToF-SIMS Imaging of Polymer Multilayer Films Using Argon Cluster Sputter Depth Profiling. *ACS Appl. Mater. Interfaces* **2015**, *7*, 2654–2659.
- (94) Prasad, A.; Salim, N. V.; Mozetič, M.; Kailas, L.; Thomas, S. Time-of-Flight Secondary Ion Mass Spectrometric Analysis of Polymer Surfaces: A Review. *J. Appl. Polym. Sci.* **2022**, *139*.
- (95) Chan, C. M.; Weng, L. T. Surface Characterization of Polymer Blends by XPS and ToF-SIMS. *Materials (Basel)*. **2016**, *9*.
- (96) Ravati, S.; Poulin, S.; Piyakis, K.; Favis, B. D. Phase Identification and Interfacial Transitions in Ternary Polymer Blends by ToF-SIMS. *Polymer (Guildf)*. **2014**, *55*, 6110–6123.
- (97) Brennan, B.; Spencer, S. J.; Belsey, N. A.; Faris, T.; Cronin, H.; Silva, S. R.; Sainsbury, T.; Gilmore, I. S.; Stoeva, Z.; Pollard, A. J. Structural, Chemical and Electrical Characterisation

- of Conductive Graphene-Polymer Composite Films. *Appl. Surf. Sci.* **2017**, *403*, 403–412.
- (98) Chen, W. Y.; Ling, Y. C.; Chen, B. J.; Shih, H. H.; Cheng, C. H. Diffusion Study of Multi-Organic Layers in OLEDs by ToF-SIMS. *Appl. Surf. Sci.* **2006**, *252*, 6594–6596.
- (99) Chan, C. M.; Weng, L. T. Surface Characterization of Polymer Blends by XPS and ToF-SIMS. *Mater. 2016, Vol. 9, Page 655* **2016**, *9*, 655.
- (100) Fardim, P.; Gustafsson, J.; Von Schoultz, S.; Peltonen, J.; Holmbom, B. Extractives on Fiber Surfaces Investigated by XPS, ToF-SIMS and AFM. *Colloids Surfaces A Physicochem. Eng. Asp.* **2005**, *255*, 91–103.
- (101) Abd Mutalib, M.; Rahman, M. A.; Othman, M. H. D.; Ismail, A. F.; Jaafar, J. Scanning Electron Microscopy (SEM) and Energy-Dispersive X-Ray (EDX) Spectroscopy. *Membr. Charact.* **2017**, 161–179.
- (102) Sakurada, T.; Hashimoto, S.; Tsuchiya, Y.; Tachibana, S.; Suzuki, M.; Shimizu, K. Lateral Resolution of EDX Analysis with Ultra Low Acceleration Voltage SEM. *sasj.jp* T Sakurada, S Hashimoto, Y Tsuchiya, S Tachibana, M Suzuki, K Shimizu *Journal Surf. Anal.* **2005**•*sasj.jp* **2005**, *12*.
- (103) Kubicek, M.; Holzlechner, G.; Opitz, A. K.; Larisegger, S.; Hutter, H.; Fleig, J. A Novel ToF-SIMS Operation Mode for Sub 100 Nm Lateral Resolution: Application and Performance. *Appl. Surf. Sci.* **2014**, *289*, 407.
- (104) Moffitt, C. Fundamental Aspects of XPS and the Development of XPS Imaging. *Micros. Today* **2011**, *19*, 16–21.

- (105) Powell, C. J.; Jablonski, A. Surface Sensitivity of X-Ray Photoelectron Spectroscopy. *Nucl. Instruments Methods Phys. Res. Sect. A Accel. Spectrometers, Detect. Assoc. Equip.* **2009**, *601*, 54–65.
- (106) Watts, J. F.; Wolstenholme, J. An Introduction to Surface Analysis by XPS and AES. *An Introd. to Surf. Anal. by XPS AES* **2003**.
- (107) Chung, Y.; Pak, C.; Park, G.-S.; Jeon, W. S.; Kim, J.-R.; Lee, Y.; Chang, H.; Seung, D. Understanding a Degradation Mechanism of Direct Methanol Fuel Cell Using {TOF-SIMS} and {XPS}. *J. Phys. Chem. C Nanomater. Interfaces* **2008**, *112*, 313–318.
- (108) Wang, K.; Composto, R. J.; Winey, K. I. ToF-SIMS Depth Profiling to Measure Nanoparticle and Polymer Diffusion in Polymer Melts. *Macromolecules* **2023**.
- (109) Harrison, E. T.; Peczonczyk, S. L.; Sharafi, A.; Wujcik, K. H.; Drews, A.; Simko, S. Surface Characterization of Battery Electrode/Electrolyte Materials Using {XPS} and {ToF-SIMS}. *Meet. abstr.* **2019**, *MA2019-01*, 521.
- (110) Balazs, A. C.; Emrick, T.; Russell, T. P. Nanoparticle Polymer Composites: Where Two Small Worlds Meet. *Science (80-.)*. **2006**, *314*, 1107–1110.
- (111) Mills, P. J.; Green, P. F.; Palmstrøm, C. J.; Mayer, J. W.; Kramer, E. J. Polydispersity Effects on Diffusion in Polymers: Concentration Profiles of d-Polystyrene Measured by Forward Recoil Spectrometry. *J. Polym. Sci. Part B Polym. Phys.* **1986**, *24*, 1–9.
- (112) Green, P. F.; Kramer, E. J. Matrix Effects on the Diffusion of Long Polymer Chains. *Macromolecules* **1986**, *19*, 1108–1114.

- (113) Mackay, M. E.; Dao, T. T.; Tuteja, A.; Ho, D. L.; van Horn, B.; Kim, H.-C.; Hawker, C. J. Nanoscale Effects Leading to Non-Einstein-like Decrease in Viscosity. *Nat. Mater.* **2003**, *2*, 762–766.
- (114) Composto, R. J.; Mayer, J. W.; Kramer, E. J.; White, D. M. Fast Mutual Diffusion in Polymer Blends. *Phys. Rev. Lett.* **1986**, *57*, 1312–1315.
- (115) Composto, R. J.; Kramer, E. J.; White, D. M. Mutual Diffusion in the Miscible Polymer Blend Polystyrene/Poly(Xylenyl Ether). *Macromolecules* **1988**, *21*, 2580–2588.
- (116) Barrat, J.-L.; Fredrickson, G. H. Diffusion of a Symmetric Block Copolymer in a Periodic Potential. *Macromolecules* **1991**, *24*, 6378–6383.
- (117) Gam, S.; Meth, J. S.; Zane, S. G.; Chi, C.; Wood, B. A.; Seitz, M. E.; Winey, K. I.; Clarke, N.; Composto, R. J. Macromolecular Diffusion in a Crowded Polymer Nanocomposite. *Macromolecules* **2011**, *44*, 3494–3501.
- (118) Shrestha, U. M.; Han, L.; Saito, T.; Schweizer, K. S.; Dadmun, M. D. Mechanism of Soft Nanoparticle Diffusion in Entangled Polymer Melts. *Macromolecules* **2020**, *53*, 7580–7589.
- (119) Imel, A. E.; Rostom, S.; Holley, W.; Baskaran, D.; Mays, J. W.; Dadmun, M. D. The Tracer Diffusion Coefficient of Soft Nanoparticles in a Linear Polymer Matrix. *RSC Adv.* **2017**, *7*, 15574–15581.
- (120) Jo, K. Il; Oh, Y.; Kim, T. H.; Bang, J.; Yuan, G.; Satija, S. K.; Sung, B. J.; Koo, J. Position-Dependent Diffusion Dynamics of Entangled Polymer Melts Nanoconfined by Parallel

- Immiscible Polymer Films. *ACS Macro Lett.* **2020**, *9*, 1483–1488.
- (121) Lin, C.-C.; Griffin, P. J.; Chao, H.; Hore, M. J. A.; Ohno, K.; Clarke, N.; Riggleman, R. A.; Winey, K. I.; Composto, R. J. Grafted Polymer Chains Suppress Nanoparticle Diffusion in Athermal Polymer Melts. *J. Chem. Phys.* **2017**, *146*, 203332.
- (122) Mills, P. J.; Green, P. F.; Palmstrom, C. J.; Mayer, J. W.; Kramer, E. J. Analysis of Diffusion in Polymers by Forward Recoil Spectrometry. *Appl. Phys. Lett.* **1998**, *45*, 957.
- (123) Martín, J.; Hernández-Vélez, M.; de Abril, O.; Luna, C.; Muñoz-Martin, A.; Vázquez, M.; Mijangos, C. Fabrication and Characterization of Polymer-Based Magnetic Composite Nanotubes and Nanorods. *Eur. Polym. J.* **2012**, *48*, 712–719.
- (124) Bailey, E. J.; Griffin, P. J.; Composto, R. J.; Winey, K. I. Characterizing the Areal Density and Desorption Kinetics of Physically Adsorbed Polymer in Polymer Nanocomposite Melts. *Macromolecules* **2020**, *53*, 2744–2753.
- (125) Fit plane to 3-D point cloud - MATLAB pcfitplane
<https://www.mathworks.com/help/vision/ref/pcfitplane.html> (accessed Jun 22, 2022).
- (126) Fischler, M. A.; Bolles, R. C. Random Sample Consensus. *Commun. ACM* **1981**, *24*, 381–395.
- (127) Belu, A. M.; Davies, M. C.; Newton, J. M.; Patel, N. TOF-SIMS Characterization and Imaging of Controlled-Release Drug Delivery Systems. *Anal. Chem.* **2000**, *72*, 5625–5638.
- (128) Méar, F.; Coillot, D.; Podor, R.; Montagne, L. Self-Healing Nanocomposites: Role and

- Activation of Inorganic Moieties and Hybrid Nanophases. In *{Self-Healing} at the Nanoscale*; CRC Press, 2011; pp 188–223.
- (129) Mallakpour, S.; Naghdi, M. {Polymer/SiO₂} Nanocomposites: Production and Applications. *Prog. Mater. Sci.* **2018**, *97*, 409–447.
- (130) Young, W. W.; Katsumata, R. Intermediate Polymer Relaxation Explains the Anomalous Rheology of Nanocomposites with Ultrasmall Attractive POSS Nanoparticles. *ACS Polym. Au* **2023**, *3*, 466–474.
- (131) Lin, C.-C.; Parrish, E.; Composto, R. J. Macromolecule and Particle Dynamics in Confined Media. *Macromolecules* **2016**, *49*, 5755–5772.
- (132) Papakonstantopoulos, G. J.; Yoshimoto, K.; Doxastakis, M.; Nealey, P. F.; De Pablo, J. J. Local Mechanical Properties of Polymeric Nanocomposites. *Phys. Rev. E - Stat. Nonlinear, Soft Matter Phys.* **2005**, *72*, 031801-031801–031806.
- (133) Cheng, S.; Carroll, B.; Bocharova, V.; Carrillo, J.-M.; Sumpter, B. G.; Sokolov, A. P.; Carrillo, J.-M. Y. Perspective: Outstanding Theoretical Questions in Polymer-Nanoparticle Hybrids. *J. Chem. Phys.* **2017**, *146*, 203201.
- (134) Liu, J.; Cao, D.; Zhang, L. Molecular Dynamics Study on Nanoparticle Diffusion in Polymer Melts: A Test of the Stokes-Einstein Law. *J. Phys. Chem. C* **2008**, *112*, 6653–6661.
- (135) Mendez, N. F.; Dhara, D.; Zhang, Q.; Narayanan, S.; Schadler, L. S.; Müller, A. J.; Kumar, S. K. Nanoparticle Diffusion in Miscible Polymer Nanocomposite Melts. *Macromolecules*

2023, 56, 4658–4668.

- (136) Kwon, N. K.; Park, C. S.; Lee, C. H.; Kim, Y. S.; Zukoski, C. F.; Kim, S. Y. Tunable Nanoparticle Stability in Concentrated Polymer Solutions On the Basis of the Temperature Dependent Solvent Quality. *Macromolecules* **2016**, 20, 25.
- (137) Jin, J.; Wang, X.; Wick, C. D.; Dang, L. X.; Miller, J. D. Silica Surface States and Their Wetting Characteristics. <https://doi.org/10.1680/jsuin.19.00053> **2020**, 8, 145–157.
- (138) Watcharenwong, A.; Saijaioup, N.; Bailuang, Y.; Kajitvichyanukul, P. Morphology and Wettability of Nanoporous Aluminium Oxide Film Prepared by Anodization. *Key Eng. Mater.* **2017**, 737, 174–178.
- (139) Bronstein, N. D.; Li, L.; Xu, L.; Yao, Y.; Ferry, V. E.; Alivisatos, A. P.; Nuzzo, R. G. Luminescent Solar Concentration with Semiconductor Nanorods and Transfer-Printed Micro-Silicon Solar Cells. *ACS Nano* **2014**, 8, 44–53.
- (140) Mun, E. A.; Hannell, C.; Rogers, S. E.; Hole, P.; Williams, A. C.; Khutoryanskiy, V. V. On the Role of Specific Interactions in the Diffusion of Nanoparticles in Aqueous Polymer Solutions. *Langmuir* **2014**, 30, 308–317.
- (141) Senses, E.; Ansar, S. M.; Kitchens, C. L.; Mao, Y.; Narayanan, S.; Natarajan, B.; Faraone, A. Small Particle Driven Chain Disentanglements in Polymer Nanocomposites. *Phys. Rev. Lett.* **2017**, 118.
- (142) Gong, S.; Chen, Q.; Moll, J. F.; Kumar, S. K.; Colby, R. H. Segmental Dynamics of Polymer Melts with Spherical Nanoparticles. *ACS Macro Lett.* **2014**, 3, 773–777.

- (143) Tuteja, A.; Mackay, M. E.; Hawker, C. J.; Van Horn, B. Effect of Ideal, Organic Nanoparticles on the Flow Properties of Linear Polymers: Non-Einstein-like Behavior. *Macromolecules* **2005**, *38*, 8000–8011.
- (144) Meth, J. S.; Gam, S.; Choi, J.; Lin, C. C.; Composto, R. J.; Winey, K. I. Excluded Volume Model for the Reduction of Polymer Diffusion into Nanocomposites. *J. Phys. Chem. B* **2013**, *117*, 15675–15683.
- (145) Gam, S.; Meth, J. S.; Zane, S. G.; Chi, C.; Wood, B. A.; Winey, K. I.; Clarke, N.; Composto, R. J. Polymer Diffusion in a Polymer Nanocomposite: Effect of Nanoparticle Size and Polydispersity. *Soft Matter* **2012**, *8*, 6512.
- (146) Xue, C.; Zheng, X.; Chen, K.; Tian, Y.; Hu, G. Probing Non-Gaussianity in Confined Diffusion of Nanoparticles. *J. Phys. Chem. Lett.* **2016**, *7*, 514–519.
- (147) Babayekhorasani, F.; Dunstan, D. E.; Krishnamoorti, R.; Conrad, J. C. Nanoparticle Diffusion in Crowded and Confined Media. *Soft Matter* **2016**, *12*, 8407–8416.
- (148) Schneider, G. J.; Nusser, K.; Willner, L.; Falus, P.; Richter, D. Dynamics of Entangled Chains in Polymer Nanocomposites. *Macromolecules* **2011**, *44*, 5857–5860.
- (149) Bailey, E. J.; Riggleman, R. A.; Winey, K. I. Polymer Conformations and Diffusion through a Monolayer of Confining Nanoparticles. *Macromolecules* **2020**, *53*, 8171–8180.
- (150) Wang, K.; Winey, K. I. Vehicular and Core-Shell Nanoparticle Diffusion in Entangled Polymer Melts. Submitted.

- (151) Tonelli, A. E. Conformational Characteristics of Poly(2-Vinylpyridine). *Macromolecules* **1985**, *18*, 2579–2583.
- (152) Sko, T.; Vaghefikia, F.; Fitter, rg; Kondrat, S. Macromolecular Crowding: How Shape and Interactions Affect Diffusion. *J. Phys. Chem* **2023**, *2020*, 19.
- (153) Hao, T.; Riman, R. E. Calculation of Interparticle Spacing in Colloidal Systems. *J. Colloid Interface Sci.* **2006**, *297*, 374–377.
- (154) Brouwers, H. J. H. Particle-Size Distribution and Packing Fraction of Geometric Random Packings. *Phys. Rev. E - Stat. Nonlinear, Soft Matter Phys.* **2006**, *74*, 031309.
- (155) Karatrantos, A.; Composto, R. J.; Winey, K. I.; Clarke, N. Nanorod Diffusion in Polymer Nanocomposites by Molecular Dynamics Simulations. *Macromolecules* **2019**, *52*, 2513–2520.
- (156) Asgari, N.; Baaske, M. D.; Orrit, M. Burst-by-Burst Measurement of Rotational Diffusion at Nanosecond Resolution Reveals Hot-Brownian Motion and Single-Chain Binding. *ACS Nano* **2023**, *17*, 12684–12692.
- (157) Jouault, N.; Zhao, D.; Kumar, S. K. Role of Casting Solvent on Nanoparticle Dispersion in Polymer Nanocomposites. **2014**.
- (158) Murphy, T. M.; Langhe, D. S.; Ponting, M.; Baer, E.; Freeman, B. D.; Paul, D. R. Physical Aging of Layered Glassy Polymer Films via Gas Permeability Tracking. *Polymer (Guildf)*. **2011**, *52*, 6117–6125.

- (159) Karen, A.; Ito, K.; Kubo, Y. {TOF-SIMS} Analysis of Lithium Air Battery Discharge Products Utilizing Gas Cluster Ion Beam Sputtering for Surface Stabilization. *Surf. Interface Anal.* **2014**, *46*, 344–347.
- (160) Foley, J. D.; Fischler, M. A.; Bolles, R. C. Graphics and Image Processing Random Sample Consensus: A Paradigm for Model Fitting with Apphcatlons to Image Analysis and Automated Cartography. **1981**.
- (161) Point Cloud Processing - MATLAB & Simulink
<https://www.mathworks.com/help/vision/point-cloud-processing.html> (accessed May 6, 2024).
- (162) Wang, X.; Tilley, R. D.; Watkins, J. J. Simple Ligand Exchange Reactions Enabling Excellent Dispersibility and Stability of Magnetic Nanoparticles in Polar Organic, Aromatic, and Protic Solvents. *Langmuir* **2014**, *30*, 1514–1521.
- (163) Cook, E.; Labiento, G.; Chauhan, B. P. S. Fundamental Methods for the Phase Transfer of Nanoparticles. *Molecules* **2021**, *26*.

APPENDIX A : SUPPORTING INFORMATION FOR CHAPTER 2

A.1 NP and Polymer Characterization

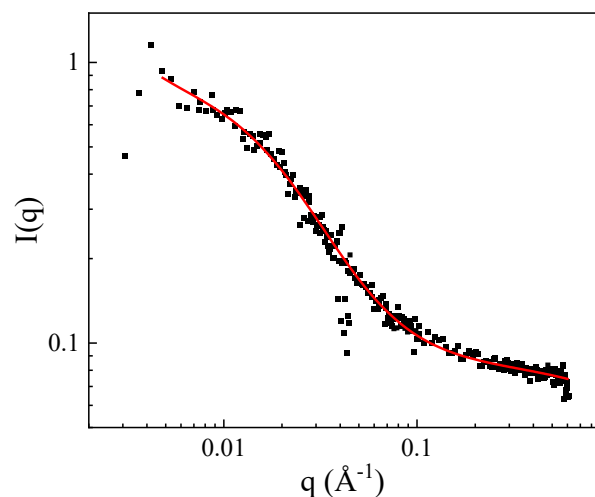


Figure A.1: SANS data of 100 kg/mol P2VP in methanol solvent fit to a Gaussian polymer chain model results in an R_g of 7.2 nm and PDI of 1.34.

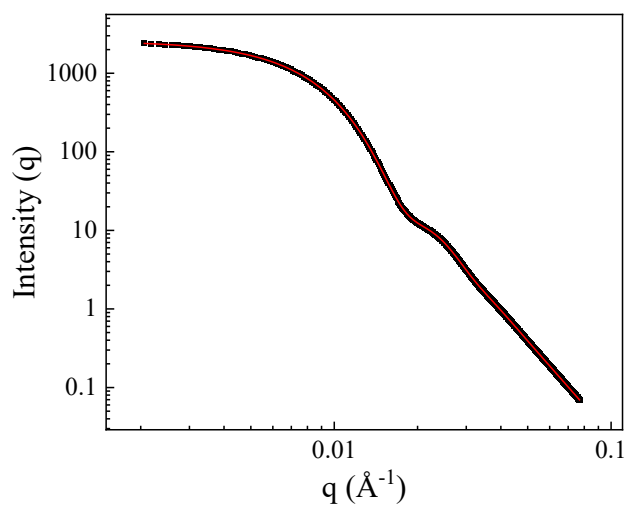


Figure A.2: SAXS data displaying the form factor of the Nissan-STL NP system fit to the hard sphere model (red). Results in $R_{NP} = 26.1$ nm with a size dispersity of 1.19.

A.2 Pixel Resolution and Depth Measurements

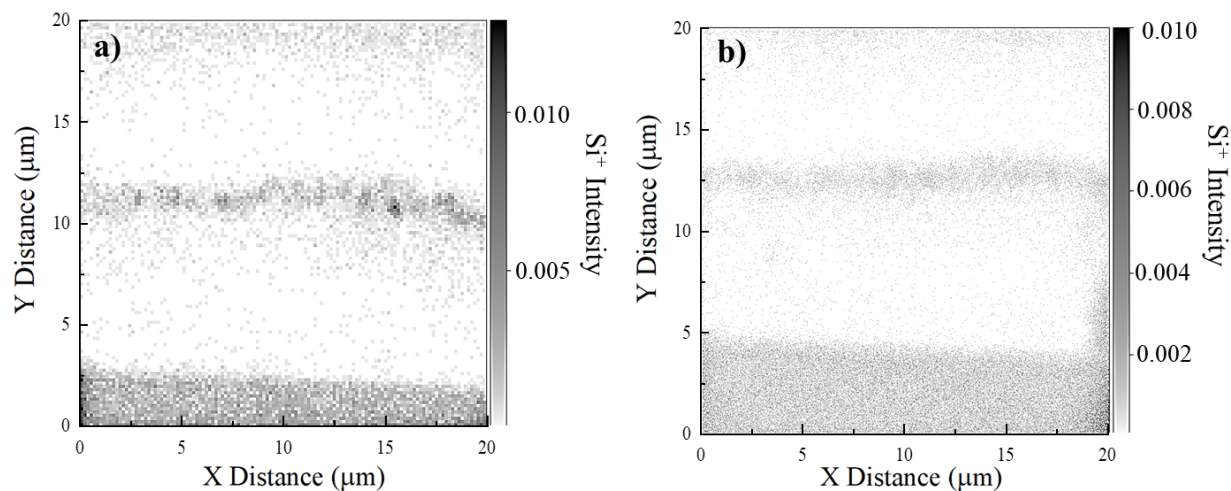


Figure A.3 : **a)** 15 vol% NP sample (3 day anneal) taken with 256×256 pixel resolution with a rate of 4 mins/300 frames (pixel size = 156 nm post 2×2 binning). **b)** Same sample taken at 1024×1024 pixel resolution at a rate of 52 mins/300 frames (pixel size = 39 nm post 2×2 binning).

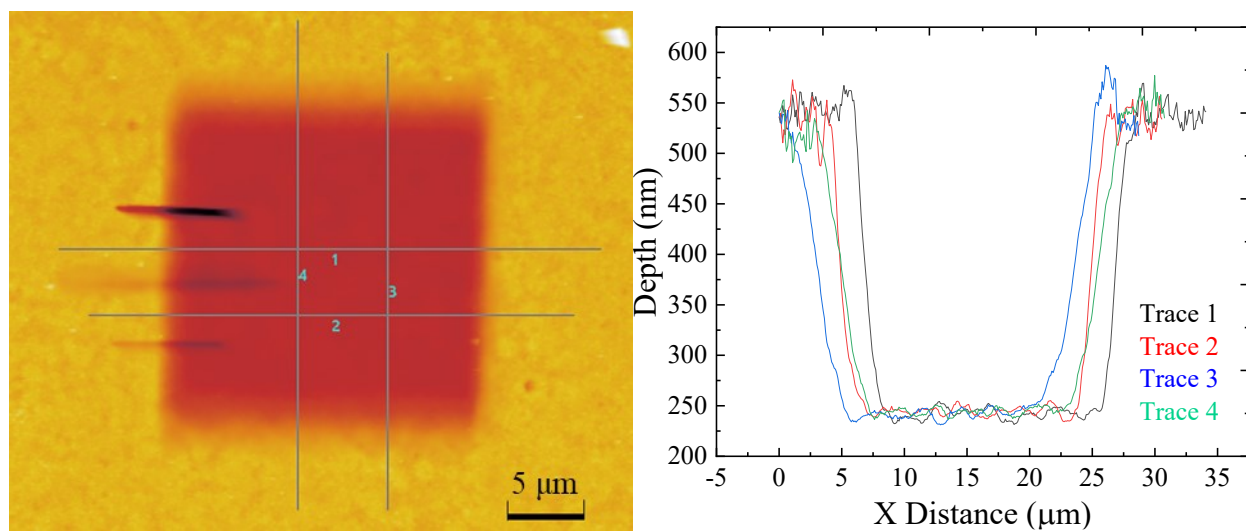


Figure A.4: a) AFM image of a PNC film of 500 nm thickness after 300 frames of ToF-SIMS collection (100 pA, 30 keV accelerating voltage, 20 μm FoV, 512 x 512 pixels post 2 \times 2 binning). b) Depth of traces shown in (a) with an average depth of 280 ± 5.3 nm.

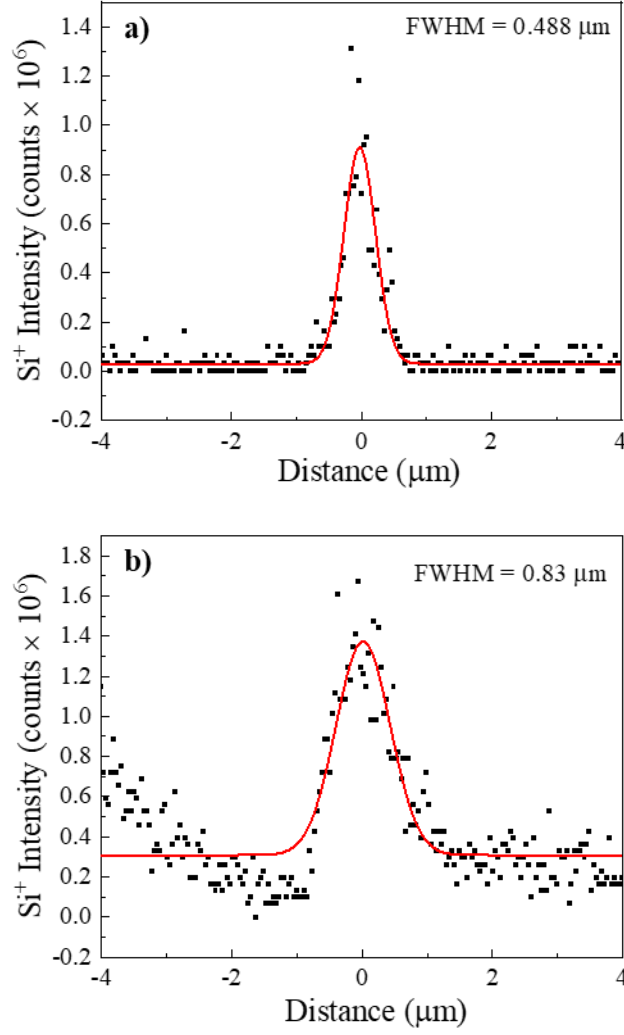


Figure A.5: **a)** The Si^+ concentration profile of an unannealed trilayer sample measured with a 10 pA beam current displays a FWHM of 0.49 μm . **b)** The same sample measured with a 300 pA beam current has a FWHM of 0.83 μm . Si^+ concentration profiles were integrated after the tilt correction described in the manuscript.

A.3 Fit Quality (R^2)

Table A.1: Table summarizing quality of fits (R^2) for **Figure 2.4** and **Figure 2.5**. Best fit is bolded.

Volume Fraction	Days Annealed	Fit	$D_{NP} (*10^{-14} \text{ cm}^2/\text{s})$	R^2
0.10	1 day	BEST	2.2	0.992
0.10	1 day	$D_{NP}+\delta$	2.5	0.988
0.10	1 day	$D_{NP}-\delta$	1.9	0.989
0.05	3 day	BEST	2.0	0.926
0.10	3 day	BEST	1.9	0.990
0.10	3 day	$D_{NP}+\delta$	2.2	0.982
0.10	3 day	$D_{NP}-\delta$	1.6	0.988
0.15	3 day	BEST	0.36	0.969
0.10	5 day	BEST	2.5	0.993
0.10	5 day	$D_{NP}+\delta$	2.8	0.991
0.10	5 day	$D_{NP}-\delta$	2.2	0.986

A.4 Theoretical D_{NP} Calculations

D_{NP} for Comparison

Given we are using the same P2VP-SiO₂ attractive surface chemistry as Griffin et al.⁴⁵ and our particles fall in the size regime described by the hydrodynamic Stokes-Einstein equation ($R_{NP} = 26.1 \text{ nm} \gg R_g = 7.2 \text{ nm}$), we assume Stokes-Einstein behavior where

$$D_{NP} = \frac{k_B T}{6\pi\eta_{PNC}R_{eff}} \quad (\text{A.1})$$

where k_B is the Boltzmann constant, T is the annealing temperature in Kelvin, η_{PNC} is the PNC viscosity in Pa·s, and R_{eff} is the radius of the particle including the strongly bound layer, $R_{eff} = R_g + R_{NP} = 7.2 \text{ nm} + 26.1 \text{ nm} = 33.3 \text{ nm}$.

We account for the bound layer increasing the effective volume fraction of NP in the system by defining an effective volume fraction for the system during diffusion, φ_{eff} , as

$$\varphi_{eff} = \varphi_{NP} \left(\frac{R_{eff}}{R_{NP}} \right)^3 \quad (\text{A.2})$$

In Griffin et al.⁴⁵, where the initial film has $\varphi_{NP} = 0.1$, a $\varphi_{NP} = 0.025$ (the dilute limit) is instead used to estimate the true concentration of the entire system as NPs diffuse outwards from the initial film. Since this limit is set somewhat arbitrarily, we use the initial $\varphi_{NP} = 0.1$ from the unannealed time and two lower values ($\varphi_{NP} = 0.01, 0.025$) to account for the NP dilution during the experiment and to calculate φ_{eff} .

We then use these φ_{eff} values to account for the increase in viscosity due to the addition of NPs, where $\eta_{poly} = 3 \times 10^3 \text{ Pa}\cdot\text{s}$ for 100 kg/mol P2VP at 180°C.⁴⁵

$$\eta_{PNC} = \eta_{poly} (1 + 2.5\varphi_{eff} + 6.2\varphi_{eff}^2) \quad (\text{A.3})$$

Using Eqn. A.1, we calculate the expected D_{NP} for $R_{NP} = 26.1 \text{ nm}$ given an estimated φ_{NP} .

Table A.2: Expected D_{NP} range for $R_{NP} = 26.1$ nm using Eqn. S1-3 with ϕ_{eff} and η_{PNC} values.

Estimated ϕ_{NP}	ϕ_{eff}	η_{PNC} ($\times 10^3$ Pa·s)	Expected D_{NP} ($\times 10^{-14}$ cm ² /s)
0.01	0.0204	3.08	3.3
0.025	0.051	3.43	2.9
0.1 (initial)	0.204	5.24	1.9

A.5 Deuterated Polymer ToF-SIMS Images and Measurements

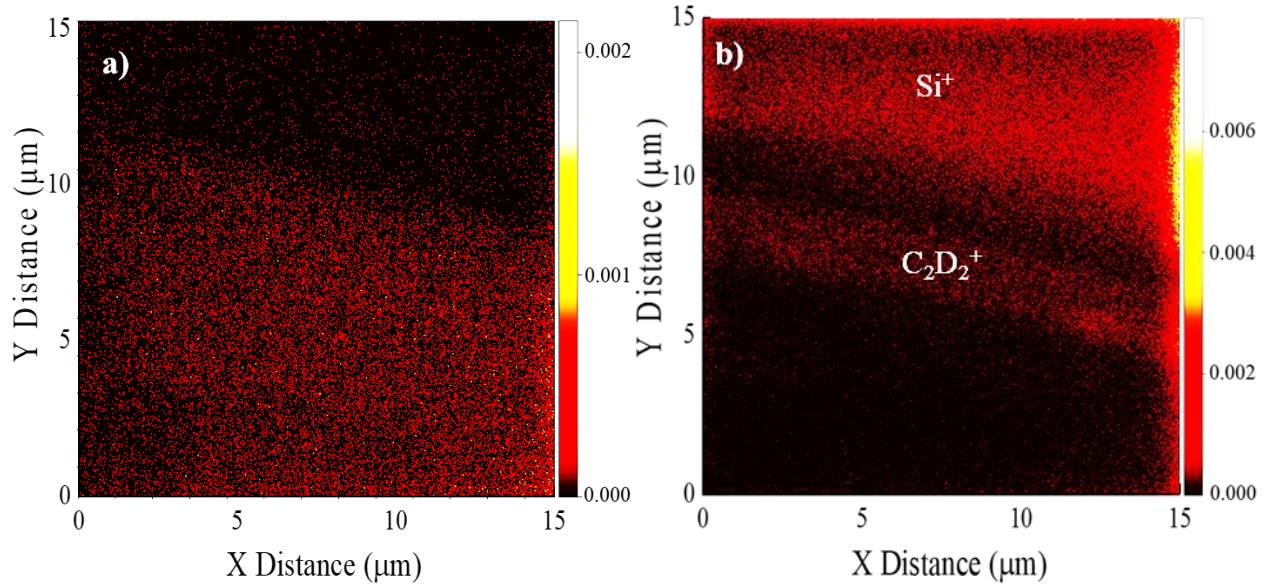


Figure A.6: **a)** 2D C^+ ($m/q = 12$) concentration map and **b)** $C_2D_2^+/Si^+$ ($m/q = 28$) composition maps from a single data set (423 k – 450 k dPS/PS, annealed for 1 day at 174°C). High $m/q = 28$ signal that is commensurate with high $m/q = 12$ signal indicates the location of dPS and the

presence of $C_2D_2^+$ ions. Conversely, high $m/q = 28$ signal and to low intensity in C^+ indicate Si^+ ions from the Si wafer.

Table A.3: D_{dps} from individual fits and their respective R^2 values, for various annealing times.

M_w	Annealing Time	$D_{PS} (cm^2/s)$	R^2
450k-423k hPS/dPS	1 d	2.8×10^{-14}	0.923
450k-423k hPS/dPS	3 d	3.0×10^{-14}	0.811
65k-69k hPS/dPS	1 hr	1.0×10^{-12}	0.939
65k-69k hPS/dPS	3 hr	1.3×10^{-12}	0.440

A.6 D_{poly} Comparison to Literature Values

D_{dPS} for Comparison

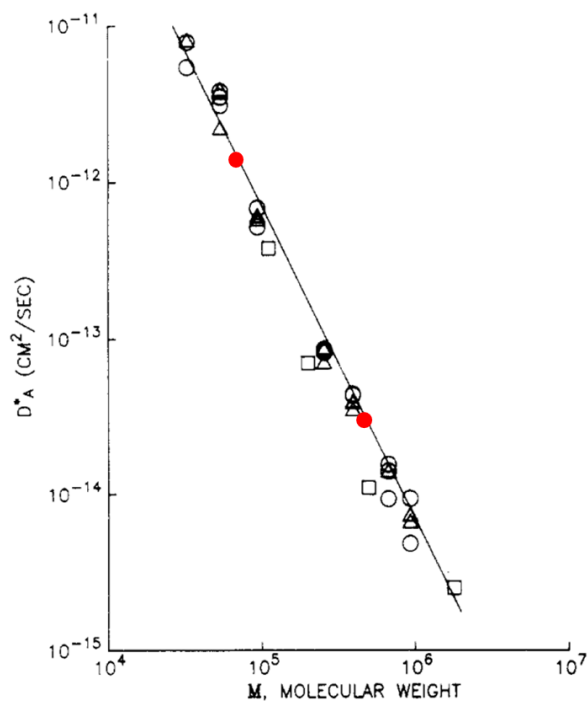


Figure A.7 : Data (black) reproduction from Green et al. for the tracer diffusion coefficient of dPS into PS ($M_w = 2 \times 10^7$) as a function of dPS molecular weight. Their linear fit corresponds to $D_{\text{dPS}} = 0.008M^{-2}$. The results from this study using ToF-SIMS are shown in red.

A.7 References

- (1) Griffin, P. J.; Bocharova, V.; Middleton, L. R.; Composto, R. J.; Clarke, N.; Schweizer, K. S.; Winey, K. I. Influence of the Bound Polymer Layer on Nanoparticle Diffusion in Polymer Melts. *ACS Macro Lett.* 2016, 5, 1141–1145.
- (2) Green, P. F.; Palmstrom, C. J.; Mayer, J. W.; Kramer, E. J. Marker Displacement Measurements of Polymer-Polymer Interdiffusion. *Macromolecules* 1985, 18, 501–507.

APPENDIX B : SUPPORTING INFORMATION FOR CHAPTER 3

B.1 Processing Conditions and Data Fits

Table B.1: Molecular weight characterization of poly(2-vinylpyridine) and calculated R_g . All samples were measured with tetrahydrofuran as the carrier solvent and normalized using a polystyrene standard. The radius of gyration was calculated using Rubinstein and Colby.³⁴

M_w (kg/mol)	M_n (kg/mol)	PDI	Calculated R_g (nm)
14.0	13.7	1.04	3.2
41.0	40.8	1.01	5.5
158	149	1.06	10.9
219	197	1.11	12.8
310	290	1.07	15.3
474	446	1.06	18.8
1,220*	1100*	1.11	30.2

*Indicates values provided by the supplier.

Table B.2 : Spincoating conditions to create poly(2-vinylpyridine) films. Parameters include weight-averaged molecular weights, solution concentrations, spincoating speeds, and spin times to create the ~4 μm thick P2VP matrix films.

M_w (kg/mol)	Solution Concentration (g/L)	Spin Speed (rpm)	Spin time (sec)
14.0	450	1000	120
41.0	300	1000	120
158	250	1500	90
219	180	1500	60
310	170	2000	60
474	150	2000	60
1,220	50	1500	60

Table B.3: Spincoating conditions to create polymer nanocomposite films. Parameters include weight-averaged molecular weights, solution concentrations, spincoating speeds, and spin times to create thin PNC center layers (200 ± 60 nm).

M_w (kg/mol)	Solution Concentration (g/L)	Spin Speed (rpm)	Spin time (sec)
14.0	70	1500	60
41.0	60	2000	60
158	50	2000	60
219	40	2000	60
310	35	2000	60
474	30	2000	60
1,220	20	2000	60

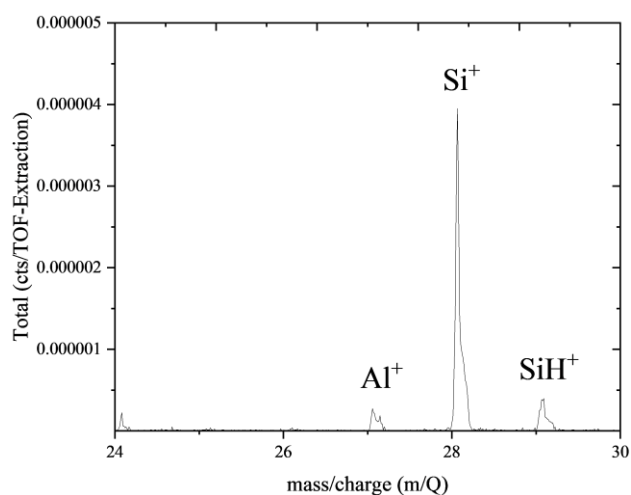


Figure B.1: Mass spectra from ToF-SIMS displaying distinct $m/q = 27$ (Al^+) and $m/q = 28$ (Si^+) peaks. This mass spectra demonstrates the ability to use ToF-SIMS to distinguish silica and alumina nanoparticles. Sample is 158 kDa P2VP sample with 5 vol% Al_2O_3 NPs and 5 vol% SiO_2 NPs. ToF-SIMS was collected at 100 pA and 30 kV conditions for 400 frames. In ToF-SIMS relative peak intensities do not quantitatively indicate sample composition.

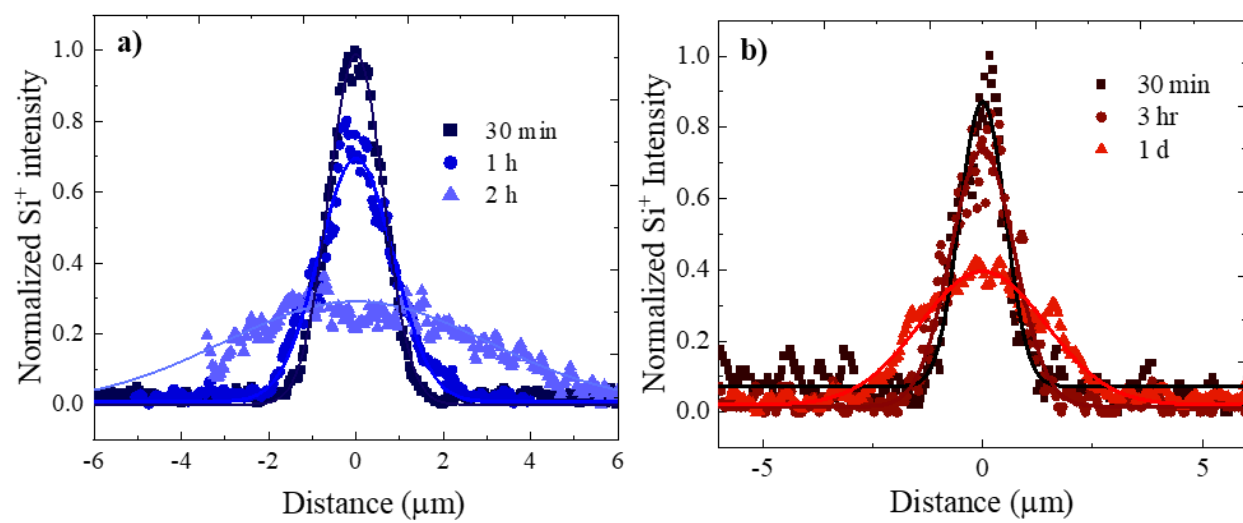
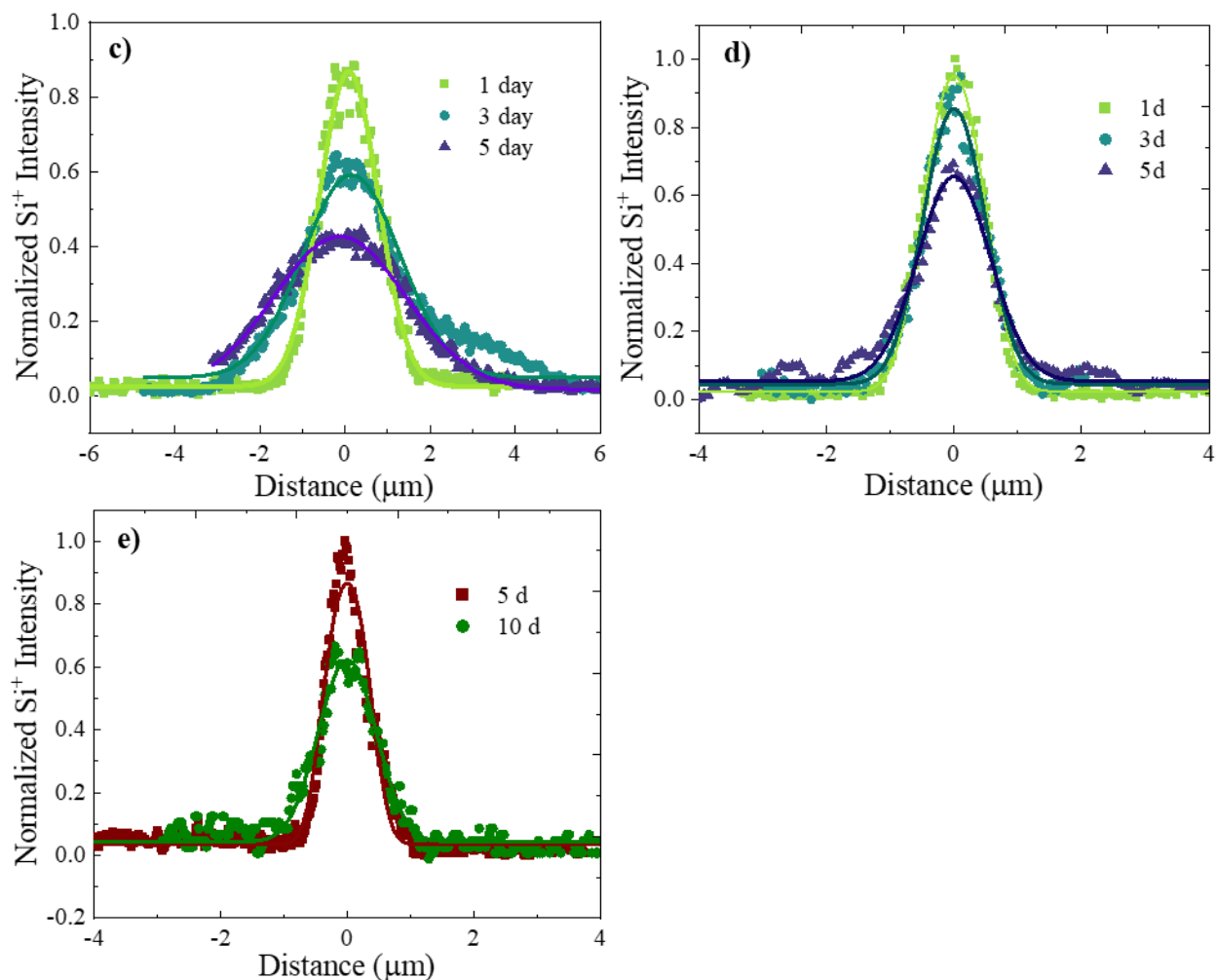


Figure continues on the next page. Figure caption on next page.



B.2Figure B.2: Normalized concentration profiles from ToF-SIMS for SiO₂ nanoparticles ($R_{NP} = 26.2$ nm) diffusing into P2VP. (a) 14.0 kDa, (b) 41.0 kDa, (c) 158 kDa, (d) 310 kDa, and (e) 474 kDa. Lines correspond to Fick's 2nd law and the D_{NP} and R^2 values are tabulated in Table B.4. Tabulated Diffusion Coefficients

Table B.4

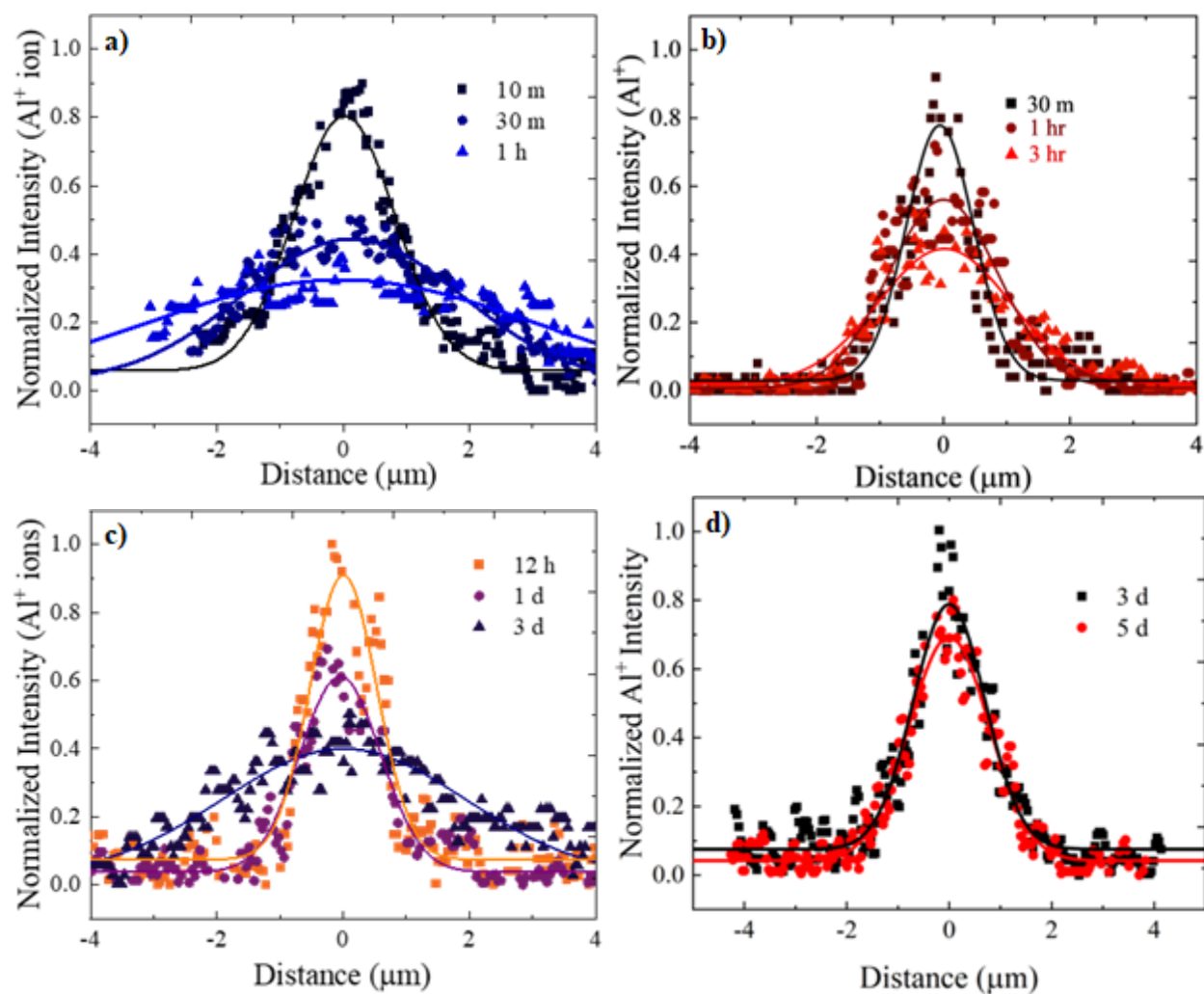


Figure continues on the next page. Figure caption on next page.

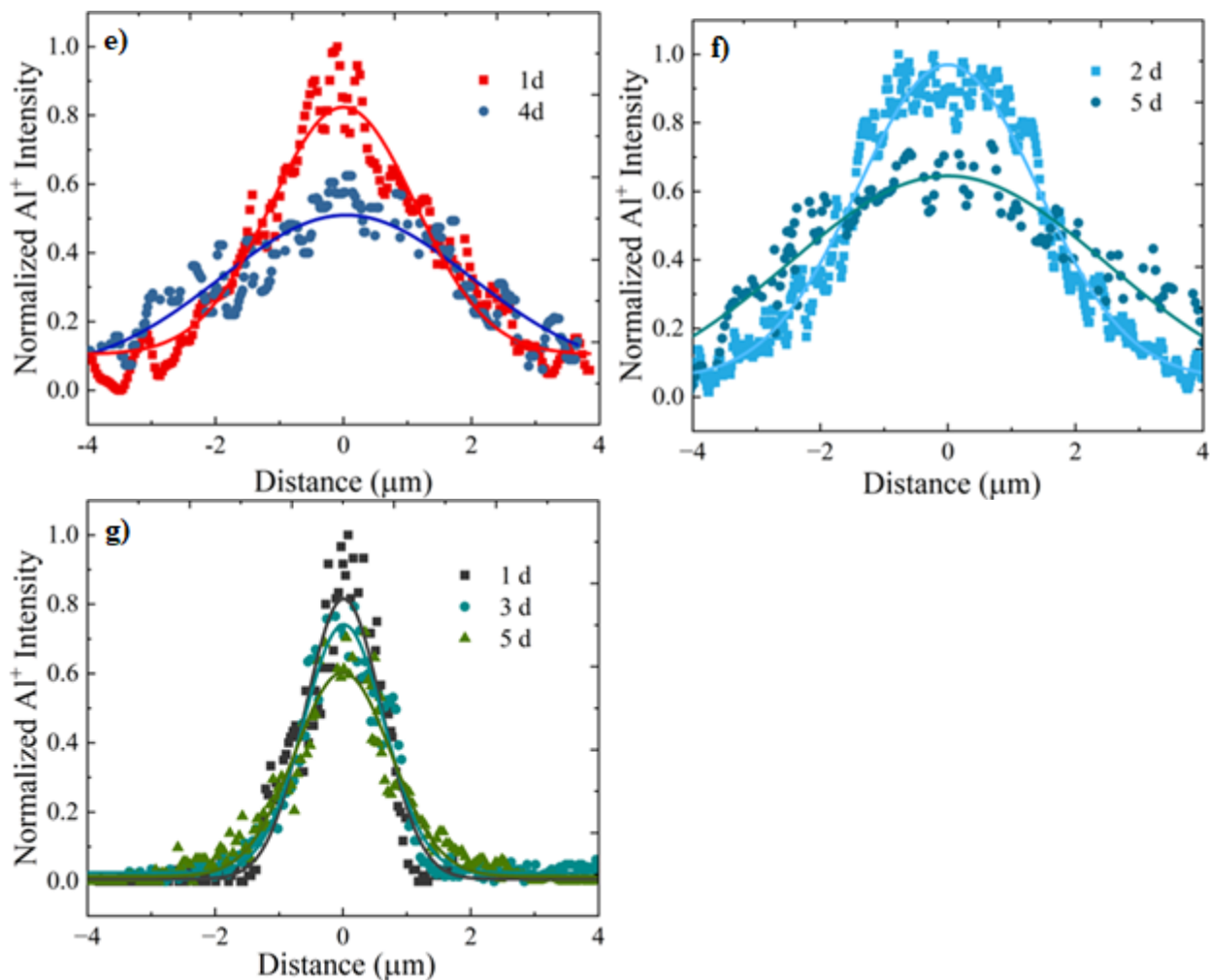


Figure B.3 : Normalized concentration profiles from ToF SIM for Al_2O_3 nanoparticles ($R_{NP} = 6.5$ nm) diffusing into P2VP ($M_w = 14.0 - 1220$ kDa). (a) 14.0 kDa, (b) 41.0 kDa, (c) 158 kDa, (d) 219 kDa e) 310 kDa, (f) 474 kDa, (g) 1220 kDa. Lines correspond to Fick's 2nd law and the D_{NP} and R^2 values are tabulated in

Table B.5.

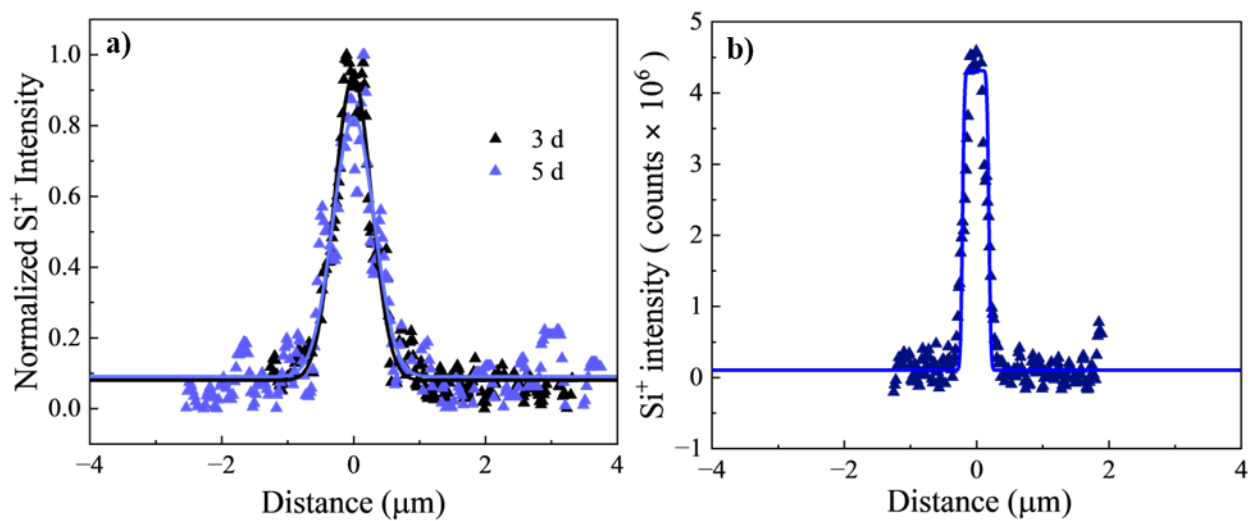


Figure B.4: Normalized concentration profiles from ToF SIM for SiO₂ nanoparticles ($R_{NP} = 8.3$ nm) diffusing into P2VP ($M_w = 474$ and 1220 kDa). (a) 474 kDa and (b) 1220 kDa. Lines correspond to Fick's 2nd law and the D_{NP} and R^2 values are tabulated in Table B.6.

B.3 Tabulated Diffusion Coefficients

Table B.4: Measured diffusion coefficients for large SiO₂ ($R_{NP} = 26.2$ nm) in P2VP (14.0 – 474 kDa). Annealing times range from 30 min to 10 days.

	Sample 1		Sample 2		Sample 3		Average \pm STD
M_w (kDa)	t₁	D_{NP} (cm²/s) R²	t₂	D_{NP} (cm²/s) R²	t₃	D_{NP} (cm²/s) R²	D_{NP} (cm²/s)
14.0	30 m	1.1×10^{-12} 0.988	1 h	1.0×10^{-12} 0.968	2 h	6.2×10^{-12} 0.831	$2.8 \pm 3.0 \times 10^{-12}$
41.0	30 m	5.0×10^{-13} 0.932	3 h	2.2×10^{-13} 0.958	1 d	1.2×10^{-13} 0.942	$2.8 \pm 2.0 \times 10^{-13}$
158	1 d	2.2×10^{-14} 0.992	3 d	1.9×10^{-14} 0.990	5 d	2.5×10^{-14} 0.993	$2.2 \pm 0.3 \times 10^{-14}$
310	1 d	5.7×10^{-15} 0.991	3 d	3.4×10^{-15} 0.986	5 d	3.8×10^{-15} 0.972	$4.3 \pm 1.2 \times 10^{-15}$
474	5 d	5.0×10^{-16} 0.945	10 d	8.5×10^{-16} 0.952			$6.8 \pm 2.5 \times 10^{-16}$

Table B.5: Measured diffusion coefficients for small Al₂O₃ ($R_{NP} = 6.5$ nm) in P2VP (14.0 – 1220 kDa). Annealing times range from 10 min to 5 days.

	Sample 1		Sample 2		Sample 3		Average \pm STD
M_w (kDa)	t₁	D_{NP} (cm²/s) R²	t₂	D_{NP} (cm²/s) R²	t₃	D_{NP} (cm²/s) R²	D_{NP} (cm²/s)
14.0	10 m	5.3×10^{-12} 0.956	30 m	9.0×10^{-12} 0.902	1 h	1.3×10^{-11} 0.867	$9.1 \pm 3.8 \times 10^{-12}$
41.0	30 m	7.4×10^{-13} 0.852	1 h	1.0×10^{-12} 0.910	3 h	4.9×10^{-13} 0.900	$7.4 \pm 2.5 \times 10^{-13}$
158	12 h	3.3×10^{-14} 0.851	1 d	2.6×10^{-14} 0.883	3 d	7.1×10^{-14} 0.894	$4.3 \pm 2.4 \times 10^{-14}$
219	3 d	8.7×10^{-15} 0.917	5 d	6.7×10^{-15} 0.944			$7.7 \pm 1.5 \times 10^{-15}$
310	1 d	7.4×10^{-14} 0.934	4 d	5.4×10^{-14} 0.841			$6.4 \pm 1.4 \times 10^{-14}$
474	2 d	5.4×10^{-14} 0.967	5 d	7.8×10^{-14} 0.881			$6.6 \pm 1.7 \times 10^{-14}$
1,220	1 d	2.1×10^{-14} 0.920	3 d	8.3×10^{-15} 0.939	5 d	8.3×10^{-15} 0.945	$1.3 \pm 0.73 \times 10^{-14}$

Table B.6 : Measured diffusion coefficients for small SiO₂ ($R_{NP} = 8.3$ nm) in P2VP (474 and 1220 kDa). Annealing times range from 3 to 5 days.

	Sample 1		Sample 2	
M_w (kDa)	t₁	D_{NP} (cm²/s) R²	t₂	D_{NP} (cm²/s) R²
474	3 d	1.2×10^{-15} 0.958	5 d	9.5×10^{-16} 0.881
1,220	5 d	6.9×10^{-18} 0.976		

B.4 Vehicular and Core-shell Diffusion Calculations

Table B.7: Nanoparticle diffusion coefficients from the core-shell model ($D_{core-shell}$) at $T = 180\text{ }^{\circ}\text{C}$ as a function of molecular weight. Due to the lower ($\phi_{NP} = 0.05$) initial Al_2O_3 concentration, $\phi_{NP} = 0.01$ is used as the dilute limit. Details of the calculations are below.

M_w (kDa)	R_g (nm)	$D_{core-shell}$ (cm ² /s) Al_2O_3 ($R_{NP} = 6.5$ nm)	$D_{core-shell}$ (cm ² /s) SiO_2 ($R_{NP} = 8.3$ nm)	$D_{core-shell}$ (cm ² /s) SiO_2 ($R_{NP} = 26.2$ nm)
14.0	3.2	1.4×10^{-11}		4.4×10^{-12}
41.0	5.5	9.0×10^{-13}		3.1×10^{-13}
158	10.9	2.4×10^{-14}		9.9×10^{-15}
219	12.8	9.9×10^{-15}		
310	15.3	3.7×10^{-15}		1.6×10^{-15}
474	18.8	1.1×10^{-15}	1.1×10^{-15}	5.1×10^{-16}
1,220	30.2	5.6×10^{-17}	8.1×10^{-17}	

In the core-shell model⁴⁵ the nanoparticle diffusion coefficient ($D_{core-shell}$) follows Stokes-Einstein behavior

$$D_{core-shell} = \frac{k_B T}{6\pi\eta_{PNC}R_{eff}} \quad (\text{B1})$$

where k_B is the Boltzmann constant, T is the annealing temperature in Kelvin, η_{PNC} is the viscosity of the polymer nanocomposite in Pa·s, and R_{eff} is the effective radius of the particle that includes a strongly polymer bound layer, $R_{eff} = R_{NP} + R_g$.

The viscosity of the PNC is a function of the polymer molecular weight and the volume fraction of the nanoparticles. In the core-shell model, strongly bound polymers increase the effective size of the nanoparticles that also increasing the effective volume fraction of nanoparticles, as given by

$$\phi_{eff} = \phi_{NP} \left(\frac{R_{eff}}{R_{NP}} \right)^3 \quad (\text{B2})$$

As the NPs diffuse from the PNC mid-layer into the P2VP matrix layers, ϕ_{eff} decreases. Here, from the unannealed film concentration of $\phi_{NP-SiO_2} = 0.1$, we estimate the matrix $\phi_{NP-SiO_2} = 0.0250$ to account for the NP dilution during the experiment. Likewise, for our Al_2O_3 samples, where the unannealed $\phi_{NP-Al_2O_3} = 0.05$, we estimate the matrix $\phi_{NP-Al_2O_3} = 0.01$ after dilution. Following work by Griffin *et al.*,⁴⁵ we account compute the PNC viscosity using.

$$\eta_{PNC} = \eta_{poly}(1 + 2.5\phi_{eff} + 6.2\phi_{eff}^2) \quad (B3)$$

To incorporate the effect of molecular weight, we need to modify the expressions for R_g and h_{poly} .

The molecular weight dependence of R_g is well-established. Rubinstein and Colby³⁴ by

$$R_g^2 = C_\infty n l^2 \quad (B4)$$

where l is the bond length, n is the number of backbone bonds, and C_∞ is the characteristic ratio. For P2VP, C-C backbone bond length $l = 1.54 \text{ \AA}$, $C_\infty = 10$,¹⁵¹ and $n = 2 * M_w / M_{2VP \text{ monomer}}$. Thus, the molecular weight dependence of the of R_g for P2VP is

$$R_g^2 = \frac{C_\infty n l^2}{6} = \frac{C_\infty \frac{M_w}{M_{2VP}} l^2}{3} \quad (B5)$$

$$\mathbf{B.5} \quad R_g(M_w) = l \left(\frac{C_\infty \frac{M_w}{M_{2VP}}}{3} \right)^{1/2} \quad (\mathbf{B6})$$

Vehicular and Core-

shell Diffusion Calculations

Table B.7Eqn. B6 was substituted into $R_{eff} = R_{NP} + R_g$ to reflect the molecular weight dependence of R_{eff} in Eqn. B1.

The molecular weight dependence of η_{poly} at 180 °C is provided from previous experimental measurements done by Griffin et al.⁴⁵ (black triangles) and new results from this study (black squares).

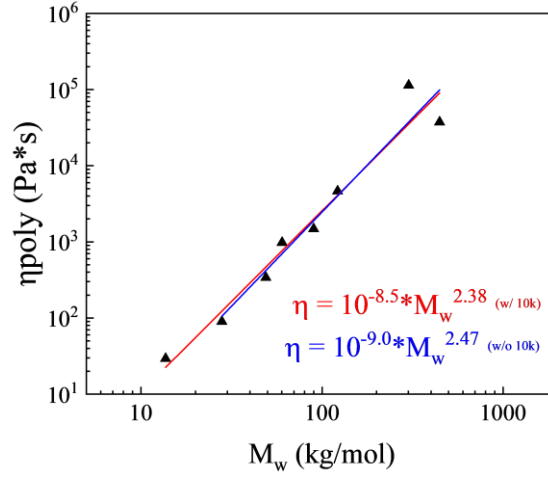


Figure B.5 : Experimental measurements of η_{poly} with linear fit used in red, including the unentangled molecular weight, and in blue to demonstrate the minimal difference in scaling when excluding the unentangled sample.

The figure includes two fits to this experimental data both with and without the lowest molecular weight P2VP sample. Although the entanglement molecular weight of P2VP is 18 kDa, the quality of the fit to the data is comparable. Thus, for Vehicular and Core-shell Diffusion Calculations

Table B.7, Eqn. B3 uses

$$\eta_{P2VP} = 10^{-8.5} * M_w^{2.38} \quad (B7)$$

to capture the molecular weight dependence of η_{poly} .

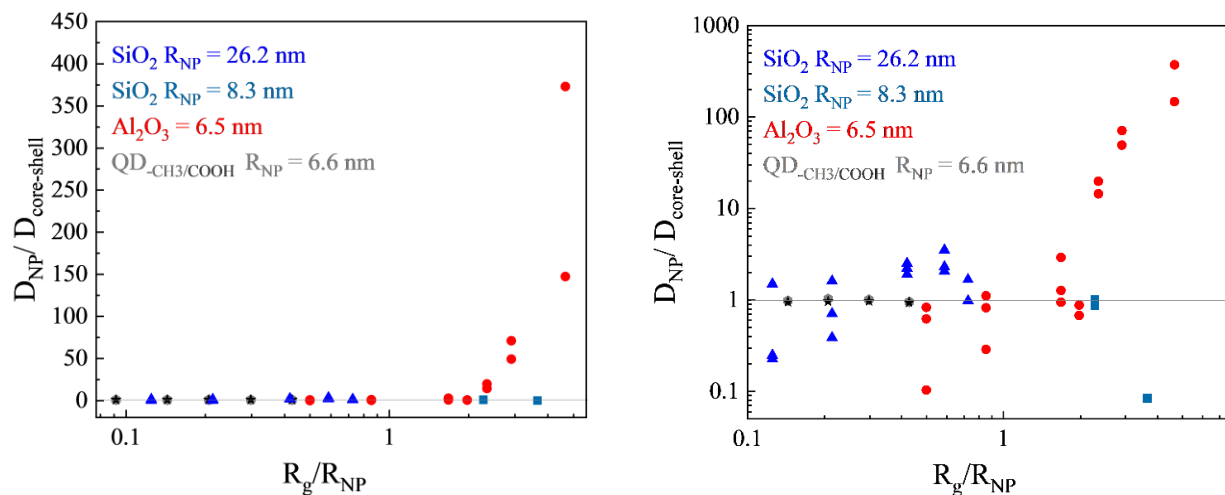


Figure B.6 : $D_{NP}/D_{core-shell}$ versus R_g/R_{NP} showing data from all annealing times. Silica nanoparticles are displayed in blue triangles ($R_{NP} = 26.2$ nm) and light blue squares ($R_{NP} = 8.3$ nm). Alumina nanoparticles are displayed in red circles ($R_{NP} = 6.5$ nm). Specific annealing times are provided in **Tabulated Diffusion Coefficients**

Table B.4. Additional data from single particle tracking experiments of methyl-capped (black stars) or carboxyl-capped (gray circles) quantum dot nanoparticles ($R_{NP} = 6.6$ nm) in poly(propylene glycol) ($M_w = 0.425 - 8$ kDa; $R_g = 0.6 - 2.8$ nm).³⁵

Table B.8: Evidence for Regime II vehicular diffusion. The difference between the average D_{NP} and $D_{core-shell}$ for Al_2O_3 NPs ($R_{NP} = 6.5$ nm) as a function of molecular weight. When $R_g/R_{NP} \geq 2.4$ (blue highlight), the difference becomes independent of molecular weight.

M_w (kDa)	R_g/R_{NP}	$\langle D_{NP} \rangle / D_{core-shell}$	$\langle D_{NP} \rangle - D_{core-shell}$
14.0	0.54	0.65	-5.3×10^{-12}
41.0	0.84	0.82	-1.6×10^{-13}
158	1.7	1.8	1.9×10^{-14}
219	2.0	0.78	-2.2×10^{-15}
310	2.4	17.2	6.0×10^{-14}
474	2.9	60.0	6.5×10^{-14}
1,220	4.6	232	1.3×10^{-14}

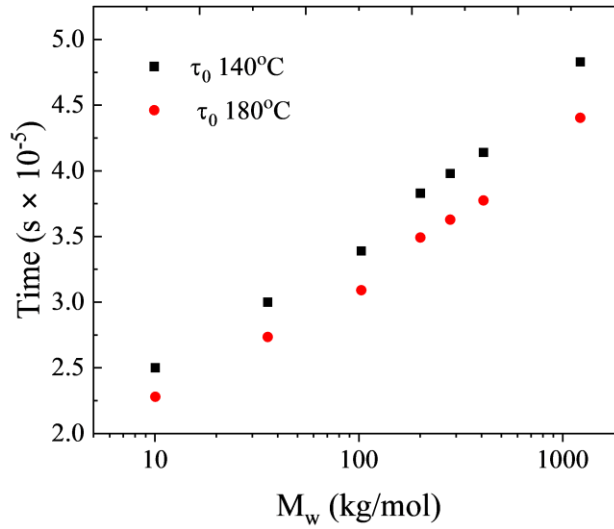


Figure B.7: Shortest Rouse time (τ_0) for P2VP measured at 140 °C and scaled to 180 °C. The τ_0 values were measured at 140 °C (black) using dielectric relaxation spectroscopy.²⁶ Data scaled to 180 °C (red) by assuming $\tau_0 \sim 1/T$ (Kelvin).

B.6 References

- (1) Kumar, S. K.; Benicewicz, B. C.; Vaia, R. A.; Winey, K. I. 50th Anniversary Perspective: Are Polymer Nanocomposites Practical for Applications? *Macromolecules* **2017**, *50*, 714–731.
- (2) Iqbal, A.; Saeed, A.; Ul-Hamid, A. A Review Featuring the Fundamentals and Advancements of Polymer/CNT Nanocomposite Application in Aerospace Industry. *Polym. Bull.* **2021**, *78*, 539–557.
- (3) Thakur, V. K.; Kessler, M. R. Self-Healing Polymer Nanocomposite Materials: A Review. *Polymer (Guildf)*. **2015**, *69*, 369–383.
- (4) Rafique, M. M. A.; Kandare, E.; Sprenger, S. Fiber-Reinforced Magneto-Polymer Matrix Composites (FR-MPMCs) - A Review. *J. Mater. Res.* **2017**, *32*, 1020–1046.
- (5) Shah, V.; Bhaliya, J.; Patel, G. M.; Deshmukh, K. Advances in Polymeric Nanocomposites for Automotive Applications: A Review. *Polym. Adv. Technol.* **2022**, *33*, 3023–3048.
- (6) Kedzior, S. A.; Zoppe, J. O.; Berry, R. M.; Cranston, E. D. Recent Advances and an Industrial Perspective of Cellulose Nanocrystal Functionalization through Polymer Grafting. **2018**.
- (7) Mu, M.; Composto, R. J.; Clarke, N.; Winey, K. I. Minimum in Diffusion Coefficient with Increasing {MWCNT} Concentration Requires Tracer Molecules to Be Larger than Nanotubes. *Macromolecules* **2009**, *42*, 8365–8369.
- (8) Cheng, S.; Carroll, B.; Bocharova, V.; Carrillo, J. M.; Sumpter, B. G.; Sokolov, A. P. Focus: Structure and Dynamics of the Interfacial Layer in Polymer Nanocomposites with Attractive Interactions. *J. Chem. Phys.* **2017**, *146*, 203201.
- (9) Lin, C.-C.; Gam, S.; Meth, J. S.; Clarke, N.; Winey, K. I.; Composto, R. J. Do Attractive Polymer–Nanoparticle Interactions Retard Polymer Diffusion in Nanocomposites? **2013**, *46*, 42.
- (10) Lin, Y.; Li, P.; Liu, W.; Chen, J.; Liu, X.; Jiang, P.; Huang, X. Application-Driven High-Thermal-Conductivity Polymer Nanocomposites. *ACS Nano* **2024**, *18*, 3851–3870.
- (11) Bocharova, V.; Genix, A.-C.; Carrillo, J.-M. Y.; Kumar, R.; Carroll, B.; Erwin, A.; Voylov, D.; Kisliuk, A.; Wang, Y.; Sumpter, B. G.; Sokolov, A. P. Addition of Short Polymer Chains Mechanically Reinforces Glassy Poly(2-Vinylpyridine)–Silica Nanoparticle Nanocomposites. *Cite This ACS Appl. Nano Mater* **2021**, *2020*, 21.

- (12) Raemdonck, K.; Braeckmans, K.; Demeester, J.; De Smedt, S. C. Merging the Best of Both Worlds: Hybrid Lipid-Enveloped Matrix Nanocomposites in Drug Delivery. *Chem. Soc. Rev* **2014**, *43*, 444.
- (13) Parrish, E.; Caporizzo, M. A.; Composto, R. J. Network Confinement and Heterogeneity Slows Nanoparticle Diffusion in Polymer Gels. *J. Chem. Phys.* **2017**, *146*, 203318.
- (14) Merkel, T. C.; Freeman, B. D.; Spontak, R. J.; He, Z.; Pinnau, I.; Meakin, P.; Hill, A. J. Ultrapermearable, Reverse-Selective Nanocomposite Membranes. *Science (80-.)*. **2002**, *296*, 519–522.
- (15) Yin, J.; Deng, B. Polymer-Matrix Nanocomposite Membranes for Water Treatment. *J. Memb. Sci.* **2015**, *479*, 256–275.
- (16) Duncan, T. V. Applications of Nanotechnology in Food Packaging and Food Safety: Barrier Materials, Antimicrobials and Sensors. *J. Colloid Interface Sci.* **2011**, *363*, 1–24.
- (17) Huang, J.-Y.; Li, X.; Zhou, W. Safety Assessment of Nanocomposite for Food Packaging Application. **2015**.
- (18) Beecroft, L. L.; Ober, C. K. Nanocomposite Materials for Optical Applications. *Chem. Mater.* **1997**, *9*, 1302–1317.
- (19) Barna, E.; Bommer, B.; Kürsteiner, J.; Vital, A.; Trzebiatowski, O. V; Koch, W.; Schmid, B.; Graule, T. Innovative, Scratch Proof Nanocomposites for Clear Coatings.
- (20) Buitrago, C. F.; Pressly, J. F.; Yang, A. S.; Gordon, P. A.; Riggelman, R. A.; Natarajan, B.; Winey, K. I. Creep Attenuation in Glassy Polymer Nanocomposites with Variable Polymer–Nanoparticle Interactions. *Soft Matter* **2020**, *16*, 8912–8924.
- (21) Vilay, V.; Mariatti, M.; Ahmad, Z.; Pasomsouk, K.; Todo, M. Characterization of the Mechanical and Thermal Properties and Morphological Behavior of Biodegradable Poly(L-Lactide)/Poly(ϵ -Caprolactone) and Poly(L-Lactide)/Poly(Butylene Succinate-L-Lactate) Polymeric Blends. *J. Appl. Polym. Sci.* **2009**, *114*, 1784–1792.
- (22) Mutiso, R. M.; Winey, K. I. Electrical Properties of Polymer Nanocomposites Containing Rod-like Nanofillers. *Prog. Polym. Sci.* **2015**, *40*, 63–84.
- (23) Lebedev, O. V.; Goncharuk, G. P.; Ozerin, A. N. Changes in Electrical Conductance of Polymer Composites Melts Due to Carbon Nanofiller Particles Migration. *Polym. 2021, Vol. 13, Page 1030* **2021**, *13*, 1030.
- (24) Tuteja, A.; Mackay, M. E.; Narayanan, S.; Asokan, S.; Wong, M. S. Breakdown of the Continuum Stokes-Einstein Relation for Nanoparticle Diffusion. *Nano Lett.* **2007**, *7*, 1276–

- (25) Bailey, E. J.; Winey, K. I. Dynamics of Polymer Segments, Polymer Chains, and Nanoparticles in Polymer Nanocomposite Melts: A Review. *Prog. Polym. Sci.* **2020**, *105*, 101242.
- (26) Bailey, E. J.; Griffin, P. J.; Composto, R. J.; Winey, K. I. Multiscale Dynamics of Small, Attractive Nanoparticles and Entangled Polymers in Polymer Nanocomposites. *Macromolecules* **2019**, *52*, 2181–2188.
- (27) Grabowski, C. A.; Mukhopadhyay, A. Size Effect of Nanoparticle Diffusion in a Polymer Melt. *Macromolecules* **2014**, *47*, 7238–7242.
- (28) Shrestha, U. M.; Han, L.; Saito, T.; Schweizer, K. S.; Dadmun, M. D. Mechanism of Soft Nanoparticle Diffusion in Entangled Polymer Melts. **2022**, *14*, 45.
- (29) Cheng, S.; Xie, S.-J.; Carrillo, J.-M. Y.; Carroll, B.; Martin, H.; Cao, P.-F.; Dadmun, M. D.; Sumpter, B. G.; Novikov, V. N.; Schweizer, K. S.; Sokolov, A. P. Big Effect of Small Nanoparticles: A Shift in Paradigm for Polymer Nanocomposites. *ACS Nano* **2017**, *11*, 752–759.
- (30) Cruickshank, C. The Stokes-Einstein Law for Diffusion in Solution. *Proc. R. Soc. London. Ser. A, Contain. Pap. a Math. Phys. Character* **1924**, *106*, 724–749.
- (31) Kalathi, J. T.; Yamamoto, U.; Schweizer, K. S.; Grest, G. S.; Kumar, S. K. Nanoparticle Diffusion in Polymer Nanocomposites. *Phys. Rev. Lett.* **2014**, *112*, 108301.
- (32) Grabowski, C. A.; Mukhopadhyay, A. Size Effect of Nanoparticle Diffusion in a Polymer Melt. *Macromolecules* **2014**, *47*, 7238–7242.
- (33) Karatrantos, A.; Composto, R. J.; Winey, K. I.; Clarke, N. Polymer and Spherical Nanoparticle Diffusion in Nanocomposites. *J. Chem. Phys.* **2017**, *146*, 203331.
- (34) Rubinstein, M.; Colby, R. H. *Polymer Physics*; Oxford University Press, 2003.
- (35) Park, J.; Bailey, E. J.; Composto, R. J.; Winey, K. I. Single-Particle Tracking of Nonsticky and Sticky Nanoparticles in Polymer Melts. *Macromolecules* **2020**, *53*, 3933–3939.
- (36) Brochard Wyart, F.; de Gennes, P. G. Viscosity at Small Scales in Polymer Melts. *Eur. Phys. J. E Soft Matter* **2000**, *1*, 93–97.
- (37) Wang, L.; Ma, J.; Hong, W.; Zhang, H.; Lin, J. Nanoscale Diffusion of Polymer-Grafted Nanoparticles in Entangled Polymer Melts. *Macromolecules* **2020**, *53*, 8393–8399.
- (38) Sorichetti, V.; Hugouvieux, V.; Kob, W. Dynamics of Nanoparticles in Polydisperse

- Polymer Networks: From Free Diffusion to Hopping. *Macromolecules* **2021**, *54*, 8575–8589.
- (39) Cai, L. H.; Panyukov, S.; Rubinstein, M. Hopping Diffusion of Nanoparticles in Polymer Matrices. *Macromolecules* **2015**, *48*, 847–862.
 - (40) Cai, L.-H.; Panyukov, S.; Rubinstein, M. Mobility of Nonsticky Nanoparticles in Polymer Liquids. *Macromolecules* **2011**, *44*, 7853–7863.
 - (41) Maldonado-Camargo, L.; Rinaldi, C. Breakdown of the Stokes-Einstein Relation for the Rotational Diffusivity of Polymer Grafted Nanoparticles in Polymer Melts. *Nano Lett.* **2016**, *16*, 6767–6773.
 - (42) Park, J.; Bailey, E. J.; Composto, R. J.; Winey, K. I. Single-Particle Tracking of Nonsticky and Sticky Nanoparticles in Polymer Melts. *Macromolecules* **2020**, *53*, 3933–3939.
 - (43) Jimenez, A. M.; Zhao, D.; Misquitta, K.; Jestin, J.; Kumar, S. K. Exchange Lifetimes of the Bound Polymer Layer on Silica Nanoparticles. *ACS Macro Lett.* **2019**, *8*, 166–171.
 - (44) Harton, S. E.; Kumar, S. K.; Yang, H.; Koga, T.; Hicks, K.; Lee, H.; Mijovic, J.; Liu, M.; Vallery, R. S.; Gidley, D. W. Immobilized Polymer Layers on Spherical Nanoparticles. *Macromolecules* **2010**, *43*, 3415–3421.
 - (45) Griffin, P. J.; Bocharova, V.; Middleton, L. R.; Composto, R. J.; Clarke, N.; Schweizer, K. S.; Winey, K. I. Influence of the Bound Polymer Layer on Nanoparticle Diffusion in Polymer Melts. *ACS Macro Lett.* **2016**, *5*, 1141–1145.
 - (46) Holt, A. P.; Griffin, P. J.; Bocharova, V.; Agapov, A. L.; Imel, A. E.; Dadmun, M. D.; Sangoro, J. R.; Sokolov, A. P. Dynamics at the Polymer/Nanoparticle Interface in Poly(2-Vinylpyridine)/ Silica Nanocomposites. *Macromolecules* **2014**, *47*, 1837–1843.
 - (47) Holt, A. P.; Sangoro, J. R.; Wang, Y.; Agapov, A. L.; Sokolov, A. P. Chain and Segmental Dynamics of Poly(2-Vinylpyridine) Nanocomposites. **2013**.
 - (48) Gong, C.; Weiblen, D.; Rende, D.; Akcora, P.; Ozisik, R. Stability of Particle Dispersion and Heterogeneous Interfacial Layers in Polymer Nanocomposites. *Polymer (Guildf)*. **2021**, *226*, 123813.
 - (49) Giovino, M.; Pribyl, J.; Benicewicz, B.; Kumar, S.; Schadler, L. Linear Rheology of Polymer Nanocomposites with Polymer-Grafted Nanoparticles. *Polymer (Guildf)*. **2017**, *131*, 104–110.
 - (50) Yang, S.; Akcora, P. Deformation of Chemically Heterogeneous Interfacial Layers of Polymer Nanocomposites. **2019**, *8*, 1635–1641.

- (51) Carroll, B.; Bocharova, V.; Carrillo, J.-M. Y.; Kisliuk, A.; Cheng, S.; Yamamoto, U.; Schweizer, K. S.; Sumpter, B. G.; Sokolov, A. P. Diffusion of Sticky Nanoparticles in a Polymer Melt: Crossover from Suppressed to Enhanced Transport. *Macromolecules* **2018**, *51*, 2268–2275.
- (52) Yamamoto, U.; Carrillo, J.-M. Y.; Bocharova, V.; Sokolov, A. P.; Sumpter, B. G.; Schweizer, K. S. Theory and Simulation of Attractive Nanoparticle Transport in Polymer Melts. *Macromolecules* **2018**, *51*, 2258–2267.
- (53) Mun, E. A.; Hannell, C.; Rogers, S. E.; Hole, P.; Williams, A. C.; Khutoryanskiy, V. V. On the Role of Specific Interactions in the Diffusion of Nanoparticles in Aqueous Polymer Solutions. *Langmuir* **2014**, *30*, 308–317.
- (54) Al-Obaidi, H.; Florence, A. T. Nanoparticle Delivery and Particle Diffusion in Confined and Complex Environments. *J. Drug Deliv. Sci. Technol.* **2015**, *30*, 266–277.
- (55) Wang, D.; Kou, R.; Choi, D.; Yang, Z.; Nie, Z.; Li, J.; Saraf, L. V.; Hu, D.; Zhang, J.; Graff, G. L.; Liu, J.; Pope, M. A.; Aksay, I. A. Ternary Self-Assembly of Ordered Metal Oxide-Graphene Nanocomposites for Electrochemical Energy Storage. *ACS Nano* **2010**, *4*, 1587–1595.
- (56) Gong, M.; Zhang, L.; Wan, P. Polymer Nanocomposite Meshes for Flexible Electronic Devices. *Prog. Polym. Sci.* **2020**, *107*, 101279.
- (57) Ge, T. Scaling Perspective on Dynamics of Nanoparticles in Polymers: Length- and Time-Scale Dependent Nanoparticle-Polymer Coupling. *Macromolecules* **2023**, *56*, 3809–3837.
- (58) Bailey, E. J.; Griffin, P. J.; Composto, R. J.; Winey, K. I. Multiscale Dynamics of Small, Attractive Nanoparticles and Entangled Polymers in Polymer Nanocomposites. *Macromolecules* **2019**, *52*, 2181–2188.
- (59) Genix, A.-C.; Bocharova, V.; Kisliuk, A.; Carroll, B.; Zhao, S.; Oberdisse, J.; Sokolov, A. P. Enhancing the Mechanical Properties of Glassy Nanocomposites by Tuning Polymer Molecular Weight. **2018**.
- (60) Holt, A. P.; Bocharova, V.; Cheng, S.; Kisliuk, A. M.; White, B. T.; Saito, T.; Uhrig, D.; Mahalik, J. P.; Kumar, R.; Imel, A. E.; Etampawala, T.; Martin, H.; Sikes, N.; Sumpter, B. G.; Dadmun, M. D.; Sokolov, A. P. Controlling Interfacial Dynamics: Covalent Bonding versus Physical Adsorption in Polymer Nanocomposites. *ACS Nano* **2016**, *10*, 6843–6852.
- (61) Cheng, S.; Holt, A. P.; Wang, H.; Fan, F.; Bocharova, V.; Martin, H.; Etampawala, T.; White, B. T.; Saito, T.; Kang, N.-G.; Dadmun, M. D.; Mays, J. W.; Sokolov, A. P. Unexpected Molecular Weight Effect in Polymer Nanocomposites. *Phys. Rev. Lett.* **2016**, *116*, 038302-1–4.

- (62) Holt, A. P.; Bocharova, V.; Cheng, S.; Kisliuk, A. M.; White, B. T.; Saito, T.; Uhrig, D.; Mahalik, J. P.; Kumar, R.; Imel, A. E.; Etampawala, T.; Martin, H.; Sikes, N.; Sumpter, B. G.; Dadmun, M. D.; Sokolov, A. P. Controlling Interfacial Dynamics: Covalent Bonding versus Physical Adsorption in Polymer Nanocomposites. **2016**.
- (63) Holt, A. P.; Griffin, P. J.; Bocharova, V.; Agapov, A. L.; Imel, A. E.; Dadmun, M. D.; Sangoro, J. R.; Sokolov, A. P. Dynamics at the Polymer/Nanoparticle Interface in Poly(2-Vinylpyridine)/ Silica Nanocomposites. *Macromolecules* **2014**, *47*, 1837–1843.
- (64) Bailey, E. J.; Griffin, P. J.; Tyagi, M.; Winey, K. I. Segmental Diffusion in Attractive Polymer Nanocomposites: A Quasi-Elastic Neutron Scattering Study. *Macromolecules* **2019**, *52*, 669–678.
- (65) Popov, I.; Carroll, B.; Bocharova, V.; Genix, A.-C.; Cheng, S.; Khamzin, A.; Kisliuk, A.; Sokolov, A. P. Strong Reduction in Amplitude of the Interfacial Segmental Dynamics in Polymer Nanocomposites. **2020**.
- (66) Lin, C. C.; Parrish, E.; Composto, R. J. Macromolecule and Particle Dynamics in Confined Media. *Macromolecules* **2016**, *49*, 5755–5772.
- (67) Roseker, W.; Hruszkewycz, S. O.; Lehmkuhler, F.; Walther, M.; Schulte-Schrepping, H.; Lee, S.; Osaka, T.; Strüder, L.; Hartmann, R.; Sikorski, M.; Song, S.; Robert, A.; Fuoss, P. H.; Sutton, M.; Stephenson, G. B.; Grübel, G. Towards Ultrafast Dynamics with Split-Pulse X-Ray Photon Correlation Spectroscopy at Free Electron Laser Sources. *Nat. Commun.* **2018**, *9*, 1–6.
- (68) Guo, H.; Bourret, G.; Lennox, R. B.; Sutton, M.; Harden, J. L.; Leheny, R. L. Entanglement-Controlled Subdiffusion of Nanoparticles within Concentrated Polymer Solutions. *Phys. Rev. Lett.* **2012**, *109*, 055901.
- (69) Manzo, C.; Garcia-Parajo, M. F. A Review of Progress in Single Particle Tracking: From Methods to Biophysical Insights. *Reports Prog. Phys.* **2015**, *78*, 124601.
- (70) Rose, K. A.; Molaei, M.; Boyle, M. J.; Lee, D.; Crocker, J. C.; Composto, R. J. Particle Tracking of Nanoparticles in Soft Matter. *J. Appl. Phys.* **2020**, *127*, 191101.
- (71) Kohli, I.; Mukhopadhyay, A. Diffusion of Nanoparticles in Semidilute Polymer Solutions: Effect of Different Length Scales. *Macromolecules* **2012**, *45*, 6143–6149.
- (72) Grabowski, C. A.; Adhikary, B.; Mukhopadhyay, A. Dynamics of Gold Nanoparticles in a Polymer Melt. *Appl. Phys. Lett.* **2009**, *94*, 021903.
- (73) Composto, R. J.; Kramer, E. J. Mutual Diffusion Studies of Polystyrene and Poly(Xylenyl Ether) Using Rutherford Backscattering Spectrometry. *J. Mater. Sci.* **1991**, *26*, 2815–2822.

- (74) Composto, R. J.; Walters, R. M.; Genzer, J. Application of Ion Scattering Techniques to Characterize Polymer Surfaces and Interfaces. *Mater. Sci. Eng. R Reports* **2002**, *38*, 107–180.
- (75) Cole, D. H.; Shull, K. R.; Rehn, L. E.; Baldo, P. M. RBS Analysis of the Diffusion of Nano-Size Spheres in a Polymer Matrix. *Nucl. Instruments Methods Phys. Res. Sect. B Beam Interact. with Mater. Atoms* **1998**, *136–138*, 283–289.
- (76) Green, P. F.; Palmstrom, C. J.; Mayer, J. W.; Kramer, E. J. Marker Displacement Measurements of Polymer-Polymer Interdiffusion. *Macromolecules* **1985**, *18*, 501–507.
- (77) Choi, J.; Cargnello, M.; Murray, C. B.; Clarke, N.; Winey, K. I.; Composto, R. J. Fast Nanorod Diffusion through Entangled Polymer Melts. *ACS Macro Lett.* **2015**, *4*, 952–956.
- (78) Spool, A. M. *The Practice of TOF-SIMS: Time of Flight Secondary Ion Mass Spectrometry - Alan M. Spool - Google Books*; Momentum Press, 2016.
- (79) Mei, H.; Laws, T. S.; Terlier, T.; Verduzco, R.; Stein, G. E. Characterization of Polymeric Surfaces and Interfaces Using Time-of-Flight Secondary Ion Mass Spectrometry. *Journal of Polymer Science*. John Wiley and Sons Inc April 1, 2021, pp 1174–1198.
- (80) Zhang, A. C.; Maguire, S. M.; Ford, J. T.; Composto, R. J. Using Focused Ion Beam Time-of-Flight Secondary Ion Mass Spectrometry to Depth Profile Nanoparticles in Polymer Nanocomposites. *Microsc. Microanal.* **2023**, *29*, 1557–1565.
- (81) Karar, N.; Gupta, T. K. Study of Polymers and Their Blends Using TOF-SIMS Ion Imaging. *Vacuum* **2015**, *111*, 119–123.
- (82) Smentkowski, V.; Goswami, S.; Kollmer, F.; Zakel, J.; Arlinghaus, H.; Rading, D. Analysis of Thin Film Specimens Using {ToF-SIMS} Wedge Protocol, A Comparison with Depth Profiling. *Microsc. Microanal.* **2021**, *27*, 1564–1565.
- (83) Sui, T.; Song, B.; Dluhos, J.; Lu, L.; Korsunsky, A. M. Nanoscale Chemical Mapping of Li-Ion Battery Cathode Material by {FIB-SEM} and {TOF-SIMS} Multi-Modal Microscopy. *Nano Energy* **2015**, *17*, 254–260.
- (84) Karar, N.; Singh, B. P.; Elizabeth, I. Analysis of Multi-Wall Carbon Nanotube Based Porous Li Battery Electrodes' Using {TOF-SIMS} Ion Imaging. *Appl. Surf. Sci.* **2015**, *349*, 644–649.
- (85) Richardin, P.; Mazel, V.; Walter, P.; Lapr v te, O.; Brunelle, A. Identification of Different Copper Green Pigments in Renaissance Paintings by Cluster-TOF-SIMS Imaging Analysis. *J. Am. Soc. Mass Spectrom.* **2011**, *22*, 1729–1736.

- (86) Prasad, A.; Salim, N. V.; Mozetič, M.; Kailas, L.; Thomas, S. Time-of-flight Secondary Ion Mass Spectrometric Analysis of Polymer Surfaces: A Review. *J. Appl. Polym. Sci.* **2022**, 52286.
- (87) Kobayashi, K.; Watanabe, H.; Maekawa, K.; Kashiwara, K.; Yamaguchi, T.; Asai, K.; Hirose, Y. Oxygen Distribution in Nickel Silicide Films Analyzed by Time-of-Flight Secondary Ion Mass Spectrometry. *Micron* **2010**, 41, 412–415.
- (88) Lianos, L.; Quet, C.; Duc, T. M. Surface Structural Studies of Polyethylene, Polypropylene and Their Copolymers with ToF SIMS. *Surf. Interface Anal.* **1994**, 21, 14–22.
- (89) Priebe, A.; Aribia, A.; Sastre, J.; Romanyuk, Y. E.; Michler, J. 3D High-Resolution Chemical Characterization of Sputtered Li-Rich NMC811 Thin Films Using TOF-SIMS. *Anal. Chem.* **2023**, 95, 1074–1084.
- (90) Poleunis, C.; Médard, N.; Bertrand, P. Additive Quantification on Polymer Thin Films by ToF-SIMS: Aging Sample Effects. *Appl. Surf. Sci.* **2004**, 231–232, 269–273.
- (91) Xie, W.; Weng, L. T.; Yeung, K. L.; Chan, C. M. Segregation of Dioctyl Phthalate to the Surface of Polystyrene Films Characterized by ToF-SIMS and XPS. *Surf. Interface Anal.* **2018**, 50, 1302–1309.
- (92) Lu, X.; Sjövall, P.; Soenen, H. Structural and Chemical Analysis of Bitumen Using Time-of-Flight Secondary Ion Mass Spectrometry (TOF-SIMS). *Fuel* **2017**, 199, 206–218.
- (93) Bailey, J.; Havelund, R.; Shard, A. G.; Gilmore, I. S.; Alexander, M. R.; Sharp, J. S.; Scurr, D. J. 3D ToF-SIMS Imaging of Polymer Multilayer Films Using Argon Cluster Sputter Depth Profiling. *ACS Appl. Mater. Interfaces* **2015**, 7, 2654–2659.
- (94) Prasad, A.; Salim, N. V.; Mozetič, M.; Kailas, L.; Thomas, S. Time-of-Flight Secondary Ion Mass Spectrometric Analysis of Polymer Surfaces: A Review. *J. Appl. Polym. Sci.* **2022**, 139.
- (95) Chan, C. M.; Weng, L. T. Surface Characterization of Polymer Blends by XPS and ToF-SIMS. *Materials (Basel)*. **2016**, 9.
- (96) Ravati, S.; Poulin, S.; Piyakis, K.; Favis, B. D. Phase Identification and Interfacial Transitions in Ternary Polymer Blends by ToF-SIMS. *Polymer (Guildf)*. **2014**, 55, 6110–6123.
- (97) Brennan, B.; Spencer, S. J.; Belsey, N. A.; Faris, T.; Cronin, H.; Silva, S. R.; Sainsbury, T.; Gilmore, I. S.; Stoeva, Z.; Pollard, A. J. Structural, Chemical and Electrical Characterisation of Conductive Graphene-Polymer Composite Films. *Appl. Surf. Sci.* **2017**, 403, 403–412.

- (98) Chen, W. Y.; Ling, Y. C.; Chen, B. J.; Shih, H. H.; Cheng, C. H. Diffusion Study of Multi-Organic Layers in OLEDs by ToF-SIMS. *Appl. Surf. Sci.* **2006**, *252*, 6594–6596.
- (99) Chan, C. M.; Weng, L. T. Surface Characterization of Polymer Blends by XPS and ToF-SIMS. *Mater. 2016, Vol. 9, Page 655* **2016**, *9*, 655.
- (100) Fardim, P.; Gustafsson, J.; Von Schoultz, S.; Peltonen, J.; Holmbom, B. Extractives on Fiber Surfaces Investigated by XPS, ToF-SIMS and AFM. *Colloids Surfaces A Physicochem. Eng. Asp.* **2005**, *255*, 91–103.
- (101) Abd Mutalib, M.; Rahman, M. A.; Othman, M. H. D.; Ismail, A. F.; Jaafar, J. Scanning Electron Microscopy (SEM) and Energy-Dispersive X-Ray (EDX) Spectroscopy. *Membr. Charact.* **2017**, 161–179.
- (102) Sakurada, T.; Hashimoto, S.; Tsuchiya, Y.; Tachibana, S.; Suzuki, M.; Shimizu, K. Lateral Resolution of EDX Analysis with Ultra Low Acceleration Voltage SEM. *sasj.jp T Sakurada, S Hashimoto, Y Tsuchiya, S Tachibana, M Suzuki, K Shimizu Journal Surf. Anal. 2005•sasj.jp* **2005**, *12*.
- (103) Kubicek, M.; Holzlechner, G.; Opitz, A. K.; Larisegger, S.; Hutter, H.; Fleig, J. A Novel ToF-SIMS Operation Mode for Sub 100 Nm Lateral Resolution: Application and Performance. *Appl. Surf. Sci.* **2014**, *289*, 407.
- (104) Moffitt, C. Fundamental Aspects of XPS and the Development of XPS Imaging. *Microsc. Today* **2011**, *19*, 16–21.
- (105) Powell, C. J.; Jablonski, A. Surface Sensitivity of X-Ray Photoelectron Spectroscopy. *Nucl. Instruments Methods Phys. Res. Sect. A Accel. Spectrometers, Detect. Assoc. Equip.* **2009**, *601*, 54–65.
- (106) Watts, J. F.; Wolstenholme, J. An Introduction to Surface Analysis by XPS and AES. *An Introd. to Surf. Anal. by XPS AES* **2003**.
- (107) Chung, Y.; Pak, C.; Park, G.-S.; Jeon, W. S.; Kim, J.-R.; Lee, Y.; Chang, H.; Seung, D. Understanding a Degradation Mechanism of Direct Methanol Fuel Cell Using {TOF-SIMS} and {XPS}. *J. Phys. Chem. C Nanomater. Interfaces* **2008**, *112*, 313–318.
- (108) Wang, K.; Composto, R. J.; Winey, K. I. ToF-SIMS Depth Profiling to Measure Nanoparticle and Polymer Diffusion in Polymer Melts. *Macromolecules* **2023**.
- (109) Harrison, E. T.; Peczonczyk, S. L.; Sharafi, A.; Wujcik, K. H.; Drews, A.; Simko, S. Surface Characterization of Battery Electrode/Electrolyte Materials Using {XPS} and {ToF-SIMS}. *Meet. abstr.* **2019**, *MA2019-01*, 521.

- (110) Balazs, A. C.; Emrick, T.; Russell, T. P. Nanoparticle Polymer Composites: Where Two Small Worlds Meet. *Science* (80-.). **2006**, *314*, 1107–1110.
- (111) Mills, P. J.; Green, P. F.; Palmstrøm, C. J.; Mayer, J. W.; Kramer, E. J. Polydispersity Effects on Diffusion in Polymers: Concentration Profiles of d-Polystyrene Measured by Forward Recoil Spectrometry. *J. Polym. Sci. Part B Polym. Phys.* **1986**, *24*, 1–9.
- (112) Green, P. F.; Kramer, E. J. Matrix Effects on the Diffusion of Long Polymer Chains. *Macromolecules* **1986**, *19*, 1108–1114.
- (113) Mackay, M. E.; Dao, T. T.; Tuteja, A.; Ho, D. L.; van Horn, B.; Kim, H.-C.; Hawker, C. J. Nanoscale Effects Leading to Non-Einstein-like Decrease in Viscosity. *Nat. Mater.* **2003**, *2*, 762–766.
- (114) Composto, R. J.; Mayer, J. W.; Kramer, E. J.; White, D. M. Fast Mutual Diffusion in Polymer Blends. *Phys. Rev. Lett.* **1986**, *57*, 1312–1315.
- (115) Composto, R. J.; Kramer, E. J.; White, D. M. Mutual Diffusion in the Miscible Polymer Blend Polystyrene/Poly(Xylenyl Ether). *Macromolecules* **1988**, *21*, 2580–2588.
- (116) Barrat, J.-L.; Fredrickson, G. H. Diffusion of a Symmetric Block Copolymer in a Periodic Potential. *Macromolecules* **1991**, *24*, 6378–6383.
- (117) Gam, S.; Meth, J. S.; Zane, S. G.; Chi, C.; Wood, B. A.; Seitz, M. E.; Winey, K. I.; Clarke, N.; Composto, R. J. Macromolecular Diffusion in a Crowded Polymer Nanocomposite. *Macromolecules* **2011**, *44*, 3494–3501.
- (118) Shrestha, U. M.; Han, L.; Saito, T.; Schweizer, K. S.; Dadmun, M. D. Mechanism of Soft Nanoparticle Diffusion in Entangled Polymer Melts. *Macromolecules* **2020**, *53*, 7580–7589.
- (119) Imel, A. E.; Rostom, S.; Holley, W.; Baskaran, D.; Mays, J. W.; Dadmun, M. D. The Tracer Diffusion Coefficient of Soft Nanoparticles in a Linear Polymer Matrix. *RSC Adv.* **2017**, *7*, 15574–15581.
- (120) Jo, K. Il; Oh, Y.; Kim, T. H.; Bang, J.; Yuan, G.; Satija, S. K.; Sung, B. J.; Koo, J. Position-Dependent Diffusion Dynamics of Entangled Polymer Melts Nanoconfined by Parallel Immiscible Polymer Films. *ACS Macro Lett.* **2020**, *9*, 1483–1488.
- (121) Lin, C.-C.; Griffin, P. J.; Chao, H.; Hore, M. J. A.; Ohno, K.; Clarke, N.; Riggleman, R. A.; Winey, K. I.; Composto, R. J. Grafted Polymer Chains Suppress Nanoparticle Diffusion in Athermal Polymer Melts. *J. Chem. Phys.* **2017**, *146*, 203332.
- (122) Mills, P. J.; Green, P. F.; Palmstrom, C. J.; Mayer, J. W.; Kramer, E. J. Analysis of Diffusion

- in Polymers by Forward Recoil Spectrometry. *Appl. Phys. Lett.* **1998**, *45*, 957.
- (123) Martín, J.; Hernández-Vélez, M.; de Abril, O.; Luna, C.; Muñoz-Martin, A.; Vázquez, M.; Mijangos, C. Fabrication and Characterization of Polymer-Based Magnetic Composite Nanotubes and Nanorods. *Eur. Polym. J.* **2012**, *48*, 712–719.
 - (124) Bailey, E. J.; Griffin, P. J.; Composto, R. J.; Winey, K. I. Characterizing the Areal Density and Desorption Kinetics of Physically Adsorbed Polymer in Polymer Nanocomposite Melts. *Macromolecules* **2020**, *53*, 2744–2753.
 - (125) Fit plane to 3-D point cloud - MATLAB pcfitplane <https://www.mathworks.com/help/vision/ref/pcfitplane.html> (accessed Jun 22, 2022).
 - (126) Fischler, M. A.; Bolles, R. C. Random Sample Consensus. *Commun. ACM* **1981**, *24*, 381–395.
 - (127) Belu, A. M.; Davies, M. C.; Newton, J. M.; Patel, N. TOF-SIMS Characterization and Imaging of Controlled-Release Drug Delivery Systems. *Anal. Chem.* **2000**, *72*, 5625–5638.
 - (128) Méar, F.; Coillot, D.; Podor, R.; Montagne, L. Self-Healing Nanocomposites: Role and Activation of Inorganic Moieties and Hybrid Nanophases. In *{Self-Healing} at the Nanoscale*; CRC Press, 2011; pp 188–223.
 - (129) Mallakpour, S.; Naghdi, M. {Polymer/SiO₂} Nanocomposites: Production and Applications. *Prog. Mater. Sci.* **2018**, *97*, 409–447.
 - (130) Young, W. W.; Katsumata, R. Intermediate Polymer Relaxation Explains the Anomalous Rheology of Nanocomposites with Ultrasmall Attractive POSS Nanoparticles. *ACS Polym. Au* **2023**, *3*, 466–474.
 - (131) Lin, C.-C.; Parrish, E.; Composto, R. J. Macromolecule and Particle Dynamics in Confined Media. *Macromolecules* **2016**, *49*, 5755–5772.
 - (132) Papakonstantopoulos, G. J.; Yoshimoto, K.; Doxastakis, M.; Nealey, P. F.; De Pablo, J. J. Local Mechanical Properties of Polymeric Nanocomposites. *Phys. Rev. E - Stat. Nonlinear, Soft Matter Phys.* **2005**, *72*, 031801-031801–031806.
 - (133) Cheng, S.; Carroll, B.; Bocharova, V.; Carrillo, J.-M.; Sumpter, B. G.; Sokolov, A. P.; Carrillo, J.-M. Y. Perspective: Outstanding Theoretical Questions in Polymer-Nanoparticle Hybrids. *J. Chem. Phys.* **2017**, *146*, 203201.
 - (134) Liu, J.; Cao, D.; Zhang, L. Molecular Dynamics Study on Nanoparticle Diffusion in Polymer Melts: A Test of the Stokes-Einstein Law. *J. Phys. Chem. C* **2008**, *112*, 6653–6661.

- (135) Mendez, N. F.; Dhara, D.; Zhang, Q.; Narayanan, S.; Schadler, L. S.; Müller, A. J.; Kumar, S. K. Nanoparticle Diffusion in Miscible Polymer Nanocomposite Melts. *Macromolecules* **2023**, *56*, 4658–4668.
- (136) Kwon, N. K.; Park, C. S.; Lee, C. H.; Kim, Y. S.; Zukoski, C. F.; Kim, S. Y. Tunable Nanoparticle Stability in Concentrated Polymer Solutions On the Basis of the Temperature Dependent Solvent Quality. *Macromolecules* **2016**, *20*, 25.
- (137) Jin, J.; Wang, X.; Wick, C. D.; Dang, L. X.; Miller, J. D. Silica Surface States and Their Wetting Characteristics. <https://doi.org/10.1680/jsuin.19.00053> **2020**, *8*, 145–157.
- (138) Watcharenwong, A.; Saijaioup, N.; Bailuang, Y.; Kajitvichyanukul, P. Morphology and Wettability of Nanoporous Aluminium Oxide Film Prepared by Anodization. *Key Eng. Mater.* **2017**, *737*, 174–178.
- (139) Bronstein, N. D.; Li, L.; Xu, L.; Yao, Y.; Ferry, V. E.; Alivisatos, A. P.; Nuzzo, R. G. Luminescent Solar Concentration with Semiconductor Nanorods and Transfer-Printed Micro-Silicon Solar Cells. *ACS Nano* **2014**, *8*, 44–53.
- (140) Mun, E. A.; Hannell, C.; Rogers, S. E.; Hole, P.; Williams, A. C.; Khutoryanskiy, V. V. On the Role of Specific Interactions in the Diffusion of Nanoparticles in Aqueous Polymer Solutions. *Langmuir* **2014**, *30*, 308–317.
- (141) Senses, E.; Ansar, S. M.; Kitchens, C. L.; Mao, Y.; Narayanan, S.; Natarajan, B.; Faraone, A. Small Particle Driven Chain Disentanglements in Polymer Nanocomposites. *Phys. Rev. Lett.* **2017**, *118*.
- (142) Gong, S.; Chen, Q.; Moll, J. F.; Kumar, S. K.; Colby, R. H. Segmental Dynamics of Polymer Melts with Spherical Nanoparticles. *ACS Macro Lett.* **2014**, *3*, 773–777.
- (143) Tuteja, A.; Mackay, M. E.; Hawker, C. J.; Van Horn, B. Effect of Ideal, Organic Nanoparticles on the Flow Properties of Linear Polymers: Non-Einstein-like Behavior. *Macromolecules* **2005**, *38*, 8000–8011.
- (144) Meth, J. S.; Gam, S.; Choi, J.; Lin, C. C.; Composto, R. J.; Winey, K. I. Excluded Volume Model for the Reduction of Polymer Diffusion into Nanocomposites. *J. Phys. Chem. B* **2013**, *117*, 15675–15683.
- (145) Gam, S.; Meth, J. S.; Zane, S. G.; Chi, C.; Wood, B. A.; Winey, K. I.; Clarke, N.; Composto, R. J. Polymer Diffusion in a Polymer Nanocomposite: Effect of Nanoparticle Size and Polydispersity. *Soft Matter* **2012**, *8*, 6512.
- (146) Xue, C.; Zheng, X.; Chen, K.; Tian, Y.; Hu, G. Probing Non-Gaussianity in Confined Diffusion of Nanoparticles. *J. Phys. Chem. Lett.* **2016**, *7*, 514–519.

- (147) Babayekhorasani, F.; Dunstan, D. E.; Krishnamoorti, R.; Conrad, J. C. Nanoparticle Diffusion in Crowded and Confined Media. *Soft Matter* **2016**, *12*, 8407–8416.
- (148) Schneider, G. J.; Nusser, K.; Willner, L.; Falus, P.; Richter, D. Dynamics of Entangled Chains in Polymer Nanocomposites. *Macromolecules* **2011**, *44*, 5857–5860.
- (149) Bailey, E. J.; Riggleman, R. A.; Winey, K. I. Polymer Conformations and Diffusion through a Monolayer of Confining Nanoparticles. *Macromolecules* **2020**, *53*, 8171–8180.
- (150) Wang, K.; Winey, K. I. Vehicular and Core-Shell Nanoparticle Diffusion in Entangled Polymer Melts. Submitted.
- (151) Tonelli, A. E. Conformational Characteristics of Poly(2-Vinylpyridine). *Macromolecules* **1985**, *18*, 2579–2583.
- (152) Sko, T.; Vaghefikia, F.; Fitter, rg; Kondrat, S. Macromolecular Crowding: How Shape and Interactions Affect Diffusion. *J. Phys. Chem* **2023**, *2020*, 19.
- (153) Hao, T.; Riman, R. E. Calculation of Interparticle Spacing in Colloidal Systems. *J. Colloid Interface Sci.* **2006**, *297*, 374–377.
- (154) Brouwers, H. J. H. Particle-Size Distribution and Packing Fraction of Geometric Random Packings. *Phys. Rev. E - Stat. Nonlinear, Soft Matter Phys.* **2006**, *74*, 031309.
- (155) Karatrantos, A.; Composto, R. J.; Winey, K. I.; Clarke, N. Nanorod Diffusion in Polymer Nanocomposites by Molecular Dynamics Simulations. *Macromolecules* **2019**, *52*, 2513–2520.
- (156) Asgari, N.; Baaske, M. D.; Orrit, M. Burst-by-Burst Measurement of Rotational Diffusion at Nanosecond Resolution Reveals Hot-Brownian Motion and Single-Chain Binding. *ACS Nano* **2023**, *17*, 12684–12692.
- (157) Jouault, N.; Zhao, D.; Kumar, S. K. Role of Casting Solvent on Nanoparticle Dispersion in Polymer Nanocomposites. **2014**.
- (158) Murphy, T. M.; Langhe, D. S.; Ponting, M.; Baer, E.; Freeman, B. D.; Paul, D. R. Physical Aging of Layered Glassy Polymer Films via Gas Permeability Tracking. *Polymer (Guildf)*. **2011**, *52*, 6117–6125.
- (159) Karen, A.; Ito, K.; Kubo, Y. {TOF-SIMS} Analysis of Lithium Air Battery Discharge Products Utilizing Gas Cluster Ion Beam Sputtering for Surface Stabilization. *Surf. Interface Anal.* **2014**, *46*, 344–347.
- (160) Foley, J. D.; Fischler, M. A.; Bolles, R. C. Graphics and Image Processing Random Sample

Consensus: A Paradigm for Model Fitting with Applications to Image Analysis and Automated Cartography. **1981**.

- (161) Point Cloud Processing - MATLAB & Simulink
<https://www.mathworks.com/help/vision/point-cloud-processing.html> (accessed May 6, 2024).
- (162) Wang, X.; Tilley, R. D.; Watkins, J. J. Simple Ligand Exchange Reactions Enabling Excellent Dispersibility and Stability of Magnetic Nanoparticles in Polar Organic, Aromatic, and Protic Solvents. *Langmuir* **2014**, *30*, 1514–1521.
- (163) Cook, E.; Labiento, G.; Chauhan, B. P. S. Fundamental Methods for the Phase Transfer of Nanoparticles. *Molecules* **2021**, *26*.

APPENDIX C : SUPPORTING INFORMATION FOR CHAPTER 4

Materials and Experimental Methods in Detail

Materials: Poly(2-vinyl pyridine) (P2VP) of 158 kDa, PDI = 1.06, $R_g = 10.9$ nm, was obtained from Scientific Polymer Products Inc. and used as received. The molecular weight and polydispersity index (PDI) were verified using gel permeation chromatography. R_g was calculated according to Rubinstein and Colby by $R_g^2 = C_\infty n l^2$ where l is the bond length, n is the number of backbone bonds, and C_∞ is the characteristic ratio.³⁸ For P2VP, C-C backbone bond length $l = 1.54$ Å, $n = 2 * M_w / M_{2VP \text{ monomer}}$, and $C_\infty = 10$.³⁹ Nissan-STL silica (SiO₂) nanoparticles ($R_{NP-SiO_2} = 26.2$ nm, PDI = 1.19) and aluminum oxide (Al₂O₃) nanoparticles from Sigma Aldrich ($R_{NP-Al_2O_3} = 6.5$ nm, PDI = 1.14) were chosen to probe smaller NPs diffusing into a nanocomposite with larger NPs. The SiO₂ NPs were transferred from methyl-ethyl ketone (MEK) to methanol (MeOH) to facilitate dispersion. Al₂O₃ NPs were prepared in a 50 g/L MeOH solution and treated with a small amount of P2VP to promote a bound polymer layer and thereby prevent aggregation. Dynamic light scattering was used to confirm particle size, dispersity, and NP dispersion in solution.

Trilayer Sample Preparation: **Figure 1a** shows a schematic illustrating the trilayer sample geometry in which Al₂O₃ NPs diffuse from a thin center layer into SiO₂-loaded P2VP thick outer layers. The diffusion experiments use trilayer configurations comprising of a $\phi_{Al_2O_3} = 0.01$, 200 ± 60 nm Al₂O₃-P2VP layer sandwiched between two ~ 4 μm SiO₂-P2VP matrix layers of varying ϕ_{SiO_2} (0.001, 0.005, 0.010, 0.025, 0.050). The thick P2VP-SiO₂ polymer nanocomposite (PNC) layers were spin-coated onto silicon wafers using conditions estimated by the effective viscosity of the NP suspension based on particle loading. The Al₂O₃-P2VP PNC mid-layer was spin-coated onto silicon wafers from a suspension of NPs, P2VP, and MeOH. Layer thicknesses

were confirmed with scanning electron microscopy (SEM). Similar to our previous procedures,²⁷ the Al₂O₃-P2VP mid-layers of the trilayer sample were transferred onto SiO₂-P2VP base-layers by etching the spuncoated Al₂O₃-P2VP layers off the SiO₂ wafer using a 20 wt% NaOH solution. This process resulted in a floating Al₂O₃-P2VP film that was rinsed with DI water and stacked on top of the SiO₂-P2VP base-layer. The top SiO₂-P2VP layer was transferred to the bilayer in the same manner.

Annealing and Diffusion Measurement: The assembled trilayer samples were annealed at 180 °C under vacuum (< 50 Pa) to induce nanoparticle diffusion. The duration of annealing (1-6 h) was varied to allow the smaller Al₂O₃ nanoparticles to traverse different distances into the SiO₂-P2VP matrix. Note that given our prior study,²⁶ we expect the larger SiO₂ NPs to be nominally stationary during these annealing conditions and this is confirmed in our results. By varying the diffusion time, we evaluated whether or not the Al₂O₃ nanoparticle diffusion was independent of *t* annealing time.

ToF-SIMS Analysis: Time-of-flight secondary mass spectroscopy (ToF-SIMS) was employed to measure the cross-sectional nanoparticle concentration profiles within the trilayer samples. ToF-SIMS finds wide-ranging applications in polymer science, particularly for analyzing surface and interface properties of polymers and polymer composites. Our previous research measured accurate diffusion coefficients for SiO₂ nanoparticles and polystyrene using ToF-SIMS, establishing it as a technique for measuring both nanoparticle and polymer diffusion.²⁷ This method requires that the diffusing species produces ions that are distinct from the matrix. Trilayer samples were cross sectioned by snapping along a crystallographic plane of the silicon wafer using a diamond scribe. A focused beam of high-energy ions sputter molecular fragments from the

freshly exposed cross-section and these fragments are analyzed by a mass spectrometer to determine their mass-to-charge (m/q) ratio. This process generates a 2D compositional map as each layer is removed, and these 2D maps are compiled into a 3D compositional data set.

ToF-SIMS experiments was conducted using a Tescan S8252X FIB-SEM equipped with a Xe^+ beam, with specific ion beam conditions optimized to maximize resolution and data quality.²⁷ In this case, measurements were taken with Xe^+ FIB parameters at 30 keV and 100 pA with 1024×1024 pixel resolution on positive ion mode for 400 frames across all samples. Critical for this study, ToF-SIMS clearly distinguishes between the Al^+ ($m/q = 27$) and Si^+ ($m/q = 28$) ions to provide sufficient contrast to identify the diffusing Al_2O_3 NPs from the background SiO_2 NPs. **Figure S1** provides mass spectra and XY compositional maps of the Al^+ and Si^+ ions that demonstrate the ability of ToF SIMS to delineate these two elements.

C.1 ToF-SIMS Characterization of the SiO₂-Al₂O₃-PNC trilayer Films

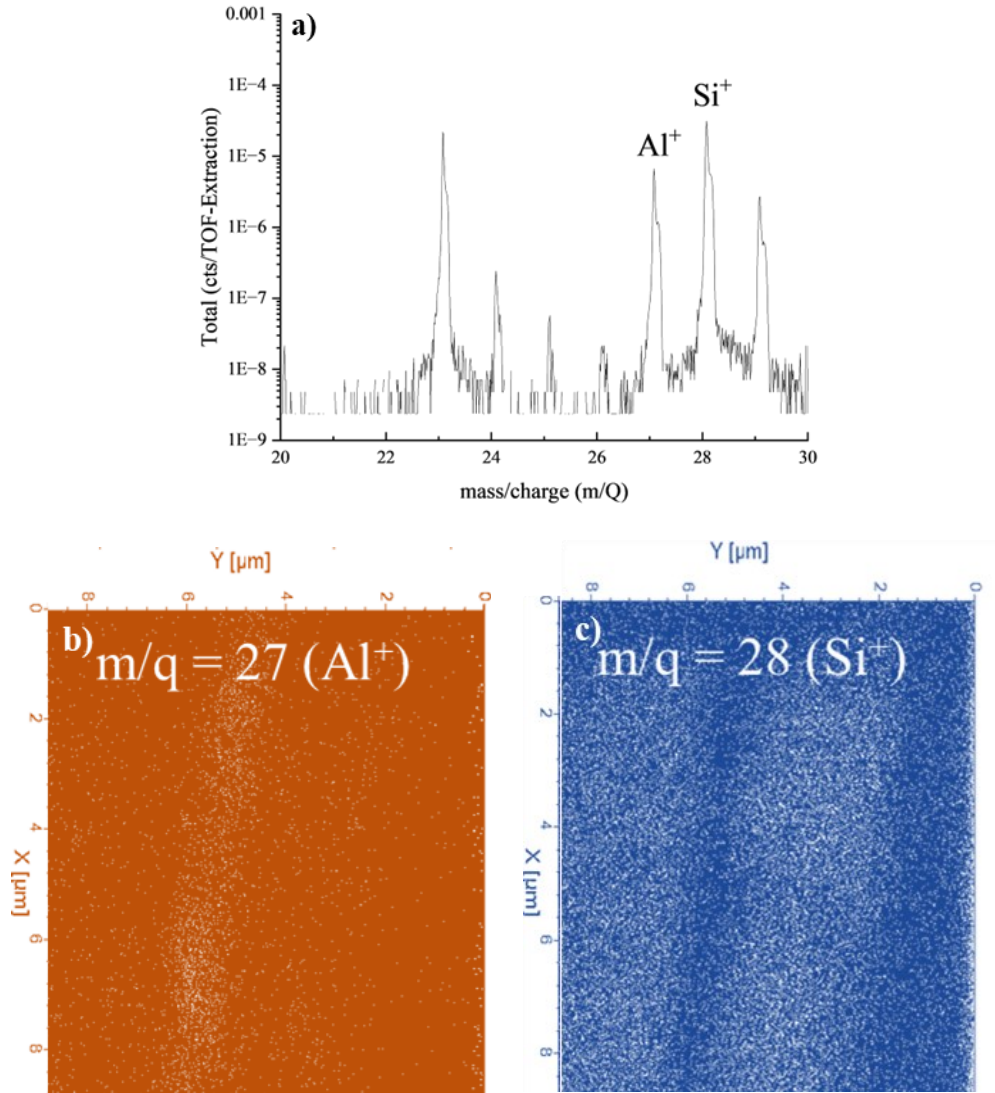


Figure C.1: ToF-SIMS mass spectra and compositional maps for Al⁺ ($m/q = 27$) and Si⁺ ($m/q = 28$) ions. ToF-SIMS mass spectra and compositional maps for Al⁺ ($m/q = 27$) and Si⁺ ($m/q = 28$) ions where white indicates signal. Trilayer sample of 5 vol% SiO₂ NP / 5 vol% Al₂O₃ NP / 5 vol% SiO₂ NP in P2VP and annealed for 3 h at 180 °C. **a)** Total mass spectra from $m/q = 20 - 30$ with Al⁺ ($m/q = 27$) and Si⁺ ($m/q = 28$) peaks labeled. ToF-SIMS mass spectra images collapsed along

the z-axis for **b)** Al^+ ($m/q = 27$) and **c)** Si^+ ($m/q = 28$). Images demonstrate that ToF SIMS distinguishes the Al_2O_3 NPs in the midlayer (~ 500 nm) and the SiO_2 NPs in the thicker top and bottom layers.

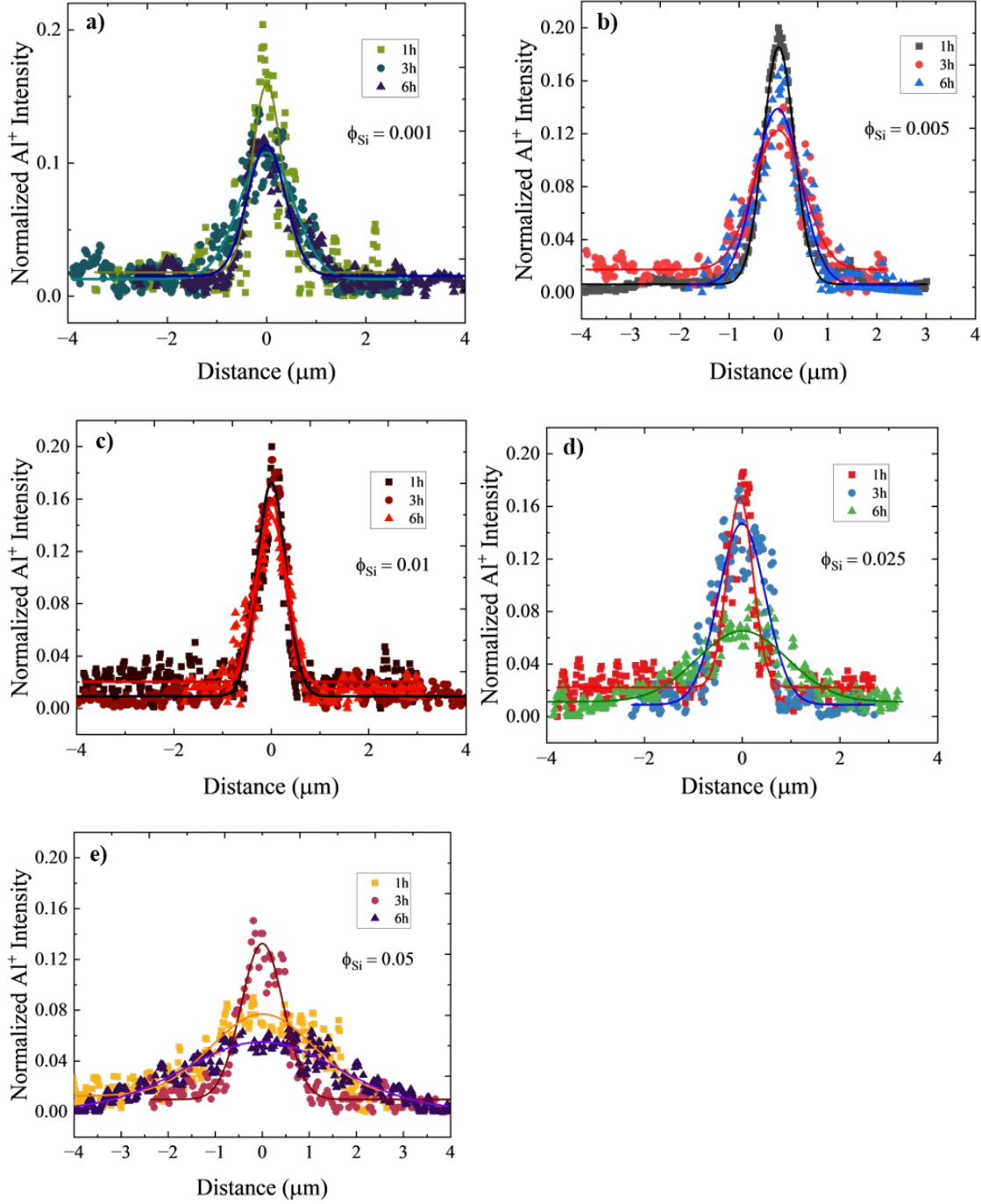


Figure C.2 : Normalized concentration profiles from ToF-SIMS for Al_2O_3 nanoparticles

($R_{\text{NP}} = 6.5 \text{ nm}$) diffusing into polymer nanocomposites with $\phi_{\text{SiO}_2} = 0.001 - 0.050$. a) $\phi_{\text{SiO}_2} =$

0.001 , b) $\phi_{\text{SiO}_2} = 0.005$, c) $\phi_{\text{SiO}_2} = 0.01$, d) $\phi_{\text{SiO}_2} = 0.025$, and e) $\phi_{\text{SiO}_2} = 0.05$. Areas were

normalized to 0.2 such that the initial film of thickness 0.2 μm is a square function of
intensity = 1 from -0.1 to 0.1 μm .

C.2 Diffusion Coefficients for Al_2O_3

Table C.1: D_{NP} values for Al_2O_3 nanoparticles from composites with $\phi_{\text{Al}_2\text{O}_3} = 0.01$ and annealed for 1 - 6 hours at 180 °C. Fits are shown above in Figure C.2.

ϕ_{SiO_2}	$D_{NP} (\text{cm}^2/\text{s})$ $t = 1 \text{ h}$ R^2	$D_{NP} (\text{cm}^2/\text{s})$ $t = 3 \text{ h}$ R^2	$D_{NP} (\text{cm}^2/\text{s})$ $t = 6 \text{ h}$ R^2	Average D_{NP} ($\text{cm}^2/\text{s}) \pm$ STD
0.001	7.4×10^{-14} 0.821	1.1×10^{-13} 0.880	3.1×10^{-14} 0.882	7.2 ± 3.9 $\times 10^{-14}$
0.005	1.2×10^{-13} 0.979	7.6×10^{-14} 0.913	4.4×10^{-14} 0.901	8.0 ± 3.8 $\times 10^{-14}$
0.010	8.5×10^{-14} 0.854	3.1×10^{-14} 0.960	4.5×10^{-14} 0.923	5.4 ± 2.8 $\times 10^{-14}$
0.025	1.0×10^{-13} 0.878	9.9×10^{-14} 0.882	2.2×10^{-13} 0.816	2.1 ± 1.8 $\times 10^{-13}$
0.050	8.1×10^{-13} 0.809	8.6×10^{-14} 0.935	6.3×10^{-13} 0.913	4.4 ± 3.6 $\times 10^{-13}$

C.3 Derivation of Bimodal Interparticle Distance Model and Calculation

Here we derive an expression for the interparticle distance in a polymer nanocomposite with nanoparticles of two size that are randomly packed. Our approach is based on the derivation of the interparticle distance in systems with randomly packed monodisperse nanoparticles.

Total Excess Volume, V_x

The total excess volume, V_x , is defined as the difference between the maximum nanoparticle packing volume and the volume occupied by nanoparticles (NPs) in the PNC.

$$V_x = V_{max} - V_{NP} = V_{PNC} * \varphi_{max} - V_{PNC} * \varphi_{NP} \quad (C1)$$

where V_{max} is the nanoparticle volume at maximum packing, which can be experimentally determined or theoretically estimated; V_{NP} is the volume occupied by the nanoparticles, calculated and is the product of the nanocomposite volume V_{PNC} and the nanoparticle volume fraction φ_{NP} ; and φ_{max} is the volume fraction at maximum nanoparticle packing as derived from simulations or theoretical models (e.g., 0.630 for dense random packing of monodisperse spheres).¹⁵⁴ Here the r_L/r_s ratio is ~ 4 , and a combination of experimental and computational methods provides $\varphi_{max-bi} \sim 0.606$.¹⁵⁴

Excess Volume per Particle, ψ

The excess volume per particle, ψ , is calculated by dividing the total excess volume V_x by the total number of nanoparticles n_{Total}

$$\psi = \frac{V_x}{n_{Total}} \quad (C2)$$

$$n_{Total} = n_L + n_S \quad (C3)$$

where n_L and n_S are the number of large and small nanoparticles. The number of large and small nanoparticles is given by

$$n_L = \frac{V_{NP-L}}{V_{iL}} = \frac{V_{PNC} * \phi_L}{\frac{4}{3}\pi r_L^3} \quad (C4)$$

$$n_S = \frac{V_{NP}}{V_{iS}} = \frac{V_{PNC} * \phi_S}{\frac{4}{3}\pi r_S^3} \quad (C5)$$

where ϕ_L and ϕ_S are their respective volume fractions and V_{iL} and V_{iS} assuming are the volumes of the individual spherical particles. Substituting n_L and n_S into the expression for ψ , we get:

$$\psi = \frac{V_X}{\frac{V_{PNC} * \phi_L}{\frac{4}{3}\pi r_L^3} + \frac{V_{PNC} * \phi_S}{\frac{4}{3}\pi r_S^3}} = \frac{(\phi_{Max} - \phi_L - \phi_S)}{\frac{\phi_L}{\frac{4}{3}\pi r_L^3} + \frac{\phi_S}{\frac{4}{3}\pi r_S^3}} \quad (C6)$$

Cell Radius, r_{cell}

The cell radius r_{cell} is derived from the volume of a "cell" V_{cell} , which includes the volume of an average particle plus the excess volume per particle ψ .

$$V_{cell} = V_{average\ particle} + \psi \quad (C7)$$

Defining the average particle volume as a weighted sum of large and small particle volumes, and using the expression for ψ derived above, we can express V_{cell} as:

$$\begin{aligned} V_{cell} &= V_{ip-L} \frac{n_L}{n_{Total}} + V_{ip-S} \frac{n_S}{n_{Total}} + \psi \\ &= \frac{4}{3}\pi r_L^3 * \frac{n_L}{n_{Total}} + \frac{4}{3}\pi r_S^3 * \frac{n_S}{n_{Total}} + \psi \end{aligned} \quad (C8)$$

The cell radius r_{cell} can then be calculated from V_{cell} using the formula for the volume of a sphere:

$$r_{cell} = \left[\frac{3V_{cell}}{4\pi} \right]^{1/3} = \left[r_L^3 \frac{n_L}{n_{Total}} + r_S^3 \frac{n_S}{n_{Total}} + \frac{3}{4\pi} \psi \right]^{1/3} \quad (C9)$$

Interparticle Distance in a Bimodal System, ID_{bi}

Finally, the interparticle distance (ID) in a bimodal system is defined by the distance each particle occupies (twice the cell radius) minus the number-weighted average nanoparticle radius, \bar{r}_{NP} :

$$ID_{bi} = 2(r_{cell} - \bar{r}_{NP}) = 2([r_L^3 \frac{n_L}{n_{Total}} + r_S^3 \frac{n_S}{n_{Total}} + \frac{3}{4\pi} \psi]^{\frac{1}{3}} - \bar{r}_{NP})) \quad (C10)$$

$$\bar{r}_{NP} = \frac{n_L r_L + n_S r_S}{n_{Total}} \quad (C11)$$

This expression accounts for the average volume occupied by a particle, including the excess volume, and accounts for the nanoparticle sizes and their concentrations.

Table C.2: Tabulated intensities taken from individual samples at the FWHM, the calculated $\phi_{Al_2O_3-local}$, the number of small and larger NPs used for bimodal interparticle distance calculation, and ID_{bi} .

ϕ_{SiO_2}	Annealing Time (h)	Intensity At FWHM	$\phi_{Al_2O_3-local}$ ($\phi_{Al_2O_3} * I_{FWHM}$)	nSiO ₂	nAl ₂ O _{3,local}	ID_{bi} (nm)
0.001	1	0.092	0.00092	80	160	69
0.005	1	0.100	0.00100	398	174	53
0.010	1	0.106	0.00106	796	184	45
0.025	1	0.088	0.00088	1991	153	39
0.050	1	0.030	0.00030	3982	52	38
		--	--		--	
0.001	3	0.069	0.00069	80	119	78
0.005	3	0.070	0.00070	398	122	62
0.010	3	0.122	0.00122	796	212	42
0.025	3	0.062	0.00062	1991	108	45
0.050	3	0.070	0.00070	3982	122	31
		--	--		--	
0.001	6	0.035	0.00035	80	61	101
0.005	6	0.074	0.00074	398	129	60
0.010	6	0.064	0.00064	796	111	57
0.025	6	0.032	0.00032	1991	56	56
0.050	6	0.024	0.00024	3982	42	40

C.4 Higher Loading ($\phi_{Al_2O_3} = 0.05$) Arrested Diffusion at $ID_{bi} < 1$.

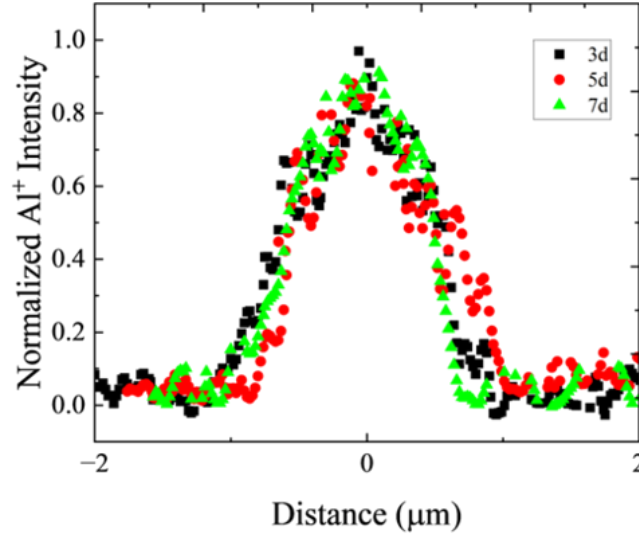


Figure C.3 : Concentration profiles for $\phi_{Al_2O_3} = 0.05$ annealed from 1 - 7 days. The profiles overlap and exhibit no significant broadening of the FWHM, indicating restricted diffusion behavior over these extended annealing periods at these nanoparticle concentrations.

Table C.3: D_{NP} values for Al_2O_3 nanoparticles from composites with $\phi_{Al_2O_3} = 0.05$ and annealed for 1 - 7 days at 180 °C. These diffusion coefficients decrease systematically with annealing time indicating that system has evolved upon annealing. Crossed out cells indicate no sample was measured.

ϕ_{SiO_2}	D_{NP} (cm ² /s) 1 d	D_{NP} (cm ² /s) 3 d	D_{NP} (cm ² /s) 5 d	D_{NP} (cm ² /s) 7 d
0		4.3×10^{-14}		
0.010	4.1×10^{-14}		1.2×10^{-14}	
0.025		4.9×10^{-15}		1.3×10^{-15}
0.050		6.5×10^{-15}	3.0×10^{-15}	1.1×10^{-15}
0.100		1.7×10^{-15}	1.0×10^{-15}	3.2×10^{-16}

APPENDIX D : TOF-SIMS OPERATION AND DATA ANALYSIS

D.1 Introduction to Tescan S8252X FIB-SEM

The Tescan S8252X, present in the Singh Center, is a dual-beam plasma focused ion beam scanning electron microscope (FIB-SEM), equipped with a versatile variable gas plasma ion source. This instrument is particularly noted for its time-of-flight secondary ion mass spectrometer (ToF-SIMS), an energy-dispersive X-ray spectrometer (EDX), and additional advanced features such as a cryogenic stage and sample transfer mechanism. These capabilities enable site-specific imaging, materials analysis, and sample manipulation over a wide range of temperatures and sample types. The inclusion of a cryogenic stage allows for handling frozen or temperature-sensitive samples, broadening the scope of potential applications.

The Tescan FIB-SEM systems are optimized for performance and throughput, with electron and ion beam focal points designed to coincide. This allows for simultaneous SEM imaging during FIB milling tasks, enhancing precision for diverse applications. The Tescan systems offer a choice between Gallium ions and Xenon ion plasma sources; Gallium ions provide higher precision in fabrication and nanopatterning, while Xenon plasma FIBs are known for their high ion beam currents, facilitating the removal of large material volumes up to 50 times faster compared to Gallium-FIBs.⁷⁸ At Penn, we have a Xenon plasma FIB system.

D.1.1 Fundamentals of ToF-SIMS

The Tescan S8252X FIB-SEM, equipped with a Xenon (Xe^+) plasma source offers great capabilities for surface analysis and depth profiling. This section aims to outline the operational

principles, advantages, and potential limitations when utilizing the Tescan S8252X for time-of-flight secondary ion mass spectrometry (ToF-SIMS) analysis.

The operational principles of the Tescan S8252X FIB-SEM involve directing a focused beam of Xe^+ ions toward the sample surface. This interaction leads to the sputtering of surface atoms, a portion of which become ionized and ejected as secondary ions. These ions undergo analysis based on their time-of-flight to a charged detector (positive or negative), which allows for the determination of their mass-to-charge ratios (m/q). This sophisticated process facilitates the identification of the sample's elemental and molecular composition at the surface with remarkable spatial resolution.

The standout feature of ToF-SIMS analysis on the Tescan S8252X is its ability to deliver detailed chemical information at sub-micron spatial resolution. The technique's capacity for depth profiling, achieved through sequential sputtering and analysis, enables the investigation of layered structures and the distribution of various elements and compounds within a sample. The ToF-SIMS's high mass resolution and sensitivity make it an asset for the study of complex material systems, such as polymers, composites, and thin films.

The advantages of employing the Tescan S8252X for ToF-SIMS analysis are numerous. The Xe^+ plasma source enhances the instrument's spatial resolution, allowing for detailed surface and cross-sectional analysis with a spot size of ~ 100 nm. The depth profiling capability offers three-dimensional data on the distribution of elements and compounds within a sample. Moreover, the ToF-SIMS analysis can detect a broad range of elements and molecules, providing a qualitative understanding of the sample's chemical composition especially in the $m/q < 50$ range. With combined use of a quantitative chemical composition method like X-ray photoelectron

spectroscopy (XPS), chemical composition can be determined as well. Compared to techniques like XPS and energy dispersive X-ray spectroscopy (EDX), ToF-SIMS excels in delivering high-resolution 3D imaging. It provides a clearer view of the sample's chemical composition across different layers, including depth profiles. Furthermore, it is particularly useful for samples with intricate topography due to its ability to capture detailed images without interference from surface irregularities. The secondary electron images collected alongside the ion spectra offer an additional layer of contextual information.

However, there are limitations to consider. ToF-SIMS is inherently surface-sensitive, primarily providing information about the sample's uppermost layers, which may restrict its effectiveness for bulk material analysis without depth profiling. For example, when milling P2VP for 300 frames at 100 pA (~1 hour of instrument time), this only probes the top ~300 nm of sample. Measurement parameter choices (beam current, accelerating voltage, area size of milling) and material milled will determine the depth measured, and therefore surface sensitivity. Depth measurement must also be done geometrically through using the SEM capabilities, or via atomic force microscopy (AFM), to obtain the average depth per frame. Additionally, the focused ion beam might cause damage or alter sensitive materials through cross-linking, potentially complicating the interpretation of results.

Matrix effects, influenced by the chemical and structural composition of the sample, also play a significant role in signal quality.⁷⁹ Materials with greater electronegativity or electropositive ions typically produce higher ion yields. Hydrocarbon saturation, cross-linking, and surface charge further impact the ion formation and survivability processes, which are crucial for obtaining a

representative analysis.⁷⁸ Therefore, understanding these mechanisms is essential for interpreting data accurately and improving future experiments.

The data analysis process for ToF-SIMS data obtained from the Tescan S8252X is rigorous and involves interpreting mass spectra, identifying specific element and compound peaks, and quantifying their distribution within the sample. In the following sections, I provide one example of ToF-data processing using MATLAB to tilt correct cross-sectional data, however the 3D nature of the data results in many other possibilities for sample orientation and design.

The Tescan S8252X FIB-SEM, when equipped with a ToF-SIMS analysis detector, presents a powerful approach for examination of material surfaces and interfaces. Its application in exploring nanoparticle dynamics within polymer nanocomposites exemplifies its adaptability and effectiveness in tackling intricate research questions within materials science and engineering. This guide is intended to serve as a foundational resource for those aiming to leverage the capabilities of the Tescan S8252X in their future polymer studies.

D.1.2 Primary vs. Cluster Ion Beams in ToF Systems

When considering ToF-SIMS analysis, the distinction between primary and cluster ion beams is crucial, as each has distinct advantages and implications for material analysis. Primary ion beams are typically composed of single ions, such as Gallium or Xenon. Primary ion beams offer high spatial resolution and are excellent for precise sputtering and depth profiling. They are particularly effective for hard materials or when high precision is required in nanopatterning and were therefore used widely in the semiconductor industry. The focused nature of primary ion beams ensures detailed surface analysis and depth profiling with minimal sample damage, suitable

for a wide range of materials including metals, semiconductors, and certain polymers. In our system, Xe^+ ($z = 54$) offers better milling capabilities and lower penetration depth compared to Gallium ($z = 31$) systems due to its higher mass, while Gallium beams would provide better lateral resolution.⁷⁸

Cluster ion beams consist of aggregated ions, which provide a softer sputtering effect, reducing the damage to the sample surface. This makes them preferable for analyzing beam-sensitive materials, organic samples, and biological specimens. Cluster ion beams distribute energy over a larger area, minimizing the alteration of the chemical state of the surface being analyzed. They are particularly beneficial for obtaining high mass resolution and sensitivity, crucial for analyzing complex organic molecules and polymers. Most modern polymer applications utilize a cluster ion beam for depth profiling or surface analysis rather than the Xe^+ beam in the Singh Center.^{81,88,93,159} We therefore optimize our sample collection parameters to account for these differences compared to polymer literature.

D.2 ToFWERK Software

ToFWERK's software suite by Tescan is specifically designed to enhance the capabilities of time-of-flight mass spectrometers. The suite includes several key components such as TofDaq and Tofware, each tailored for different aspects of mass spectrometry operations. TofDaq is primarily used for data acquisition and is present on the FIB desktop. TofDaq captures and manages the data generated during mass spectrometry analyses, enabling real-time monitoring and adjustments through viewing depth profile, XY, and XZ imaging for each m/q value.

ToFware is geared towards post-processing. It processes the raw data collected during experiments to extract meaningful insights and results. This includes data analysis, visualization, and the generation of comprehensive reports that detail the findings of the mass spectrometry analysis. This software is integral to extracting, analyzing, and interpreting the complex data generated during mass spectrometry experiments. ToFware provides users with a suite of analysis tools that support a broad range of functionalities from basic to advanced data manipulation.

ToFware provides a comprehensive toolset for analyzing mass spectrometry data, encompassing advanced visualization and spectral processing features. By leveraging its robust data analysis capabilities, users can examine spectra and ion images in high resolution, facilitating precise identification of mass-to-charge (m/q) ratios and accurate mapping of ion distributions within samples.

Key spectral processing tools, including smoothing, baseline correction, and peak deconvolution, enhance the signal-to-noise ratio and resolve overlapping spectral peaks, enabling precise identification of signals less than 1 m/q apart. This precision is critical for chemical analyses that demand high specificity, such as differentiating between D^+ and H_2^+ ions for deuterated materials. This allows for more precise analysis of deuterated polymer materials. ToFware also supports quantitative analysis by integrating peak areas and comparing ion intensities across multiple samples, allowing for accurate quantification of specific elements or molecules. This quantitative functionality empowers researchers to obtain reliable insights from their mass spectrometry data, ensuring precise and consistent analytical results.

Notably, ToFware performs the raw data processing converting the highly complex (3D pixel cube for each m/q peak) into individual .raw files. By exporting the .raw file for a specific m/q, you obtain a 4D matrix given X, Y, Z (frames), and intensity at each location. I import these .raw files for data processing in MATLAB.

D.3 Tilt-Correction Program – MATLAB Code

This section describes the custom MATLAB code used for tilt correction and 3D ToF-SIMS data analysis of bi/trilayer samples, leveraging MATLAB's Computer Vision Toolbox. The code was conceptualized to address the specific challenges associated with the analysis of raw 3D data obtained from ToF-SIMS experiments. Given the inherent complexity and ~10 Gb size of the data sets, which includes the need for spatial orientation correction (tilt correction) and the extraction of meaningful concentration profiles, an efficient computational approach was necessary. The MATLAB environment had the necessary built-in tools for improving the visualization of the 3D raw ToF-SIMS data files and Computer Vision Toolbox streamlined the data processing step.

D.3.1 The Computer Vision Toolbox

A key feature of the developed code is its employment of MATLAB's Computer Vision Toolbox, which provides algorithms and functions for 3D point cloud processing. This toolbox was instrumental in enabling the efficient manipulation and analysis of 3D data sets, particularly through functions like **pcfitplane**, which facilitates the fitting of a geometric plane to a set of 3D points. This capability is crucial for the tilt correction step, where the orientation of the data set needs to be normalized based on the plane of greatest intensity within a defined Region of Interest

(ROI).¹²⁵ These functions are based on the RANSAC algorithm, an iterative method designed for robustly fitting a model to data that includes outliers.¹²⁶ It operates by repeatedly selecting a random subset of the data to estimate model parameters, and then determining which data points fit this model within a defined threshold. This process effectively segregates inliers (data consistent with the model) from outliers, ensuring the model is influenced only by relevant data. The algorithm's strength lies in its ability to handle datasets heavily contaminated with outliers, making it ideal for applications where data integrity varies widely, such as identifying signal with significant background noise.¹⁶⁰

The decision to convert raw matrix data into a point cloud representation before analysis was driven by several considerations: One, spatial clarity: point clouds offer a more intuitive understanding of the spatial distribution of data points, making it easier to identify patterns, anomalies, and areas of interest.¹²⁵ Two, efficiency: By focusing on non-zero data points, the point cloud approach reduces the computational load, allowing for more efficient data processing. The raw file contains significant zero signal points which can increase processing time by an order of magnitude. Three, flexibility: the point cloud format is amenable to a variety of geometric transformations and analyses, including plane fitting and ROI extraction, which are integral to the tilt correction process. For example, the processability of the point cloud data format is commonly

used for robotics applications, where translating large 3D data sets of physical objects to vector distances is useful for navigation.

D.3.2 Workflow Overview

The code initiates with the importation of raw ToF-SIMS data, followed by the transformation of this data into a point cloud object. A plane is then fitted to the area of greatest intensity within the specified ROI, facilitating the correction of data tilt. Subsequent steps involve the visualization of the tilt-corrected data and the extraction of a 1D concentration profile, which is pivotal for understanding the compositional gradients within the sample. This returns three figures. Figure 1 displays the raw data and plane fit for visual evaluation. Figure 2 displays the integrated 1D concentration profile used for fitting a diffusion coefficient. Figure 3 shows the collapsed XY view of the tilt-corrected data set.¹⁶¹

It is essential to visually evaluate all three figures to ensure a good plane fit, as each plane fit is done using the RANSAC algorithm, which generates a random initial seed for procedural fitting. An initial bad seed may result in a less robust fit. This occurs rarely, but if it does, please re-run the code and evaluate the fit visually once again. The best fit is obtained by setting the most accurate region of interest (ROI), where the diffusing film is to guide the initial seed and model for a good “first guess” for procedural fitting.

This computational toolset streamlines the processing workflow but also enhances the accuracy and interpretability of the results, thus providing support for ToF-SIMS users when investigating diffusion profiles along a cross-section. This code can be applied to other layered

geometries too, if you are aiming to tilt-correct to a certain plane, however it is not optimized for that use. Large heterogeneities will cause spikes in the signal, resulting in the plane-fitting being overly biased.

Below is my MATLAB Code...


```

%% HEADER %%
%
*****
***** %
% date
%   Author: Kait Wang 2023
%   created: 22 May 2022
%   last revision: 13 Jun 2023
% purpose
%   load in ToFSIMS 3D data and fits a plane to data for tilt correction
%   centers data around zero for fitting

% operation
%   how it works
%   takes in .raw files from ToF-SIMS Explorer export and converts to
%   pointcloud object. A plane is fit to the area of greatest intensity
%   within a given ROI and tilt correct it
%

% requirements
%   sample  --  name of file containing raw data
%              has .raw extension
%   pix      --  image size after binning
%   Threshold -- distance from plane that should be considered in fitting

% returns
%   makes 3 graphs ...
%   figure 1 : Raw data in 3D visualized with fitted plane.
%   figure 2 : Creates 1D concentration profile from tilt corrected data
%   figure 3 : XY view of corrected data
%   .txt file of the 1D concentration profile
%
*****
***** %

%% CLEAR SPACE %%

%start timer, clear command window, clear variables
clc ;
clearvars ;
imtool close all ;

```

```

% format time in seconds
format longG ;
format compact ;
iptsetpref('ImshowBorder','tight') ; %image preferences

%% INITIALIZE VARIABLES %%
% Must input file name in Mw_annealed_Xpix_YFoV_Zframes_# for
% autopopulating
% ex '400k1a0_1024pix_10umFoV_700frames_1.raw'
sample_file = ('100ka6h_1024pix_10umFoV_400frames_mq27_1.raw') ;
excel_name = sample_file(1:7);

frame      = str2double(sample_file(25:27)) ;
FoV = str2double(sample_file(17:18)) ; % microns defined by original
image collection
pix      = str2double(sample_file(9:12))/2;      % # of pixels in
image (XZ) plane
pixel_size = FoV/pix ; % micron/pixel

% ROI inputs
ROI_x_low  = 000 ; % ROI for plane fitting
ROI_x_high = 412 ; % end x coordinate defining ROI
ROI_y_low  = 000 ; % ROI for plane fitting
ROI_y_high = 400 ; % end y coordinate defining ROI
ROI_z_low  = 100 ; % z limit to consider for fitting (bottom) based
on number of frames
ROI_z_high = 400 ; % upper z limit to consider for integration
Threshold  = 25 ; % set distance threshold for finding plane (pixels)

screen_location_x      = 2 ; % x position of figure appearing, in
inches
screen_location_y      = 2 ; % y position of figure appearing, in
inches
%FIGURE SIZE FOR ACS
width  = 3.25 ; % width of figure, in inches
height = 4 ; % height of figures, in inches
% %FIGURE SIZE for PPT
% width  = 3 ; % width of figure, in inches
% height = 3 ; % height of figures, in inches

%% LOAD AND FORMAT RAW DATA %%

```

```

% open file
% import data into raw_data, given volume of box and uint data type
% close file
file_id = fopen( sample_file );
raw_data = fread( file_id, pix*pix*frame, 'uint16' ) ;
fclose( file_id ) ;

% reshape raw_data into 1x3 matrix
raw_data = reshape( raw_data, [pix,pix,frame] ) ;

% transpose matrix so xyz are columns
for i = 1:frame
    raw_data(:, :, i) = raw_data(:, :, i)' ;
end

% reshape again?
raw_data = reshape( raw_data, [pix*pix*frame, 1] ) ;

% find where data points does not = 0
raw_data_nonzero = find( raw_data~=0 ) ;
raw_data         = raw_data( raw_data_nonzero ) ;

% make 512 grey value locations for X and Y
grey_value_x = 1:1:pix ;
grey_value_y = 1:1:pix ;
grey_value_z = 1:1:frame ;

% 3D grid coordinates of vectors grey_value_x grey_value_y grey_value_z,
with grey values built in
[X, Y, Z] = meshgrid( grey_value_x, grey_value_y, grey_value_z ) ;

%% create matrix of non-zero data points
coords = [X(:), Y(:), Z(:)] ;
coords = coords( raw_data_nonzero, : ) ;

% focus on region of interest: ROI_y_low < y < ROI_y_high, z > ROI_z_low
index_in_ROI = find( (coords(:,2) > ROI_y_low ) & (coords(:,2) <
ROI_y_high) & (coords(:,3) > ROI_z_low) ) ;
coords_in_ROI = coords( index_in_ROI, : ) ;

%% CALCULATE PLANE OF FIT %%
% convert Mx3 data matrix into pointcloud object for FILM area

```

```

pointcloud_in_ROI = pointCloud( coords_in_ROI ) ;
%
fitted_plane_in_ROI = pcfitplane( pointcloud_in_ROI, Threshold) ;

% Identify parameters of plane as  $ax + by + cz + d = 0$ 
% Identify normal_vector of plane

plane_parameters = fitted_plane_in_ROI.Parameters;
plane_normal_vector = fitted_plane_in_ROI.Normal;

%% PLOT FIGURE 1 -- RAW DATA + PLANE FIT %%

figure(1) %xy view (0,90)
% scatter3(coords(:,1),coords(:,2),coords(:,3),2.5,raw_data,'filled') ;
colormap gray(256) ; %
% pcshow(pointcloud_in_ROI,'BackgroundColor',[1 1 1])
pcshow(pointcloud_in_ROI)

xlim([ROI_x_low,ROI_x_high]);
ylim([ROI_y_low, ROI_y_high]);
zlim([ROI_z_low, frame]);

% view(270,45)
set(gcf,'units','inches', 'Position',[screen_location_x
screen_location_y width height]);
set(gca,'FontSize',12,'FontName','times')
set(gca, 'TickDir', 'in')
xlabel('X (pixels)','FontName','times', 'FontSize',12) ;
ylabel('Y (pixels)','FontName','times', 'FontSize',12) ;
zlabel('Z (frames)','FontName','times', 'FontSize',12) ;
grid off
daspect([1 1 1]) %control aspect ratio
hold on ;

% Creates grid to plot plane on
plane_x_coord = linspace(0,pix);
plane_y_coord = linspace(ROI_y_low, ROI_y_high);
[plane_x,plane_y] = meshgrid(plane_x_coord,plane_y_coord);

% Equation  $z = -1/c*(ax + by + d)$  defines z coordinates of plane of fit
and
% plots plane and normal vector

```

```

plane_z = (-1/plane_parameters(3))*(plane_parameters(1)*plane_x +
plane_parameters(2)*plane_y + plane_parameters(4));
surf(plane_x,plane_y,plane_z,'FaceAlpha',0.6,'FaceColor','c','EdgeColor',
'r','texturemap');

hold off

%% CALCULATE ROTATIONAL MATRIX %%

nx1 = plane_normal_vector(1) ;
ny1 = plane_normal_vector(2) ; %populated from Tof-SIMS.m vector
dimensions
nz1 = plane_normal_vector(3) ;

theta= atand(nx1/ny1) ; %theta in degrees based on geometry

alpharot = atand(-nz1/(ny1*sind(theta)+ny1*cosd(theta))); % define
second angle of rotation from x-axis

%Rotate vector n to the y-z plane.
Ry = [cosd(theta), -sind(theta), 0; sind(theta), cosd(theta), 0; 0, 0 ,
1];

%Rotational vector of n to y axis

Rx = [1, 0, 0; 0 , cosd(alpharot), -sind(alpharot) ; 0, sind(alpharot),
cosd(alpharot)]; %rotation around x axis

Rotation = Rx*Ry; %define rotational matrix

% n_check= Rotation.*plane_normal_vector ; %check n_check should be
approx [0 1 0];
%%
%Rotate matrix to new coordinates
coord_new = zeros(3,length(coords)) ;
for i = 1:length(coords)
coord_new(:,i) = Rotation*coords(i,:)' ;
end

coord_new = coord_new' ;

```

```

% limit pixels for profile
y_min = ROI_y_low ;
y_max = ROI_y_high ;
x_min = ROI_x_low;
x_max = ROI_x_high;

y_pixel = y_min:1:y_max ; y_pixel = y_pixel' ;
y_micron = y_pixel*pixel_size ;

profile = zeros(y_max-y_min+1,1) ;
for k = y_min:y_max
    idx_temp = find( coords(:,2) > k-0.5      & coords(:,2) < k+0.5 & ...
                    coords(:,3) > ROI_z_low & coords(:,3) < ROI_z_high
& ...
                    coords(:,1) > x_min      & coords(:,1) < x_max );
    idx_temp = find( coord_new(:,2) > k-0.5      & coord_new(:,2) < k+0.5
& ...
                    coord_new(:,3) > ROI_z_low & coord_new(:,3) <
ROI_z_high & ...
                    coord_new(:,1) > x_min      & coord_new(:,1) < x_max
);

    profile(k-y_min+1) = sum(raw_data(idx_temp)) ;
end
%find peak location for centering with threshold level to define as a
peak

[pks,locs,widths,proms] =
findpeaks(profile,y_micron,'MinPeakProminence',100000,'Annotate','exte
nts','WidthReference','halfheight','Threshold',10000);
%evaluates if locs is unlimited or empty to see plot

% if isempty(locs) == 1 || isnan(locs)
% locs = 0 ;
% else
% end
% % define profile for plotting
Profile_final = [y_micron, profile] ;

%% WRITE TO TXT FILE + CREATE FIGURES 2+3 %%

%write(Profile_final, excel_name)

```

```

chr2string_sampname = convertCharsToStrings(excel_name);
samp_name = [chr2string_sampname, ".txt"];
fid=fopen(join(samp_name), 'w');
fprintf(fid, '%6.2f %12.8f\n', Profile_final');
fclose(fid);
%writematrix(Profile_final, excel_name, "WriteMode", "overwrite", "FileType", "text", "Delimiter", 'tab');
%writetable(Profile_final, 'test')

% 1D PROFILE PLOT
figure(2)

plot(Profile_final(:,1),
Profile_final(:,2), "Marker", ".", "LineStyle", "none") ;
set(gcf, 'units', 'inches', 'Position', [screen_location_x+3
screen_location_y width height]);
xlabel('Y (\mu m)', 'FontName', 'times', 'FontSize', 12)
ylabel('Intensity(a.u.)', 'FontName', 'times', 'FontSize', 12)
xlim([-6, 6]);

coordreal = coord_new.*pixel_size ; %rel tilt corrected film

%centers film at 0,0
% coordreal(:,2) = coordreal(:,2)-locs(1);

% % PLOT XY VIEW OF CORRECTED DATA
figure(3)
scatter3(coordreal(:,1), coordreal(:,2), coordreal(:,3), 0.5) ;
colormap hot(256) ; %plot raw data
view(90, 90)
set(gcf, 'units', 'inches', 'Position', [screen_location_x+6
screen_location_y width height]);
set(gca, 'FontSize', 12, 'FontName', 'times')
xlabel('X (\mu m)', 'FontName', 'times', 'FontSize', 12) ;
ylabel('Y (\mu m)', 'FontName', 'times', 'FontSize', 12) ;
zlabel('Z (frames)', 'FontName', 'times', 'FontSize', 12) ;
% xlim([-4 FoV+4]) ;
% ylim([-6 6]);
% zlim([3.90625, 10]);
grid off
daspect([1 1 1])

```

D.4 References

- (1) Kumar, S. K.; Benicewicz, B. C.; Vaia, R. A.; Winey, K. I. 50th Anniversary Perspective: Are Polymer Nanocomposites Practical for Applications? *Macromolecules* **2017**, *50*, 714–731.
- (2) Iqbal, A.; Saeed, A.; Ul-Hamid, A. A Review Featuring the Fundamentals and Advancements of Polymer/CNT Nanocomposite Application in Aerospace Industry. *Polym. Bull.* **2021**, *78*, 539–557.
- (3) Thakur, V. K.; Kessler, M. R. Self-Healing Polymer Nanocomposite Materials: A Review. *Polymer (Guildf)*. **2015**, *69*, 369–383.
- (4) Rafique, M. M. A.; Kandare, E.; Sprenger, S. Fiber-Reinforced Magneto-Polymer Matrix Composites (FR-MPMCs) - A Review. *J. Mater. Res.* **2017**, *32*, 1020–1046.
- (5) Shah, V.; Bhaliya, J.; Patel, G. M.; Deshmukh, K. Advances in Polymeric Nanocomposites for Automotive Applications: A Review. *Polym. Adv. Technol.* **2022**, *33*, 3023–3048.
- (6) Kedzior, S. A.; Zoppe, J. O.; Berry, R. M.; Cranston, E. D. Recent Advances and an Industrial Perspective of Cellulose Nanocrystal Functionalization through Polymer Grafting. **2018**.
- (7) Mu, M.; Composto, R. J.; Clarke, N.; Winey, K. I. Minimum in Diffusion Coefficient with Increasing {MWCNT} Concentration Requires Tracer Molecules to Be Larger than Nanotubes. *Macromolecules* **2009**, *42*, 8365–8369.
- (8) Cheng, S.; Carroll, B.; Bocharova, V.; Carrillo, J. M.; Sumpter, B. G.; Sokolov, A. P. Focus: Structure and Dynamics of the Interfacial Layer in Polymer Nanocomposites with Attractive Interactions. *J. Chem. Phys.* **2017**, *146*, 203201.
- (9) Lin, C.-C.; Gam, S.; Meth, J. S.; Clarke, N.; Winey, K. I.; Composto, R. J. Do Attractive Polymer–Nanoparticle Interactions Retard Polymer Diffusion in Nanocomposites? **2013**, *46*, 42.
- (10) Lin, Y.; Li, P.; Liu, W.; Chen, J.; Liu, X.; Jiang, P.; Huang, X. Application-Driven High-Thermal-Conductivity Polymer Nanocomposites. *ACS Nano* **2024**, *18*, 3851–3870.
- (11) Bocharova, V.; Genix, A.-C.; Carrillo, J.-M. Y.; Kumar, R.; Carroll, B.; Erwin, A.; Voylov, D.;

- Kisliuk, A.; Wang, Y.; Sumpter, B. G.; Sokolov, A. P. Addition of Short Polymer Chains Mechanically Reinforces Glassy Poly(2-Vinylpyridine)–Silica Nanoparticle Nanocomposites. *Cite This ACS Appl. Nano Mater* **2021**, *2020*, 21.
- (12) Raemdonck, K.; Braeckmans, K.; Demeester, J.; De Smedt, S. C. Merging the Best of Both Worlds: Hybrid Lipid-Enveloped Matrix Nanocomposites in Drug Delivery. *Chem. Soc. Rev* **2014**, *43*, 444.
 - (13) Parrish, E.; Caporizzo, M. A.; Composto, R. J. Network Confinement and Heterogeneity Slows Nanoparticle Diffusion in Polymer Gels. *J. Chem. Phys.* **2017**, *146*, 203318.
 - (14) Merkel, T. C.; Freeman, B. D.; Spontak, R. J.; He, Z.; Pinnau, I.; Meakin, P.; Hill, A. J. Ultrapervious, Reverse-Selective Nanocomposite Membranes. *Science (80-.)*. **2002**, *296*, 519–522.
 - (15) Yin, J.; Deng, B. Polymer-Matrix Nanocomposite Membranes for Water Treatment. *J. Memb. Sci.* **2015**, *479*, 256–275.
 - (16) Duncan, T. V. Applications of Nanotechnology in Food Packaging and Food Safety: Barrier Materials, Antimicrobials and Sensors. *J. Colloid Interface Sci.* **2011**, *363*, 1–24.
 - (17) Huang, J.-Y.; Li, X.; Zhou, W. Safety Assessment of Nanocomposite for Food Packaging Application. **2015**.
 - (18) Beecroft, L. L.; Ober, C. K. Nanocomposite Materials for Optical Applications. *Chem. Mater.* **1997**, *9*, 1302–1317.
 - (19) Barna, E.; Bommer, B.; Kürsteiner, J.; Vital, A.; Trzebiatowski, O. V; Koch, W.; Schmid, B.; Graule, T. Innovative, Scratch Proof Nanocomposites for Clear Coatings.
 - (20) Buitrago, C. F.; Pressly, J. F.; Yang, A. S.; Gordon, P. A.; Riggleman, R. A.; Natarajan, B.; Winey, K. I. Creep Attenuation in Glassy Polymer Nanocomposites with Variable Polymer–Nanoparticle Interactions. *Soft Matter* **2020**, *16*, 8912–8924.
 - (21) Vilay, V.; Mariatti, M.; Ahmad, Z.; Pasomsouk, K.; Todo, M. Characterization of the Mechanical

- and Thermal Properties and Morphological Behavior of Biodegradable Poly(L-Lactide)/Poly(ϵ -Caprolactone) and Poly(L-Lactide)/Poly(Butylene Succinate-L-Lactate) Polymeric Blends. *J. Appl. Polym. Sci.* **2009**, *114*, 1784–1792.
- (22) Mutiso, R. M.; Winey, K. I. Electrical Properties of Polymer Nanocomposites Containing Rod-like Nanofillers. *Prog. Polym. Sci.* **2015**, *40*, 63–84.
- (23) Lebedev, O. V.; Goncharuk, G. P.; Ozerin, A. N. Changes in Electrical Conductance of Polymer Composites Melts Due to Carbon Nanofiller Particles Migration. *Polym. 2021, Vol. 13, Page 1030* **2021**, *13*, 1030.
- (24) Tuteja, A.; Mackay, M. E.; Narayanan, S.; Asokan, S.; Wong, M. S. Breakdown of the Continuum Stokes-Einstein Relation for Nanoparticle Diffusion. *Nano Lett.* **2007**, *7*, 1276–1281.
- (25) Bailey, E. J.; Winey, K. I. Dynamics of Polymer Segments, Polymer Chains, and Nanoparticles in Polymer Nanocomposite Melts: A Review. *Prog. Polym. Sci.* **2020**, *105*, 101242.
- (26) Bailey, E. J.; Griffin, P. J.; Composto, R. J.; Winey, K. I. Multiscale Dynamics of Small, Attractive Nanoparticles and Entangled Polymers in Polymer Nanocomposites. *Macromolecules* **2019**, *52*, 2181–2188.
- (27) Grabowski, C. A.; Mukhopadhyay, A. Size Effect of Nanoparticle Diffusion in a Polymer Melt. *Macromolecules* **2014**, *47*, 7238–7242.
- (28) Shrestha, U. M.; Han, L.; Saito, T.; Schweizer, K. S.; Dadmun, M. D. Mechanism of Soft Nanoparticle Diffusion in Entangled Polymer Melts. **2022**, *14*, 45.
- (29) Cheng, S.; Xie, S.-J.; Carrillo, J.-M. Y.; Carroll, B.; Martin, H.; Cao, P.-F.; Dadmun, M. D.; Sumpter, B. G.; Novikov, V. N.; Schweizer, K. S.; Sokolov, A. P. Big Effect of Small Nanoparticles: A Shift in Paradigm for Polymer Nanocomposites. *ACS Nano* **2017**, *11*, 752–759.
- (30) Cruickshank, C. The Stokes-Einstein Law for Diffusion in Solution. *Proc. R. Soc. London. Ser. A, Contain. Pap. a Math. Phys. Character* **1924**, *106*, 724–749.

- (31) Kalathi, J. T.; Yamamoto, U.; Schweizer, K. S.; Grest, G. S.; Kumar, S. K. Nanoparticle Diffusion in Polymer Nanocomposites. *Phys. Rev. Lett.* **2014**, *112*, 108301.
- (32) Grabowski, C. A.; Mukhopadhyay, A. Size Effect of Nanoparticle Diffusion in a Polymer Melt. *Macromolecules* **2014**, *47*, 7238–7242.
- (33) Karatrantos, A.; Composto, R. J.; Winey, K. I.; Clarke, N. Polymer and Spherical Nanoparticle Diffusion in Nanocomposites. *J. Chem. Phys.* **2017**, *146*, 203331.
- (34) Rubinstein, M.; Colby, R. H. *Polymer Physics*; Oxford University Press, 2003.
- (35) Park, J.; Bailey, E. J.; Composto, R. J.; Winey, K. I. Single-Particle Tracking of Nonsticky and Sticky Nanoparticles in Polymer Melts. *Macromolecules* **2020**, *53*, 3933–3939.
- (36) Brochard Wyart, F.; de Gennes, P. G. Viscosity at Small Scales in Polymer Melts. *Eur. Phys. J. E Soft Matter* **2000**, *1*, 93–97.
- (37) Wang, L.; Ma, J.; Hong, W.; Zhang, H.; Lin, J. Nanoscale Diffusion of Polymer-Grafted Nanoparticles in Entangled Polymer Melts. *Macromolecules* **2020**, *53*, 8393–8399.
- (38) Sorichetti, V.; Hugouvieux, V.; Kob, W. Dynamics of Nanoparticles in Polydisperse Polymer Networks: From Free Diffusion to Hopping. *Macromolecules* **2021**, *54*, 8575–8589.
- (39) Cai, L. H.; Panyukov, S.; Rubinstein, M. Hopping Diffusion of Nanoparticles in Polymer Matrices. *Macromolecules* **2015**, *48*, 847–862.
- (40) Cai, L.-H.; Panyukov, S.; Rubinstein, M. Mobility of Nonsticky Nanoparticles in Polymer Liquids. *Macromolecules* **2011**, *44*, 7853–7863.
- (41) Maldonado-Camargo, L.; Rinaldi, C. Breakdown of the Stokes-Einstein Relation for the Rotational Diffusivity of Polymer Grafted Nanoparticles in Polymer Melts. *Nano Lett.* **2016**, *16*, 6767–6773.
- (42) Park, J.; Bailey, E. J.; Composto, R. J.; Winey, K. I. Single-Particle Tracking of Nonsticky and Sticky Nanoparticles in Polymer Melts. *Macromolecules* **2020**, *53*, 3933–3939.
- (43) Jimenez, A. M.; Zhao, D.; Misquitta, K.; Jestin, J.; Kumar, S. K. Exchange Lifetimes of the Bound

- Polymer Layer on Silica Nanoparticles. *ACS Macro Lett.* **2019**, *8*, 166–171.
- (44) Harton, S. E.; Kumar, S. K.; Yang, H.; Koga, T.; Hicks, K.; Lee, H.; Mijovic, J.; Liu, M.; Vallery, R. S.; Gidley, D. W. Immobilized Polymer Layers on Spherical Nanoparticles. *Macromolecules* **2010**, *43*, 3415–3421.
- (45) Griffin, P. J.; Bocharova, V.; Middleton, L. R.; Composto, R. J.; Clarke, N.; Schweizer, K. S.; Winey, K. I. Influence of the Bound Polymer Layer on Nanoparticle Diffusion in Polymer Melts. *ACS Macro Lett.* **2016**, *5*, 1141–1145.
- (46) Holt, A. P.; Griffin, P. J.; Bocharova, V.; Agapov, A. L.; Imel, A. E.; Dadmun, M. D.; Sangoro, J. R.; Sokolov, A. P. Dynamics at the Polymer/Nanoparticle Interface in Poly(2-Vinylpyridine)/ Silica Nanocomposites. *Macromolecules* **2014**, *47*, 1837–1843.
- (47) Holt, A. P.; Sangoro, J. R.; Wang, Y.; Agapov, A. L.; Sokolov, A. P. Chain and Segmental Dynamics of Poly(2-Vinylpyridine) Nanocomposites. **2013**.
- (48) Gong, C.; Weiblen, D.; Rende, D.; Akcora, P.; Ozisik, R. Stability of Particle Dispersion and Heterogeneous Interfacial Layers in Polymer Nanocomposites. *Polymer (Guildf)*. **2021**, *226*, 123813.
- (49) Giovino, M.; Pribyl, J.; Benicewicz, B.; Kumar, S.; Schadler, L. Linear Rheology of Polymer Nanocomposites with Polymer-Grafted Nanoparticles. *Polymer (Guildf)*. **2017**, *131*, 104–110.
- (50) Yang, S.; Akcora, P. Deformation of Chemically Heterogeneous Interfacial Layers of Polymer Nanocomposites. **2019**, *8*, 1635–1641.
- (51) Carroll, B.; Bocharova, V.; Carrillo, J.-M. Y.; Kisliuk, A.; Cheng, S.; Yamamoto, U.; Schweizer, K. S.; Sumpter, B. G.; Sokolov, A. P. Diffusion of Sticky Nanoparticles in a Polymer Melt: Crossover from Suppressed to Enhanced Transport. *Macromolecules* **2018**, *51*, 2268–2275.
- (52) Yamamoto, U.; Carrillo, J.-M. Y.; Bocharova, V.; Sokolov, A. P.; Sumpter, B. G.; Schweizer, K. S. Theory and Simulation of Attractive Nanoparticle Transport in Polymer Melts. *Macromolecules*

- 2018**, *51*, 2258–2267.
- (53) Mun, E. A.; Hannell, C.; Rogers, S. E.; Hole, P.; Williams, A. C.; Khutoryanskiy, V. V. On the Role of Specific Interactions in the Diffusion of Nanoparticles in Aqueous Polymer Solutions. *Langmuir* **2014**, *30*, 308–317.
 - (54) Al-Obaidi, H.; Florence, A. T. Nanoparticle Delivery and Particle Diffusion in Confined and Complex Environments. *J. Drug Deliv. Sci. Technol.* **2015**, *30*, 266–277.
 - (55) Wang, D.; Kou, R.; Choi, D.; Yang, Z.; Nie, Z.; Li, J.; Saraf, L. V.; Hu, D.; Zhang, J.; Graff, G. L.; Liu, J.; Pope, M. A.; Aksay, I. A. Ternary Self-Assembly of Ordered Metal Oxide-Graphene Nanocomposites for Electrochemical Energy Storage. *ACS Nano* **2010**, *4*, 1587–1595.
 - (56) Gong, M.; Zhang, L.; Wan, P. Polymer Nanocomposite Meshes for Flexible Electronic Devices. *Prog. Polym. Sci.* **2020**, *107*, 101279.
 - (57) Ge, T. Scaling Perspective on Dynamics of Nanoparticles in Polymers: Length- and Time-Scale Dependent Nanoparticle-Polymer Coupling. *Macromolecules* **2023**, *56*, 3809–3837.
 - (58) Bailey, E. J.; Griffin, P. J.; Composto, R. J.; Winey, K. I. Multiscale Dynamics of Small, Attractive Nanoparticles and Entangled Polymers in Polymer Nanocomposites. *Macromolecules* **2019**, *52*, 2181–2188.
 - (59) Genix, A.-C.; Bocharova, V.; Kisliuk, A.; Carroll, B.; Zhao, S.; Oberdisse, J.; Sokolov, A. P. Enhancing the Mechanical Properties of Glassy Nanocomposites by Tuning Polymer Molecular Weight. **2018**.
 - (60) Holt, A. P.; Bocharova, V.; Cheng, S.; Kisliuk, A. M.; White, B. T.; Saito, T.; Uhrig, D.; Mahalik, J. P.; Kumar, R.; Imel, A. E.; Etampawala, T.; Martin, H.; Sikes, N.; Sumpter, B. G.; Dadmun, M. D.; Sokolov, A. P. Controlling Interfacial Dynamics: Covalent Bonding versus Physical Adsorption in Polymer Nanocomposites. *ACS Nano* **2016**, *10*, 6843–6852.
 - (61) Cheng, S.; Holt, A. P.; Wang, H.; Fan, F.; Bocharova, V.; Martin, H.; Etampawala, T.; White, B.

- T.; Saito, T.; Kang, N.-G.; Dadmun, M. D.; Mays, J. W.; Sokolov, A. P. Unexpected Molecular Weight Effect in Polymer Nanocomposites. *Phys. Rev. Lett.* **2016**, *116*, 038302-1–4.
- (62) Holt, A. P.; Bocharova, V.; Cheng, S.; Kisliuk, A. M.; White, B. T.; Saito, T.; Uhrig, D.; Mahalik, J. P.; Kumar, R.; Imel, A. E.; Etampawala, T.; Martin, H.; Sikes, N.; Sumpter, B. G.; Dadmun, M. D.; Sokolov, A. P. Controlling Interfacial Dynamics: Covalent Bonding versus Physical Adsorption in Polymer Nanocomposites. **2016**.
- (63) Holt, A. P.; Griffin, P. J.; Bocharova, V.; Agapov, A. L.; Imel, A. E.; Dadmun, M. D.; Sangoro, J. R.; Sokolov, A. P. Dynamics at the Polymer/Nanoparticle Interface in Poly(2-Vinylpyridine)/ Silica Nanocomposites. *Macromolecules* **2014**, *47*, 1837–1843.
- (64) Bailey, E. J.; Griffin, P. J.; Tyagi, M.; Winey, K. I. Segmental Diffusion in Attractive Polymer Nanocomposites: A Quasi-Elastic Neutron Scattering Study. *Macromolecules* **2019**, *52*, 669–678.
- (65) Popov, I.; Carroll, B.; Bocharova, V.; Genix, A.-C.; Cheng, S.; Khamzin, A.; Kisliuk, A.; Sokolov, A. P. Strong Reduction in Amplitude of the Interfacial Segmental Dynamics in Polymer Nanocomposites. **2020**.
- (66) Lin, C. C.; Parrish, E.; Composto, R. J. Macromolecule and Particle Dynamics in Confined Media. *Macromolecules* **2016**, *49*, 5755–5772.
- (67) Roseker, W.; Hruszkewycz, S. O.; Lehmkuhler, F.; Walther, M.; Schulte-Schrepping, H.; Lee, S.; Osaka, T.; Strüder, L.; Hartmann, R.; Sikorski, M.; Song, S.; Robert, A.; Fuoss, P. H.; Sutton, M.; Stephenson, G. B.; Grübel, G. Towards Ultrafast Dynamics with Split-Pulse X-Ray Photon Correlation Spectroscopy at Free Electron Laser Sources. *Nat. Commun.* **2018**, *9*, 1–6.
- (68) Guo, H.; Bourret, G.; Lennox, R. B.; Sutton, M.; Harden, J. L.; Leheny, R. L. Entanglement-Controlled Subdiffusion of Nanoparticles within Concentrated Polymer Solutions. *Phys. Rev. Lett.* **2012**, *109*, 055901.
- (69) Manzo, C.; Garcia-Parajo, M. F. A Review of Progress in Single Particle Tracking: From Methods

- to Biophysical Insights. *Reports Prog. Phys.* **2015**, 78, 124601.
- (70) Rose, K. A.; Molaei, M.; Boyle, M. J.; Lee, D.; Crocker, J. C.; Composto, R. J. Particle Tracking of Nanoparticles in Soft Matter. *J. Appl. Phys.* **2020**, 127, 191101.
- (71) Kohli, I.; Mukhopadhyay, A. Diffusion of Nanoparticles in Semidilute Polymer Solutions: Effect of Different Length Scales. *Macromolecules* **2012**, 45, 6143–6149.
- (72) Grabowski, C. A.; Adhikary, B.; Mukhopadhyay, A. Dynamics of Gold Nanoparticles in a Polymer Melt. *Appl. Phys. Lett.* **2009**, 94, 021903.
- (73) Composto, R. J.; Kramer, E. J. Mutual Diffusion Studies of Polystyrene and Poly(Xylenyl Ether) Using Rutherford Backscattering Spectrometry. *J. Mater. Sci.* **1991**, 26, 2815–2822.
- (74) Composto, R. J.; Walters, R. M.; Genzer, J. Application of Ion Scattering Techniques to Characterize Polymer Surfaces and Interfaces. *Mater. Sci. Eng. R Reports* **2002**, 38, 107–180.
- (75) Cole, D. H.; Shull, K. R.; Rehn, L. E.; Baldo, P. M. RBS Analysis of the Diffusion of Nano-Size Spheres in a Polymer Matrix. *Nucl. Instruments Methods Phys. Res. Sect. B Beam Interact. with Mater. Atoms* **1998**, 136–138, 283–289.
- (76) Green, P. F.; Palmstrom, C. J.; Mayer, J. W.; Kramer, E. J. Marker Displacement Measurements of Polymer-Polymer Interdiffusion. *Macromolecules* **1985**, 18, 501–507.
- (77) Choi, J.; Cargnello, M.; Murray, C. B.; Clarke, N.; Winey, K. I.; Composto, R. J. Fast Nanorod Diffusion through Entangled Polymer Melts. *ACS Macro Lett.* **2015**, 4, 952–956.
- (78) Spool, A. M. *The Practice of TOF-SIMS: Time of Flight Secondary Ion Mass Spectrometry* - Alan M. Spool - Google Books; Momentum Press, 2016.
- (79) Mei, H.; Laws, T. S.; Terlier, T.; Verduzco, R.; Stein, G. E. Characterization of Polymeric Surfaces and Interfaces Using Time-of-Flight Secondary Ion Mass Spectrometry. *Journal of Polymer Science*. John Wiley and Sons Inc April 1, 2021, pp 1174–1198.
- (80) Zhang, A. C.; Maguire, S. M.; Ford, J. T.; Composto, R. J. Using Focused Ion Beam Time-of-Flight

- Secondary Ion Mass Spectrometry to Depth Profile Nanoparticles in Polymer Nanocomposites. *Microsc. Microanal.* **2023**, *29*, 1557–1565.
- (81) Karar, N.; Gupta, T. K. Study of Polymers and Their Blends Using TOF-SIMS Ion Imaging. *Vacuum* **2015**, *111*, 119–123.
- (82) Smentkowski, V.; Goswami, S.; Kollmer, F.; Zakel, J.; Arlinghaus, H.; Rading, D. Analysis of Thin Film Specimens Using {ToF-SIMS} Wedge Protocol, A Comparison with Depth Profiling. *Microsc. Microanal.* **2021**, *27*, 1564–1565.
- (83) Sui, T.; Song, B.; Dluhos, J.; Lu, L.; Korsunsky, A. M. Nanoscale Chemical Mapping of Li-Ion Battery Cathode Material by {FIB-SEM} and {TOF-SIMS} Multi-Modal Microscopy. *Nano Energy* **2015**, *17*, 254–260.
- (84) Karar, N.; Singh, B. P.; Elizabeth, I. Analysis of Multi-Wall Carbon Nanotube Based Porous Li Battery Electrodes' Using {TOF-SIMS} Ion Imaging. *Appl. Surf. Sci.* **2015**, *349*, 644–649.
- (85) Richardin, P.; Mazel, V.; Walter, P.; Lapr v te, O.; Brunelle, A. Identification of Different Copper Green Pigments in Renaissance Paintings by Cluster-TOF-SIMS Imaging Analysis. *J. Am. Soc. Mass Spectrom.* **2011**, *22*, 1729–1736.
- (86) Prasad, A.; Salim, N. V.; Mozeti , M.; Kailas, L.; Thomas, S. Time-of-flight Secondary Ion Mass Spectrometric Analysis of Polymer Surfaces: A Review. *J. Appl. Polym. Sci.* **2022**, 52286.
- (87) Kobayashi, K.; Watanabe, H.; Maekawa, K.; Kashiara, K.; Yamaguchi, T.; Asai, K.; Hirose, Y. Oxygen Distribution in Nickel Silicide Films Analyzed by Time-of-Flight Secondary Ion Mass Spectrometry. *Micron* **2010**, *41*, 412–415.
- (88) Lianos, L.; Quet, C.; Duc, T. M. Surface Structural Studies of Polyethylene, Polypropylene and Their Copolymers with ToF SIMS. *Surf. Interface Anal.* **1994**, *21*, 14–22.
- (89) Priebe, A.; Aribia, A.; Sastre, J.; Romanyuk, Y. E.; Michler, J. 3D High-Resolution Chemical Characterization of Sputtered Li-Rich NMC811 Thin Films Using TOF-SIMS. *Anal. Chem.* **2023**,

95, 1074–1084.

- (90) Poleunis, C.; Médard, N.; Bertrand, P. Additive Quantification on Polymer Thin Films by ToF-SIMS: Aging Sample Effects. *Appl. Surf. Sci.* **2004**, *231–232*, 269–273.
- (91) Xie, W.; Weng, L. T.; Yeung, K. L.; Chan, C. M. Segregation of Dioctyl Phthalate to the Surface of Polystyrene Films Characterized by ToF-SIMS and XPS. *Surf. Interface Anal.* **2018**, *50*, 1302–1309.
- (92) Lu, X.; Sjövall, P.; Soenen, H. Structural and Chemical Analysis of Bitumen Using Time-of-Flight Secondary Ion Mass Spectrometry (TOF-SIMS). *Fuel* **2017**, *199*, 206–218.
- (93) Bailey, J.; Havelund, R.; Shard, A. G.; Gilmore, I. S.; Alexander, M. R.; Sharp, J. S.; Scurr, D. J. 3D ToF-SIMS Imaging of Polymer Multilayer Films Using Argon Cluster Sputter Depth Profiling. *ACS Appl. Mater. Interfaces* **2015**, *7*, 2654–2659.
- (94) Prasad, A.; Salim, N. V.; Mozetič, M.; Kailas, L.; Thomas, S. Time-of-Flight Secondary Ion Mass Spectrometric Analysis of Polymer Surfaces: A Review. *J. Appl. Polym. Sci.* **2022**, *139*.
- (95) Chan, C. M.; Weng, L. T. Surface Characterization of Polymer Blends by XPS and ToF-SIMS. *Materials (Basel)*. **2016**, *9*.
- (96) Ravati, S.; Poulin, S.; Piyakis, K.; Favis, B. D. Phase Identification and Interfacial Transitions in Ternary Polymer Blends by ToF-SIMS. *Polymer (Guildf)*. **2014**, *55*, 6110–6123.
- (97) Brennan, B.; Spencer, S. J.; Belsey, N. A.; Faris, T.; Cronin, H.; Silva, S. R.; Sainsbury, T.; Gilmore, I. S.; Stoeva, Z.; Pollard, A. J. Structural, Chemical and Electrical Characterisation of Conductive Graphene-Polymer Composite Films. *Appl. Surf. Sci.* **2017**, *403*, 403–412.
- (98) Chen, W. Y.; Ling, Y. C.; Chen, B. J.; Shih, H. H.; Cheng, C. H. Diffusion Study of Multi-Organic Layers in OLEDs by ToF-SIMS. *Appl. Surf. Sci.* **2006**, *252*, 6594–6596.
- (99) Chan, C. M.; Weng, L. T. Surface Characterization of Polymer Blends by XPS and ToF-SIMS. *Mater.* **2016**, *Vol. 9, Page 655* **2016**, *9*, 655.
- (100) Fardim, P.; Gustafsson, J.; Von Schoultz, S.; Peltonen, J.; Holmbom, B. Extractives on Fiber

- Surfaces Investigated by XPS, ToF-SIMS and AFM. *Colloids Surfaces A Physicochem. Eng. Asp.* **2005**, 255, 91–103.
- (101) Abd Mutalib, M.; Rahman, M. A.; Othman, M. H. D.; Ismail, A. F.; Jaafar, J. Scanning Electron Microscopy (SEM) and Energy-Dispersive X-Ray (EDX) Spectroscopy. *Membr. Charact.* **2017**, 161–179.
- (102) Sakurada, T.; Hashimoto, S.; Tsuchiya, Y.; Tachibana, S.; Suzuki, M.; Shimizu, K. Lateral Resolution of EDX Analysis with Ultra Low Acceleration Voltage SEM. *sasj.jp* T Sakurada, S Hashimoto, Y Tsuchiya, S Tachibana, M Suzuki, K Shimizu *Journal Surf. Anal.* 2005•*sasj.jp* **2005**, 12.
- (103) Kubicek, M.; Holzlechner, G.; Opitz, A. K.; Larisegger, S.; Hutter, H.; Fleig, J. A Novel ToF-SIMS Operation Mode for Sub 100 Nm Lateral Resolution: Application and Performance. *Appl. Surf. Sci.* **2014**, 289, 407.
- (104) Moffitt, C. Fundamental Aspects of XPS and the Development of XPS Imaging. *Micros. Today* **2011**, 19, 16–21.
- (105) Powell, C. J.; Jablonski, A. Surface Sensitivity of X-Ray Photoelectron Spectroscopy. *Nucl. Instruments Methods Phys. Res. Sect. A Accel. Spectrometers, Detect. Assoc. Equip.* **2009**, 601, 54–65.
- (106) Watts, J. F.; Wolstenholme, J. An Introduction to Surface Analysis by XPS and AES. *An Introd. to Surf. Anal. by XPS AES* **2003**.
- (107) Chung, Y.; Pak, C.; Park, G.-S.; Jeon, W. S.; Kim, J.-R.; Lee, Y.; Chang, H.; Seung, D. Understanding a Degradation Mechanism of Direct Methanol Fuel Cell Using {ToF-SIMS} and {XPS}. *J. Phys. Chem. C Nanomater. Interfaces* **2008**, 112, 313–318.
- (108) Wang, K.; Composto, R. J.; Winey, K. I. ToF-SIMS Depth Profiling to Measure Nanoparticle and Polymer Diffusion in Polymer Melts. *Macromolecules* **2023**.

- (109) Harrison, E. T.; Peczonczyk, S. L.; Sharafi, A.; Wujcik, K. H.; Drews, A.; Simko, S. Surface Characterization of Battery Electrode/Electrolyte Materials Using {XPS} and {ToF-SIMS}. *Meet. abstr.* **2019**, *MA2019-01*, 521.
- (110) Balazs, A. C.; Emrick, T.; Russell, T. P. Nanoparticle Polymer Composites: Where Two Small Worlds Meet. *Science* (80-.). **2006**, *314*, 1107–1110.
- (111) Mills, P. J.; Green, P. F.; Palmstrøm, C. J.; Mayer, J. W.; Kramer, E. J. Polydispersity Effects on Diffusion in Polymers: Concentration Profiles of d-Polystyrene Measured by Forward Recoil Spectrometry. *J. Polym. Sci. Part B Polym. Phys.* **1986**, *24*, 1–9.
- (112) Green, P. F.; Kramer, E. J. Matrix Effects on the Diffusion of Long Polymer Chains. *Macromolecules* **1986**, *19*, 1108–1114.
- (113) Mackay, M. E.; Dao, T. T.; Tuteja, A.; Ho, D. L.; van Horn, B.; Kim, H.-C.; Hawker, C. J. Nanoscale Effects Leading to Non-Einstein-like Decrease in Viscosity. *Nat. Mater.* **2003**, *2*, 762–766.
- (114) Composto, R. J.; Mayer, J. W.; Kramer, E. J.; White, D. M. Fast Mutual Diffusion in Polymer Blends. *Phys. Rev. Lett.* **1986**, *57*, 1312–1315.
- (115) Composto, R. J.; Kramer, E. J.; White, D. M. Mutual Diffusion in the Miscible Polymer Blend Polystyrene/Poly(Xylenyl Ether). *Macromolecules* **1988**, *21*, 2580–2588.
- (116) Barrat, J.-L.; Fredrickson, G. H. Diffusion of a Symmetric Block Copolymer in a Periodic Potential. *Macromolecules* **1991**, *24*, 6378–6383.
- (117) Gam, S.; Meth, J. S.; Zane, S. G.; Chi, C.; Wood, B. A.; Seitz, M. E.; Winey, K. I.; Clarke, N.; Composto, R. J. Macromolecular Diffusion in a Crowded Polymer Nanocomposite. *Macromolecules* **2011**, *44*, 3494–3501.
- (118) Shrestha, U. M.; Han, L.; Saito, T.; Schweizer, K. S.; Dadmun, M. D. Mechanism of Soft Nanoparticle Diffusion in Entangled Polymer Melts. *Macromolecules* **2020**, *53*, 7580–7589.
- (119) Imel, A. E.; Rostom, S.; Holley, W.; Baskaran, D.; Mays, J. W.; Dadmun, M. D. The Tracer

- Diffusion Coefficient of Soft Nanoparticles in a Linear Polymer Matrix. *RSC Adv.* **2017**, *7*, 15574–15581.
- (120) Jo, K. Il; Oh, Y.; Kim, T. H.; Bang, J.; Yuan, G.; Satija, S. K.; Sung, B. J.; Koo, J. Position-Dependent Diffusion Dynamics of Entangled Polymer Melts Nanoconfined by Parallel Immiscible Polymer Films. *ACS Macro Lett.* **2020**, *9*, 1483–1488.
- (121) Lin, C.-C.; Griffin, P. J.; Chao, H.; Hore, M. J. A.; Ohno, K.; Clarke, N.; Riggelman, R. A.; Winey, K. I.; Composto, R. J. Grafted Polymer Chains Suppress Nanoparticle Diffusion in Athermal Polymer Melts. *J. Chem. Phys.* **2017**, *146*, 203332.
- (122) Mills, P. J.; Green, P. F.; Palmstrom, C. J.; Mayer, J. W.; Kramer, E. J. Analysis of Diffusion in Polymers by Forward Recoil Spectrometry. *Appl. Phys. Lett.* **1998**, *45*, 957.
- (123) Martín, J.; Hernández-Vélez, M.; de Abril, O.; Luna, C.; Muñoz-Martin, A.; Vázquez, M.; Mijangos, C. Fabrication and Characterization of Polymer-Based Magnetic Composite Nanotubes and Nanorods. *Eur. Polym. J.* **2012**, *48*, 712–719.
- (124) Bailey, E. J.; Griffin, P. J.; Composto, R. J.; Winey, K. I. Characterizing the Areal Density and Desorption Kinetics of Physically Adsorbed Polymer in Polymer Nanocomposite Melts. *Macromolecules* **2020**, *53*, 2744–2753.
- (125) Fit plane to 3-D point cloud - MATLAB pcfitplane
<https://www.mathworks.com/help/vision/ref/pcfitplane.html> (accessed Jun 22, 2022).
- (126) Fischler, M. A.; Bolles, R. C. Random Sample Consensus. *Commun. ACM* **1981**, *24*, 381–395.
- (127) Belu, A. M.; Davies, M. C.; Newton, J. M.; Patel, N. TOF-SIMS Characterization and Imaging of Controlled-Release Drug Delivery Systems. *Anal. Chem.* **2000**, *72*, 5625–5638.
- (128) Méar, F.; Coillot, D.; Podor, R.; Montagne, L. Self-Healing Nanocomposites: Role and Activation of Inorganic Moieties and Hybrid Nanophases. In *{Self-Healing} at the Nanoscale*; CRC Press, 2011; pp 188–223.

- (129) Mallakpour, S.; Naghdi, M. {Polymer/SiO₂} Nanocomposites: Production and Applications. *Prog. Mater. Sci.* **2018**, *97*, 409–447.
- (130) Young, W. W.; Katsumata, R. Intermediate Polymer Relaxation Explains the Anomalous Rheology of Nanocomposites with Ultrasmall Attractive POSS Nanoparticles. *ACS Polym. Au* **2023**, *3*, 466–474.
- (131) Lin, C.-C.; Parrish, E.; Composto, R. J. Macromolecule and Particle Dynamics in Confined Media. *Macromolecules* **2016**, *49*, 5755–5772.
- (132) Papakonstantopoulos, G. J.; Yoshimoto, K.; Doxastakis, M.; Nealey, P. F.; De Pablo, J. J. Local Mechanical Properties of Polymeric Nanocomposites. *Phys. Rev. E - Stat. Nonlinear, Soft Matter Phys.* **2005**, *72*, 031801-031801–031806.
- (133) Cheng, S.; Carroll, B.; Bocharova, V.; Carrillo, J.-M.; Sumpter, B. G.; Sokolov, A. P.; Carrillo, J.-M. Y. Perspective: Outstanding Theoretical Questions in Polymer-Nanoparticle Hybrids. *J. Chem. Phys.* **2017**, *146*, 203201.
- (134) Liu, J.; Cao, D.; Zhang, L. Molecular Dynamics Study on Nanoparticle Diffusion in Polymer Melts: A Test of the Stokes-Einstein Law. *J. Phys. Chem. C* **2008**, *112*, 6653–6661.
- (135) Mendez, N. F.; Dhara, D.; Zhang, Q.; Narayanan, S.; Schadler, L. S.; Müller, A. J.; Kumar, S. K. Nanoparticle Diffusion in Miscible Polymer Nanocomposite Melts. *Macromolecules* **2023**, *56*, 4658–4668.
- (136) Kwon, N. K.; Park, C. S.; Lee, C. H.; Kim, Y. S.; Zukoski, C. F.; Kim, S. Y. Tunable Nanoparticle Stability in Concentrated Polymer Solutions On the Basis of the Temperature Dependent Solvent Quality. *Macromolecules* **2016**, *20*, 25.
- (137) Jin, J.; Wang, X.; Wick, C. D.; Dang, L. X.; Miller, J. D. Silica Surface States and Their Wetting Characteristics. <https://doi.org/10.1680/jsuin.19.00053> **2020**, *8*, 145–157.
- (138) Watcharenwong, A.; Saijaioup, N.; Bailuang, Y.; Kajitvichyanukul, P. Morphology and Wettability

- of Nanoporous Aluminium Oxide Film Prepared by Anodization. *Key Eng. Mater.* **2017**, 737, 174–178.
- (139) Bronstein, N. D.; Li, L.; Xu, L.; Yao, Y.; Ferry, V. E.; Alivisatos, A. P.; Nuzzo, R. G. Luminescent Solar Concentration with Semiconductor Nanorods and Transfer-Printed Micro-Silicon Solar Cells. *ACS Nano* **2014**, 8, 44–53.
- (140) Mun, E. A.; Hannell, C.; Rogers, S. E.; Hole, P.; Williams, A. C.; Khutoryanskiy, V. V. On the Role of Specific Interactions in the Diffusion of Nanoparticles in Aqueous Polymer Solutions. *Langmuir* **2014**, 30, 308–317.
- (141) Senses, E.; Ansar, S. M.; Kitchens, C. L.; Mao, Y.; Narayanan, S.; Natarajan, B.; Faraone, A. Small Particle Driven Chain Disentanglements in Polymer Nanocomposites. *Phys. Rev. Lett.* **2017**, 118.
- (142) Gong, S.; Chen, Q.; Moll, J. F.; Kumar, S. K.; Colby, R. H. Segmental Dynamics of Polymer Melts with Spherical Nanoparticles. *ACS Macro Lett.* **2014**, 3, 773–777.
- (143) Tuteja, A.; Mackay, M. E.; Hawker, C. J.; Van Horn, B. Effect of Ideal, Organic Nanoparticles on the Flow Properties of Linear Polymers: Non-Einstein-like Behavior. *Macromolecules* **2005**, 38, 8000–8011.
- (144) Meth, J. S.; Gam, S.; Choi, J.; Lin, C. C.; Composto, R. J.; Winey, K. I. Excluded Volume Model for the Reduction of Polymer Diffusion into Nanocomposites. *J. Phys. Chem. B* **2013**, 117, 15675–15683.
- (145) Gam, S.; Meth, J. S.; Zane, S. G.; Chi, C.; Wood, B. A.; Winey, K. I.; Clarke, N.; Composto, R. J. Polymer Diffusion in a Polymer Nanocomposite: Effect of Nanoparticle Size and Polydispersity. *Soft Matter* **2012**, 8, 6512.
- (146) Xue, C.; Zheng, X.; Chen, K.; Tian, Y.; Hu, G. Probing Non-Gaussianity in Confined Diffusion of Nanoparticles. *J. Phys. Chem. Lett.* **2016**, 7, 514–519.
- (147) Babayekhorasani, F.; Dunstan, D. E.; Krishnamoorti, R.; Conrad, J. C. Nanoparticle Diffusion in

- Crowded and Confined Media. *Soft Matter* **2016**, *12*, 8407–8416.
- (148) Schneider, G. J.; Nusser, K.; Willner, L.; Falus, P.; Richter, D. Dynamics of Entangled Chains in Polymer Nanocomposites. *Macromolecules* **2011**, *44*, 5857–5860.
- (149) Bailey, E. J.; Riggleman, R. A.; Winey, K. I. Polymer Conformations and Diffusion through a Monolayer of Confining Nanoparticles. *Macromolecules* **2020**, *53*, 8171–8180.
- (150) Wang, K.; Winey, K. I. Vehicular and Core-Shell Nanoparticle Diffusion in Entangled Polymer Melts. Submitted.
- (151) Tonelli, A. E. Conformational Characteristics of Poly(2-Vinylpyridine). *Macromolecules* **1985**, *18*, 2579–2583.
- (152) Sko, T.; Vaghefikia, F.; Fitter, rg; Kondrat, S. Macromolecular Crowding: How Shape and Interactions Affect Diffusion. *J. Phys. Chem* **2023**, *2020*, 19.
- (153) Hao, T.; Riman, R. E. Calculation of Interparticle Spacing in Colloidal Systems. *J. Colloid Interface Sci.* **2006**, *297*, 374–377.
- (154) Brouwers, H. J. H. Particle-Size Distribution and Packing Fraction of Geometric Random Packings. *Phys. Rev. E - Stat. Nonlinear, Soft Matter Phys.* **2006**, *74*, 031309.
- (155) Karatrantos, A.; Composto, R. J.; Winey, K. I.; Clarke, N. Nanorod Diffusion in Polymer Nanocomposites by Molecular Dynamics Simulations. *Macromolecules* **2019**, *52*, 2513–2520.
- (156) Asgari, N.; Baaske, M. D.; Orrit, M. Burst-by-Burst Measurement of Rotational Diffusion at Nanosecond Resolution Reveals Hot-Brownian Motion and Single-Chain Binding. *ACS Nano* **2023**, *17*, 12684–12692.
- (157) Jouault, N.; Zhao, D.; Kumar, S. K. Role of Casting Solvent on Nanoparticle Dispersion in Polymer Nanocomposites. **2014**.
- (158) Murphy, T. M.; Langhe, D. S.; Ponting, M.; Baer, E.; Freeman, B. D.; Paul, D. R. Physical Aging of Layered Glassy Polymer Films via Gas Permeability Tracking. *Polymer (Guildf)*. **2011**, *52*, 6117–

6125.

- (159) Karen, A.; Ito, K.; Kubo, Y. {TOF-SIMS} Analysis of Lithium Air Battery Discharge Products Utilizing Gas Cluster Ion Beam Sputtering for Surface Stabilization. *Surf. Interface Anal.* **2014**, *46*, 344–347.
- (160) Foley, J. D.; Fischler, M. A.; Bolles, R. C. Graphics and Image Processing Random Sample Consensus: A Paradigm for Model Fitting with Apphcatlons to Image Analysis and Automated Cartography. **1981**.
- (161) Point Cloud Processing - MATLAB & Simulink <https://www.mathworks.com/help/vision/point-cloud-processing.html> (accessed May 6, 2024).
- (162) Wang, X.; Tilley, R. D.; Watkins, J. J. Simple Ligand Exchange Reactions Enabling Excellent Dispersibility and Stability of Magnetic Nanoparticles in Polar Organic, Aromatic, and Protic Solvents. *Langmuir* **2014**, *30*, 1514–1521.
- (163) Cook, E.; Labiento, G.; Chauhan, B. P. S. Fundamental Methods for the Phase Transfer of Nanoparticles. *Molecules* **2021**, *26*.

APPENDIX E : PREPARATION OF ALUMINA NANOPARTICLES

Dispersing dry oxide particles in a solvent improves the variety of material options available for formulating polymer nanocomposite (PNC) solutions. However, unmodified NP surfaces, especially in oxide particles, have a strong tendency to aggregate when placed in solvent. This section briefly describes the procedure to disperse dry alumina oxide nanoparticles in methanol through functionalizing the surface with a P2VP bound layer.

E.1 Preparation of Alumina-P2VP Solution

Dry aluminum oxide (Al_2O_3) NPs were purchased from Sigma Aldrich of $R_{\text{NP}} = 6.5$ nm in 100 g quantities. Due to the easily airborne nature of the powdered particles, the entire procedure is conducted in a hood to prevent inhalation. The main goal of this procedure is to remove existing aggregates and prevent aggregation of the NPs in solution. It must be assumed due to the dry nature of the particles that surface sintering has occurred, and many aggregates exist prior to the addition of solvent.

The primary mechanism of aggregation in solution is bare NP contact, resulting in strong van der Waals and hydrogen bonding creating nearly irreversible aggregation. Particle aggregation in solution is reduced in three ways in this procedure: 1) Adding minimal amounts of dry particle at a time to the solution, 2) adding dry particles directly to a dilute P2VP solutions while using a stir bar, and 3) sonication for an intermediate amount of time. The secondary cause of aggregation is prior surface sintered NPs in the dry state. These aggregates are 1) broken apart during the sonication phase or 2) filtered out.

This procedure must be done sequentially and in one session to avoid aggregation.

1). Prepare a bulk 100 g/L P2VP-methanol solution of any molecular weight. Using this bulk solution, create a separate dilute solution of 10 mg/mL and set aside. I arbitrarily choose a dilute amount of P2VP chains in excess of the number of particles. For a more precise minimum amount of polymer, calculate the projected surface area of a single chain onto the surface area of the

particle, then multiply the resulting polymer concentration by ~ 4 . Excess polymer in the solution improves the chance of bound layer formation before aggregation can occur.

2) Obtain 3 vials. In the first one, add a stir bar, then 20 mg/mL P2VP, then 10 mg of raw Al_2O_3 NPs per mL of solution present, with constant stirring. The solution should appear milky white. Immediately transfer the solution into a syringe and pass through a 1 μm filter into the second vial. There will be significant resistance due to the large number of aggregates, and this step will remove the largest aggregates immediately. We assume very little to none of the polymer is filtered out at this stage due to the large size of the filter.

3) The resulting solution in the second vial should appear cloudy, but not solid white due to the presence of intermediately sized aggregates. At this step, ~ 15 minutes of sonication aids in breaking aggregates along with vortexing the solution for ~ 30 seconds.

4) Immediately transfer to a clean syringe and pass through a 0.200 μm filter. When filtering, there should not be strong resistance to pass the solution through. The vast majority of aggregates should have been removed in step 2, and the filter should be able to be used at least 4-5 times. The resulting solution should be clear with no cloudiness.

5) The filtration process will reduce the total yield of NPs to 5-10% of the initial amount. To achieve higher concentrations of NPs, allow solution to stir uncovered in the hood to evaporate excess solvent off. Additionally, repeat the procedure and add more dilute Al_2O_3 solution to the same vial, and continue to evaporate. Slow gas flow (N_2) over the surface of the solution (just perturb the surface) and heating to $\sim 100^\circ\text{C}$ allows for faster evaporation. Under gas flow and

with heating, the solution evaporates at about ~1 mL/hour. Do not allow the solution to evaporate completely.

6) Test concentration of the solution by removing a select amount (200 μ L is suitable) and heating to completely evaporate solvent and weighing the resultant solid. Subtract out the mg/mL of P2VP in the solution to obtain the amount of NP present/mL. TGA measurements or full drying in a box oven can provide more accurate results if necessary.

7) Repeat this process to desired NP concentration. For my experiments, this was about 10 times. After creating well dispersed Al_2O_3 NPs, ensure good dispersion with DLS, and add concentrated P2VP/methanol solution to the desired concentration.

E.2 Qualitative Notes

1) The stoichiometry of this experiment becomes quite complicated due to the addition of bound polymer to the NP in solution with every cycle of the process. Keeping good notes of the number of repeats of the process is essential to obtain accurate weight measurements.

2) I have not found excessive sonication to improve NP yield in the final solution (> 15 minutes). Initial sonication is necessary and seems to break up weakly aggregated NPs, but after these are separated, the larger strongly aggregated NPs never separate and need to be filtered. Additionally, sonication without the presence of the bound layer will **create** rather than break aggregates due to particle-particle contacts. Sonication also heats the solution. This is why the dry NPs should never

be sonicated in pure solvent. If after sonication the solution is more opaque, bound layer formation did not occur.

3) Visual and tactile observation during this process is the quickest and most important tool for checking your results. Excessive tactile resistance during filtering, or any visual cloudiness indicates the formation of aggregates. Completing this process as quickly as possible will result in highest NP yield, due to getting the NPs in a dilute solution with excess polymer quickly. Waiting in between steps allows for more aggregation of the particles, as well as particle sedimentation. The bound layer prevents these issues, especially in more concentrated polymer PNC solutions.

4) I attempted to add excess polymer to the initial solution, however the increased viscosity made it difficult to pass through the filtration steps, as well as more difficult to quantify the amount of polymer in the resulting solution. Processing and filtering the solutions with dilute amounts of polymer (~ 4 chains/NP) allows for higher accuracy in recreating the PNC.

APPENDIX F : SOLVENT EXCHANGE OF LUDOX NANOPARTICLES

F.1 Materials and Motivation

Ludox Silica Nanoparticles (NPs) are colloidal suspensions of silica particles in water, known for their uniformity and high surface area. This solvent exchange process entails transitioning these NPs from a water to an ethanol solvent system. This process is crucial for applications requiring a non-aqueous medium, such as for spincoating applications. Traditional solvent exchange methodology, involving crashing the particles out with a poor solvent and centrifuging the particles into a solid pellet, often results in irreversible aggregation of the silica NPs due to the lack of surface modification that would allow for re-dispersal of the particles. In developing this methodology, I adapt the concept of a miscible solvent exchange to avoid the centrifugal step that would result in aggregation.¹⁶²

Poly 2-vinyl pyridine (P2VP) polymer is introduced to the Ludox NPs during the exchange process as an easy spontaneous surface functionalization. P2VP, soluble in ethanol, serves to form a bound layer around the nanoparticles. This polymer layer is key to preventing aggregation, ensuring the nanoparticles remain stable and dispersed throughout the solvent exchange process as we exchange the particles to ethanol. The resulting ethanol-P2VP-SiO₂ solution is suitable for solvent casting or spincoating polymer films.

F.2 Miscible Solvent Exchange Preparation

Miscible solvent exchange is a technique commonly used in the drug delivery field to modify the solvation environment around a solute, such as nanoparticles or polymers, without precipitating the solute. The process involves the gradual replacement of one solvent in which the

solute is dissolved with another solvent that is miscible with the first. This is often done to change the properties of the solution, such as viscosity, polarity, or to initiate processes like nanoparticle formation or polymerization.¹⁶³

The goal is to ensure that the transition from one solvent to another does not destabilize or change the structural integrity of the solute. This technique is particularly useful in the synthesis and stabilization of nanoparticles, where controlling the surface chemistry and solvation can critically affect the properties like dispersion stability, particle size, and functionality. Successful exchange relies on the compatibility of the two solvents, controlled addition rates to prevent shock to the system, and maintaining conditions that preserve the stability of the solutes. Pros include the ability to adapt materials for different environments and enhance reaction outcomes. Cons involve potential solute instability and the complexity of managing large volumes. Unlike centrifuging, which physically separates phases, miscible exchange maintains a single phase, offering smoother transitions but requiring careful control to avoid solute destabilization.¹⁶³

Factors causing solute destabilization during miscible solvent exchange include rapid solvent addition, leading to osmotic shocks or changes in solute-solvent interactions. Temperature fluctuations can also disrupt solute stability by altering solvent properties and solute solubility. The presence of impurities or incompatible solvents may induce precipitation or phase separation. Careful control over exchange conditions, such as gradual solvent addition and temperature stability, is crucial to prevent destabilization.¹⁶³

Sample Preparation

Ludox NP solution is typically highly concentrated (~ 31 wt% = 376 g/L SiO_2), allowing very small amounts of water to contain a large number of particles. Calculate the total amount of

NP volume desired in the final solution (choose a final volume), then add this amount to a vial with a stir bar.

This procedure details the preparation of a PNC solution containing Ludox nanoparticles (NPs) and poly(2-vinylpyridine) (P2VP) of 30 g/L P2VP, and 5 vol% Ludox SiO₂. The following steps outline the preparation process:

1. **Prepare a concentrated P2VP Solution:** Add 0.450 mL of 100 g/L P2VP-ethanol solution to a vial with a stir bar. We aim to expose the bare SiO₂ NPs to as little ethanol solvent as possible prior to the formation of the polymer bound layer. Therefore, addition of a small amount of concentrated polymer solution aids bound layer formation while avoiding NP crashing.
2. **Incorporate NPs into the P2VP Solution:** Introduce the Ludox NPs gradually to the P2VP/EtOH solution with continuous stirring. In this case, we add 0.0362 mL of Ludox NP solution (31 wt% in H₂O, 376 g/L SiO₂) dropwise with a 20-200 µL pipette. This results in a highly viscous NP-P2VP mixture totaling 0.48 mL. Addition of ethanol solution too quickly with polymer will result in spontaneous gelation, or P2VP precipitation. If you observe white strings (polymer) or the stir bar becoming frozen, the solution was added too quickly, and gelation or precipitation occurred.
3. **Adjust the Ethanol Content:** Add ethanol drop by drop to the NP-P2VP mixture until achieving the desired concentration of NPs and P2VP, with constant stirring. The final volume should be about 1.5 mL after adding 1.01 mL of ethanol.

4. **Ensure Thorough Mixing:** Stir the final solution continuously for at least an hour (ideally overnight) to ensure proper mixing and uniform distribution of P2VP and bound layer formation.

This process results in small amounts of the original carrier in final solution; since Ludox particles are highly concentrated luckily there is very little resultant water. This naturally puts a NP concentration upper limit on the final PNC solution, fully dependent on the initial dispersed NP solution purchased. This presents an alternative method to performing NP solvent exchange while avoiding addition of a poor solvent, and the centrifuging step in the case of NPs that have a high tendency to aggregate.

In Figure F.1, using 158 kDa P2VP, Ludox NPs in ethanol display good dispersion via DLS, with a hydrodynamic diameter of $2 \cdot R_{hydro} = 27 \pm 10$ nm. With R_{NP} (= 8.3 nm) + R_g (= 10.9 nm) \sim 19 nm, an effective hydrodynamic diameter of \sim 38 nm is expected. This may demonstrate a smaller R_g than expected in the ethanol/water mix, consistent with water being a poor solvent for P2VP, or a bound layer that hydrodynamically appears smaller than the melt R_g . Nonetheless, this demonstrates the SiO₂ NPs are well-dispersed after solvent exchange.

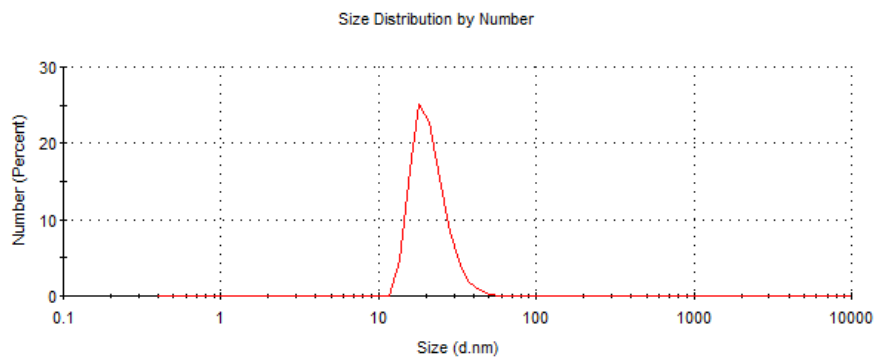


Figure F.1: The DLS size distribution by number shows a single, well-defined peak, indicating the absence of significant aggregation or large aggregate peaks. $2 \cdot R_{\text{hydro}} = 27 \pm 10$ nm.